Synthesis and Properties of Ion-Containing Block and Segmented Copolymers and Their Composites

Renlong Gao

Dissertation submitted to the faculty of the
Virginia Polytechnic Institute and State University
in partial fulfillment of the requirements for the degree of

Doctor of Philosophy
in
Chemistry

Timothy E. Long, Chair
Robert B. Moore
Louis A. Madsen
S. Richard Turner
Pavlos P. Vlachos

March 16, 2012
Blacksburg, Virginia

Keywords: step-growth polymerization, sulfonated polyurethane, sulfonated block copolymer, multi-walled carbon nanotubes, ionic liquids, nanocomposites, electroactive actuator

Synthesis and Properties of Ion-Containing Block and Segmented Copolymers and Their Composites

Renlong Gao

ABSTRACT

Ion-containing segmented polyurethanes exhibit unique morphology and physical properties due to synergistic interactions of electrostatic, hydrogen bonding, and hydrophobic interactions. A fundamental investigation on a series of well-defined ion-containing polyurethanes elucidated the influence of charge placement, charge density, and soft segment structure on physical properties, hydrogen bonding, and morphologies. An unprecedented comparison of poly(ethylene oxide)(PEO)-based sulfonated polyurethanes containing sulfonate anions either in the soft segments or hard segments revealed that sulfonate charge placement dramatically influenced microphase separation and physical properties of segmented polyurethanes, due to altered hydrogen bonding and thermodynamic immiscibility between soft and hard segments. Moreover, studies on sulfonated polyurethanes with identical sulfonated hard segments but different soft segment structures indicated that soft segment structure tailored sulfonated polyurethanes for a wide range of mechanical properties.

Sulfonated polyurethanes incorporated with ammonium-functionalized multi-walled carbon nanotubes (MWCNTs) generated novel polyurethane nanocomposites with significantly enhanced mechanical performance. Modification of MWCNTs followed a dendritic strategy, which doubled the functionality by incorporating two ammonium cations per acid site. Complementary characterization demonstrated successful covalent functionalization and formation of surface-bound ammonium salts. Upon comparison with pristine MWCNTs, ammonium-functionalized MWCNTs exhibited significantly enhanced dispersibility in both

DMF and sulfonated polyurethane matrices due to good solvation of ammonium cations and intermolecular ionic interactions between anionic polyurethanes and cationic MWCNTs.

Segmented polyurethanes containing sulfonated PEO-based soft segments and nonionic hard segments were incorporated with various contents of room temperature ionic liquid, 1-ethyl-3-methylimidazolium ethylsulfate (EMIm ES), to investigate the influence of ionic liquid on physical properties, morphologies, and ionic conductivity. Results indicated that EMIm ES preferentially located in the sulfonated PEO soft phase, leading to significantly enhanced ionic conductivity and well-maintained mechanical properties. These properties are highly desirable for electromechanical transducer applications. Electromechanical actuators fabricated with sulfonated polyurethane/IL composite membranes exhibited effective response under a low applied voltage (4 V). However, in the case of an imidazolium-containing segmented polyurethane with imidazolium ionic hard segments and hydrophobic poly(tetramethylene oxide) (PTMO) soft segments, EMIm ES selectively located into the imidazolium ionic hard domains, as evidenced with a constant PTMO soft segment glass transition temperature (T_g) and systematically reduced imidazolium hard segment T_g. Dielectric relaxation spectroscopy demonstrated that ionic conductivity of imidazolium-containing segmented polyurethanes increased by five orders of magnitude upon incorporation of 30 wt% EMIm ES.

Imidazolium-containing sulfonated pentablock copolymers were also investigated to elucidate the influence of imidazolium counter cation structures on solution rheology, morphology, and thermal and mechanical properties. Combination of living anionic polymerization and post functionalization strategies provided well-defined sulfonated pentablock copolymers containing structured imidazolium cations in sulfonated polystyrene middle block. Varying alkyl substitute length on imidazolium cations tailored physical properties and

morphologies of sulfonated pentablock copolymers. Results indicated that long alkyl substitutes (octyl and dodecyl) on imidazolium cations significantly influenced solution rheological behavior, morphology, and water uptake properties of sulfonated pentablock copolymers due to the altered characteristic of imidazolium cations. Imidazolium-containing sulfonated pentablock copolymers exhibited systematically tailored mechanical properties due to the plasticizing effect of alkyl substitutes. In addition, incorporation of ionic liquids into sulfonated pentablock copolymers further tailored their mechanical properties and ionic conductivity, which made these materials suitable for electromechanical transducer applications. All sulfonated pentablock copolymers were successfully fabricated into actuator devices, which exhibited effective actuation under a low applied voltage (4 V).

ACKNOWLEDGEMENTS

I would like to firstly thank my advisor, Prof. Timothy E. Long, for his guidance and tremendous support throughout the course of my graduate career. I really appreciate his patience, encouragement, and confidence in me since the first day I joined the group. I would like to extend my gratitude to the rest of my committee: Prof. S Richard Turner, Prof. Robert B. Moore, Prof. Louis A. Madsen, and Prof. Pavlos P. Vlachos, for their guidance and support with my graduate study at Virginia Tech.

I would like to thank the funding agencies for providing financial support to my research: National Science Foundation, ICTAS, ILEAD MURI, Bayer Materials Science, Kraton Polymers LLC. I would also like to thank my collaborators: Prof. Robert B. Moore, Mingqiang Zhang, and Ninad Dixit at Chemistry Department at Virginia Tech, Prof. Ralph Colby and Shih-wa Wang at Penn State University, Prof. Heflin and Dong Wang in Physics Department at Virginia Tech, Prof. David Green and Jeremy Fowler at University of Virginia, Carl Willis at Kraton Polymer LLC, Karl Haider and Serkan Unal at Bayer Materials Science, and Steve McCartney at NCFL for their great work and support with my research.

Additionally, the research could not have been accomplished without the support of many people that I have been working with closely. I would like to thank Valerie Owens, Naya, Tammy Jo Hinner, Laurie Good, and Mary Jane Smith, who have been truly helpful with all kinds of meeting schedule, ordering, traveling, etc. I would also like to thank all the post-docs and graduate students in our research group: Tomonori, Sean Ramirez, Erin, Daisuke, Rebecca, Matt Cashion, Andy, Gozde, Sharlene, Takeo, Matt Hunley, Emily, Shijing, Mana, Tianyu, Matt Green, Eva, Steve, Mike, Nancy, Ali, Sean Hemp, David, Alie, Alex, Ashley, Chainika, Keren, and Evan. I would also like to thank all my good friends in blacksburg: Tianyu, Jianbo,

Xiaosong, Jing Sun, Jiajia, Xu, Jing Wang, Furong, and bin for all the good times we spent together.

Lastly, I want to thank my family for their constant love and support throughout my life, especially my mom and dad. I want to express my special thanks to Yannan, who has been one of the most important people in my life. Thanks for her love and support throughout the years of graduate school.

Table of Contents

List of Figures

List of Tables

List of Schemes

Chapter 1: Introduction

1.1 Dissertation Overview

This dissertation focuses on the synthesis and characterization of ion-containing block and segmented copolymers and fabrication of polymer nanocomposites with tailored mechanical properties and enhanced ionic conductivity. The initial chapters focus on sulfonated segmented polyurethanes to elucidate their structure-morphology-property relationships and investigate the influence of carbon nanotubes and ionic liquids on their physical properties and morphologies. The subsequent two chapters describe the synthesis and characterization of novel imidazolium-containing segmented polyurethanes and their ionic liquid-based nanocomposites. The final chapters discuss the modification of sulfonated pentablock copolymers with structured imidazolium counter cations and imidazolium-based ionic liquids.

Chapter two reviews the synthesis, characterization, and application of sulfonated block and segmented copolymers. Chapter three focuses on the influence of sulfonate charge placement on physical properties and morphologies of segmented polyurethanes containing poly(ethylene oxide) (PEO)-based soft segments. PEO-based sulfonated polyurethanes were synthesized through direct polymerization of sulfonated monomers, which afforded controlled sulfonate charge placement either in the soft segments or hard segments. Sulfonate charge in different segments significantly influenced microphase separation behavior of sulfonated polyurethanes, leading to dramatically tailored thermal and mechanical properties. Chapter four focuses on sulfonated polyurethanes with identical sulfonated hard segments but different soft segments to elucidate the influence of soft segment structure on physical properties and morphology. Chapter five describes the influence of ionic liquid on performance of PEO-based sulfonated polyurethanes. Due to preferential incorporation of 1-ethyl-3-methylimidazolium ethylsulfate (EMIm ES) into sulfonated PEO soft phase, sulfonated polyurethane/EMIm ES composite

membranes exhibited significantly enhanced ionic conductivity and well-maintained mechanical properties. Chapter six describes the modification of multi-walled carbon nanotubes (MWCTNs) with surface-bound ammonium cations and the fabrication of PEO-based sulfonated polyurethane/ammonium-functionalized MWCNTs nanocomposites. Complementary characterization using TGA, XPS, and Raman spectroscopy demonstrated successful covalent functionalization and formation of surface-bound ammonium cations. Ammonium-functionalized MWCNTs exhibited uniform dispersion in sulfonated polyurethane matrices, leading to linearly increased Young's moduli of sulfonated polyurethanes as a function of MWCNT contents.

Chapter seven details the synthesis and characterization of novel ion-containing segmented polyurethanes bearing imidazolium cations in the hard segments (IPU), and chapter eight discusses the influence of ionic liquid, EMIm ES, on performance of imidazolium-containing polyurethanes. In comparison of sulfonated polyurethane/EMIm ES composite membranes, where EMIm ES preferentially located in the ionic soft segments, IPU exhibited preferential incorporation of EMIm ES in the imidazolium ionic hard segments, as evidenced with systematically reduced hard segment T_g and increased inter-domain spacings.

Chapter nine describes the influence of imidazolium counter cation structures on solution rheology, morphology, thermal and mechanical properties, and water uptake properties of sulfonated pentablock copolymers. Characterization results indicated that varying alkyl substitute length on imidazolium cations dramatically tailored the morphology and physical properties of sulfonated pentablock copolymers. Chapter ten studies the influence of ionic liquid on mechanical properties of sulfonated pentablock copolymers and describes the application of sulfonated pentablock copolymer/ionic liquid composite membrane for electromechanical actuators.

Chapter 2: Literature Review: Sulfonated Block and Segmented Copolymers for Emerging Technologies

2.1 Introduction

Non-covalent interactions such as hydrogen bonding, ionic interaction, and Van der Waals interaction play an important role in controlling the structure and properties of polymers. Researchers have utilized non-covalent interactions to design novel polymer structures with various desired functions.[1-12] Compared with hydrogen bonding and Van der Waals interactions, ionic interaction is much stronger and thus performs better in tailoring the chemical and physical properties of polymers.[13]

Sulfonated block and segmented copolymers are a unique class of ion-containing polymers that have attracted significant attention because of their current and future applications in biomedical materials, water treatments, fuel cells, solar cells, and electroactive devices.[14-27] Combination of the properties of different blocks and segments affords sulfonated block and segmented copolymers outstanding mechanical properties and high conductivities. Properties of sulfonated block and segmented copolymers depend strongly on their chemical architectures including block composition, molecular weight and molecular weight distribution on each block, sulfonation level, and counteraction structures.[28-30] Nafion® is an important class of commercially available sulfonated copolymers, which has been extensively studied since it was discovered by Dupont in 1962.[31-38] The use of Nafion® (Figure 2.1) as proton conductor for proton-exchange-membrane fuel cells (PEMFC) enables to fabricate environmentally friendly devices that convert chemical energy from fuels directly into electrical energy. However, high costs, high methanol permeability as well as low conductivity at high temperatures (above 80 ^{o}C) and low humidity have seriously limited their applications.[39] New efforts have been devoted to

exploiting new sulfonated copolymers for proton-exchange-membranes.[22,40-49] In addition, sulfonated block and segmented copolymers, e.g. sulfonated poly(styrene-*b*-ethylene/butylenes-*b*-styrene), are also biocompatible and possess antithrombogenic properties.[50] Researchers have utilized these polymers to modify the surface of medical devices such as stents and catheters. Currently, there is a high demand for biocompatible materials designed for emerging biomedical applications.[51] In order to tailor sulfonated polymers for desired properties and to explore novel sulfonated polymer structures, a fundamental understanding of structure-morphology-property relationships of sulfonated block and segmented copolymers is necessary, which requires the synthesis of sulfonated copolymers with well-defined structures.

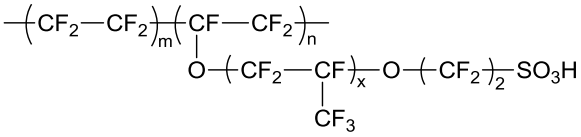

Figure 2.1 General structure of Nafion®

2.2 Synthesis of Sulfonated Block and Segmented Copolymers

2.2.1 Synthesis via post-sulfonation polymerization

Fitzgerald and Weiss et al. conducted detailed studies on the synthesis and characterization of sulfonated block copolymers in 1988.[52] In contrast to carboxylate ionomers, which are usually synthesized through copolymerization of corresponding monomers, post-sulfonation of block copolymer precursors has been a typical strategy to synthesize sulfonated block copolymers.[53] According to different approaches of introducing sulfonate groups into the polymer structures, post-sulfonation reactions were divided into several classes. One specific class is the post-sulfonation of aromatic-containing block copolymers (e.g. styrenic block copolymers), which has been one of the most significant routes to prepare sulfonated block copolymers. [54,55] Saito and

Long et al. recently reported the synthesis of sulfonated graft copolymers with site-specific sulfonation on the polymer architectures.[56] The synthesis involved living anionic polymerization of styrene and isoprene to synthesize hydroxyl-terminated block polymer precursor, hydrogenation of polyisoprene block, reaction of hydroxyl-terminated precursor with methacryloly chloride to synthesize methacrylate macromonomer, and conventional free radical polymerization of methacrylate macromonomer with methyl methacrylate. Selective sulfonation of polystyrene block with acetyl sulfate in dichloroethane generated sulfonated graft copolymers, as shown in **Scheme 2.1**.

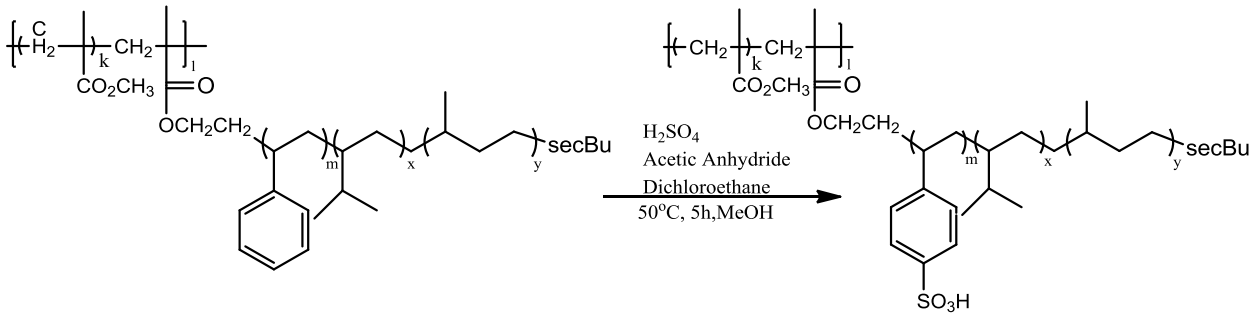

Scheme 2.1 Synthesis of sulfonated graft copolymers[56]

Many other sulfonated block copolymers, such as sulfonated polystyrene-*b*-poly(ethylene-*r*-butylene)-*b*-polystyrene (SSEBS),[57,58] sulfonated polystyrene-*b*-polyisobutylene-*b*-polystyrene (SSIBS),[59] sulfonated poly(acrylic acid)-*b*-polystyrene (SAAS),[60] and sulfonated polystyrene-*b*-polyvinyl chloride have been synthesized in a similar manner.[61] **Scheme 2.2** depicts the general approach to synthesize sulfonated block copolymers.

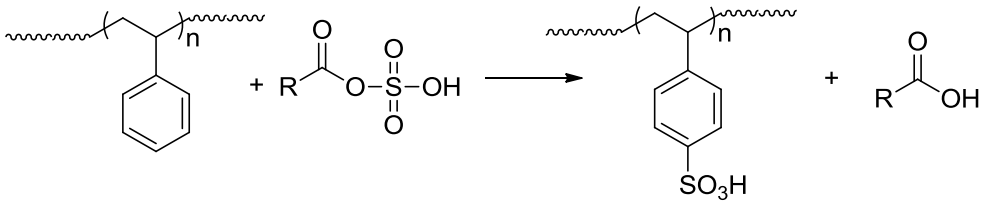

Scheme 2.2 General synthetic scheme of sulfonated styrenic block copolymers

Dado et al. reviewed the sulfonation methods of block copolymers in respect of block copolymer precursors, sulfonation agents, and reaction medias.[62] A general configuration of A-B-A, A-B-A-B-A, $(A\text{-}B\text{-}A)_nX$, or $(A\text{-}B)_nX$ (n: integer from 1-30; X: coupling agent residue) is preferred for the block copolymer precursors. Here, each end polymer block A is resistant to sulfonation while the interior saturated block B is susceptible to sulfonation. The ideal molecular weight (M_n) for end block A is in the range between 1000 and 6000 g/mol, while the interior block possesses a M_n in the range between 10,000 to 300,000 g/mol. Mild sulfonation agents such as acetyl sulfate have been most widely used and can be readily prepared from carboxylic acid anhydrides and sulfuric acids.[63] Generally, non-halogenated solvents are advantageous over the halogenated ones because they are more environmentally friendly and free of isolations prior to sulfonation.

Another typical sulfonation strategy involves the use of 1,3-propanesultone to synthesize sulfonated segmented polyurethanes.[64-66] **Scheme 2.3** exemplifies a typical sulfonation process of segmented polyurethanes. Polyurethane precursor was initially treated with NaH at -5−0 ^oC for 45 min and subsequently reacted with a stoichiometric amount of 1,3-propansultone. Cooper et al. synthesized various sulfonated polyurethanes using this strategy and investigated the influence sulfonate anions on thermal and mechanical properties, morphology, and biocompatibility of sulfonated polyurethanes.[67,68]

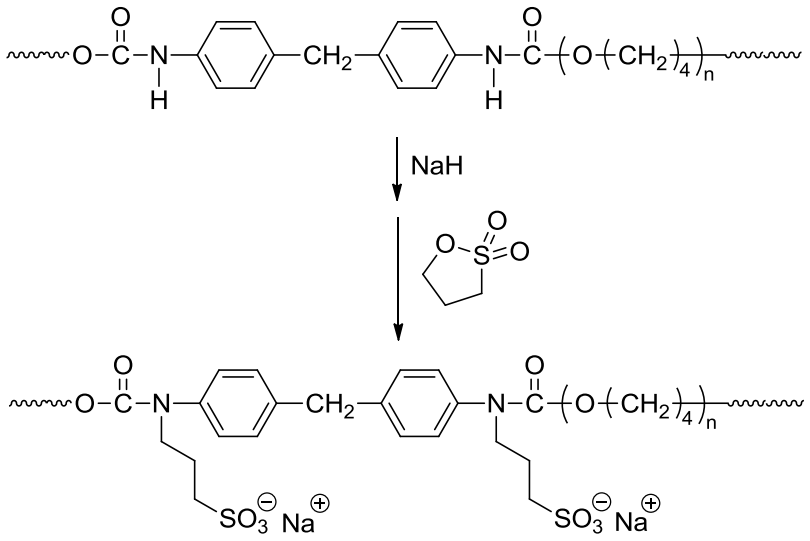

Scheme 2.3 Post-sulfonation of polyurethane

Phillips and Moore et al. have developed another synthetic route for preparation of sulfonated copolymers (as shown in **Scheme 2.4**).[69] Sulfonic acid groups were readily introduced when cross-linking poly(ethylene-*co*-vinyl alcohol) (EVOH) with sulfosuccinic acid in dimethyl sulfoxide with a vigorous stirring and heat.

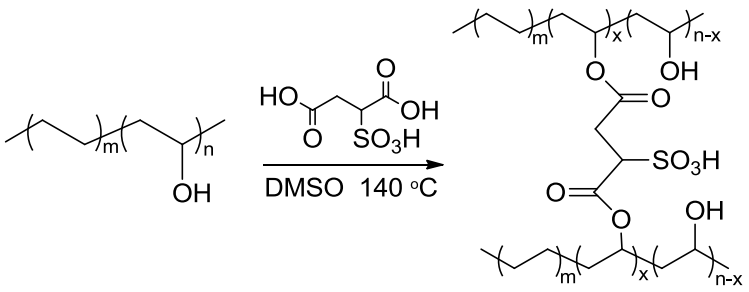

Scheme 2.4 Cross-linking of EVOH with sulfosuccinic acid

Although post-sulfonation is a suitable and frequently used approach to synthesize sulfonated block and segmented copolymers, there are significant drawbacks to the synthetic process and therefore limit their applications. Moreover, post-sulfonation involves the reaction between the

sulfonation agents and high molecular weight polymers, which is difficult to control the degree of sulfonation and the distribution of sulfonate groups on the polymer architectures. Some may argue that the degree of sulfonation can be controlled through the reaction conditions. However, the dependence of the degree of sulfonation on reaction conditions such as reaction time, temperature, and concentrations of sulfonation agents and polymers was inconsistent in varying cases. Additional negative attribute of the post-sulfonation method is different side reactions such as cross-linking, branching, and chain scission occurred during the sulfonation process.[70] In addition, incorporation of highly hydrophilic sulfonate groups significantly reduce the solubility of the copolymers in organic solvents, changing a homogenous system into a heterogeneous one.

2.2.2 Direct polymerization of sulfonated monomers

In comparison with post-sulfonation procedures, direct copolymerization of sulfonated monomers has great advantages of avoiding the possible side reactions and affording a good control of both the degree of sulfonation and distribution of the sulfonate groups through the entire polymer architecture. Park and McGrath et.al recently described the synthesis of highly chlorine-tolerant sulfonated copolymers used for water desalination.[71] Random copolymerization of 3，3’-disulfonato-4,4’-dichlorodiphenyl sulfone (SDCDPS) with other monomers (e.g. 4,4’-biphenol) produced disulfonated poly(arylene ether sulfone) copolymers with a precisely controlled degree of sulfonation. Shi and Palmer et al. reported a sulfonated acrylamide copolymers synthesized through copolymerization of 2-arylamido-2-methyl-1-propanesulfonic acid (AMPS) with lauryl methacrylamide (LMAm) (as shown in **Scheme 2.5**).[72]

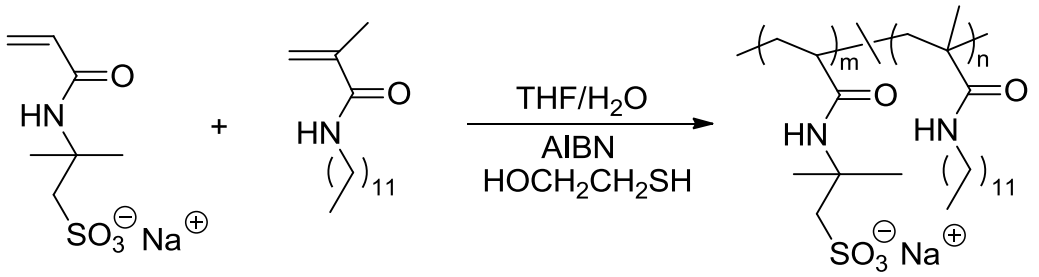

Scheme 2.5 Copolymerization of AMPS and LMAm

Direct copolymerization of sodium-3,3'-disulfonate-bis[4-(3-aminophenoxy)phenyl] sulfone (SDADPS) (see **Figure 2.2**) with other monomers produced the naphthalene dianhydride based sulfonated polyimide copolymers. These polymers can be potentially used as proton-exchange-membrane fuel cells.[73] Using direct copolymerization of sulfonated monomers, many other sulfonated block and segmented copolymers such as poly(ether sulfone),[74,75] poly(ether ether ketone)s,[75,76] and sulfonated polyimide copolymers[77,78] have been synthesized.

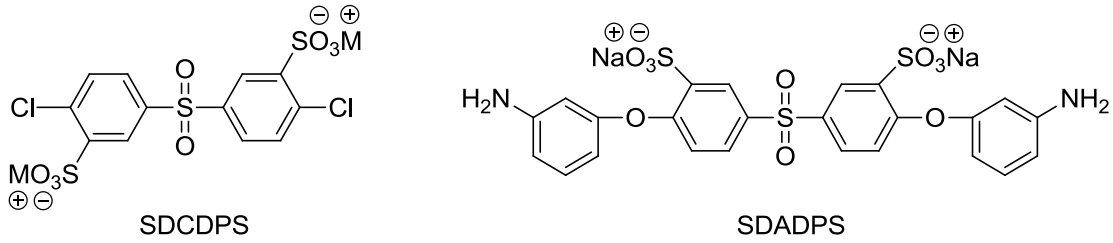

Figure 2.2 Monomers used for sulfonated copolymers

However, commercially available sulfonated monomers are very limited. A large number of specific monomers are necessary to satisfy different property requirements. Currently a lot of efforts have focused on designing and synthesizing novel sulfonated monomers. Early in 1973, Kangas reviewed the synthesis of sulfonated monomers such as sodium vinyl sulfonate, sulfoethyl methacrylate as well as others.[79] Earlier studies by Colby et al. on the synthesis of poly(ethylene glycol)-based single-ion conductor provided a sufficient way to prepare sulfonated

monomers for segmented polyurethanes through the transesterification reaction between dimethyl 5-sulfoisophthalate sodium salt and poly(ethylene glycol) using the catalyst of titanium isopropoxide at 210 ^{o}C~230 ^{o}C.[80] Lam and Barrie et al. described the synthesis of sulfonated diols for the use of preparing segmented polyurethane copolymers.[81] The synthetic scheme is shown as follows.

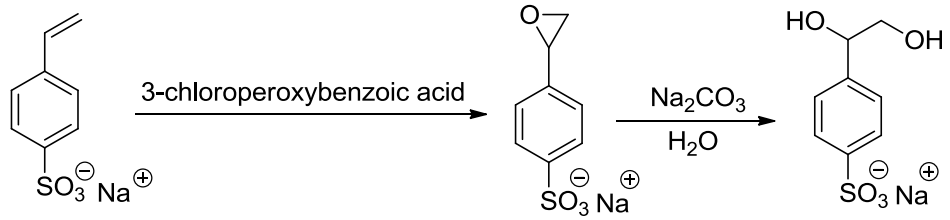

Scheme 2.6 Synthesis of sulfonated diol[81]

There are also some aqueous reactions that can be used to prepare sulfonated monomers. Mandrekar reported a novel sulfonated polymer for nuclear track detection.[82] They introduced the sulfonate group into the structure through the substitution reaction of allyl chloride with aqueous sodium sulphite. Generally, the compounds with the structures of Cl− or Br−CH(R)COR', or halogenated alcohols, ethers, and esters can be sulfonated in the similar manner.[83] The addition reaction of $NaHSO_3$ to C=C also served as a good sulfonation method (see **Scheme 2.7**).

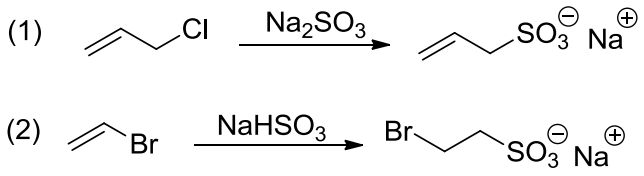

Scheme 2.7 Two aqueous sulfonation reactions

Recently, Cavicchi reviewed various substituted sulfonated monomers that were suitable for synthesis of sulfonated copolymers (**Figure 2.3**).[70] Researchers have demonstrated that some of these monomers with long alkyl substitutes on ammonium cations allowed for controlled free radical polymerization to synthesize sulfonated block copolymers. For example, Matyjaszewski et al. reported the synthesis of sulfonated block copolymers through controlled free radical polymerization of sulfonated monomers.[84] **Scheme 2.8** depicts the atom transfer radical polymerization (ATRP) of 2-acrylamido-2-methyl propanesulfonate using a difunctional acrylate macroinitiators, which provided sulfonated block copolymers with well-defined architectures.

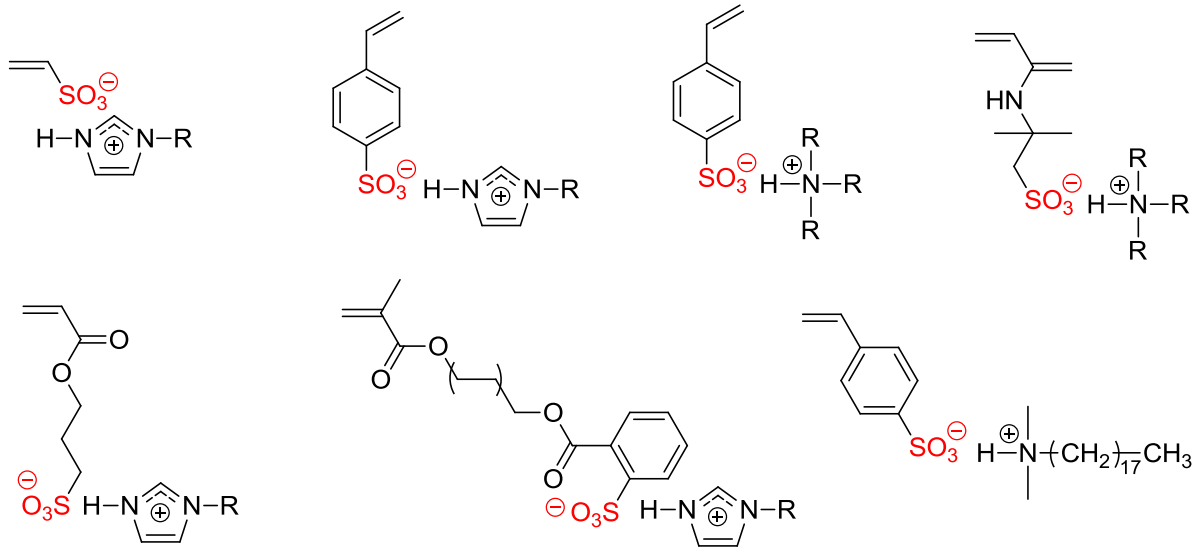

Figure 2.3 Substituted ammonium sulfonated monomers for synthesis of sulfonated block copolymers

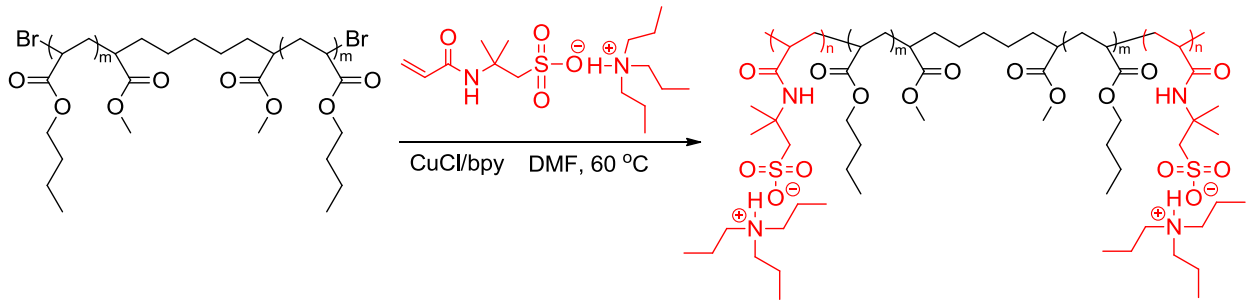

Scheme 2.8 Synthesis of sulfonated block copolymers using ATRP

2.3 Factors that Affect the Properties of Sulfonated Copolymers

2.3.1 General concept of ionomers

Ionomer is the more general term applied to these ion-containing polymers that contain maximum ionic groups of approximately 15~20 mol%.[85] The percentage of the ionic groups is calculated from the number of the atoms on the polymer backbone or the repeat units containing ionic groups. Properties of ionomers depend strongly on the interactions of ionic groups, which associate at different scales. In order to correlate ionomer morphology with their structure and properties, researchers have built up different models to understand the arrangement of ion associations in ionomers, including hard-sphere model,[86] core-shell model,[87] and Eisenberg-Hird-Moore (EHM) model,[88,89] In the hard-sphere model, ionic aggregates are regarded as small particles and ionomer peak in small angle X-ray scattering (SAXS) profiles arises from the interparticle scattering. The core-shell model illustrates a two-shell-core structure, where an ionic core is surrounded with a shell of non-ionic polymers, which in turn, is surrounded with a second shell consisting of the polymers with a high ionic density. This model suggests that the ionomer peaks result from the intra-particle distance of the two ion-rich regions, rather than the distance between particles. In the EHM model, Eisenberg, Hird, and Moore et al. introduced the concept of *multiplets*, which consist of several ion pairs. The number of ion pairs in the multiplets depends on the size of the ion pairs, steric restrictions, and dielectric constant of the polymer backbones. A schematic representation of a multiplet is shown in **Figure 2.4**.

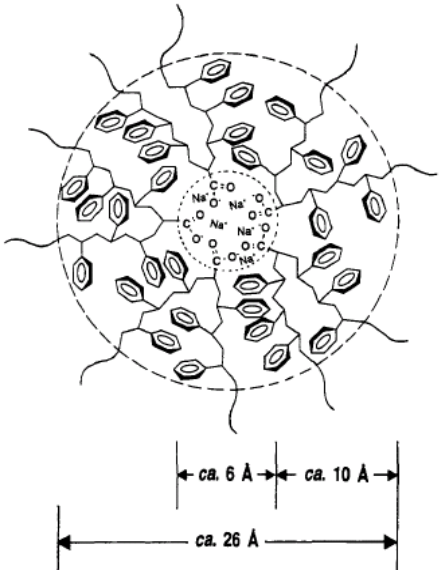

Figure 2.4 Schematic diagram for a multiplet in poly(styrene-*co*-sodium methacrylate) system[88]

2.3.2 Effect of charge density

Charge density is expected to play an important role in determining thermal and mechanical properties, conductivity, and morphologies of ion-containing polymers.[49,90-95] In general, both the matrix glass transition temperature (T_g) and cluster T_g increase with increasing charge density due to the restricted mobility of polymer chains in the presence of ion association. However, the values of $\frac{dT_g}{dc}$ vary for different polymer systems, where T_g is the glass transition temperature and c is the charge density. Moreover, Gromadzki and Stepanek et al. studied the effect of sulfonation level on the ionic transport properties and morphologies of polystyrene-*b*-poly(ethylene-*alt*-propylene) (PS-PEP) block copolymers.[96] Results indicated that the conductivity increased almost exponentially with the degree of sulfonation. Additionally, morphological studies with SAXS revealed a progressive transformation of the lamellar morphology of the block copolymers into the disordered morphology as the degree of

sulfonation increased. Mauritz et al. studied the dynamic mechanical properties of lightly sulfonated poly(styrene-*b*-(ethylene/butylene)-*b*-styrene) block copolymers, which exhibited extended rubbery plateau to higher temperatures with increasing the sulfonation level.[97]

2.3.3 Effect of charge location

The locations of sulfonate groups also have a significant effect on the properties of sulfonated block copolymer. [40,98-101] Sulfonate groups can either locate on the polymer backbone or the pendant side chains of the block copolymers. Tsang and Holdcroft et al. compared the sulfonated graft copolymers bearing sulfonic acid groups on the graft chains with sulfonated diblock copolymers bearing sulfonic acid groups on the backbones.[98] They demonstrated that sulfonated graft copolymers exhibited better mechanical properties and higher water uptake relative to the sulfonated diblock copolymers. Pang and Jiang et al. synthesized sulfonated poly(arylene ether)s bearing pendant sulfoalkyl groups.[102] Keeping the hydrophilic sulfonate groups away from the hydrophobic polymer backbones considerably reduced the swelling ratio and increased the conductivity, which were attributed to the high mobility of pendant sulfonate groups. In the case of segmented sulfonated copolymers, sulfonate groups located either in the soft segments or the hard segments dramatically influenced the properties of segmented copolymers, including thermal and mechanical properties, hydrogen bonding, and microphase separation.[103,104] Long et al. recently studied the influence of sulfonate charge placement on performance of poly(ethylene oxide) (PEO)-based segmented polyurethanes containing sulfonate charge either in the soft segments or hard segments. They demonstrated that polyurethanes containing sulfonate charge in the hard segments exhibited significantly increased PEO soft segment T_g and reduced modulus due to phase mixing between polar PEO soft segments and sulfonated ionic hard segments, as evidenced in atomic force microscopy (AFM) and SAXS.

2.3.4 Effect of counterions

The types of counterions and their properties such as charge number, size of cations, and mobility will significantly influence the properties of sulfonated copolymers.[105-108] Ding and Cooper et al. investigated poly(tetramethylene oxide) (PTMO)/toluene diisocyanate (TDI)-based sulfonated polyurethanes neutralized with different counterions, such as Ca^{2+}, Ni^{2+}, Zn^{2+}, Cd^{2+}, Cs^{+}, and Eu^{3+} to elucidate the influence of counterions on the polymer microstructures.[108] Extended X-ray absorption fine structure (EXAFS) data indicated that all samples had similar coordination in the first shell. However, only the samples neutralized with Ni^{2+} and Eu^{3+} displayed clear second coordination shells. In contrast, samples neutralized with Ca^{2+} and Cd^{2+} afforded low order second shells and samples neutralized with Zn^{2+} and Cs^{+} did not possess the second shell at all. Li and Chan et al investigated the effect of transition metal counterions of Cu^{2+}, Ni^{2+}, Zn^{2+} on the affinity of sulfonated poly(ether sulfone) membranes and found that all three types of transition metal counterions increased the affinity of the sulfonated polymers thus enhanced the protein separation performance.[105] However, membranes in the Cu^{2+} form displayed the best protein separation performance, leading to high-purity target protein. Suleiman and Crawford et al compared the thermal stabilities of sulfonated poly(styrene-isobutylene-styrene) (SIBS) block copolymers neutralized with Mg^{2+}, Ca^{2+}, and Ba^{2+}.[106] The desulfonation temperatures of the neutralized polymers increased almost 300 ^{o}C. However, the degradation temperatures of the polymer backbones remain the same. Additionally, cross-links resulting from the ionic interactions in the polymers reduced the water swelling and stabilized the membrane. Recently, Colby et al. studied a series of sulfonated polyester ionomers with various ammonium cations.[109] They found that ionic conductivity of sulfonated polyester

increased by four orders of magnitude when sodium cations were exchanged into tetramethylammonium and tetrabutylamonium cations.

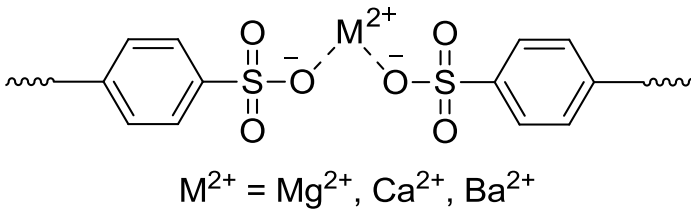

Figure 2.5 Cross-links in SIBS-metal complex

2.4 Microphase separation of sulfonated block and segmented copolymers

Sulfonated block and segmented copolymers undergo microphase separation due to the thermodynamic immiscibility between different blocks and segments. Tailoring sequence length, molecular weight distribution, and chemical composition of each block generate various nanostructured materials for applications in water purification, fuel cell membranes, and energy storage.[14-27] Properties of sulfonated polymers depend strongly on their morphologies. Thus, a fundamental understanding of microphase separation behavior of sulfonated block and segmented copolymers is necessary to tailor polymeric materials for desired properties.

Small-angle X-ray scattering (SAXS) is a useful tool to study microphase-separated morphologies of sulfonated block copolymers.[96,110-113] X-ray scattering is very sensitive to the periodic fluctuations in electron density of ion-containing polymers. When the microphase separation occurs in the polymer systems, X-rays are scattered coherently and the so-called ionic peaks will show up in the SAXS profile, which provide the information of morphologies. Story and Baugh studied the morphology characteristic of the discontinuous domains in sulfonated poly(styrene-*b*-isobutylene-*b*-styrene) block copolymers based on the scattering vector values (q) relative to the scattering vector of the first-order scattering peak.[114] Relative q values of $1,\sqrt{2}$

,$\sqrt{3}$, $\sqrt{4}$ indicate the morphology of the spheres arranged in cubic lattice and values of 1, $\sqrt{3}$, $\sqrt{7}$, $\sqrt{9}$, $\sqrt{12}$ indicate the cylinders arranged in hexagonal lattice.[114] Higher q values of 1,2,3,4 indicate the lamellar morphology.[115] In SAXS experiment, samples are normally prepared in two ways, one is solution casting while the other is compression molding. How the samples are prepared is critical because sometimes they will significantly influence the morphology of the polymers. Kim and Ihn et al. investigated the effect of casting solvent (MeOH/THF) on the morphology and physical properties of partially sulfonated polystyrene-*b*-poly(ethylene-*r*-butylene)-*b*-polystyrene copolymers and found that the increased MeOH transformed a well-ordered lamellar morphology into a disordered morphology.[110]

Atomic force microcopy (AFM) provides a facile way to visualize surface morphology of sulfonated block copolymers.[14,116-119] In a typical AFM phase images, high-modulus high-T_g domains appear as bright regions and low-T_g soft domains appear as darker regions. For example, McGrath et al. studied the microphase separation of a segmented sulfonated poly(arylene ether sulfone)-*b*-polyimide copolymer (BPSH m-PI n, where m×10^3 g/mol is the number-average molecular weight (M_n) of BPSH block and n×10^3 g/mol is the M_n of PI block) using AFM.[120] **Figure 2.6** displays the AFM phase and height images of BPSH-PI with different block lengths. It clearly showed that bright nonionic domains converted from irregular round domains into well-defined, continuous lamellar morphology as block length increased from 5000 g/mol (BPSH)-5000 g/mol (PI) to 15000 g/mol (BPSH)-15000 g/mol (PI). Mauritz and Beyer et al. imaged the surface morphology of sulfonated poly(styrene-*b*-ethylene-*co*-butylene-*b*-styrene) using AFM. Morphological features revealed with AFM correlated well with X-ray scattering data.[117]

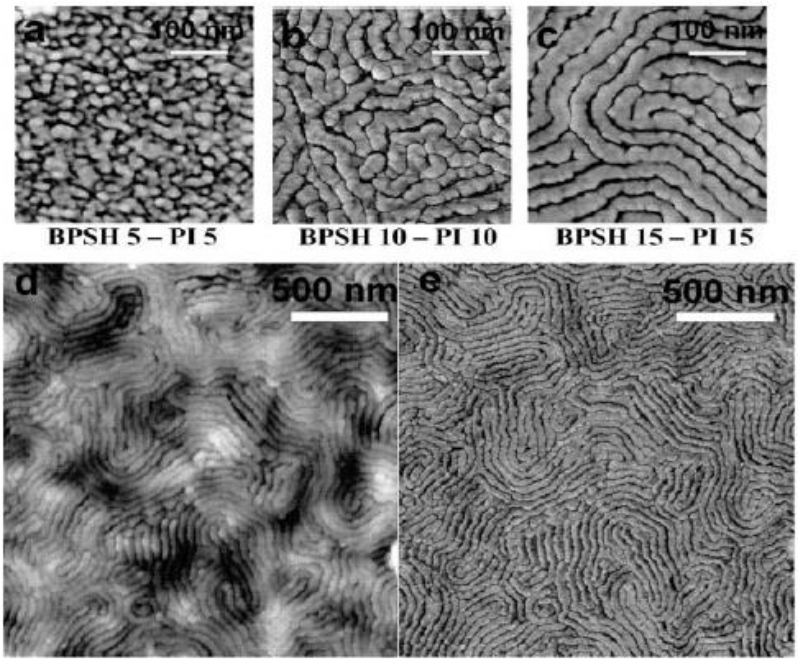

Figure 2.6 (a)-(c) Tapping mode AFM phase images of BPSH-PI multiblock copolymers with different block lengths, (d) height image, and (e) phase image of BPSH15-PI15 demonstrating long-range order[120]

Transmission electron microscopy (TEM) enables to visualize bulk morphology of sulfonated block and segmented copolymers. Mezzenga et al. investigated the dependence of proton conductivity on the morphologies of sulfonated polystyrene-*b*-poly(methyl methacrylate) diblock copolymers.[121] They demonstrated that water vapor annealing favored formation of highly ordered, lamellar and hexagonally perforated lamellar morphology, as demonstrated with TEM images in **Figure 2.7**. Additionally, proton conductivity and water swelling properties of these sulfonated block copolymer depended strongly on their morphology. Polymers with a lamellar morphology exhibited higher proton conductivity and higher water uptake.

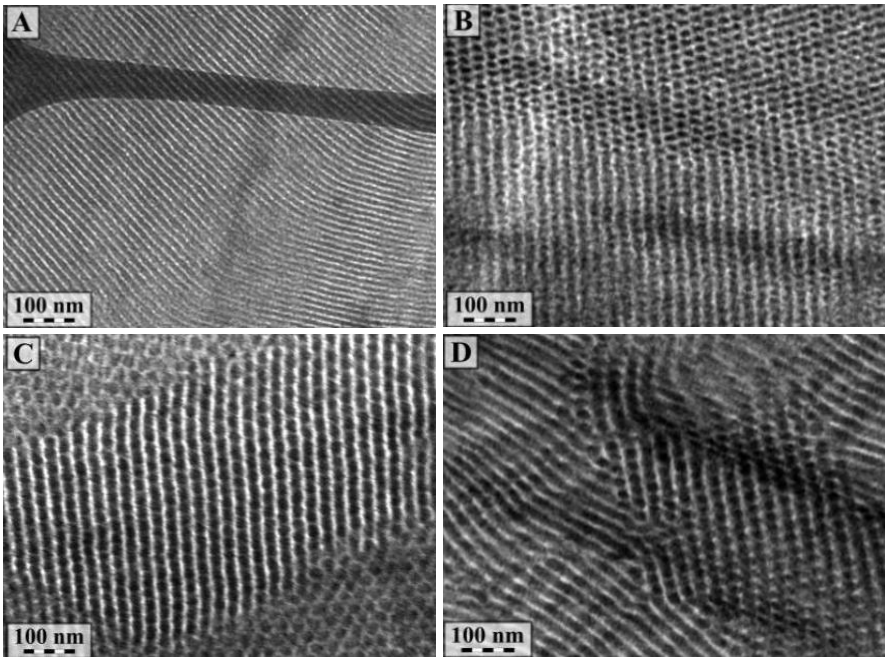

Figure 2.7 TEM images of vapor annealing for samples: (a) S1_20 (IEC=1.66), (b) S1_17 (IEC=0.353), (C) S2_35 (IEC=0.766), and (d) S3_37 (IEC=0.564).[121]

2.5 Sulfonated block and segmented copolymers for electromechanical transducers

Electromechanical polymeric transducers have received significant attention recently for many emerging applications, including electromechanical actuators, sensors, electro-active coatings, and artificial muscles. **Figure 2.8** shows schematic representation of an ionomeric polymer actuator, which contains a central, ionomeric membrane, conductive network composite (CNC) layers, and electrode layers. The actuator mechanically deforms (actuates) upon an applied potential. Desirable properties for polymeric membranes in electromechanical transducers include high ionic conductivity, tunable modulus *versus* temperature behavior, efficient response at relatively low voltages (<5 V), and facile fabrication processes. Currently, perfluorinated sulfonated copolymers, e.g. Nafion®, exhibited good properties and performance in electromechanical actuator applications.[122] However, to overcome the limits of perfluorinated sulfonated copolymers and obtain more tunable properties, researchers have extensively

investigated various block and segmented copolymers. Sulfonated block and segmented copolymers emerge as suitable candidates for applications in electromechanical transducers. Lee et al. fabricated electromechanical actuators using sulfonated poly(styrene-*b*-ethylene-*co*-butylene-*b*-styrene).[123] **Figure 2.9** demonstrated that the resulting actuators exhibited harmonic response of displacement and current at 0.2 Hz sinusoidal signal with 1.5 V amplitude. More recently, Spontak et al. reported polymeric electromechanical actuators fabricated from a sulfonated pentablock copolymers, poly(*t*-butyl styrene-*b*-(ethylene/propylene)-*b*-(styrene-ran-styrenesulfonate)-*b*-(ethyelen/propylene)-*b*-*t*-butyl styrene).[124] **Figure 2.10** displays the digital images showing the bending behavior of resulting actuators. It indicated that actuators swollen with glycerol bended towards the anode (a); however, actuators swollen with ethylene glycol displayed bending to the cathode (b). This study suggested that swollen solvents regulated actuation direction of the sulfonated pentablock copolymer-based actuators.

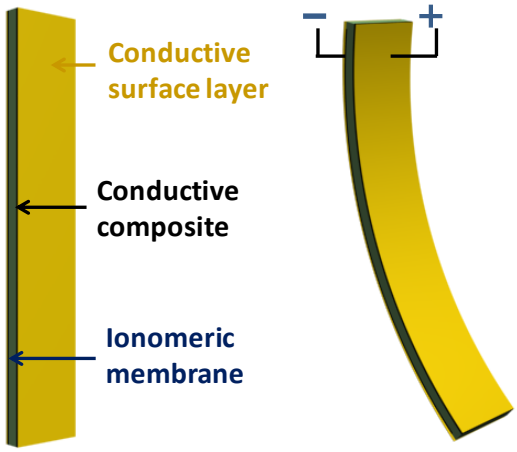

Figure 2.8 Schematic representation of an ionomeric polymer actuator, which exhibits bending under applied voltages.

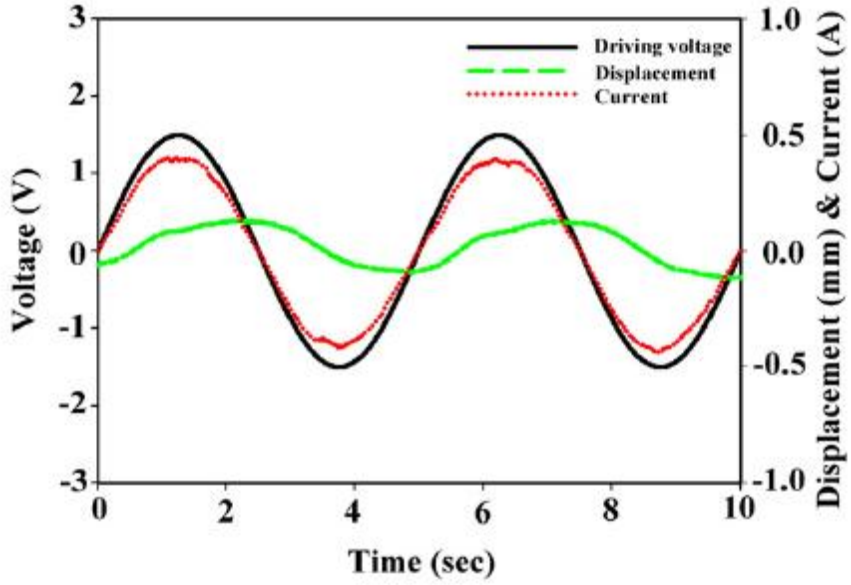

Figure 2.9 Harmonic response of displacement and current of sulfonated poly(styrene-*b*-ethylene-*co*-butylene-*b*-styrene)-based actuator at 0.2 Hz sinusoidal signal with 1.5 V amplitude[123]

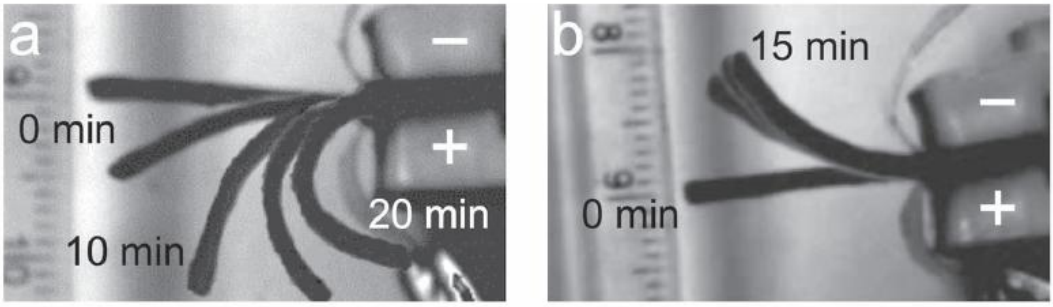

Figure 2.10 Digital images of actuation performance of sulfonated pentablock copolymer based-actuators swollen with (a) glycerol and (b) ethylene glycol[124]

To optimize the properties and performance of polymeric membranes for electromechanical transducer applications, ionic liquids have been utilized as diluents to enhance ionic conductivity of polymeric membranes. Ionic liquids, which are defined as organic salts with melting temperatures below 100 ^{o}C, possess a unique set of desirable properties including high ionic conductivity, high electrochemical and thermal stability, and low volatility.[125,126] However,

polymeric membranes incorporated with ionic liquids often suffered reduced mechanical performance due to the plasticizing effect of ionic liquids. In order to enhance the ionic conductivity with ionic liquids while maintaining the mechanical properties, researchers have designed various ABA triblock copolymers, where "A" blocks form nonionic, high-T_g domains that serve as physical cross-links and provide desirable mechanical strength even in the presence of ionic liquid, and B blocks are low-T_g, ion-rich domains that provide ion transport pathway and impart high ionic conductivity. Most current studies have focused on ion-containing diblock copolymers or PEO-based triblock copolymers and networks to fundamentally understand the influence of ionic liquids on morphologies and ionic conductivity.[127-129] Studies on ion-containing multiblock and segmented copolymers are much less noted in the literature, which will be one of the major focuses of this dissertation.

2.6 References

1. Cao, Z. Q.; Liu, W. G.; Liang, D. C.; Guo, G.; Zhang, J. Y. *Adv. Funct. Mater.* **2007**, *17*, 246.
2. Okoshi, K.; Sakurai, S.; Ohsawa, S.; Kuniaki, J.; Yashima, E. *Angew. Chem.-Int. Ed.* **2006**, *45*, 8173.
3. Karikari, A. S.; Edwards, W. F.; Mecham, J. B.; Long, T. E. *Biomacromolecules* **2005**, *6*, 2866.
4. Asanuma, H.; Ban, T.; Gotoh, S.; Hishiya, T.; Komiyama, M. *Macromolecules* **1998**, *31*, 371.
5. Lee, H.; Mensire, R.; Cohen, R. E.; Rubner, M. F. *Macromolecules* **2012**, *45*, 347.
6. Mattia, J.; Painter, P. *Macromolecules* **2007**, *40*, 1546.
7. Ruokolainen, J.; tenBrinke, G.; Ikkala, O.; Torkkeli, M.; Serimaa, R. *Macromolecules* **1996**, *29*, 3409.
8. Li, M. H.; Xu, P.; Yang, J. G.; Ying, H.; Haubner, K.; Dunsch, L.; Yang, S. F. *J. Phys. Chem. C* **2011**, *115*, 4584.
9. Panzeter, P. L.; Realini, C. A.; Althaus, F. R. *Biochemistry* **1992**, *31*, 1379.
10. Cheng, S. J.; Zhang, M. Q.; Wu, T. Y.; Hemp, S. T.; Mather, B. D.; Moore, R. B.; Long, T. E. *J. Polym. Sci., Part A: Polym. Chem.* **2012**, *50*, 166.
11. Cheng, S. J.; Beyer, F. L.; Mather, B. D.; Moore, R. B.; Long, T. E. *Macromolecules* **2011**, *44*, 6509.
12. Green, M. D.; Allen, M. H.; Dennis, J. M.; Salas-de la Cruz, D.; Gao, R. L.; Winey, K. I.; Long, T. E. *Eur. Polym. J.* **2011**, *47*, 486.
13. Colby, R. H.; Rubinstein, M. *Polymer Physics.* **2003**, *Oxford University Press*.
14. Ghassemi, H.; McGrath, J. E.; Zawodzinski, T. A. *Polymer* **2006**, *47*, 4132.
15. Chen, K. C.; Hu, Z. X.; Endo, N.; Higa, M.; Okamoto, K. *Polymer* **2011**, *52*, 2255.
16. Poppe, D.; Frey, H.; Kreuer, K. D.; Heinzel, A.; Mulhaupt, R. *Macromolecules* **2002**, *35*, 7936.
17. Fang, J. H.; Guo, X. X.; Harada, S.; Watari, T.; Tanaka, K.; Kita, H.; Okamoto, K. *Macromolecules* **2002**, *35*, 9022.
18. Deimede, V.; Voyiatzis, G. A.; Kallitsis, J. K.; Qingfeng, L.; Bjerrum, N. J. *Macromolecules* **2000**, *33*, 7609.
19. Othman, M. H. D.; Ismail, A. F.; Mustafa, A. *J. Membr. Sci.* **2007**, *299*, 156.
20. Li, X. F.; Liu, C. P.; Lu, H.; Zhao, C. J.; Wang, Z.; Xing, W.; Na, H. *J. Membr. Sci.* **2005**, *255*, 149.
21. Li, L.; Zhang, J.; Wang, Y. X. *J. Membr. Sci.* **2003**, *226*, 159.
22. Zhang, J. G.; Dubay, M. R.; Houtman, C. J.; Severtson, S. J. *Macromolecules* **2009**, *42*, 5080.
23. Knychala, P.; Banaszak, M.; Park, M. J.; Balsara, N. P. *Macromolecules* **2009**, *42*, 8925.
24. Jeong, M. H.; Lee, K. S.; Lee, J. S. *J. Membr. Sci.* **2009**, *337*, 145.
25. Liang, C.; Maruyama, T.; Ohmukai, Y.; Sotani, T.; Matsuyama, H. *J. Appl. Polym. Sci.* **2009**, *114*, 1793.
26. Kang, S. W.; Choi, S. K.; Hwang, S. S.; Baek, K. Y.; Choi, H. M. *Macromolecular Research* **2009**, *17*, 455.
27. Khalfan, A. N.; Sanchez, L. M.; Kodiweera, C.; Greenbaum, S. G.; Bai, Z. W.; Dang, T. D. *J. Power Sources* **2 2007**, *173*, 853.
28. Carvalho, A. J. F.; Curvelo, A. A. S. *Macromolecules* **2003**, *36*, 5304.
29. Young, A. M.; Higgins, J. S.; Peiffer, D. G.; Rennie, A. R. *Polymer* **1995**, *36*, 691.
30. Lefelar, J. A.; Weiss, R. A. *Macromolecules* **1984**, *17*, 1145.
31. Chen, S. L.; Bocarsly, A. B.; Benziger, J. *J. Power Sources* **2005**, *152*, 27.

32. Choi, J.; Kim, I. T.; Kim, S. C.; Hong, Y. T. *Macromolecular Research* **2005**, *13*, 514.
33. Iwai, Y.; Hiroki, A.; Tamada, M.; Yamanishi, T. *J. Membr. Sci.* **2008**, *322*, 249.
34. Jung, D. J.; Piao, M. H.; Oh, S. H.; Woo, J. C.; Choi, S. H. *J. Nanoscience and Nanotechnology* **2010**, *10*, 6855.
35. Kim, S. H.; Oh, J. H.; Yoo, B.; Jung, D. J.; Piao, M. H.; Choi, S. H. *Multi-Functional Materials and Structures, Pts 1 and 2* **2008**, *47-50*, 1474.
36. Lund, A.; Macomber, L. D.; Danilczuk, M.; Stevens, J. E.; Schlick, S. *J. Phys. Chem. B* **2007**, *111*, 9484.
37. Tian, A. H.; Kim, J. Y.; Shi, J. Y.; Kim, K. *J. Power Sources* **2008**, *183*, 1.
38. Yen, C. Y.; Lee, C. H.; Lin, Y. F.; Lin, H. L.; Hsiao, Y. H.; Liao, S. H.; Chuang, C. Y.; Ma, C. C. M. *J. Power Sources* **2007**, *173*, 36.
39. Wang, Z.; Ni, H. Z.; Zhao, C. J.; Li, X. F.; Zhang, G.; Shao, K.; Na, H. *J. Membr. Sci.* **2006**, *285*, 239.
40. Ghassemi, H.; McGrath, J. E. *Polymer* **2004**, *5847*, 5847.
41. Gu, S.; He, G. H.; Wu, X. M.; Li, C. N.; Liu, H. J.; Lin, C.; Li, X. C. *J. Membr. Sci.* **2006**, *281*, 121.
42. Hu, Z. X.; Yin, Y.; Kita, H.; Okamoto, K. I.; Suto, Y.; Wang, H. G.; Kawasato, H. *Polymer* **2007**, *48*, 1962.
43. Lee, H. S.; Roy, A.; Lane, O.; Lee, M.; McGrath, J. E. *J. Polym. Sci., Part A: Polym. Chem.* **2010**, *48*, 214.
44. Li, X. F.; Zhao, C. J.; Lu, H.; Wang, Z.; Na, H. *Polymer* **2005**, *46*, 5820.
45. Pang, J. H.; Zhang, H. B.; Li, X. F.; Wang, L. F.; Liu, B. J.; Jiang, Z. H. *J. Membr. Sci.* **2008**, *318*, 271.
46. Saito, T.; Moore, H. D.; Hickner, M. A. *Macromolecules* **2010**, *43*, 599.
47. Tigelaar, D. M.; Palker, A. E.; He, R. H.; Scheiman, D. A.; Petek, T.; Savinell, R.; Yoonessi, M. *J. Membr. Sci.* **2011**, *369*, 455.
48. Xu, H. J.; Chen, K. C.; Guo, X. X.; Fang, J. H.; Yin, J. *Polymer* **2007**, *48*, 5556.
49. Zhao, C. Z.; Li, X. F.; Wang, Z.; Dou, Z. Y.; Zhong, S. L.; Na, H. *J. Membr. Sci.* **2006**, *280*, 643.
50. Tarrant, L. B.; Tangredi, T. N.; Wnek, G. E.; Nicolosi, R. J. *United States Patent* **1998**, *5840387*.
51. Han, D. K.; Park, K. D.; Kim, Y. H. *J. Biomater. Sci., Polym. Ed.* **1998**, *9*, 163.
52. Fitzgerald, J. J.; Weiss, R. A. *J. Macromol. Sci., Pure Appl. Chem.* **1988**, *C28*, 99.
53. Tant, M. R.; Mauritz, K. A.; Wilkes, G. L. *ionomers Synthesis, structure, properties and applications* **1996**, 10.
54. Tang, H.; Pintauro, P. N. *J. Appl.Polym.Sci.* **1999**, *71*, 387.
55. Manea, C.; Mulder, M. *J. Membr.Sci* **2002**, *206*, 443.
56. Saito, T.; Mather, B. D.; Costanzo, P. J.; Beyer, F. L.; Long, T. E. *Macromolecules* **2008**, *41*, 3503.
57. Serpico, J. M.; Ehrenberg, S. G.; Fontanella, J. J.; Jiao, X.; Perahia, D.; McGrady, K. A.; Sanders, E. H.; Kellogg, G. E.; Wnek, G. E. *Macromolecules* **2002**, *35*, 5916.
58. Ganguly, A.; Bhowmick, A. K.; Li, Y. J. *Macromolecules* **2008**, *41*, 6246.
59. Edmondson, C. A.; Fontanella, J. J.; Chung, S. H.; Greenbaum, S. G.; Wnek, G. E. *Electrochim. Acta* **2001**, *46*, 1623.
60. Yap, H. P.; Hao, X. J.; Tjipto, E.; Gudipati, C.; Quinn, J. F.; Davis, T. P.; Barner-Kowollik, C.; Stenzel, M. H.; Caruso, F. *Langmuir* **2008**, *24*, 8981.
61. Fu, R. Q.; Woo, J. J.; Seo, S. J.; Lee, J. S.; Moon, S. H. *J. Membr. Sci.* **2008**, *309*, 156.
62. Dado, G. P.; Handlin, D. L., Jr; Willis, C. L. *PCT Int. Appl.* **2008**, *68pp*.

63. Noshay, A.; Robeson, L. M. *J. Appl. Polym. Sci.* **1976**, *20*.
64. Ding, Y. S.; Register, R. A.; Yang, C. Z.; Cooper, S. L. *Polymer* **1989**, *30*, 1204.
65. Ding, Y. S.; Register, R. A.; Yang, C. Z.; Cooper, S. L. *Polymer* **1989**, *30*, 1221.
66. Silver, J. H.; Hart, A. P.; Williams, E. C.; Cooper, S. L.; Charef, S.; Labarre, D.; Jozefowicz, M. *Biomaterials* **1992**, *13*, 339.
67. Register, R. A.; Pruckmayr, G.; Cooper, S. L. *Macromolecules* **1990**, *23*, 3023.
68. Silver, J. H.; Marchant, J. W.; Cooper, S. L. *J. Biomed. Mater. Res. A.* **1993**, *27*, 1443.
69. Phillips, A. K.; Moore, R. B. *Polymer* **2005**, *46*, 7788.
70. Cavicchi, K. A. *ACS applied Materials and Interfaces* **2012**, *ASAP*.
71. Park, H. B.; Freeman, B. D.; Zhang, Z.-B.; Sankir, M.; E.McGrath, J. *Angew.Chem.Int.Ed.* **2008**, *47*, 6019.
72. Shi, W.; Watson, C. J.; Palmer, C. P. *J. Chromatogr. A* **2001**, *905*, 281.
73. Einsla, B. R.; Hong, Y. T.; Kim, Y. S.; Wang, F.; Gunduz, N.; Mcgrath, J. E. *J. Polym. Sci., Part A: Polym. Chem.* **2004**, *42*, 862.
74. Oh, Y. S.; Lee, H. J.; Yoo, M.; Kim, H. J.; Han, J. H.; Kim, K.; Hong, J. D.; Kim, T. H. *Chem. Commun.* **2008**, 2028.
75. Zhang, X. P.; Liu, S. Z.; Liu, L. F.; Yin, J. *Polymer* **2005**, *46*, 1719.
76. Wang, J. L.; Song, Y. L.; Zhang, C.; Ye, Z. B.; Liu, H.; Lee, M. H.; Wang, D. H. J., J.B. *Macromol. Chem. Phys.* **2008**, *209*, 1495.
77. Bai, H.; Winston Ho, W. S. *J. Membr. Sci.* **2008**, *313*, 75.
78. Miyatake, K. Y., T.; Watanabe, M. *J. Polym. Sci., Part A: Polym. Chem.* **2008**, *46*, 4469.
79. Kangas, D. A. *Funct. Monomers: Their Prep., Polym., Appl.* **1973**, *1*, 489.
80. Dou, S.; Zhang, S.; Klein, R. J.; Runt, J.; Colby, R. H. *Chem. Mater.* **2006**, *18*, 4288.
81. Lam, R. K. H.; Geoge, M. H.; Barrie, J. A. *Polymer* **1989**, *30*, 2320.
82. Mandrekar, V. K.; Tilve, S. G.; Nadkarni, V. S. *Radiat. Phys. Chem.* **2008**, *77*, 1027.
83. Everett Eddy, G. *Sulfonation and Related Reactions* **1964**, *Chapter 3*, 133.
84. McCullough, L. A.; Dufour, B.; Matyjaszewski, K. *Macromolecules* **2009**, *42*, 8129.
85. Tant, M. R.; Mauritz, K. A.; Wilkes, G. L. *Inomers Synthesis, Structure, Properties and Applications* **1996**, *Chapter 1*, 3.
86. Marx, C. L.; Caulfield, D. F.; Cooper, S. L. *Macromolecules* **1973**, *6*, 344.
87. Roche, E. J.; Stein, R. S.; Russell, T. P.; MacKnight, W. J. *J. Polym. Sci., Polym. Phys. Ed.* **1980**, *18*, 1497.
88. Eisenberg, A.; Hird, B.; Moore, R. B. *Macromolecules* **1990**, *23*, 4098.
89. Eisenberg, A.; Sasada, T. *Physics of Non-Crystalline Solids, Pins, J.A.,Ed., North-Holland, Amsterdam* **1965**, 99.
90. Wang, X. Y.; Xie, X. L.; Cai, C. F.; Rytting, E.; Steele, T.; Kiseel, T. *Macromolecules* **2008**, *41*, 2791.
91. Zhang, P.; Qian, J. W.; An, Q. F.; Du, B. Y.; Liu, X. Q.; Zhao, Q. *Langmuir* **2008**, *24*, 2110.
92. Zhang, X. P. L., S.Z.; Liu, L.F.; Yin, J. *Polymer* **2005**, *46*, 1719.
93. Chen, Z. M.; Jiao, Z. L., Z.Q. *J. Appl. Polym. Sci.* **2008**, *110*, 1664.
94. Kim, J.; Kim, B.; Jung, B. *J. Membr. Sci.* **2002**, *207*, 129.
95. Rubatat, L.; Li, C. L.; Dietsch, H.; Nykanen, A.; Ruokolainen, J.; Mezzenga, R. *Macromolecules* **2008**, *41*, 8130.

96. Gromadzki, D.; Gernoch, P.; Janata, M.; Kudela, V.; Nallet, F.; Diat, O.; Stepanek, P. *Eur. Polym. J.* **2006**, *42*, 2486.
97. Blackwell, R. I.; Mauritz, K. A. *Polymer* **2004**, *45*, 3457.
98. Tsang, E. M. W.; Zhang, Z. B.; Shi, Z. Q.; Soboleca, T.; Holdcroft, S. *J. Am. Chem. Soc.* **2007**, *129*, 15106.
99. Yin, Y.; Yamada, O.; Suto, Y.; Mishima, T.; Tanaka, K.; Kita, H.; Okamoto, K. I. *J. Polym. Sci., Part A: Polym. Chem.* **2004**, *43*, 1545.
100. Pang, J. H. Z., H.B.; Li, X.F.; Wang,L.F.; Liu, B.J.; Jiang, Z.H. *J. Membr. Sci.* **2008**, *318*, 271.
101. Hu, Z. X.; Yin, Y.; Chen, S. W.; Yamada, O.; Tanaka, K.; Kita, H.; Okamoto, K. I. *J. Polym. Sci., Part A: Polym. Chem.* **2006**, *44*, 2862.
102. Pang, J.; Zhang, H.; Li, X.; Jiang, Z. *Macromolecules* **2007**, *40*, 9435.
103. Wei, X.; Yu, X. *J. Polym. Sci., Part B: Polym. Phys.* **1997**, *35*, 225.
104. Yang, C. Z.; Grasel, T. G.; Bell, J. L.; Register, R. A.; Cooper, S. L. *J. Polym. Sci., Part B: Polym. Phys.* **1991**, *29*, 581.
105. Li, Y.; Chung, T. S.; Chan, S. Y. *J. Chromatogr. A* **2008**, *1187*, 285.
106. Suleiman, D.; Napadensky, E.; Solan, J. E.; Craford, D. M. *Thermochim. Acta* **2007**, *460*, 35.
107. Vyprachticky, D.; Morawetz, H. *Macromolecules* **1993**, *26*, 339.
108. Ding, Y. S.; Richard, A. R.; Yang, C.-z. *Polymer* **1988**, *30*, 1221.
109. Tudryn, G. J.; Liu, W. J.; Wang, S. W.; Colby, R. H. *Macromolecules* **2011**, *44*, 3572.
110. Kim, J. H.; Kim, B. Y.; Jung, B. S.; Kang, Y. S.; Ha, H. Y.; Oh, I. H.; Ihn, K. J. *Macromol. Rapid Commun.* **2002**, *23*, 753.
111. Ganguly, A.; Bhowmick, A. K. *Macromolecules* **2008**, *41*, 6246.
112. Lu, X. Y.; Steckle, W. P.; Weiss, R. A. *Macromolecules* **1993**, *26*, 6525.
113. Kim, B.; Kim, J. W.; Jung, B. *J. Membr. Sci.* **2005**, *250*, 175.
114. Storey, R. F.; Baugh, D. W. *Polymer* **2000**, *41*, 3205.
115. Sakurai, S.; Momii, T.; Taie, K.; Shibayama, M.; Nomura, S.; Hashimoto, T. *Macromolecules* **1993**, *26*, 5796.
116. Yang, J. E.; Lee, J. S. *Electrochim. Acta* **2004**, *50*, 617.
117. Mauritz, K. A.; Blackwell, R. I.; Beyer, F. L. *Polymer* **2004**, *45*, 3001.
118. Won, J.; Choi, S. W.; Kang, Y. S.; Ha, H. Y.; Oh, I. H.; Kim, H. S.; Kim, K. T.; Jo, W. H. *J. Membr. Sci.* **2003**, *214*, 245.
119. Li, N. W.; Hwang, D. S.; Lee, S. Y.; Liu, Y. L.; Lee, Y. M.; Guiver, M. D. *Macromolecules* **2011**, *44*, 4901.
120. Lee, H. S.; Badami, A. S.; Roy, A.; Mcgrath, J. E. *J. Polym. Sci. Part a-Polym. Chem.* **2007**, *45*, 4879.
121. Rubatat, L.; Li, C. X.; Dietsch, H.; Nykanen, A.; Ruokolainen, J.; Mezzenga, R. *Macromolecules* **2008**, *41*, 8130.
122. Duncan, A. J.; Leo, D. J.; Long, T. E. *Macromolecules* **2008**, *41*, 7765.
123. Moreira, F. T. C.; Dutra, R. A. F.; Noronha, J. P. C.; Sales, M. G. F. *Biosensors & Bioelectronics* **2011**, *26*, 4760.
124. Vargantwar, P. H.; Roskov, K. E.; Ghosh, T. K.; Spontak, R. J. *Macromol. Rapid Commun.* **2012**, *33*, 61.
125. Green, M. D.; Long, T. E. *Polymer Reviews* **2009**, *49*, 291.
126. Green, O.; Grubjesic, S.; Lee, S. W.; Firestone, M. A. *Polymer Reviews* **2009**, *49*, 339.

127. He, Y. Y.; Li, Z. B.; Simone, P.; Lodge, T. P. *J. Am. Chem. Soc.* **2006**, *128*, 2745.
128. Simone, P. M.; Lodge, T. P. *Acs Applied Materials & Interfaces* **2009**, *1*, 2812.
129. Matsumoto, K.; Endo, T. *J. Polym. Sci. Part a-Polym. Chem.* **2011**, *49*, 3582.

Chapter 3: Influence of Ionic Charge Placement on Performance of Poly(ethylene glycol)-Based Sulfonated Polyurethanes

(Gao, R.; Zhang, M.; Dixit, N.; Moore, R.B.; Long, T.E.* *Polymer* **2012**, 53, 1203-1211)

3.1 Abstract

Poly(ethylene glycol) (PEG)-based sulfonated polyurethanes bearing either sulfonated soft segments (SSSPU) or sulfonated hard segments (SHSPU) were synthesized using sulfonated monomers. Differential scanning calorimetry (DSC) revealed that sulfonate anions either in the soft segments or hard segments both increased the glass transition temperatures (T_g's) of the soft segments and suppressed their crystallization. Moreover, dynamic mechanical analysis (DMA) and tensile analysis demonstrated that SSSPU possessed a higher modulus and tensile strength relative to SHSPU. Fourier transform infrared (FTIR) spectroscopy revealed that hydrogen bonding interactions in SHSPU were suppressed compared to SSSPU and noncharged PU. This observation suggested a high level of phase-mixing for SHSPU. In addition, atomic force microscopy (AFM) phase images revealed that both SSSPU and noncharged PU formed well-defined microphase-separated morphologies, where the hard segments phase-separated into needle-like hard domains at the nanoscale. However, SHSPU showed a phase-mixed morphology, which was attributed to increased compatibility of polar PEG soft segments with sulfonated ionic hard segments and disruption of hydrogen bonds in the hard segment. The phase-mixed morphology of SHSPU was further demonstrated using small angle X-ray scattering (SAXS), which showed a featureless X-ray scattering profile. In contrast, SAXS profiles of SSSPU and noncharged PU demonstrated microphase-separated morphologies. Moreover, SSSPU also displayed a broad ionomer peak ranging in q=1~2 nm^{-1}, which resulted

from the sodium sulfonate ion pair association in the polar PEG soft phase. Morphologies of sulfonated polyurethanes correlated well with thermal and mechanical properties.

3.2 Introduction

Polyurethane (PU) is an important class of segmented block copolymers for many applications including durable coating,[1,2] foams,[3] high performance adhesives,[4] biomaterials,[5,6] and automotive materials[7]. Due to the microphase separation of the incompatible alternating hard and soft segments, polyurethanes perform as high strength thermoplastic elastomers. However, properties are further tailored with modification of the molecular structure of the hard and soft segments,[8-12] variation of volume fractions of the two different segments,[13-17] and incorporation of additional chemical or physical crosslinking sites.[18]

Among the many different types of polyurethanes, ion-containing polyurethanes, or polyurethane ionomers, have received growing attention for their unique morphology and properties, which are attributed to synergistic interactions of Coulombic, hydrogen bonding, and hydrophobic interactions. In recent years, many efforts have probed the structure-morphology-property relationships of ion-containing polyurethanes.[19-23] Researchers determined that the morphology and thermomechanical properties of ion-containing polyurethanes depend strongly on the ion concentration, ion type, and counterion structure. Cooper et al. reported a comparison of the physical properties of carboxylated polyurethane and sulfonated polyurethane ionomers.[24] They demonstrated that sulfonated polyurethane ionomers showed a higher degree of phase separation, which provided higher tensile strength than carboxylated polyurethanes. More recently, Colby et al. investigated the influence of various counter cations on performance of polyurethane-carboxylate ionomers.[25] They found that replacement of sodium cations with larger ammonium cations reduced the glass transition temperature (T_g) from 47 ^oC to -6 ^oC and

enhanced the ionic conductivity by 5 orders of magnitude. In addition to ion type and counterion structure, researchers have demonstrated that ion placement also plays an important role in determining the morphology and properties of ionomers.[26,27] Our research group reported the influence of sulfonate charge placement on morphologies of sulfonated acrylic graft copolymers. These copolymers contained sulfonated blocks either adjacent to the backbone or at the branch termini.[28] We demonstrated that only the sulfonated graft copolymer with sulfonated block at the branch termini showed ionic aggregates due to a higher mobility of the terminal sulfonated block than sites adjacent to the backbone. Several other studies on sulfonated polyetheretherketones or sulfonated polyimides also demonstrated that charge placement significantly influenced the performance of ionomers.[29-31] However, to the best of our knowledge, a systematic study that investigates the influence of charge placement on performance of PEG-based sulfonated polyurethanes does not exist in the literature.

PEG-based sulfonated polyurethanes are particularly interesting because of emerging energy and biomedical applications, and for example, sulfonated copolymers are good candidates for fuel cell membrane applications.[32-35] Moreover, PEG-containing copolymers blended with lithium salts were also reported as suitable materials for solid-state batteries and fuel cells. Studies showed that rapid segmental motion of PEG segments afforded faster ion transport and higher ionic conductivity.[36,37] In the biomedical arena, researchers have demonstrated that sulfonated polyurethanes and PEG-containing polyurethanes had enhanced biocompatibility.[38-40] For example, Shen et al. modified polyurethanes with sulfobetaine and demonstrated enhanced blood compatibility of sulfonated polyurethanes using hemolytic testing and platelet-rich plasma adhesion experiments.[41] Previous work in our group has focused on synthesis and property characterization of poly(tetramethylene oxide) (PTMO)-based polyurethanes containing

phosphonium cations in the hard segment.[42] We demonstrated that phosphonium cations in the hard segment significantly influenced hydrogen bonding interactions, which contributed to the thermal and mechanical properties of phosphonium-containing polyurethanes.

In the current study, we successfully synthesized PEG-based sulfonated polyurethanes containing sulfonate charge either in the soft segment or hard segment using a sulfonated monomer strategy. Upon comparison with a noncharged polyurethane analogue, we systematically investigated the influence of sulfonate charge placement on performance of PEG-based sulfonated polyurethanes using complementary characterization techniques. Our study demonstrated that the placement of sulfonate charge on the segmented polyurethane backbone dramatically influenced thermal and mechanical properties, hydrogen bonding interactions, and morphologies of PEG-based sulfonated polyurethanes.

3.3 Experimental

Materials

Dimethyl 5-sulfoisophthalate sodium salt (98%), ethylene glycol (99%), titanium (IV) isopropoxide, poly(ethylene glycol) (PEG) (M_n=950-1000 g/mol and M_n=2000 g/mol) were purchased from Aldrich and dried at 60 ^oC *in vacuo* overnight immediately prior to use. Anhydrous *N,N*-dimethylformamide (DMF) (99.8%) was purchased from Aldrich and used as received. The chain extender *1,4*-butanediol (BD) (99%) was purchased from Aldrich and distilled from calcium hydride. Dibutyltin dilaurate (DBTDL) (95%) was purchased from Aldrich and diluted to 1 wt% using anhydrous tetrahydrofuran. Methanol (HPLC grade) and anhydrous diethyl ether (99%) were purchased from Fisher Scientific. Dicyclohexylmethane-

4,4'-diisocyanate (HMDI) (99.5%) was kindly provided by Bayer MaterialScience and used as received.

Synthesis of bis(2-hydroxyethyl)-5-sulfoisophthalate sodium salt (SD)

In a two-necked, round-bottomed flask equipped with a stir bar and condenser, ethylene glycol (21.32 g, 0.34mol), dimethyl 5-sulfoisophthalate sodium salt (10.28 g, 0.034mol), and 0.05 wt% of titanium (IV) isopropoxide were added and purged with nitrogen. The reaction was allowed to proceed at 170 ^{o}C with nitrogen flow. ^{1}H NMR spectroscopy was used to confirm complete reaction. The excess ethylene glycol was removed by distillation under reduced pressure at 70 ^{o}C. The crude product was subsequently dissolved in methanol and precipitated into diethyl ether three times. The final product was obtained as a white solid with a yield of 91%. FAB MS negative mode: m/z=333.03. ^{1}H NMR (400 MHz, DMSO, 25 ^{o}C) (δ, ppm): 3.68-3.71 (4H, h,-C*H*$_{2}$-), 4.3 (4H, t,-C*H*$_{2}$-OH), 5.0 (2H, t, O*H*), 8.45-8.5 (3H, t, phenyl).

Synthesis of PEG-based sulfonated polyol (SPEG)

PEG-based sulfonated polyol was synthesized in a similar manner as described for the synthesis of bis(2-hydroxyethyl)-5-sulfoisophthalate sodium salt. 1K PEG (23.70 g, 23.7 mmol) and dimethyl 5-sulfoisophthalate sodium salt (3.51 g, 11.8 mmol) were added to a two-necked, round-bottomed flask equipped with a stir bar. 0.05 wt% titanium (IV) isopropoxide was used as the catalyst. The reaction was allowed to proceed at 170~190 ^{o}C under N_2 flow. Complete reaction was determined using ^{1}H NMR spectroscopy. The crude product was dissolved in acetone and precipitated in diethyl ether 3 times. ^{1}H NMR (400 MHz, DMSO, 25 ^{o}C) (δ, ppm): 3.40-3.63 (174H, broad,-C*H*$_{2}$-C*H*$_{2}$-O-), 3.78 (4H, t,-C*H*$_{2}$-OH), 4.44 (4H, t, C*H*$_{2}$-COO), 4.57 (2H, t, O*H*), 8.40-8.44 (3H, t, phenyl).

Synthesis of segmented polyurethanes bearing sulfonated soft segments (SSSPU)

The polymer was synthesized according to a typical two-step process. The first step provided HMDI end-capped SPEG. SPEG (7.25 g, 2.69 mmol) was weighed into a three-necked, round-bottomed flask equipped with an addition funnel, nitrogen inlet, and an overhead mechanical stirrer. HMDI (2.05 mL, 8.33 mmol)) was subsequently syringed into the flask. The reaction was allowed to proceed for 4 h at 80 ^{o}C under a N_2 atmosphere in the absence of solvent. 1 wt% DBTDL in THF (50 ppm) was used as the catalyst. In the second step, *1,4*-butanediol was dissolved in anhydrous DMF and added dropwise to the flask. The reaction was continued for an additional 24 h at 80 ^{o}C. FTIR spectroscopy was used to confirm complete consumption of the isocyanate groups.

Synthesis of segmented polyurethanes bearing sulfonated hard segments (SHSPU)

The SHSPU synthesis was conducted in a three-necked, round-bottomed flask equipped with an addition funnel, nitrogen inlet, and an overhead mechanical stirrer. Following a typical two-step synthetic route as described above, pre-dried PEG (M_n=2000 g/mol) was first end-capped with HMDI at 80 ^{o}C for 4 h using DBTDL (50 ppm) as the catalyst. In the second step, bis(2-hydroxyethyl)-5-sulfoisophthalate sodium salt was dissolved in anhydrous DMF (15 wt% solids) and added dropwise to the prepolymers. The reaction was allowed to proceed for 24 h at 80 ^{o}C under a N_2 atmosphere. FTIR spectroscopy demonstrated complete consumption of the isocyanate groups. Noncharged PU was synthesized similarly except that *1,4*-butanediol was used as the chain extender, rather than bis(2-hydroxyethyl)-5-sulfoisophthalate sodium salt. In this study, all polyurethane solutions were directly cast in Teflon® modes and dried in air at 23 ^{o}C for 72 h with a relative humidity (RH) of 32% to form solid membranes. The resulting membranes were subsequently dried *in vacuo* at 50 ^{o}C for additional 72 h to remove residual

solvent and moisture. All samples showed negligible weight loss at 100 ^{o}C in TGA. The samples were kept in a dessicator (RH=20%) at 23 ^{o}C, and dried *in vacuo* at 50 ^{o}C for at least 24 h immediately prior to characterization. SSSPU and SHSPU resulted in optically clear films; in sharp contrast, noncharged PU resulted in opaque films due to crystallization of PEG soft segments.

Polymer characterization

^{1}H NMR spectroscopy was performed on a Varian INOVA 400 MHz spectrometer using *d*-DMSO as the solvent. FAB-MS was obtained on a JEOL HX110 dual-focusing mass spectrometer using a negative ion mode. Size exclusion chromatography (SEC) was performed on a Waters SEC equipped with two Waters Styragel HR5E (DMF) columns, a Waters 717plus autosampler, and a Waters 2414 differential refractive index detector. The molecular weight of noncharged PU was measured at 50 ^{o}C in DMF. Differential scanning calorimetry (DSC) was performed using a TA Instruments Q2000 differential scanning calorimeter under a nitrogen flow of 50 mL/min with a heating rate of 10 ^{o}C/min. For isothermal crystallization studies, the samples were heated to 150 ^{o}C to eliminate thermal history and subsequently quenched to 0 ^{o}C. The samples were maintained at 0 ^{o}C for 120 min. Dynamic mechanical analysis (DMA) measurements were performed on a TA Instruments Q800 dynamic mechanical analyzer in the film tension mode at a frequency of 1 Hz and a temperature ramp of 3 ^{o}C/min over the range -80 to 120 ^{o}C. Tensile analysis was performed on a 5500R Instron universal testing instrument with a cross-head rate of 50 mm/min at ambient conditions. FTIR experiments were carried out using a Varian 670-IR spectrometer (DTGS detector) equipped with a Pike Technologies variable temperature GladiATR^{TM} attachment (diamond crystal). The spectra were collected at a resolution of 4 cm^{-1}, and 32 scans were averaged. For variable temperature FTIR experiments,

the spectra were collected every 10 ^{o}C starting from 30 to 140 ^{o}C with a temperature ramp of 1 ^{o}C/min. Atomic force microscopy (AFM) was conducted on a Veeco MultiMode AFM in a tapping mode at ambient conditions. SAXS and wide angle X-ray diffraction (WAXD) were performed using a Rigaku S-Max 3000 3 pinhole SAXS system equipped with a rotating anode emitting X-rays with a wavelength of 0.154 nm (Cu Kα). Scattering from a silver behenate standard was used to calibrate the sample-to-detector distance. For SAXS, the sample-to-detector distance was 1603 mm, and for WAXD, the sample-to-detector distance was 82.5 mm. Two-dimensional SAXS patterns were obtained using a fully integrated 2D multi-wire, proportional counting, gas-filled detector during an exposure time of 1 h per sample. SAXS data were corrected for sample thickness, sample transmission, and background scattering. WAXD two-dimensional diffraction patterns were obtained using an image plate with an exposure time of 1 h. All SAXS/WAXD data were analyzed using the SAXSGUI software package to obtain radially integrated SAXS/WAXD intensity versus scattering vector q (SAXS) or 2θ (WAXD) profiles, where $q=4\pi\sin(\theta)/\lambda$, θ is half of the scattering angle, and λ is the X-ray wavelength. WAXD data were corrected for sample thickness, and the profiles were vertically shifted to facilitate a comparison of peak positions.

3.4 Results and Discussion

3.4.1 Sulfonated polyurethane synthesis

Sulfonated polyurethanes with controlled sulfonate charge placement either in the soft segments (SSSPU, as shown in **Scheme 3.1**) or in the hard segments (SHSPU, as shown in **Scheme 3.2**) were synthesized using a sulfonated monomer strategy. Oligomeric sulfonated PEG and sulfonated diol, bis(2-hydroxyethyl)-5-sulfoisophthalate sodium salt, were synthesized and used as the polyol and chain extender, respectively. Sulfonate anions were readily incorporated

into the polyurethane backbone during polymerization. Post-sulfonation has been widely used for sulfonated polyurethane syntheses, however, the sulfonated monomer strategy enabled better control of sulfonation level and sulfonate charge placement while avoiding possible side reactions.[43] In addition to sulfonated polyurethanes, a noncharged polyurethane (PU) was also synthesized for comparative purposes. The polyurethane samples contained the same molecular weight of the soft segments and the same mole fraction of hard segments, which enabled the study of the influence of sulfonate charge and charge placement on polyurethane performance. In all these polyurethane syntheses, complete polymerizations were demonstrated using FTIR spectroscopy, i.e. the isocyanate stretching vibration peak at 2260 cm^{-1} completely disappeared. Moreover, molecular weight of noncharged PU was determined using DMF SEC, which showed a number-average molecular weight (M_n) of 32 kg/mol. However, no reliable SEC data were obtained for SSSPU and SHSPU due to polymer aggregation in SEC solvents, which was verified with dynamic light scattering.

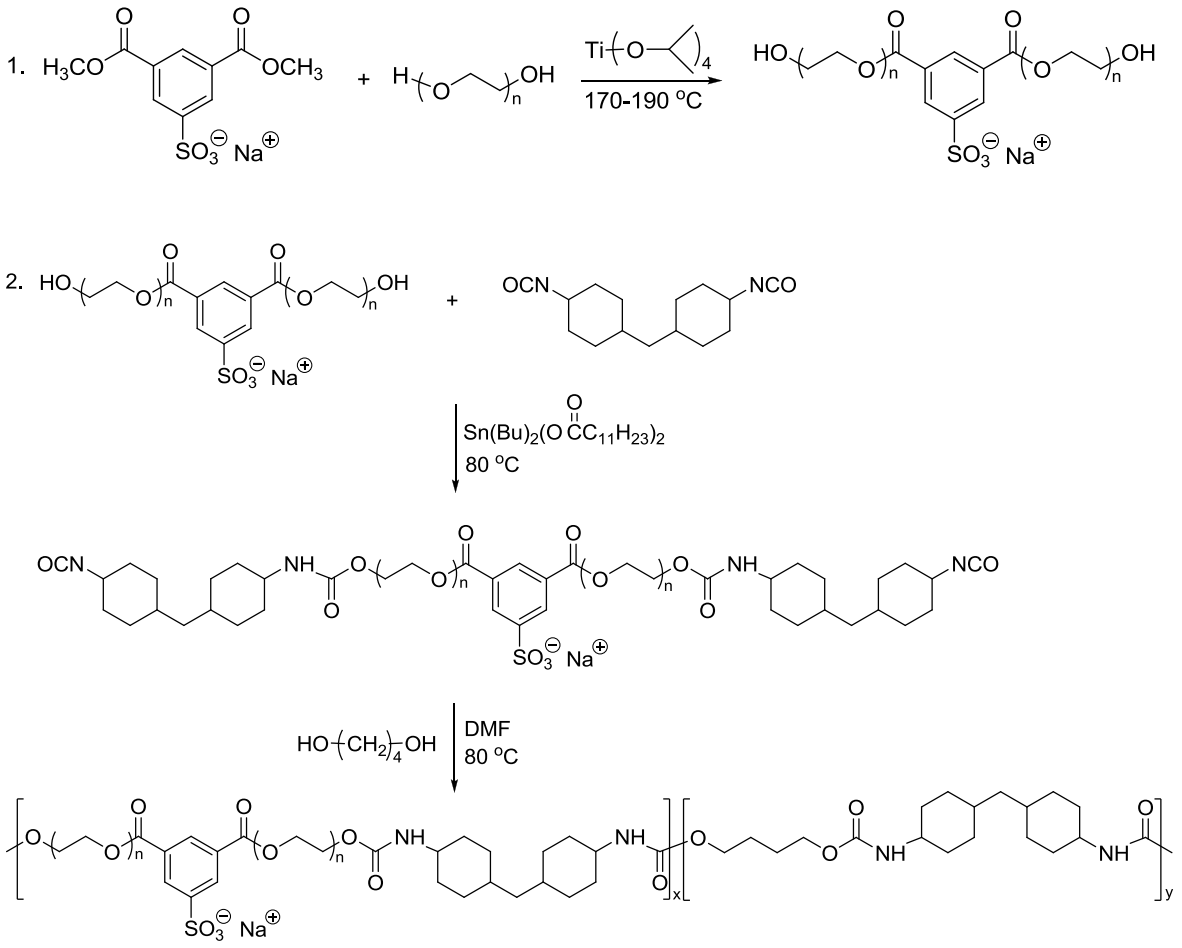

Scheme 3.1 Synthesis of sulfonated polyurethanes bearing sulfonated soft segments (SSSPU)

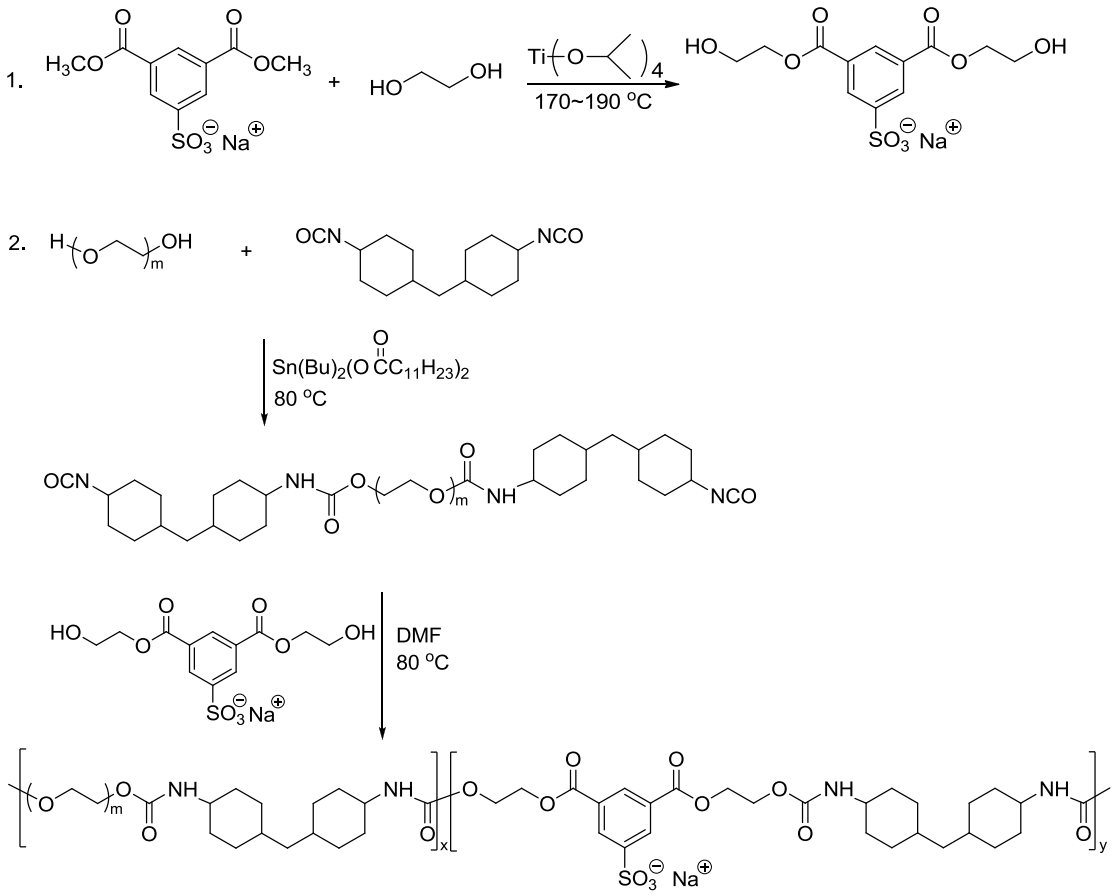

Scheme 3.2 Synthesis of sulfonated polyurethanes bearing sulfonated hard segments (SHSPU)

3.4.2 Thermal properties

DSC thermograms in **Figure 3.1** reveal the influence of sulfonate charge placement on thermal transitions of PEG-based sulfonated polyurethanes. In the first heat DSC curves as shown in **Figure 3.1**(a), noncharged PU and SSSPU showed similar endothermic transitions at 107 ^{o}C and 110 ^{o}C, respectively, which were assigned to hard segment crystallization; however, SHSPU did not show hard segment crystallinity. Several factors possibly contributed to reduced crystallinity of SHSPU hard segments. First, the bulky sulfonated diol structure disrupted the regularity of the hard segment and prevented effective chain packing. Second, ionic-dipole and dipole-dipole interactions among the sodium sulfonate ion pairs disrupted hydrogen bonding

interactions, which strongly contribute to hard segment crystallization. Finally, sulfonated hard segments underwent phase-mixing with PEG soft segments, reducing the homogeneity of the hard domains. In the second heat DSC curves, significant difference in glass transition and crystallization behavior of PEG-based soft segments was observed among these three polymers. Only the noncharged PU showed T_c at 0 ^oC, T_m at 34 ^oC, and T_g at -53 ^oC for the PEG soft segments. In contrast, both SSSPU and SHSPU showed significantly higher soft segment T_g's, which were -26 ^oC and -5 ^oC, respectively. The increased soft segment T_g of SSSPU was attributed to the reduced mobility of sulfonated PEG soft segments due to the sodium sulfonate ion pair association and the coordination of PEG ether oxygens with sodium cations. SAXS experiments, shown below, demonstrated the existence of sodium sulfonate ion pair association. In addition, Tang et al. reported that PEG-based polyurethanes containing $NaClO_4$ salt showed increased soft segment T_g due to the coordination of sodium cations with PEG ether oxygens.[44] More interestingly, SHSPU, despite bearing noncharged PEG soft segments, showed the highest soft segment T_g. It was presumed that the increased soft segment T_g of SHSPU was due to phase-mixing of hard and soft segments. In order to further demonstrate the influence of sulfonated hard segments on the glass transition and crystallization behavior of PEG soft segments, sulfonated polyurethanes, which had identical PEG soft segments but hard segments with different sulfonation levels, were prepared. The polyurethane compositions and thermal transition data are summarized in **Table 3.2**. The soft segment T_g was systematically increased with increasing the sulfonation level of the hard segments, i.e. a higher fraction of SD was used as the chain extender. Moreover, crystallization of PEG soft segments was completely suppressed at 50% SD as the chain extender. We hypothesize that the sodium sulfonate ions in the hard segments increase the compatibility of the hard segments with the polar PEG soft

segments, leading to phase-mixing.[24] Higher contents of sodium sulfonate ions in the hard segments cause more phase-mixing and higher soft segment T_g's. The influence of sulfonation level of hard segments on crystallization behavior of PEG soft segments was further studied with isothermal DSC experiments. **Figure 3.2** shows the isothermal crystallization curves of all five polymers at 0 ^oC. It is clear that the sulfonate anions significantly retarded the crystallization of PEG soft segments. Noncharged PU (BD/SD=100/0) started to crystallize immediately upon quenching to 0 ^oC, and a relatively sharp crystallization peak at $t_{1/2}$=2.6 min was observed. In contrast, the crystallization peak for SHSPU-2 (BD/SD=75/25) was retarded to $t_{1/2}$=20 min with a much longer crystallization time of 30 min. However, the noncharged PU and SHSPU-2(BD/SD=75/25) showed comparable degree of crystallinity for the PEG soft segments. It was also worth mentioning that SHSPU-3 (BD/SD=50/50) did not show crystallization over a 120-min time scale, the sample crystallized after 2 mo storage at 23 ^oC. These observations suggested that the soft segment mobility was reduced by the sulfonated hard segments. However, due to the lack of effective physical crosslinking sites, PEG soft segments remained mobile and contributed to the crystalline PEG phase.

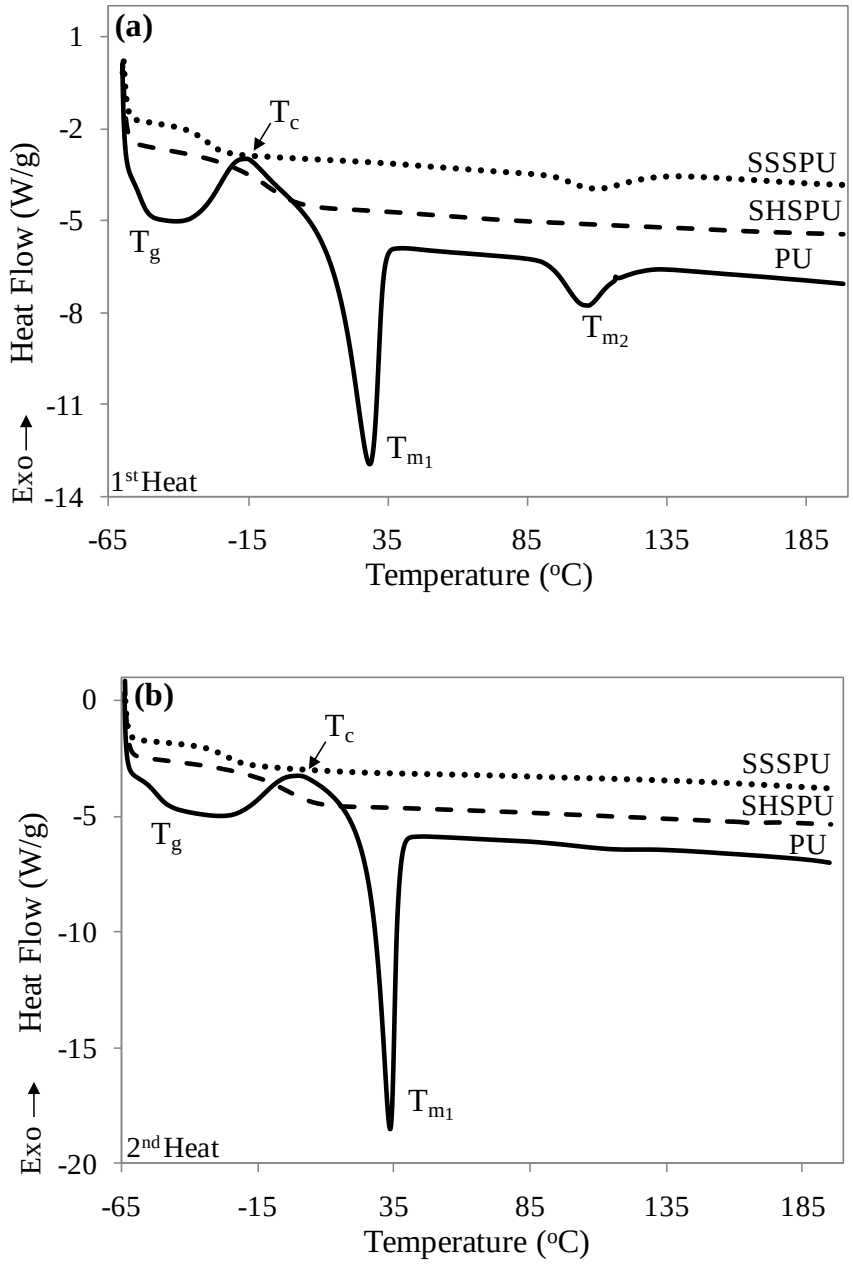

Figure 3.1 DSC traces of noncharged PU, SSSPU, and SHSPU. Conditions: 10 °C/min

Table 3.1 Chemical compositions and thermal transition temperatures of noncharged PU, SSSPU, and SHSPU

	Soft Segment	Isocyanate	Chain Extender	T_g (°C)	T_m (°C)	HS (mol%)	HS (wt%)
SSSPU	2K SPEG	HMDI	BD	-26	ND	83	30
SHSPU	2K PEG	HMDI	SD	-5	110*	83	43
PU	2K PEG	HMDI	BD	-52	34, 107*	83	33

*data obtained from 1st heat of DSC experiment; ND=not detected

Table 3.2 Thermal transitions for sulfonated polyurethanes with sulfonated hard segments at various sulfonation levels

	HMDI	PEG	BD	SD*	BD/SD	$T_{g(ss)}$(°C)	T_c (°C)	$T_{1/2}$(min)	$\Delta H_m(J/g)$	%cryst	wt% HS
PU	3	1	2	0	100/0	-52	34	2.6	29.29	22.08	33
SHSPU-2	3	1	1.5	0.5	75/25	-46	33	20	28.65	22.57	35
SHSPU-3	3	1	1	1	50/50	-24	ND	ND	ND	ND	38
SHSPU-4	3	1	0.5	1.5	25/75	-16	ND	ND	ND	ND	41
SHSPU	3	1	0	2	0/100	-5	ND	ND	ND	ND	43

*SD=bis(2-hydroxyethyl)-5-sulfoisophthalate sodium salt; ND=not detected

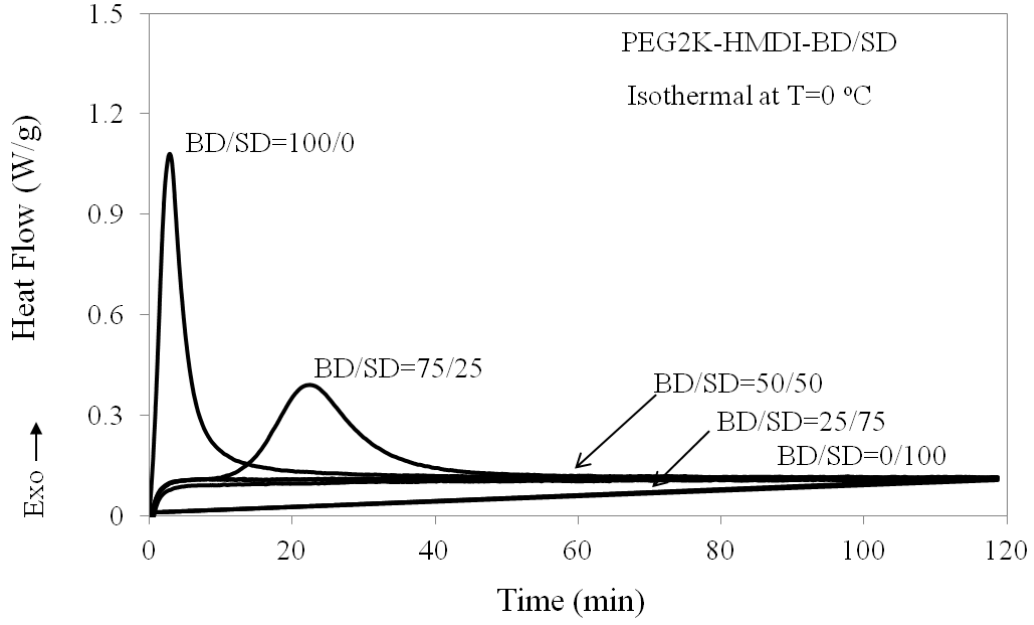

Figure 3.2. Isothermal (T=0 °C) crystallization behavior of SHSPU with various sulfonate charge densities

3.4.3 Thermomechanical behavior

Thermal dynamic mechanical properties of noncharged PU, SSSPU, and SHSPU were investigated using dynamic mechanical analysis (DMA). The temperature dependency of storage modulus (G') of these three polyurethanes is shown in **Figure 3.3**. DMA clearly demonstrated that sulfonate charge placement dramatically influenced the thermal transition behavior, which correlated well with DSC experiments. Noncharged PU possessed crystalline PEG soft segments, which showed the lowest T_g. In contrast, both SSSPU and SHSPU showed increased soft segment T_g and no soft segment crystallinity. **Figure 3.3** also indicates that sulfonate charge and sulfonate charge placement significantly influence the mechanical performance of these polymers. Due to the soft segment crystallization, noncharged PU showed a narrow rubbery plateau ranging from 50 ^oC to 85 ^oC. However, SSSPU showed a much broader rubbery plateau ranging from 10 ^oC to 110 ^oC. This suggested that incorporation of sodium sulfonate ions into the soft segments significantly increased the continuous use temperature range of PEG-based polyurethanes. In contrast, SHSPU showed a narrow rubbery plateau with a lower storage modus. This suggested that SHSPU lacked effective physical crosslinking sites, which were typically attributed to the microphase-separated hard domains. In addition, noncharged PU and SSSPU showed comparable flow temperatures at 120 ^oC. It should be noted that, due to the low storage modulus of SHSPU at high temperature, the DMA could not detect a reliable mechanical response for the SHSPU film. Thus, the experiment was stopped at 120 ^oC in all cases.

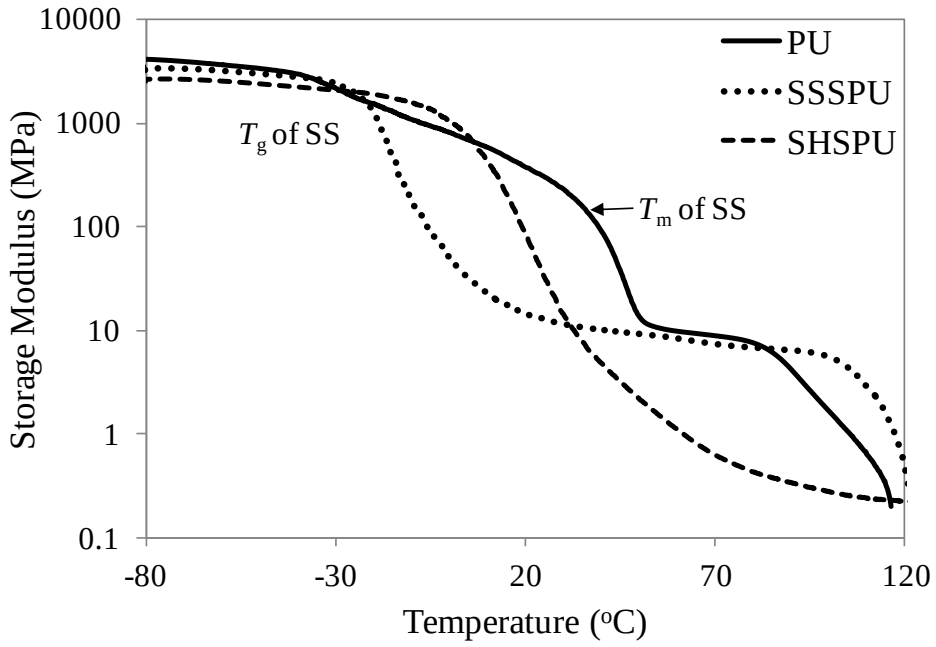

Figure 3.3 DMA curves of noncharged PU, SSSPU, and SHSPU (Conditions: 3 °C/min; 1 Hz; film tension mode)

3.4.4 Tensile analysis

Uniaxial stress-strain tensile analysis was conducted to elucidate the influence of charge placement on mechanical properties of PEG-based sulfonated polyurethanes. **Figure 3.4** shows a comparison of the stress-strain curves of noncharged PU, SSSPU, and SHSPU. The most notable difference among these polymers was the Young's modulus, which was calculated from the slope of the initial stress-strain curve below 2.5% elongation.[45] SSSPU and noncharged PU had higher Young's moduli (9.11±0.88 MPa and 14.38±2.38 MPa, respectively) than SHSPU (1.34±0.27 MPa). The difference in Young's moduli of polyurethane elastomers is often attributed to the microphase-separated structure.[46] In a strong phase-separated polyurethane, the hard segments form the high T_g hard domains, which serve as reinforcing "fillers" that provide a high modulus. More well-defined phase-separation usually results in more homogenous hard domains, which serve as more effective fillers to reinforce polyurethane elastomers. The tensile

data suggested that non-charged PU and SSSPU had more well-defined phase-separated morphology than SHSPU. Moreover, the ionic aggregates in SSSPU and crystalline PEG soft segments in noncharged PU also serve as reinforcing fillers to further enhance moduli. Another significant difference in the mechanical performance is the extent of elongation. SSSPU and SHSPU showed comparable maximum elongation, which were 803±108% and 818±156%, respectively. However, noncharged PU showed significantly reduced elongation of 391±17%, which might be due to the crystalline PEG soft segments. Hammond et al. previously reported that polyurethanes with high crystalline PEG soft segments exhibited reduced elongation.[47] Moreover, difference in molecular weights of these polyurethanes may also contribute to the different elongation, although noncharged PU showed a reasonable high molecular weight (M_n=32 kg/mol) in DMF SEC.

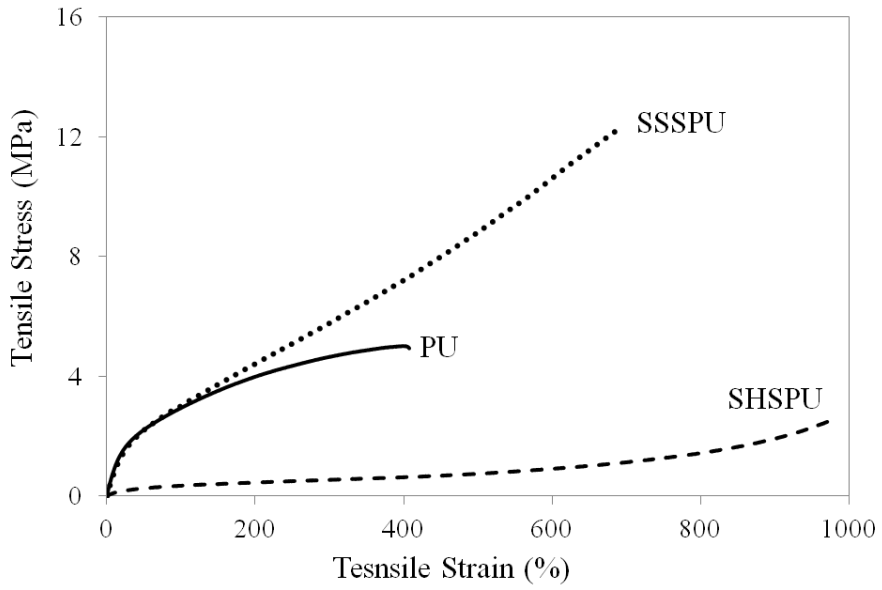

Figure 3.4 Comparison of tensile properties of noncharged PU, SSSPU, and SHSPU (Conditions: 50 mm/min, ambient conditions)

3.4.5 Hydrogen bonding characterization

Fourier transform infrared (FTIR) spectroscopy is a sensitive tool to characterize hydrogen bonding interactions of polyurethanes.[48] In a polyurethane system, C=O "acceptor" groups hydrogen-bond with the N-H "donor" groups. Due to the hydrogen bonding interactions, the electron distribution on the hydrogen-bonded C=O groups is disrupted, which shifts the C=O stretching vibration to a low wavenumber in FTIR spectra. In addition, previous studies in our laboratories demonstrated that N-H stretching peaks in FTIR spectra narrowed as the hydrogen bonding extent increased.[42] Here we utilized both the C=O stretching region and N-H stretching region (as shown in **Figure 3.5** (a) and (b), respectively) to investigate the influence of charge placement on hydrogen bonding interactions of PEG-based sulfonated polyurethanes. In **Figure 3.5** (a), the peaks at 1716 cm^{-1} were attributed to the stretching vibration mode of free C=O groups, and the peaks at 1689 $cm^{-1}$and 1662 cm^{-1} were attributed to hydrogen-bonded C=O

groups.[49] The spectra clearly showed that SHSPU did not contain hydrogen bonding interactions; however, both noncharged PU and SSSPU displayed shifted C=O peaks to a lower wavenumber, indicating the presence of hydrogen bonding interactions. In addition, the N-H stretching region in **Figure 3.5** (b) showed relatively sharp N-H stretching vibration peaks near 3300 cm^{-1} for noncharged PU and SSSPU due to the high extent of hydrogen bonding interactions, and SHSPU displayed broad N-H stretching peaks. Painter et al. reported earlier that hydrogen bonding causes self-association of polyurethane hard segments and serves as an additional driving force for polyurethane microphase separation.[50] We proposed that the absence of hydrogen bonding in SHSPU presumably arises from a phase-mixed morphology and irregular hard segment structure. However, higher extent of hydrogen bonding interactions in noncharged PU and SSSPU was consistent with a higher degree of microphase-separation. In order to further understand the correlation between hydrogen bonding and hard segment morphological features, we performed variable temperature FTIR spectroscopy to investigate the temperature dependence of hydrogen bonding interactions in noncharged PU (**Figure 3.6**-a) and SSSPU (**Figure 3.6**-b). For noncharged PU, the spectra clearly showed that absorbance of bonded carbonyl peaks at 1689 $cm^{-1}$and 1662 cm^{-1} diminished significantly at 100 ^{o}C and completely disappeared at 120 ^{o}C due to hydrogen bonding dissociation. SSSPU showed a similar shift of bonded carbonyl peaks upon heating. However, the hydrogen bonds in SSSPU started to dissociate at 120 ^{o}C and disappeared at 130 ^{o}C. The hydrogen bonding dissociation temperature correlated well with hard segment melting points (T_m's) as shown in DSC, in which, noncharged PU and SSSPU showed T_m's at 107 ^{o}C and 110 ^{o}C, respectively. This observation indicated that hydrogen bonding is strongly related to hard segment crystallization in these polyurethanes.

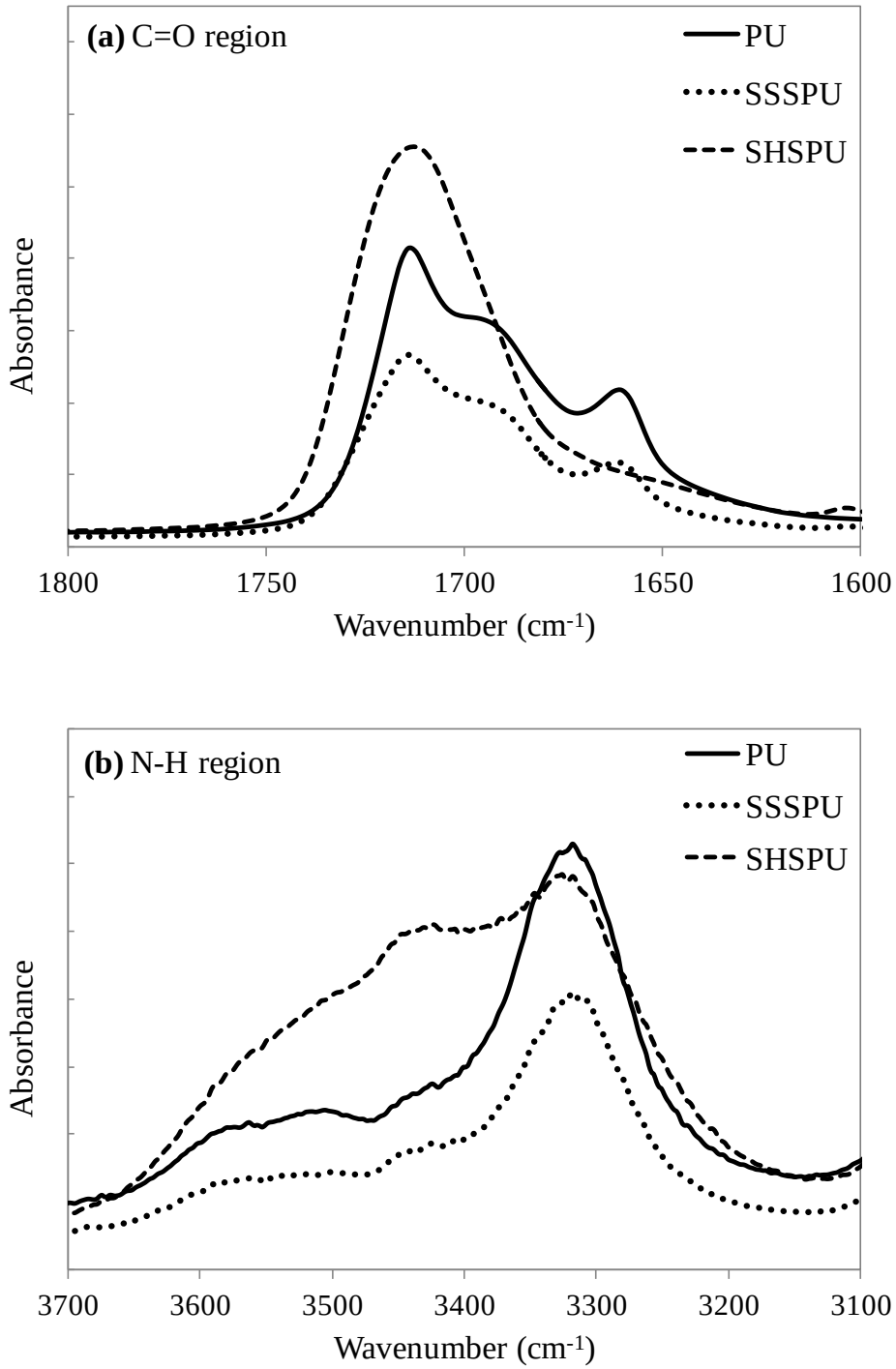

Figure 3.5 FTIR spectroscopy of the (a) C=O region and (b) N-H region of noncharged PU, SSSPU, and SHSPU

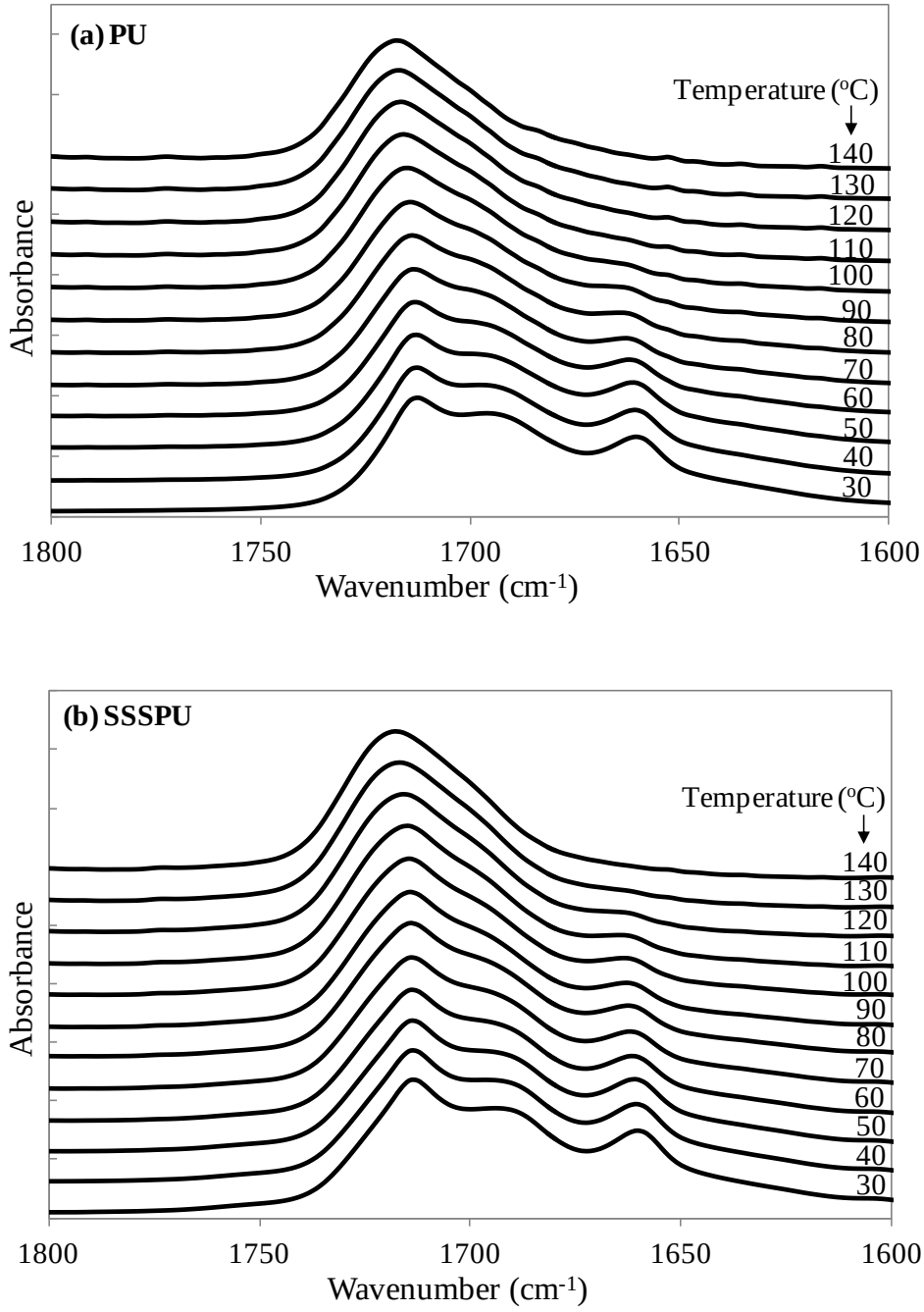

Figure 3.6 Variable temperature FTIR spectra in carbonyl region for noncharged PU (a) and SSSPU (b)

3.4.6 Morphological characterization

Morphological features of noncharged PU, SSSPU, and SHSPU were characterized using complementary techniques including atomic force microscopy (AFM), small angle X-ray scattering (SAXS), and wide angle X-ray diffraction (WAXD). Recently, AFM has been widely used to study the microphase-separation of polyurethanes.[51] In a typical AFM phase image of a microphase-separated polyurethane, the hard domains appear as lighter regions and the soft phase appears as darker regions. **Figure 3.7** shows the AFM tapping mode phase images of noncharged PU, SSSPU, and SHSPU obtained at ambient conditions. AFM indicated that both noncharged PU and SSSPU possessed well-defined microphase-separated morphologies. The hard segments phase separated from the continuous soft phase to form needle-like cylindrical hard domains. These hard domains were randomly orientated with diameters on the order of 5-10 nm. The length of the needles was approximately 50 to 100 nm. Similar AFM surface morphology of segmented polyurethanes has been reported in the literature.[47,52-54] In contrast, SHSPU showed a more phase-mixed morphology without distinct hard domains. The morphologies observed from AFM correlated well with observations in DSC, DMA, and FTIR experiments, which all indicated a microphase-separated morphology for noncharged PU and SSSPU and a phase-mixed morphology for SHSPU.

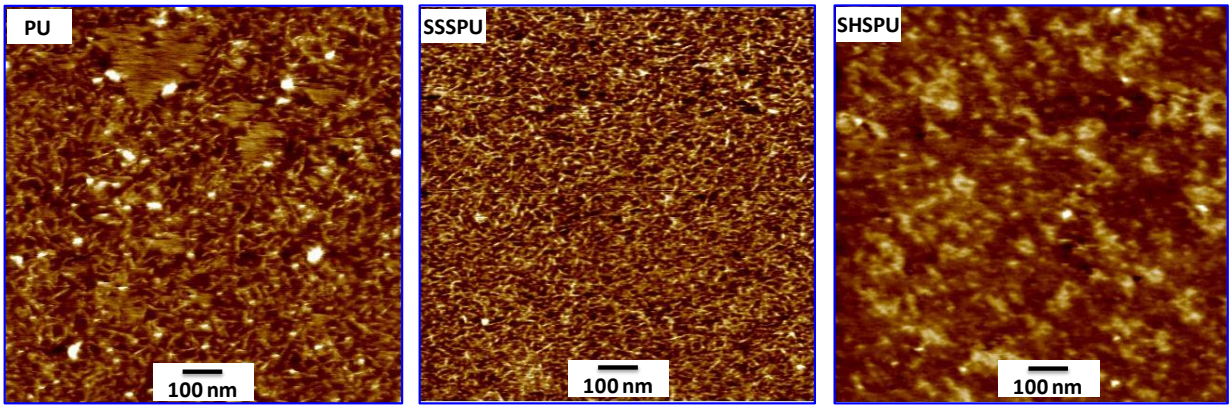

Figure 3.7 Comparison of surface morphologies of noncharged PU, SSSPU, and SHSPU using AFM phase images (Conditions: tapping mode; tip spring constant=42 N/m)

Small angle X-ray scattering and wide angle X-ray diffraction revealed the bulk morphology of noncharged PU, SSSPU, and SHSPU. The SAXS profiles plotted as scattering intensity versus scattering vector q (nm^{-1}) are shown in **Figure 3.8**. SAXS data for the noncharged PU displayed a broad scattering peak near q=0.6 nm^{-1}, arising from the microphase-separation of the hard domains and the PEG-based soft phase. The average inter-domain spacing was related to the scattering peak position by $d=2\pi/q^*$, where q* is the maximum q value at the scattering peak. The calculated inter-domain spacing for non-charged PU was approximately 10 nm, which was similar to the literature value reported for a comparable polyurethane.[52] In contrast, SSSPU showed a very weak scattering peak at q=0.5 nm^{-1}. In light of the well-defined microphase-separated features as evidenced in AFM and the X-ray scattering characteristics, it is reasonable to speculate that the weak X-ray scattering peak for SSSPU is due to the reduced electron density difference between the hard and soft phases. In addition, it is of interest to note that SSSPU shows a broad scattering peak ranging from 1 to 2 nm^{-1}, which may be attributed to sodium sulfonate ion pair association. Due to the high polarity of the PEG soft phase, sodium sulfonate ion pairs tend to form ionic aggregates with a wide size distribution, leading to a broad scattering

peak.[55] In contrast, SHSPU showed a featureless SAXS profile, where the scattering intensity decreased monotonically with the scattering vector q. The absence of ionic peak for SHSPU was due to specific interactions of sodium cations with PEO ether oxygens. Thus, sodium sulfonate ion pairs were not free to aggregate. This observation indicates a high level of phase-mixing for SHSPU.[56]

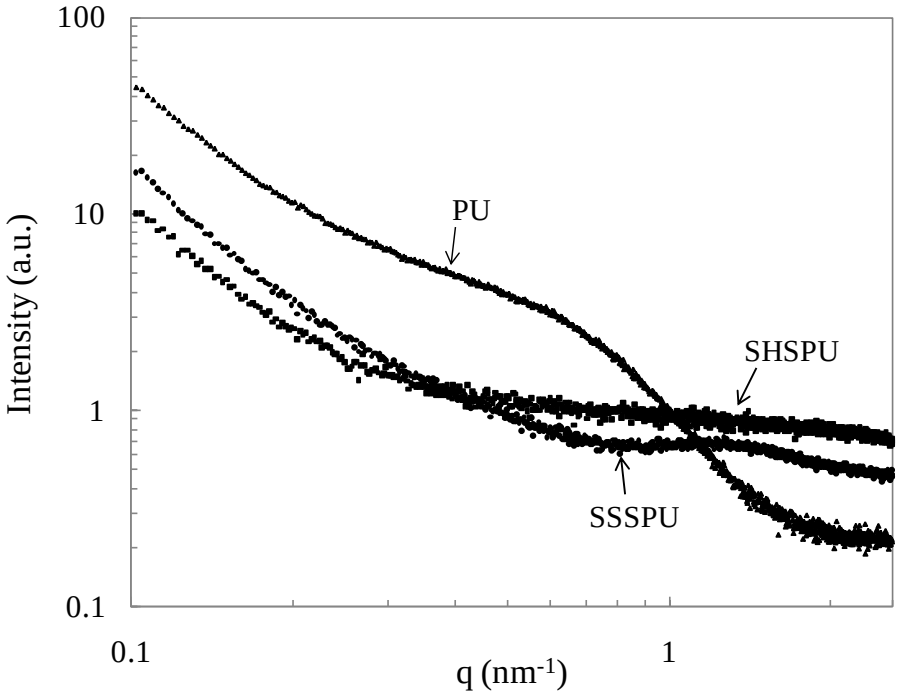

Figure 3.8 Small angle X-ray scattering intensity vs scattering vector q plotted in log-log scale for noncharged PU, SSSPU, and SHSPU

Figure 3.9 shows the WAXD data of all three polyurethanes with a PEG (2K g/mol) and a hard segment (HS) homopolymer analogue. The hard segment analogue was synthesized through the reaction of HMDI with *1,4*-butanediol at a 1:1 stoichiometry to mimic hard segments. The data indicated that PEG (2K g/mol) showed two sharp crystalline peaks at $2\theta=18.8^{o}$ and $2\theta=22.9^{o}$, and the HS analogue showed three weak crystalline peaks at $2\theta=17.9^{o}$, 18.9^{o}, and 23.5^{o}, which were in agreement with Furukawa et al.[46] However, compared to the scattering

profiles of PEG and HS analogue, SHSPU only displayed a broad amorphous peak around $2\theta=18^{o}$ without any sharp crystalline peaks. However, noncharged PU showed two sharp crystalline peaks at $2\theta=18.8^{o}$ and $2\theta=22.9^{o}$, which were attributed to the crystalline PEG soft segments. In addition, both noncharged PU and SSSPU showed a small shoulder around $2\theta=18^{o}$, which corresponded to the crystalline hard segments. It was important to note that the WAXD data agreed well with the DSC observations.

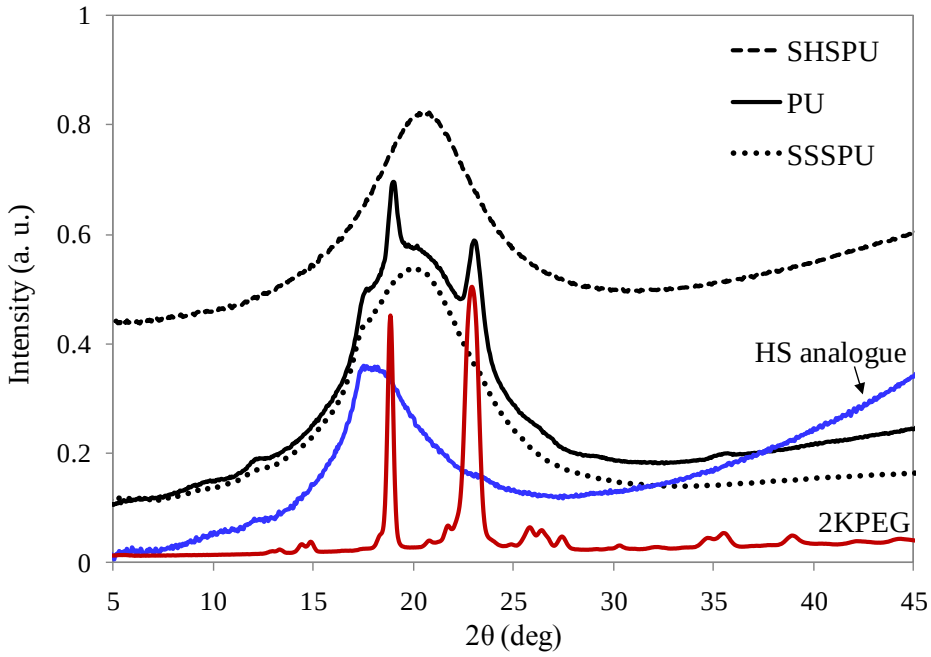

Figure 3.9 Wide-angle X-ray diffraction profiles of noncharged PU, SSSPU, SHSPU, HMDI-BD-based hard segment analogue, and PEG

3.5 Conclusions

PEG-based sulfonated polyurethanes with controlled sulfonate charge placement either in the soft segments (SSSPU) or hard segments (SHSPU) were synthesized using a sulfonated monomer strategy. For comparative purposes, a noncharged PU was also synthesized using 1,4-butanediol as the chain extender. DSC, DMA, and tensile analyses demonstrated that incorporation of sulfonate charge in polyurethane soft segments led to increased soft segment T_g (from -52 ^oC to -26 ^oC), suppressed PEG crystallization, comparably high Young's modulus (9.11±0.88 MPa), and more well-defined rubbery plateau relative to noncharged PU. In contrast, sulfonate charge in polyurethane hard segments further increased the soft segment T_g (from -52 ^oC to -5 ^oC) and suppressed crystallization of both soft and hard segments, however, charge significantly decreased the Young's modulus (1.34±0.27 MPa) and narrowed the rubbery plateau. The significantly different influence of charge placement on sulfonated polyurethane performance correlated well with morphologies. SSSPU containing sulfonate charge in the soft segments showed similar well-defined microphase-separated morphology to noncharged PU. Both showed needle-like microphase-separated hard domains in AFM and X-ray scattering peaks around q=0.5~0.6 nm^{-1} in SAXS. However, sulfonate charge in the hard segments led to phase-mixing of hard and soft segments due to increased compatibility. Additionally, both SSSPU and noncharged PU showed hydrogen bonding interactions in FTIR spectroscopy. However, the hydrogen bonding interactions in SHSPU was significantly suppressed due to the phase-mixed morphology and hard segment irregularity. An understanding of charge placement influence on sulfonated polyurethane performance will lead to precise design of polyurethane ionomers for specific applications.

3.6 Acknowledgements

This work is partially supported by the Institute for Critical Technology and Applied Science (ICTAS) at Virginia Tech. Aspects of this work were carried out using instruments in the Nanoscale Characterization and Fabrication Laboratory (NCFL) operated by ICTAS. The authors also thank the U.S. Army Research Laboratory and the U.S. Army Research Office for their support through the Ionic Liquids in Electro-Active Devices Multidisciplinary University Research Initiative (ILEAD MURI) program under Contract/Grant Number W911NF-07-1-0452. Additionally, this research was partially supported by the National Science Foundation under Grant No. DMR-0923107.

3.7 References

1. Heidarian, M.; Shishesaz, M. R.; Kassiriha, S. M.; Nematollahi, M. *Prog. Org. Coat.* **2010**, *68*, 180.
2. Zhang, Y.; Asif, A.; Shi, W. F. *Prog. Org. Coat.* **2011**, *71*, 295.
3. Hakim, A. A. A.; Nassar, M.; Emam, A.; Sultan, M. *Mater. Chem. Phys.* **2011**, *129*, 301.
4. Petrova, A. P. *Polym. Sci. C* **2007**, *49*, 251.
5. Grenier, S.; Sandig, M.; Mequanint, K. *J. Biomed. Mater. Res. A* **2007**, *82A*, 802.
6. Popescu, M. C.; Vasile, C.; Macocinschi, D.; Lungu, M.; Craciunescu, O. *Int. J. Biol. Macromol.* **2010**, *47*, 646.
7. Morita, H.; Tabana, H.; Nakao, M. *Surf. Coat. Int.* **2010**, *93*, 160.
8. Melnig, V.; Garlea, A.; Obreja, L. *J. Optoelectron. ADV. M.* **2006**, *8*, 1302.
9. Takahara, A.; Hergenrother, R. W.; Coury, A. J.; Cooper, S. L. *J. Biomed. Mater. Res. A.* **1992**, *26*, 801.
10. Wiggins, M. J.; MacEwan, M.; Anderson, J. M.; Hiltner, A. *J. Biomed. Mater. Res. A* **2004**, *68A*, 668.
11. Caracciolo, P. C.; Buffa, F.; Abraham, G. A. *J. Mater. Sci. Mater. Med.* **2009**, *20*, 145.
12. Hergenrother, R. W.; Wabers, H. D.; Cooper, S. L. *Biomaterials* **1993**, *14*, 449.
13. Meng, Q. G.; Hu, J. L.; Zhu, Y. *J. Biomater. Sci., Polym. Ed.* **2008**, *19*, 1437.
14. Oprea, S. *High Perform. Polym.* **2009**, *21*, 353.
15. Ma, C. C. M.; Kuan, H. C.; Hsieh, J. C.; Chiang, C. L. *J. Mater. Sci.* **2003**, *38*, 3933.
16. Vlad, S. *Mater. Plast.* **2005**, *42*, 63.
17. Yang, J.; Wang, G. Y.; Hu, C. P. *Acta Polymerica Sinica* **2003**, 794.
18. Athawale, W. D.; Kolekar, S. L.; Raut, S. S. *J. Macromol. Sci., Polym. Rev.* **2003**, *C43*, 1.
19. Ramesh, S.; Radhakrishnan, G. *J. Polym. Mater.* **1999**, *16*, 135.
20. Dieterich, D.; Keberle, W.; Witt, H. *Angew.Chem. Internat.Edit.* **1970**, *9*, 40.
21. Jayakumar, R.; Nanjundan, S.; Prabaharan, M. *J. Macromol. Sci., Polym. Rev.* **2005**, *C45*, 231.
22. Krol, P. *Prog. Mater Sci.* **2007**, *52*, 915.
23. Ramesh, S.; Tharanikkarasu, K.; Mahesh, G. N.; Radhakrishnan, G. *J. Macromol. Sci. R. M. C.* **1998**, *C38*, 481.
24. Visser, S. A.; Cooper, S. L. *Macromolecules* **1991**, *24*, 2576.
25. Wang, S. W.; Liu, W. J.; Colby, R. H. *Chem. Mater.* **2011**, *23*, 1862.
26. Yeo, S. C.; Eisenberg, A. *J. Macromol. Sci., Phys.* **1977**, *B13*, 441.
27. Ryu, S. W.; Trapa, P. E.; Olugebefola, S. C.; Gonzalez-Leon, J. A.; Sadoway, D. R.; Mayes, A. M. *J. Electrochem. Soc.* **2005**, *152*, A158.
28. Saito, T.; Mather, B. D.; Costanzo, P. J.; Beyer, F. L.; Long, T. E. *Macromolecules* **2008**, *41*, 3503.
29. Pang, J. H.; Zhang, H. B.; Li, X. F.; Wang, L. F.; Liu, B. J.; Jiang, Z. H. *J. Membr. Sci.* **2008**, *318*, 271.
30. Kobayashi, T.; Rikukawa, M.; Sanui, K.; Ogata, N. *Solid State Ionics* **1998**, *106*, 219.
31. Song, J. M.; Asano, N.; Miyatake, K.; Uchida, H.; Watanabe, M. *Chem. Lett.* **2005**, *34*, 996.
32. Seong, Y. H.; Won, J.; Kim, S. K.; Nam, K.; Kim, D. W. *Int. J. Hydrogen Energy* **2011**, *36*, 8492.
33. Bae, B.; Hoshi, T.; Miyatake, K.; Watanabe, M. *Macromolecules* **2011**, *44*, 3884.
34. Ghassemi, H.; McGrath, J. E.; Zawodzinski, T. A. *Polymer* **2006**, *47*, 4132.
35. Xing, P. X.; Robertson, G. P.; Guiver, M. D.; Mikhailenko, S. D.; Kaliaguine, S. *Macromolecules* **2004**, *37*, 7960.

36. Sun, H. Y.; Sohn, H. J.; Yamamoto, O.; Takeda, Y.; Imanishi, N. *J. Electrochem. Soc.* **1999**, *146*, 1672.
37. Singh, M.; Odusanya, O.; Wilmes, G. M.; Eitouni, H. B.; Gomez, E. D.; Patel, A. J.; Chen, V. L.; Park, M. J.; Fragouli, P.; Iatrou, H.; Hadjichristidis, N.; Cookson, D.; Balsara, N. P. *Macromolecules* **2007**, *40*, 4578.
38. Kim, Y. H.; Han, D. K.; Park, K. D.; Kim, S. H. *Biomaterials* **2003**, *24*, 2213.
39. Cao, J.; Chen, Y. W.; Wang, X.; Luo, X. L. *J. Biomed. Mater. Res. A* **2011**, *97A*, 472.
40. Han, D. K.; Park, K. D.; Kim, Y. H. *J. Biomater. Sci., Polym. Ed.* **1998**, *9*, 163.
41. Yuan, J.; Lin, S. C.; Shen, J. *Colloids Surf. B. Biointerfaces* **2008**, *66*, 90.
42. Williams, S. R.; Wang, W. Q.; Winey, K. I.; Long, T. E. *Macromolecules* **2008**, *41*, 9072.
43. Yoo, D. J.; Hyun, S. H.; Kim, A. R.; Kumar, G. G.; Nahm, K. S. *Polym. Int.* **2011**, *60*, 85.
44. Zhu, W.; Wang, X.; Yang, B.; Tang, X. *J. Polym. Sci., Part B: Polym. Phys.* **2001**, *39*, 1246.
45. Hepburn, C. *Polyurethane Elastomers* **1992**, *2nd Edition*, 357.
46. Kojio, K.; Nakashima, S.; Furukawa, M. *Polymer* **2007**, *48*, 997.
47. Waletzko, R. S.; Korley, L. T. J.; Pate, B. D.; Thomas, E. L.; Hammond, P. T. *Macromolecules* **2009**, *42 (6)*, 2041.
48. Yilgor, I.; Yilgor, E.; Guler, I. G.; Ward, T. C.; Wilkes, G. L. *Polymer* **2006**, *47*, 4105.
49. Sun, H. *Macromolecules* **1993**, *26*, 5924.
50. Mattia, J.; Painter, P. *Macromolecules* **2007**, *40 (5)*, 1546.
51. Laity, P. R.; Taylor, J. E.; Wong, S. S.; Khunkamchoo, P.; Norris, K.; M., C.; Andrews, G. T.; Johnson, A. F.; Cameron, R. E. *Polymer* **2004**, *45*, 7273.
52. Garrett, J. T.; Runt, J. *Macromolecules* **2000**, *33*, 6353.
53. Kaushiva, B. D.; Wilkes, G. L. *Polymer* **2000**, *41*, 6353.
54. Garrett, J. T.; Siedlecki, C. A.; Runt, J. *Macromolecules* **2001**, *34*, 7066.
55. Eisenberg, A.; Hird, B.; Moore, R. B. *Macromolecules* **1990**, *23*, 4098.
56. Pereira, I. M.; Orefice, R. L. *Macromol. Symp.* **2011**, *299 (1)*, 190.

Chapter 4: Sulfonated Polyurethane Chain-Extended with Sulfonated Diol: Correlation of Soft Segment Composition with Physical Properties and Morphology

Gao, R.; Zhang, M.; Dixit, N.; Moore, R.B.; and Long, T.E. (*prepared for publication*)

4.1 Abstract

Sulfonated polyurethanes containing different soft segments (poly(ethylene oxide) (PEO) and poly(tetramethylene oxide) (PTMO), respectively) were synthesized using a sulfonated monomer strategy, which afforded precisely controlled charge density in hard segments. A fundamental investigation of these sulfonated polyurethanes elucidated the influence of soft segment composition on properties and morphology of sulfonated polyurethane ionomers. PTMO-based sulfonated polyurethane exhibited lower soft segment glass transition temperature (T_g) and more well-defined rubbery plateau relative to PEO-based sulfonated polyurethane, as evidenced in differential scanning calorimetry (DSC) and dynamic mechanical analysis (DMA), respectively. Tensile analysis demonstrated that PTMO-based sulfonated polyurethane offered superior tensile strength compared to PEO-based sulfonated polyurethane. Moreover, Fourier transform infrared spectroscopy (FTIR) indicated that PTMO-based sulfonated polyurethane exhibited a higher degree of hydrogen bonding than PEO-based sulfonated polyurethane. Thermal and mechanical properties and hydrogen bonding of these sulfonated polyurethanes correlated well with their morphologies. Atomic force microscopy (AFM) phase images revealed clear, microphase-separated, morphological features of PTMO-based sulfonated polyurethane. Small angle X-ray scattering (SAXS) profile of PTMO-based sulfonated polyurethane displayed distinct scattering peaks at q=0.5 nm^{-1} and q=2.5 nm^{-1}, corresponding to microphase separation of hard and soft segments and sodium sulfonate ion pair association in the hard segments, respectively. In

contrast, both AFM and SAXS indicated a phase-mixed morphology for PEO-based sulfonated polyurethane.

4.2 Introduction

Segmented polyurethane is an important class of copolymers comprising alternated soft and hard segments.[1-4] Due to thermodynamic immiscibility of soft and hard segments, polyurethanes undergo microphase separation, which forms unique microstructures containing flexible, low-T_g soft domains and rigid, high-T_g hard domains.[5-8] Properties of these segmented polyurethanes depend strongly on microphase-separated structures, which are tunable through the block length,[9-12] chemical composition,[13,14] and compatibility of both soft and hard segments.[9,15,16]

Many efforts have probed the influence of hard segment structure and content on properties of segmented polyurethanes.[17-24] However, for a fixed hard segment, molecular weight, chemical composition, and crystallinity of soft segments also play important roles in microphase separation and final properties of segmented polyurethanes.[11,25-30] For example, Runt et al. compared the microphase separation behavior of three model segmented polyurethanes, which contained a fixed hard segment but different soft segment structures.[31] They demonstrated that PTMO-based polyurethane exhibited a higher degree of microphase separation than a poly(1,6-hexyl-1,2-ethyl carbonate)-based polyurethane due to weaker hydrogen bonding between PTMO soft segments and 4,4'-methylenediphenyl diisocyanate (MDI)-based hard segments. Cooper et al. demonstrated that molecular weights of soft segments significantly influenced microphase separation of polycaprolactone-based polyurethanes.[9] High molecular weight soft segments favored a higher degree of microphase separation. Researchers also determined the influence of soft segments on mechanical properties, biodegradability, and moisture-permeability of segmented polyurethanes.[11,12,32-34] However, most of these studies focused on nonionic

polyurethanes. Ion-containing polyurethanes with various soft segment structures are relatively unexplored.

Ion-containing polyurethanes, or polyurethane ionomers have attracted increasing attention for their unique properties and wide applications in biomedical materials, smart coatings, water treatment, and biocides.[35-38] Understanding the structure-morphology-property relationships of polyurethane ionomers is of great importance to design novel materials with desired properties. Our previous studies probed the influence of sulfonate charge placement on performance of PEO-based sulfonated polyurethane ionomers.[39] Characterization results indicated that sulfonate charge placement dramatically influenced morphology and physical properties of PEO-based sulfonated polyurethanes due to altered compatibility between soft and hard segments. Cooper et al. previously studied the influence of soft segment structure on physical properties and thrombogenicity of sulfonated polyurethanes, which were prepared with a post-sulfonation method.[40] However, in the current study, we aimed to correlate soft segment structures with physical properties and morphologies of sulfonated polyurethanes. As opposed to a post-sulfonation method, sulfonated monomers were directly polymerized to synthesize sulfonated polyurethanes with precisely controlled charge density in the hard segments and controlled hard segment content. These polyurethanes possessed an equal content of sulfonated hard segments (43 wt%) and same molecular weight soft segments with different chemical structures. Well-defined structures enabled to elucidate the influence of soft segment composition on physical properties and morphologies of segmented polyurethanes.

4.3 Experimental

Materials. Dimethyl 5-sulfoisophthalate sodium salt (98%), ethylene glycol (99%), titanium (IV) isopropoxide, poly(ethylene glycol) (PEG) (M_n=2000 g/mol), and poly(tetramethylene oxide) (PTMO) (M_n=2000 g/mol) were purchased from Aldrich and dried at 60 ^oC *in vacuo* overnight immediately prior to use. Anhydrous *N,N*-dimethylformamide (DMF) (99.8%) was purchased from Aldrich and used as received. Dibutyltin dilaurate (DBTDL) (95%) was purchased from Aldrich and diluted to 1 wt% using anhydrous tetrahydrofuran. Methanol (HPLC grade) and anhydrous diethyl ether (99%) were purchased from Fisher Scientific. Dicyclohexylmethane-*4,4'*-diisocyanate (HMDI) (99.5%) was kindly provided by Bayer MaterialScience and used as received.

Synthesis of Segmented Polyurethanes Containing Sulfonated Hard Segments

Synthetic details of sulfonated diol chain extender, bis(2-hydroxyethyl)-5-sulfoisophthalate sodium salt, have been described previously.[39] A typical synthesis of sulfonated polyurethane was conducted in a three-necked, round-bottomed flask equipped with an addition funnel, nitrogen inlet, and an overhead mechanical stirrer. Pre-dried PEO (M_n=2000 g/mol) or PTMO (M_n=2000 g/mol) was initially end-capped with HMDI at 80 ^oC for 4 h using DBTDL (50 ppm) as the catalyst. In the second step, bis(2-hydroxyethyl)-5-sulfoisophthalate sodium salt was dissolved in anhydrous DMF (15 wt% solids) and added dropwise to the prepolymers. The reaction was allowed to proceed for 24 h at 80 ^oC under a N_2 atmosphere. FTIR spectroscopy demonstrated complete polymerizations. Polyurethane solutions were directly cast in Teflon® molds and air-dried at 23 ^oC for 3 days. Resulting membranes were subsequently dried *in vacuo* at 50~60 ^oC for additional 72 h. All Polyurethane membranes were stored in a dessicator (relatively humidity<15%) and re-dried *in vacuo* at 60 ^oC for 24 h immediately prior to

characterization. PTMO-based sulfonated polyurethane was referred to as HMDI-SIPNa-2KPTMO, while PEO-based polyurethane was referred to as HMDI-SIPNa-2KPEO. Both polyurethanes contained 43 wt% sulfonated hard segments (HS).

Polymer Characterization

Differential scanning calorimetry (DSC) was conducted on a TA Instruments Q2000 differential scanning calorimeter under a nitrogen flow of 50 mL/min with a heating rate of 10 ^{o}C/min. Second heat DSC curves were utilized to determine thermal transition temperatures in order to minimize thermal history effect. Dynamic mechanical analysis (DMA) measurements were performed on a TA Instruments Q800 dynamic mechanical analyzer in the film tension mode at a frequency of 1 Hz with a temperature ramp of 3 ^{o}C/min over the range from -90−180 ^{o}C. Tanδ curves were utilized to determine glass transition temperatures of sulfonated polyurethanes. Tensile analysis was performed on a 5500R Instron universal testing instrument with a cross-head rate of 50 mm/min at ambient conditions. More than three samples were averaged to determine Young's modulus, maximum elongation, and tensile strength. FTIR experiments were carried out using a Varian 670-IR spectrometer (DTGS detector). The spectra were collected at a resolution of 4 cm^{-1} with 32 scans averaged. Atomic force microscopy (AFM) was performed on a Veeco MultiMode AFM in a tapping mode at ambient conditions. SAXS was performed using a Rigaku S-Max 3000 3 pinhole SAXS system equipped with a rotating anode emitting X-rays with a wavelength of 0.154 nm (Cu Kα). Scattering from a silver behenate standard was used to calibrate the sample-to-detector distance. For SAXS, the sample-to-detector distance was 1603 mm. Two-dimensional SAXS patterns were obtained using a fully integrated 2D multi-wire, proportional counting, gas-filled detector during an exposure time of 1 h per sample. SAXS data were corrected for sample thickness, sample transmission, and

background scattering. All SAXS data were analyzed using the SAXSGUI software package to obtain radially integrated SAXS intensity versus scattering vector q (SAXS), where $q=4\pi\sin(\theta)/\lambda$, θ is half of the scattering angle, and λ is the X-ray, and the profiles were vertically shifted to facilitate a comparison of peak positions.

4.4 Results and Discussion

4.4.1 Synthesis of sulfonated polyurethanes containing different soft segments

Scheme 4.1 depicts the synthesis of sulfonated polyurethanes containing PEO and PTMO-based soft segments, respectively. Chain extension of PEO- and PTMO-based polyurethane prepolymers with a sulfonated diol, bis(2-hydroxyethyl)-5-sulfoisophthalate sodium salt, provided segmented polyurethanes with controlled charge density and charge placement in the hard segments. Two sulfonated polyurethanes possessed an equal content (43 wt%) of hard segments and same molecular weight soft segments with different structures. Well-defined chemical structures of these sulfonated polyurethanes enable to elucidate the influence of soft segment composition on physical properties of sulfonated polyurethanes and correlate polyurethane structure and properties with their morphologies. In order to obtain high molecular weight polyurethanes, both polyurethane samples were synthesized with a stoichiometry of OH/NCO=1, and FTIR spectroscopy verified complete polymerizations, i.e. isocyanate peak at 2260 cm^{-1} completely disappeared at the end of the polymerization. Although reliable SEC data were not obtained due to polymer association in SEC solvent, characterization data on mechanical properties shown below suggested that both polyurethane samples were high molecular weight polymers. In this study, we assume that the influence of soft segment

composition dominates that of polyurethane total molecular weight, which is reasonable if both polymers have molecular weights above the critical molecular weight.

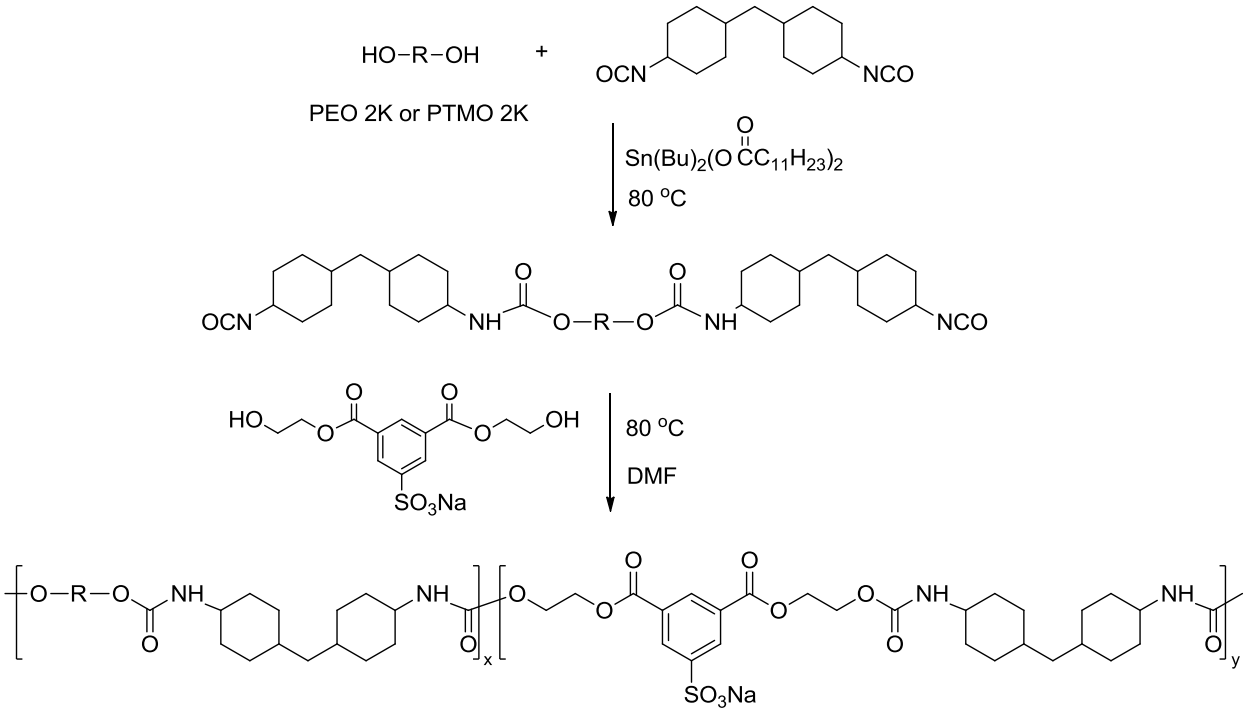

Scheme 4.1 Synthesis of sulfonated polyurethanes containing PTMO-based soft segment (HMDI-SIPNa-2KPTMO) and PEO-based soft segment (HMDI-SIPNa-2KPEO) with a same content of sulfonated hard segments (HS=43 wt%)

4.4.2 Thermal properties

Thermal properties of sulfonated polyurethanes containing different soft segments were investigated with differential scanning calorimetry (DSC). **Figure 4.1** displays the second heat DSC curves for both samples. HMDI-SIPNa-2KPTMO exhibited a thermal transition at -80 ^{o}C, which corresponded to the glass transition temperature (T_g) of PTMO-based soft segments. This glass transition was close to the T_g of pure PTMO homopolymers, indicating a high degree of microphase separation. Atomic force microscopy (AFM) and small angle X-ray scattering (SAXS) shown below verified a well-defined microphase-separated morphology for HMDI-

SIPNa-2KPTMO. In contrast, HMDI-SIPNa-2KPEO showed a PEO soft segment T_g that was approximately 50 ^oC higher than the T_g of pure PEO homopolymers (-60 ^oC). It is also interesting to note that both samples did not show any endothermic peak in both first and second heat DSC curves, indicating the absence of crystalline soft and hard segments. Our precious studies demonstrated that HMDI-SIPNa-2KPEO possessed a phase-mixed morphology, leading to increased PEO soft segment T_g and suppressed crystallization of both soft and hard segments. However, HMDI-SIPNa-2KPTMO displayed a well-defined microphase-separated morphology. Reduced hard segment crystallinity in HMDI-SIPNa-2KPTMO was presumably due to the disrupted chain regularity and sodium sulfonate ion pair association. This study also suggests that thermodynamic immiscibility between soft and hard segments, hydrogen bonding, and ionic association are the major driving forces for microphase separation of HMDI-SIPNa-2KPTMO, rather than hard segment crystallinity.

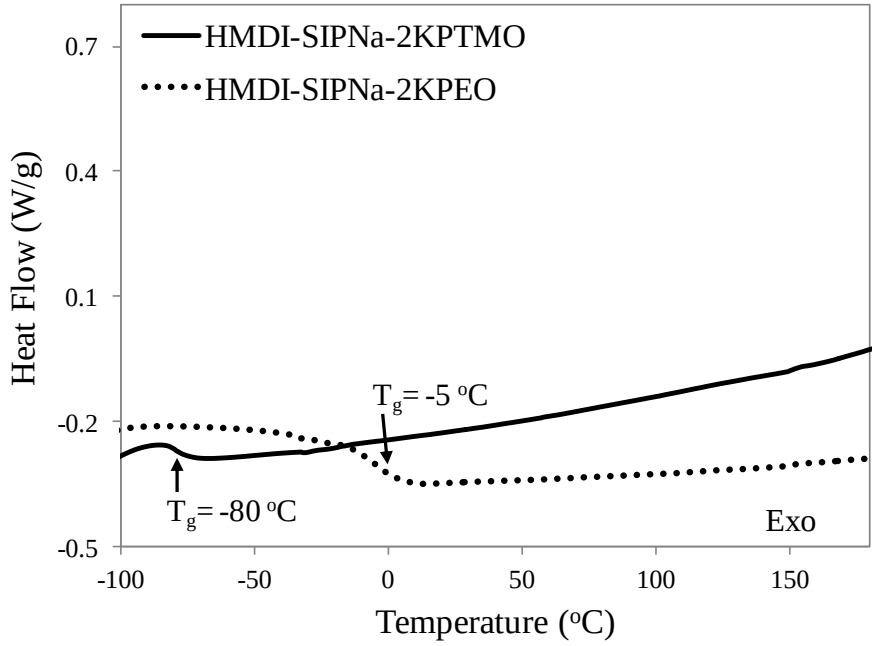

Figure 4.1 DSC traces of HMDI-SIPNa-2KPTMO (solid line, HS=43 wt%) and HMDI-SIPNa-2KPEO (dot line, HS=43 wt%). Condition: 10 ^oC/min, in Helium

4.4.3 Thermomechanical and tensile properties

Dynamic mechanical analysis (DMA) studies revealed thermomechanical properties of both PEO- and PTMO-based sulfonated polyurethanes. **Figure 4.2** depicts the temperature dependence of storage modulus (G') and tan delta (tanδ) for both sulfonated polyurethane samples. Tanδ curve of HMDI-SIPNa-2KPTMO displayed maxima at -62 ^{o}C, corresponding to the PTMO soft segment T_g. This sample also displayed a well-defined rubbery plateau above the soft segment T_g in storage modulus curve, which indicated a high degree of microphase separation. In contrast, HMDI-SIPNa-2KPEO showed a much higher PEO soft segment T_g and poor thermomechanical properties due to the phase mixing between the soft and hard segments. Cooper et al. conducted DMA studies on poly(propylene oxide)-based polyurethanes containing various contents of ammonium cations in the hard segments. They found that thermomechanical properties of these sulfonated polyurethanes strongly depended on the degree of microphase separation. Polyurethane samples with phase mixing did not show clear tanδ peak and well-defined rubbery plateaus in DMA curves.

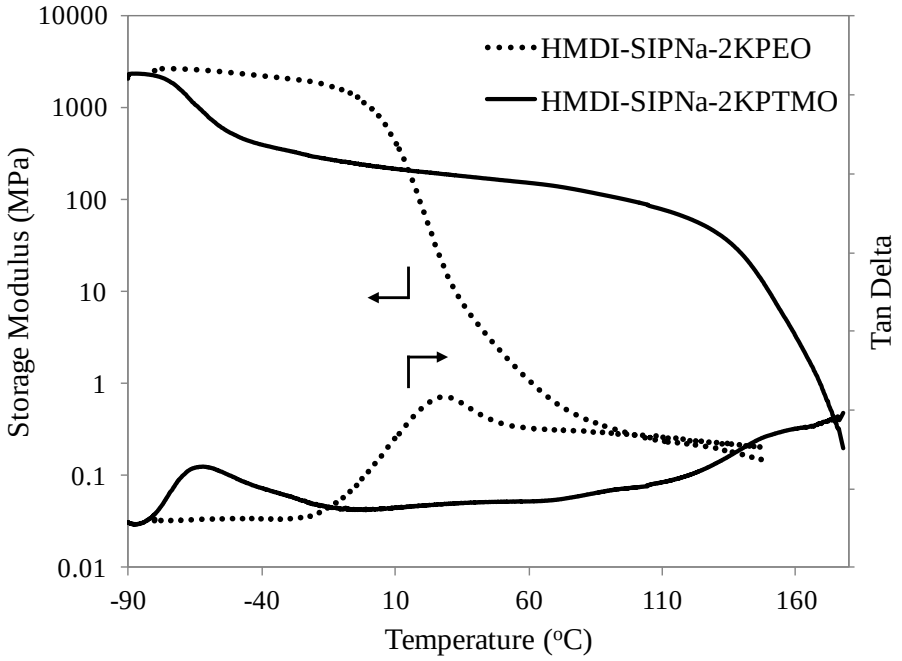

Figure 4.2 Thermomechanical properties of sulfonated polyurethanes with 2KPEO and 2KPTMO soft segments (HS=43 wt%). DMA condition: 3 °C/min, 1 Hz, film tension mode

Mechanical properties of PEO- and PTMO-based sulfonated polyurethanes were also evaluated using uniaxial stress-strain tensile analysis. **Figure 4.3** shows a comparison of the stress-strain curves of both sulfonated polyurethanes. HMDI-SIPNa-2KPTMO and HMDI-SIPNa-2KPEO showed comparable maximum elongation, which were 726±15 % and 818±156%, respectively. High maximum elongation value is usually indicative of high molecular weight polymers. However, HMDI-SIPNa-2KPTMO showed a much higher Young's modulus (127.3±0.7 MPa) relative to HMDI-SIPNa-2KPEO (1.34±0.27 MPa), as indicated with the slope of initial stress-strain curves. Many studies in the literature have determined that mechanical properties of polyurethanes depend strongly on their morphology.[16,40,41] In a microphase-separated polyurethane, high-T_g hard segment domains serve as physical cross-links to afford polyurethane mechanical strength. A higher Young's modulus of HMDI-SIPNa-2KPTMO suggested a higher degree of microphase separation. In contrast, HMDI-SIPNa-

2KPEO possessed a phase-mixed morphology, where no hard segment domains existed to serve as physical cross-links and provide the mechanical strength. In addition, HMDI-SIPNa-2KPTMO possessed much higher tensile strength than HMDI-SIPNa-2KTPMO, indicating strong cohesion of hard domains.

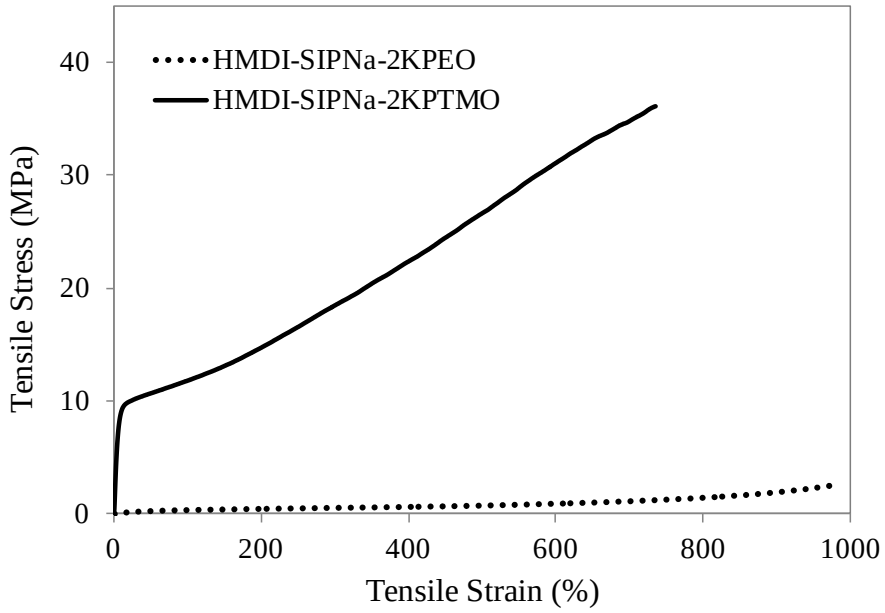

Figure 4.3 Comparison of tensile properties of sulfonated polyurethanes with 2KPEO- and 2KPTMO-based soft segments and 43 wt% sulfonated hard segments. Condition: 50 mm/min, ambient conditions

4.4.4 Hydrogen bonding characterization

A comparative study with FTIR spectroscopy elucidated the influence of soft segment composition on hydrogen bonding of sulfonated polyurethanes. **Figure 4.4** shows the FTIR spectra for both HMDI-SIPNa-2KPTMO and HMDI-SIPNa-2KPEO in the carbonyl region (1600~1800 cm^{-1}) and NH region (3100~3700 cm^{-1}). IR spectrum of HMDI-SIPNa-2KPTMO displayed two distinct peaks at 1718 cm^{-1} and 1702 cm^{-1}, which corresponded to the stretching vibration peaks of free carbonyl and hydrogen bonded carbonyl, respectively. This indicates the

presence of hydrogen bonding in HMDI-SIPNa-2KPTMO. In sharp contrast, HMDI-SIPNa-2KPEO displayed a monomodal peak at 1716 cm^{-1} for free carbonyl, indicating the absence of hydrogen bonding due to a phase-mixed morphology. In addition, IR spectrum of HMDI-SIPNa-2KPTMO in NH region displayed a sharper NH vibration peak relative to HMDI-SIPNa-2KPEO, which also indicated stronger hydrogen bonding for HMDI-SIPNa-2KPTMO than HMDI-SIPNa-2KPEO.

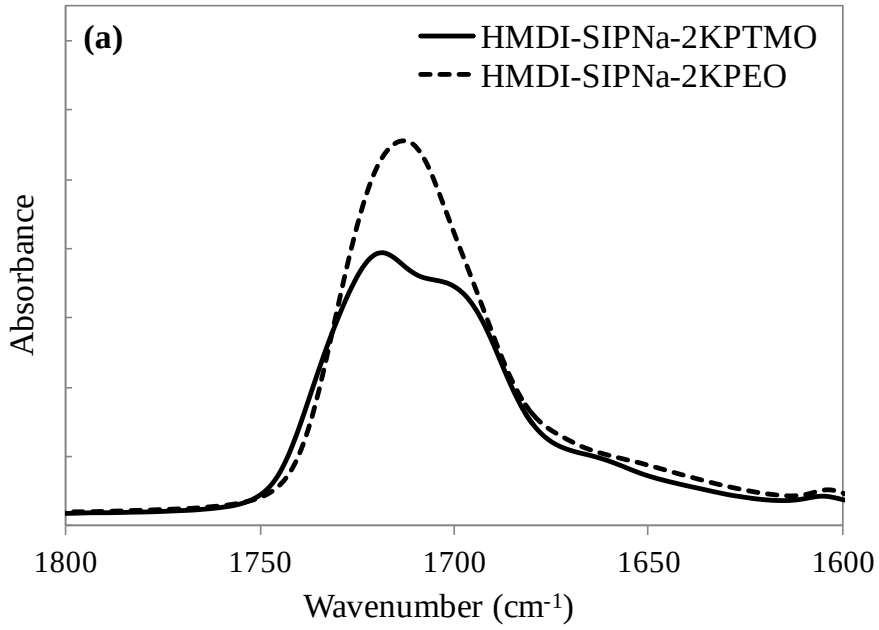

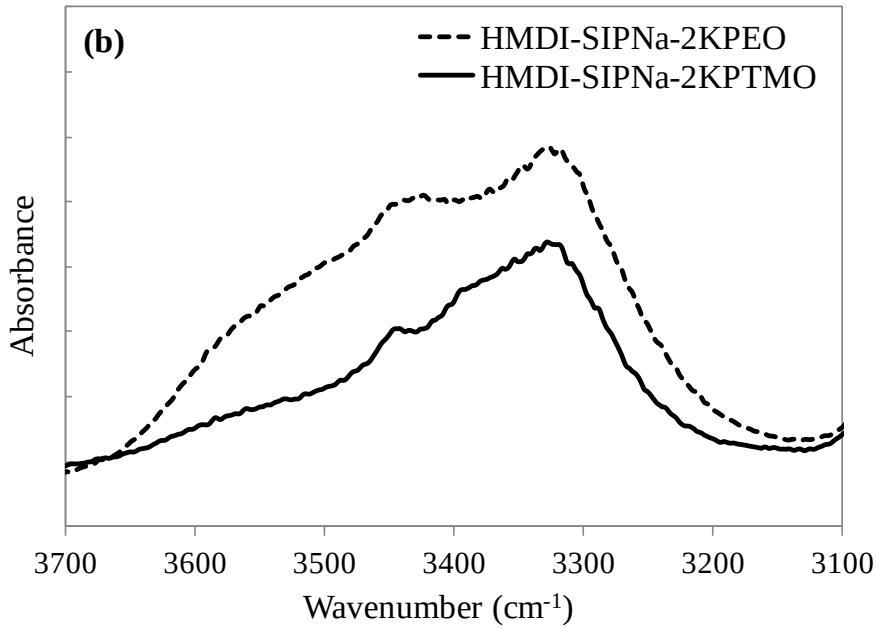

Figure 4.4 FTIR spectroscopy of the (a) C=O region and (b) N-H region of sulfonated polyurethane containing PEO- and PTMO-based soft segments.

4.4.5 Morphological characterization using AFM and SAXS

To visually compare the morphology of HMDI-SIPNa-2KPTMO and HMDI-SIPNa-2KPEO, we utilized tapping mode AFM to investigate their surface morphological features. **Figure 4.5** shows the AFM phase images of both sulfonated polyurethanes obtained at ambient conditions. In AFM phase images, high-modulus hard domains appear as bright regions and low-T_g soft phase appears as dark regions. It is clear that HMDI-SIPNa-2KPTMO exhibited well-defined microphase-separated morphology. HMDI-SIPNa hard segments formed worm-like hard domains that randomly distributed in the continuous PTMO-based soft phase. These worm-like hard domains were more or less continuous, which corresponded to the high modulus of HMDI-SIPNa-2KPTMO as determined in DMA and tensile analysis. However, HMDI-SIPNa-2KPEO did not showed any clear microphase-separated morphological features, indicating phase mixing between PEO soft segments and sulfonated ionic hard segments.

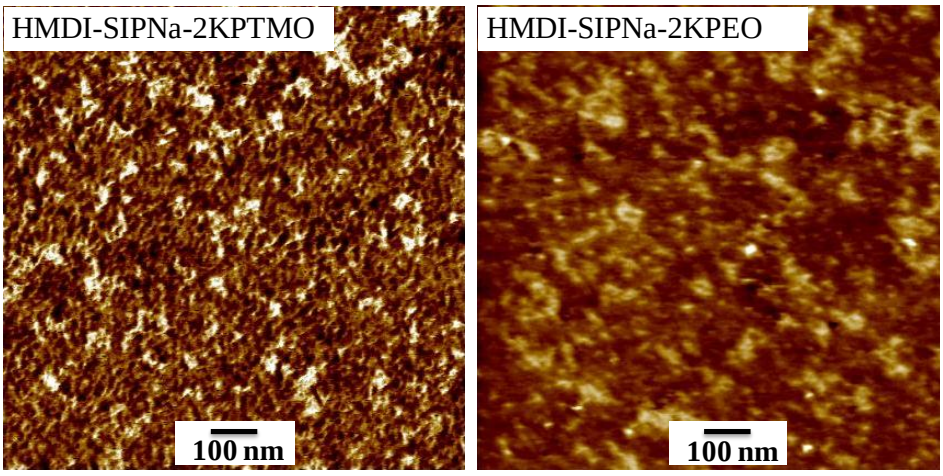

Figure 4.5 AFM phase image indicating microphase-separated morphology of HMDI-SIPNa-2KPTMO and phase-mixed morphology of HMDI-SIPNa-2KPEO. Condition: tapping mode, tip spring constant: 42 N/m

Small angle X-ray scattering (SAXS) elucidated the bulk morphologies of HMDI-SIPNa-2KPTMO and HMDI-SIPNa-2KPEO. **Figure 4.6** shows the SAXS profiles plotted as scattering intensity versus scattering vector q (nm^{-1}) at a logarithmic scale. HMDI-SIPNa-2KPTMO displayed a distinct scattering peak near q=0.5 nm^{-1} in the profile, which resulted from the microphase separation of soft and hard segments. More interestingly, a second broad scattering peak emerged at q=2~3 nm^{-1}, which corresponded to the ionomer peak arising from sodium sulfonate ion pair association. Cooper et al. reported SAXS studies on model sulfonated polyurethanes containing pendant sulfonate anions in the hard segments, which displayed ionomer peaks near q=1.2 nm^{-1}.[42,43] Several factors may be responsible for the ionomer peak at a higher q value for HMDI-SIPNa-2KPTMO. Moore and Eisenberg et al. investigated a series of styrene-based ionomers that contained different lengths of alkyl spacer between carboxylate anions and polystyrene backbone. They found that ionomers with shorter alkyl spacers displayed ionomer peaks at higher q values due to formation of larger ionic aggregates. It is not surprising that HMDI-SIPNa-2KPTMO with sulfonate anions placed on the backbone showed an ionomer

peak at q=2~3 nm^{-1}. Moreover, ionomer peak position also depends on ion concentration. AFM and SAXS studies suggested that HMDI-SIPNa-2KPTMO possessed a microphase-separated morphology. Although HMDI-SIPNa-2KPTMO had only 5.9 wt% SO_3Na ions, all sodium sulfonate ion pairs were confined within the microphase-separated hard domains. Therefore, interparticle spacing (*d*) was much smaller than what was expected for 5.9 wt% SO_3Na, which lead to a scattering peak at high q value ($q=2\pi/d$).[44] In addition, sodium sulfonate ions in rigid, high-T_g, hard domains are less likely to form large aggregates.[45] This also contributes to a smaller inter-domain spacing and ionomer peaks at a high q value for HMDI-SIP-2KPTMO. In sharp contrast, HMDI-SIPNa-2KPEO was absent of any visible scattering peak, indicating a phase-mixed morphology.

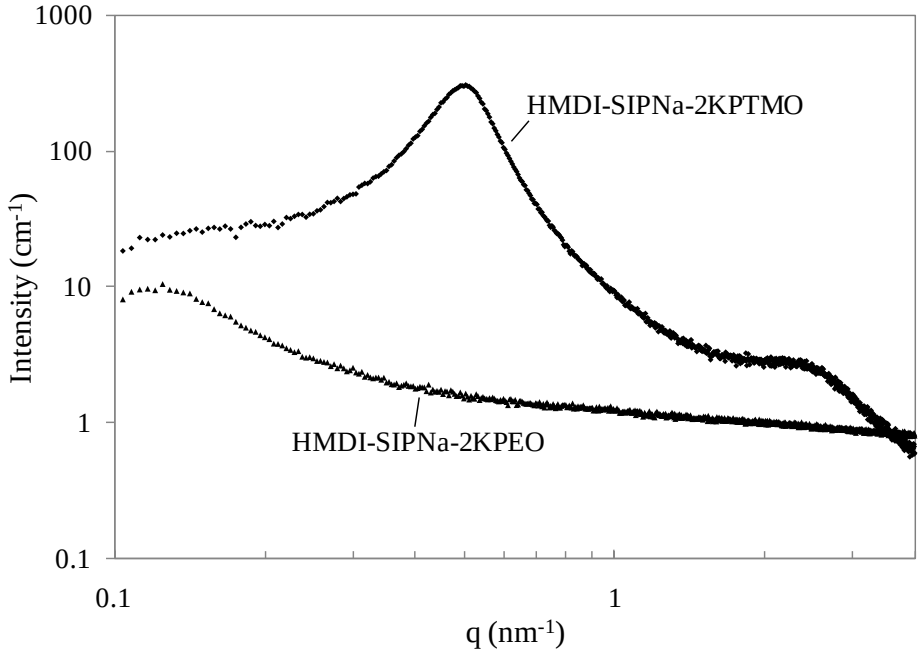

Figure 4.6 Small angle X-ray scattering intensity vs scattering vector q plotted in a log-log scale for sulfonated polyurethanes containing PEO- and PTMO-based soft segments, respectively.

4.5 Conclusions

Sulfonated polyurethanes with PEO- and PTMO-based soft segments were synthesized respectively, which contained identical sulfonated hard segments at an equal content (43 wt%). Comparative studies on these sulfonated polyurethanes elucidated the influence of soft segment composition on their physical properties and morphologies. PTMO-based sulfonated polyurethane exhibited a low soft segment T_g at -80 ^oC in DSC, a well-defined rubbery plateau in DMA, a significantly enhanced Young's modulus (127.3±0.7 MPa) and tensile strength (35.19±0.97 MPa) in tensile analysis, and a higher degree of hydrogen bonding in FTIR. All these physical properties of PTMO-based sulfonated polyurethane correlated well with its morphology. Both AFM and SAXS indicated a well-defined microphase-separated morphology for PTMO-based sulfonated polyurethanes, which was presumably due to the high immiscibility between hydrophobic PTMO soft segments and sulfonated ionic hard segments. In addition, SAXS profile of PTMO-based sulfonated polyurethane displayed an ionomer peak at q=2~3 nm^{-1}, corresponding to sodium sulfonate ion pair association. In sharp contrast, PEO-based sulfonated polyurethane possessed a phased-mixed morphology, as evidenced in AFM and SAXS. Due to the phase mixing, PEO-based sulfonated polyurethane displayed a significantly increased soft segment T_g (-5 ^oC), poor mechanical performance (Young's modulus=1.34±0.27 MPa), and no hydrogen bonding. Increased compatibility between hydrophilic PEO soft segments and sulfonated ionic hard segments were responsible for the phase-mixed morphology of PEO-based sulfonated polyurethane. A fundamental understanding of the structure-morphology-property relationships of these sulfonated polyurethanes will lead to better designs of sulfonated polyurethanes for specific applications.

4.6 Acknowledgments

This work is partially supported by the Institute for Critical Technology and Applied Science (ICTAS) at Virginia Tech. Aspects of this work were carried out using instruments in the Nanoscale Characterization and Fabrication Laboratory (NCFL) operated by ICTAS. The authors also thank the U.S. Army Research Laboratory and the U.S. Army Research Office for their support through the Ionic Liquids in Electro-Active Devices Multidisciplinary University Research Initiative (ILEAD MURI) program under Contract/Grant Number W911NF-07-1-0452. Additionally, this research was partially supported by the National Science Foundation under Grant No. DMR-0923107.

4.7 References

1. Williams, S. R.; Wang, W. Q.; Winey, K. I.; Long, T. E. *Macromolecules* **2008**, *41*, 9072.
2. Lan, P. N.; Corneillie, S.; Schacht, E.; Davies, M.; Shard, A. *Biomaterials* **1996**, *17*, 2273.
3. Pissis, P.; Kanapitsas, A.; Savelyev, Y. V.; Akhranovich, E. R.; Privalko, E. G.; Privalko, V. P. *Polymer* **1998**, *39*, 3431.
4. Wang, L. F.; Ji, Q.; Glass, T. E.; Ward, T. C.; McGrath, J. E.; Muggli, M.; Burns, G.; Sorathia, U. *Polymer* **2000**, *41*, 5083.
5. Garrett, J. T.; Runt, J.; Lin, J. S. *Macromolecules* **2000**, *33*, 6353.
6. Chu, B.; Gao, T.; Li, Y. J.; Wang, J.; Desper, C. R.; Byrne, C. A. *Macromolecules* **1992**, *25*, 5724.
7. Tao, H. J.; Meuse, C. W.; Yang, X. Z.; Macknight, W. J.; Hsu, S. L. *Macromolecules* **1994**, *27*, 7146.
8. Prisacariu, C.; Scortanu, E. *Int J Polym Anal Ch* **2010**, *15*, 277.
9. Velankar, S.; Cooper, S. L. *Macromolecules* **1998**, *31*, 9181.
10. Ma, Z. W.; Hong, Y.; Nelson, D. M.; Pichamuthu, J. E.; Leeson, C. E.; Wagner, W. R. *Biomacromolecules* **2011**, *12*, 3265.
11. Das, S.; Yilgor, I.; Yilgor, E.; Inci, B.; Tezgel, O.; Beyer, F. L.; Wilkes, G. L. *Polymer* **2007**, *48*, 290.
12. Arcana, I. M.; Bundjali, B.; Hasan, M.; Zulfikar, M. A.; Hariyawati, K. *Polym Int* **2011**, *60*, 1535.
13. Lee, D. W.; Lee, S. H.; Kim, S. C.; Char, K. H.; Park, J. H.; Bae, Y. H. *J Polym Sci Pol Phys* **2003**, *41*, 2365.
14. Choi, T.; Weksler, J.; Padsalgikar, A.; Runt, J. *Polymer* **2009**, *50*, 2320.
15. Velankar, S.; Cooper, S. L. *Macromolecules* **2000**, *33*, 382.
16. Velankar, S.; Cooper, S. L. *Macromolecules* **2000**, *33*, 395.
17. Hergenrother, R. W.; Wabers, H. D.; Cooper, S. L. *Biomaterials* **1993**, *14*, 449.
18. Nakamae, K.; Nishino, T.; Asaoka, S.; Sudaryanto *Int J Adhes Adhes* **1996**, *16*, 233.
19. Kim, Y. D.; Kim, M. K.; Jo, N. J. *Ionics* **2011**, *17*, 805.
20. Prisacariu, C.; Olley, R. H.; Caraculacu, A. A.; Bassett, D. C.; Martin, C. *Polymer* **2003**, *44*, 5407.
21. Oprea, S. *J Elastom Plast* **2010**, *42*, 163.
22. Janik, H.; Vancso, J. *Polimery-W* **2005**, *50*, 139.
23. Yoon, K. H.; Yoon, S. T.; Park, O. O. *J Appl Polym Sci* **2000**, *75*, 604.
24. Caracciolo, P. C.; Buffa, F.; Abraham, G. A. *J Mater Sci-Mater M* **2009**, *20*, 145.
25. Yen, M. S.; Tsai, H. C.; Hong, P. D. *J Appl Polym Sci* **2007**, *105*, 1391.
26. Eceiza, A.; Larranaga, M.; de la Caba, K.; Kortaberria, G.; Marieta, C.; Corcuera, M. A.; Mondragon, I. *J Appl Polym Sci* **2008**, *108*, 3092.
27. Lin, Y. H.; Chou, N. K.; Chen, K. F.; Ho, G. H.; Chang, C. H.; Wang, S. S.; Chu, S. H.; Hsieh, K. H. *Polym Int* **2007**, *56*, 1415.
28. Rogulska, M.; Kultys, A.; Pikus, S. *J Appl Polym Sci* **2008**, *110*, 1677.
29. Yilgor, I.; Eynur, T.; Bilgin, S.; Yilgor, E.; Wilkes, G. L. *Polymer* **2011**, *52*, 266.
30. Zhu, Y.; Hu, J.; Yeung, K. *Acta Biomater* **2009**, *5*, 3346.
31. Hernandez, R.; Weksler, J.; Padsalgikar, A.; Choi, T.; Angelo, E.; Lin, J. S.; Xu, L. C.; Siedlecki, C. A.; Runt, J. *Macromolecules* **2008**, *41*, 9767.
32. Silver, J. H.; Myers, C. W.; Lim, F.; Cooper, S. L. *Biomaterials* **1994**, *15*, 695.

33. Shibaya, M.; Suzuki, Y.; Doro, M.; Ishihara, H.; Yoshihara, N.; Enomoto, M. *J Polym Sci Pol Phys* **2006**, *44*, 573.
34. Sheth, J. P.; Aneja, A.; Wilkes, G. L.; Yilgor, E.; Atilla, G. E.; Yilgor, I.; Beyer, F. L. *Polymer* **2004**, *45*, 6919.
35. Han, D. K.; Park, K.; Park, K. D.; Ahn, K. D.; Kim, Y. H. *Artif Organs* **2006**, *30*, 955.
36. Silver, J. H.; Karayianni, E.; Cooper, S. L. *J Colloid Interf Sci* **1996**, *178*, 219.
37. Silver, J. H.; Lin, H. B.; Cooper, S. L. *Biomaterials* **1993**, *14*, 834.
38. Jeong, E. H.; Yang, H.; Youk, J. H. *Mater Lett* **2007**, *61*, 3991.
39. Gao, R.; Zhang, M.; Dixit, N.; Moore, R. B.; Long, T. E. *Polymer* **2012**, *(Accepted)*.
40. Silver, J. H.; Marchant, J. W.; Cooper, S. L. *J Biomed Mater Res* **1993**, *27*, 1443.
41. Visser, S. A.; Cooper, S. L. *Macromolecules* **1991**, *24*, 2576.
42. Register, R. A.; Pruckmayr, G.; Cooper, S. L. *Macromolecules* **1990**, *23*, 3023.
43. Ding, Y. S.; Register, R. A.; Yang, C. Z.; Cooper, S. L. *Polymer* **1989**, *30*, 1213.
44. Lu, X. Y.; Steckle, W. P.; Weiss, R. A. *Macromolecules* **1993**, *26*, 5876.
45. Eisenberg, A.; Hird, B.; Moore, R. B. *Macromolecules* **1990**, *23*, 4098.

Chapter 5: Influence of Ionic Liquid on Performance of Segmented Polyurethane Ionomers Containing PEG-Based Sulfonated Soft Segments

Gao, R.; Wang, S.; Zhang, M.; Colby, R.H.; and Moore, R.B.; Long, T.E. (*prepared for publications*)

5.1 Abstract

Segmented polyurethanes containing poly(ethylene glycol) (PEG)-based sulfonated soft segments (SSSPU) were synthesized. Incorporation of ionic liquid (IL), 1-ethyl-3-methylimidazolium ethylsulfate (EMIm ES), into SSSPU using both "swollen" and "cast with" methods afforded two series of novel SSSPU/IL composite materials. In both cases, IL systematically reduced glass transition temperatures (T_g's) of sulfonated PEG soft segments and maintained well-defined rubbery plateaus for sulfonated polyurethanes, as evidenced in differential scanning calorimetry (DSC) and dynamic mechanical analysis (DMA). Results also suggested that EMIm ES was miscible with sulfonated PEG soft segments and preferentially located into the soft phase. In addition, morphological characterization using atomic force microscopy (AFM) and small angle X-ray scattering (SAXS) revealed the influence of IL on SSSPU morphologies. Compared with neat SSSPU membranes, SSSPU/IL composite membranes showed longer, needle-like, microphase-separated hard domains in AFM phase images and enhanced X-ray scattering intensity of microphase separation in SAXS profiles. Moreover, dielectric relaxation spectroscopy (DRS) revealed that ionic conductivity of all SSSPU/IL composite membranes exhibited Vogel-Fulcher-Tammann (VFT) temperature dependence and systematically increased with IL content. Fundamental understanding of structure-property relationships of SSSPU/IL composites will enable fabrication of novel

materials with high ionic conductivity and excellent mechanical properties for emerging electromechanical membrane applications.

5.2 Introduction

Polymeric membranes with both high ionic conductivity and good mechanical properties are highly desirable for applications in electromechanical transducers, lithium ion batteries, and sensors.[1-7] Among the many types of materials, ionic liquid (IL)-incorporated polymeric materials are good candidates due to significantly enhanced ionic conductivity, tailored mechanical properties, and easy fabrication process.[8-12] Performance of ionic liquid-incorporated polymeric materials depends strongly on type and content of ionic liquid, ionic liquid dispersion state in the polymeric matrix, and matrix polymer structure and morphologies.[13-17] Park et al. studied partially sulfonated poly(styrenesulfonate-*b*-methylbutylene) doped with IL that contained different counterions.[18] They found that IL type significantly influenced the morphology and ionic conductivity of sulfonated poly(styrenesulfonate-*b*-methylbutylene).

To achieve the desirable ionic conductivity and mechanical properties of ionic liquid-incorporated polymeric materials, it requires choice of suitable ionic liquids and appropriate design of matrix polymer structure and morphologies, which enable effective incorporation of ionic liquid to enhance ionic conductivity and maintain good mechanical properties in the presence of ionic liquid, especially at high contents. Recent studies have focused on the microphase-separated block copolymers and PEG-based copolymers and networks.[13,19-28] For example, Winey and Elabd et al. investigated the effect of ionic liquid composition on a poly(styrene-*b*-methyl methacrylate) block copolymer.[29] Endo et al. studied PEG-based networked polymer films containing ionic liquids.[20] Here ion-containing segmented polyurethane

is particularly interesting because of the facile synthesis with well-defined segmented block structures and good mechanical properties due to a microphase-separated morphology.

In the current study, we designed a segmented polyurethane that contained PEG-based sulfonated soft segments (SSSPU). PEG-based sulfonated soft segments are advantageous for several reasons. First, PEG has been widely used in battery applications due to the relatively high conductivity and excellent solvation of cations. PEG has a low glass transition temperature (T_g). Fast segmental motions of PEG favor fast ion transport and provide high ionic conductivity.[6,30] Second, PEG-based soft segments, which form the continuous soft phase in the polyurethane solid state, have high compatibility with hydrophilic ionic liquids.[31-33] This enables effective incorporation and homogenous distribution of ionic liquid in the continuous PEG soft phase. Finally, our previous studies demonstrated that incorporation of sodium sulfonate ions into the PEG soft segments suppressed PEG crystallization and broadened the rubbery plateau, leading to a broad continuous use temperature range of these materials.[34] Moreover, sodium sulfonate ions further increase the affinity of PEG to hydrophilic ionic liquids through intermolecular ionic interactions and reduce ionic liquid leakage. Mobile sodium cations also contribute to the ionic conductivity of SSSPU membranes. In addition, SSSPU contains noncharged hard segments, which crystallize with strong hydrogen bonding and serve as effective physical crosslinking sites even in the presence of ionic liquid. Here SSSPU/IL composite membranes were prepared using both “swollen” and “cast with” methods with an IL content ranging from 5 wt% to 25 wt%. Complementary characterization revealed that ionic liquids significantly increased ionic conductivity of SSSPU membranes while maintaining thermomechanical properties.

5.3 Experimental

Materials. Dimethyl 5-sulfoisophthalate sodium salt (98%), ethylene glycol (99%), titanium (IV) isopropoxide, and poly(ethylene glycol) (PEG) (M_n=950-1000 g/mol) were purchased from Aldrich and dried at 60 ^oC *in vacuo* overnight immediately prior to use. Anhydrous *N,N*-dimethylformamide (DMF) (99.8%) was purchased from Aldrich and used as received. The chain extender *1,4*-butanediol (BD)(99%) was purchased from Aldrich and distilled from calcium hydride. Dibutyltin dilaurate (DBTDL) (95%) was purchased from Aldrich and diluted to 1 wt% using anhydrous tetrahydrofuran. Dicyclohexylmethane-*4,4'*-diisocyanate (HMDI) (99.5%) was kindly provided by Bayer MaterialScience and used as received. 1-Ethyl-3-methyimidazolium ethylsulfate (EMIm ES) was purchased from Alfa Aesar and stored over molecular sieves.

Synthesis of Segmented Polyurethanes Bearing Sulfonated Soft Segments (SSSPU)

The synthetic details have been described previously.[34] PEG-based sulfonated polyol was initially synthesized using a transesterification reaction of dimethyl 5-sulfoisophthalate sodium salt and 1000 g/mol PEG. The synthesizing sulfonated polyol was end-capped with HMDI at 80 ^oC for 4 h using DBTDL as the catalyst (50 ppm) in the absence of solvent to prepare the prepolymer. HMDI-endcapped prepolymer was chain-extended with 1,4-butanediol to synthesize high molecular weight sulfonated polyurethane. FTIR spectroscopy was utilized to confirm complete consumption of the isocyanate groups. The resulting sulfonated polyurethane was referred to as SSSPU, which contained 70 wt% of sulfonated PEG soft segments and 30 wt% HMDI-BD nonionic hard segments.

Preparation of SSSPU/IL Composite Membranes

SSSPU/IL composite membranes were prepared using both "swollen" and "cast with" methods. In a "swollen" method, SSSPU solutions in DMF (17 wt% solids) were initially cast in Teflon® molds and dried in air at 23 ^{o}C for 72 h with a relative humidity (RH) of 32% to form solid membranes. The resulting membranes were subsequently dried *in vacuo* at 60 ^{o}C for additional 72 h to remove residual solvent and moisture. Well-dried membranes were soaked in EMIm ES in a well-sealed glass vial and stored in a dessicator (RH<15%) at 23 ^{o}C. IL uptake was determined according to the equation: wt% uptake = $(m-m_0)/m_0$, where m_0 is the initial film mass and m is the swollen film mass. Membranes with different levels of IL uptake were obtained with soaking the films in EMIm ES for different times. In a "cast with" method, SSSPU DMF solutions (17 wt% solids) were initially blended with a calculated amount of EMIm ES with mechanical stirring (1000 rpm) at 23 ^{o}C for 1 h. Blended solutions were subsequently cast in Teflon® molds and dried in air (RH=31%) at 23 ^{o}C for 72 h to form solid membranes. These membranes were further dried *in vacuo* at 60 ^{o}C for 72 h.

Characterization. Differential scanning calorimetry (DSC) was performed using a TA Instruments Q2000 differential scanning calorimeter under a nitrogen flow of 50 mL/min with a heating rate of 10 ^{o}C/min. Second heat DSC curves were utilized to determine thermal transitions of SSSPU/IL composite membranes. Dynamic mechanical analysis (DMA) measurements were performed on a TA Instruments Q800 dynamic mechanical analyzer in the film tension mode at a frequency of 1 Hz and a temperature ramp of 3 ^{o}C/min over the range -60 to 120 ^{o}C. Glass transition temperatures were reported as peak values in the tanδ curves. Atomic force microscopy (AFM) was conducted on a Veeco MultiMode AFM in a tapping mode at ambient conditions. SAXS was performed using a Rigaku S-Max 3000 3 pinhole SAXS system equipped

with a rotating anode emitting X-rays with a wavelength of 0.154 nm (Cu Kα). Scattering from a silver behenate standard was used to calibrate the sample-to-detector distance, which was 1603 mm. Two-dimensional SAXS patterns were obtained using a fully integrated 2D multi-wire, proportional counting, gas-filled detector during an exposure time of 1 h per sample. SAXS data were corrected for sample thickness, sample transmission, and background scattering, and analyzed using the SAXSGUI software package to obtain radially integrated SAXS intensity versus scattering vector q profiles, where $q=4\pi\sin(\theta)/\lambda$, θ is half of the scattering angle, and λ is the wavelength of X-ray. The profiles were vertically shifted to facilitate a comparison of peak positions. Dielectric relaxation spectroscopy was conducted on a Novo-control GmbH Concept 40 broadband dielectric spectrometer. Samples were dried at 45 ^{o}C under vacuum before measurement. All sample membranes were sandwiched between two 20 mm diameter freshly polished brass electrodes. Dielectric (impedance) spectra were measured in the frequency range of 1×10^{-2} to 1×10^{7} Hz with 0.1 V amplitude. Samples were annealed at 100 ^{o}C in the equipment for 30 min and allowed to reach equilibrium with temperature for at least 5 min before each isothermal measurement.

5.4 Results and Discussion

5.4.1 Synthesis of SSSPU and preparation of SSSPU/IL composite membranes.

SSSPU containing PEG-based sulfonated soft segments was synthesized using a sulfonated monomer strategy (**Scheme 5.1**). Our previous studies demonstrated that sulfonated PEG soft segments formed ion-rich continuous soft phase with low glass transition temperature (T_g=-26 ^oC) in the absence of appreciable PEG crystallinity.[34] These characteristics of PEG soft segments enable fast ion transport in a wide temperature range and provide high ionic conductivity. SSSPU/IL composite membranes were prepared using both "swollen" and "cast with" methods. A "swollen" method enables incorporation of ionic liquid into various types of solid membranes including chemically cross-linked networks. This method is less likely to disturb the bulk morphology of matrix polymers; however, it affords a low control of IL content. In contrast, a "cast with" method enables a precise control of IL content. However, the composite membranes are cast in the presence of IL, which may influence final morphologies due to the intermolecular interaction between IL and the polyurethane. In the current study, we systematically compared these two methods to elucidate the influence of membrane preparation process on properties and morphology of SSSPU/IL composite membranes. It is also worth clarifying that all SSSPU/IL composite membranes were dried at identical conditions to eliminate the effect of the drying process. In particular, in the "cast with" method, IL uptake levels were determined using ^1H NMR spectroscopy to verify that IL was not lost during the drying process (**Figure 5.1**). The data demonstrated that a "cast with" method afforded a precise control of IL content in the composite membranes.

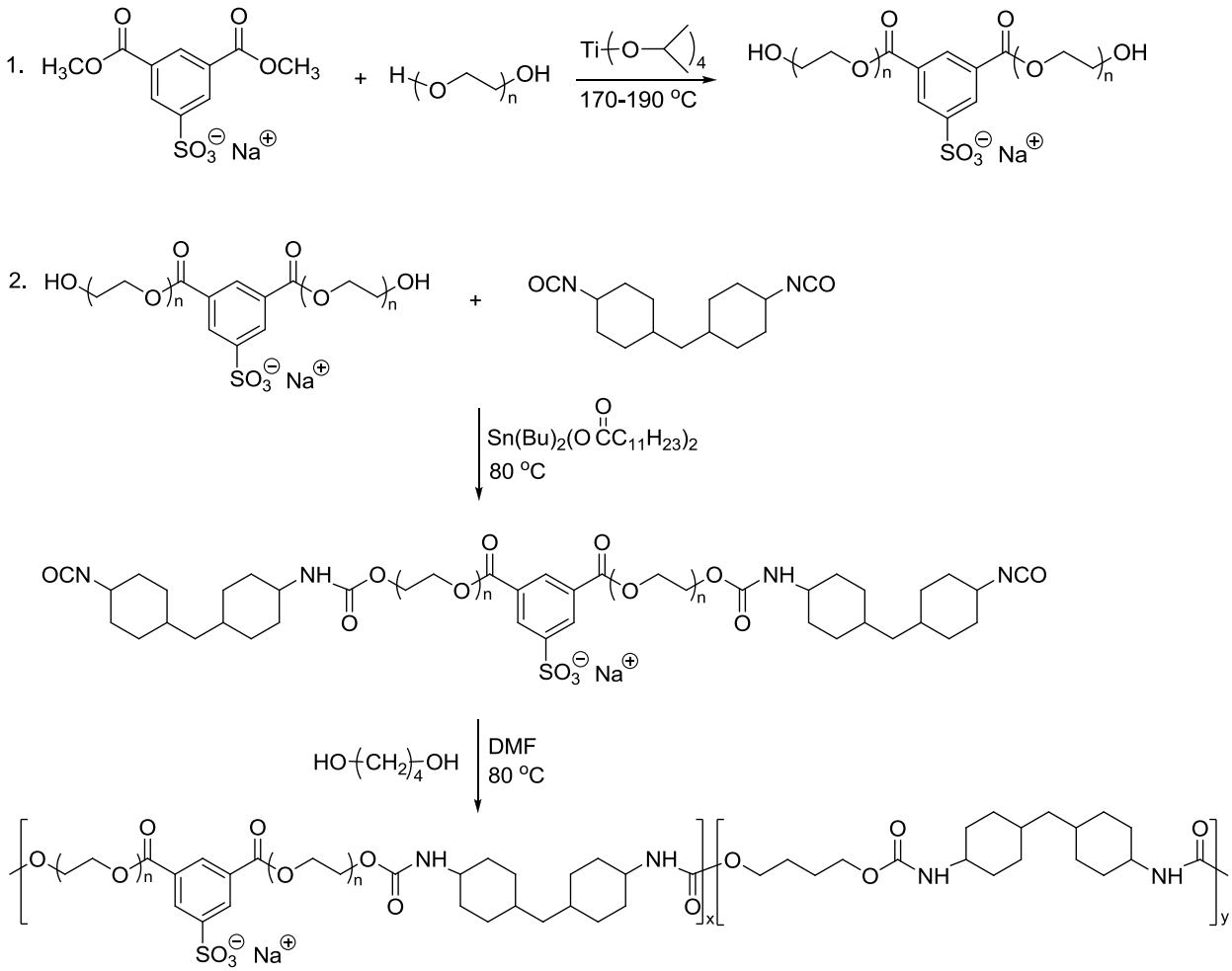

Scheme 5.1 Synthesis of sulfonated polyurethanes containing sulfonated soft segments (SSSPU) (ion exchange capacity (IEC) =0.27 mequiv/g)

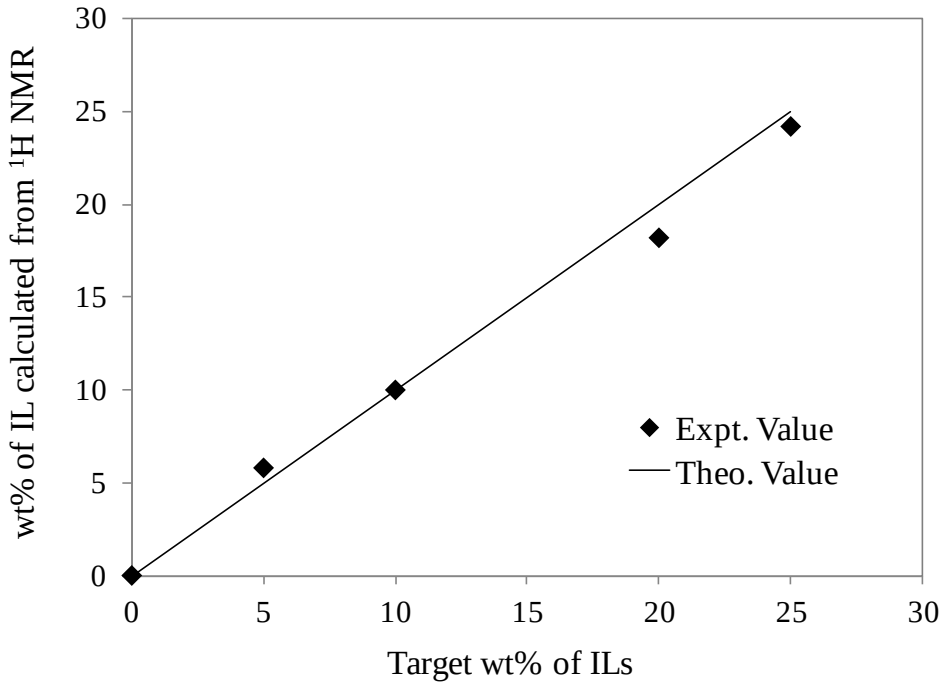

Figure 5.1 Determination of ionic liquid content cast in SSSPU membranes using ^{1}H NMR (400 MHz, DMSO-d_6, 23 ^{o}C)

5.4.2 Thermal properties

DSC thermograms in **Figure 5.2** elucidate the influence of IL (swollen with) on thermal properties of SSSPU. Well-defined transitions near -30 ^{o}C corresponded to T_g's of sulfonated PEG soft segments, which systematically decreased from -26 ^{o}C to -40 ^{o}C with increasing IL content from 0 wt% to 25 wt%. Low T_g's of PEG soft segments are particularly interesting because they enable low continuous use temperature of these composite materials. Moreover, low T_g PEG soft segments exhibit fast segmental motions, which contribute to high ionic conductivity. **Figure 5.3** shows DSC thermograms of SSSPU cast with various contents of IL. The data indicated that IL (cast with) systematically reduced T_g's of PEG soft segments, which was consistent with observations in **Figure 5.2**. It is also interesting to note that all SSSPU/IL composite membranes did not show any PEG crystallinity. Song et al. reported that crystallized

PEG in lithium battery applications exhibited low ionic conductivity below the melting point and limited the battery operation temperature range.[35] Therefore, PEG soft segments free of crystallinity are of great importance because they will enable a much broader continuous use temperature range for these composites materials. For comparative purposes, **Figure 5.4** shows T_g's of SSSPU sulfonated PEG soft segments as a function of IL content for both "swollen" and "cast with" samples. In both cases, SSSPU soft segment T_g linearly decreased with increasing IL content, although "swollen" samples showed a slightly higher T_g than "cast with" samples at each IL content. This suggests that PEG soft segments are compatible with incorporated EMIm ES ionic liquid. In order to gain greater insight into the compatibility between EMIm ES ionic liquid and SSSPU sulfonated PEG soft segments, **Figure 5.4** also shows the relationship of soft segment T_g and IL content predicted according to the Fox equation:[36,37]

$$\frac{1}{T_g} = \frac{W_{(ss)}}{T_{g(ss)}} + \frac{W_{(IL)}}{T_{g(IL)}} \quad (1)$$

where T_g is the predicted glass transition temperatures of PEG soft segments incorporated with EMIm ES ionic liquid. Here, we hypothesize that PEG soft segments completely phase-separate from the hard segments and IL selectively locates in the PEG soft phase. Therefore, IL incorporated PEG soft phase is a compatible binary system. Thus, $T_{g(SS)}$ is the SSSPU soft segment T_g (-26 ^oC), $T_{g(IL)}$ is the T_g of EMIm ES (-70 ^oC), and $W_{(SS)}$ and $W_{(IL)}$ are the weight fraction of PEG soft segment and IL, respectively. It is important to note that dependence of soft segments T_g on IL content determined with DSC agreed well with relationship predicted with Fox equation. This observation confirmed our hypothesis that PEG soft segments phase-separated from SSSPU hard segments, and IL preferentially located in the PEG soft phase. In addition, Forsyth et al. reported that the Fox equation also described glass transition behavior of

poly(vinylpyrrolidone-*co*-vinyl acetate) copolymers doped with IL due to the high compatibility between matrix polymer and IL.[38] Here, our data indicated that EMIm ES ionic liquid was completely dissolved in the sulfonated PEG soft segments.

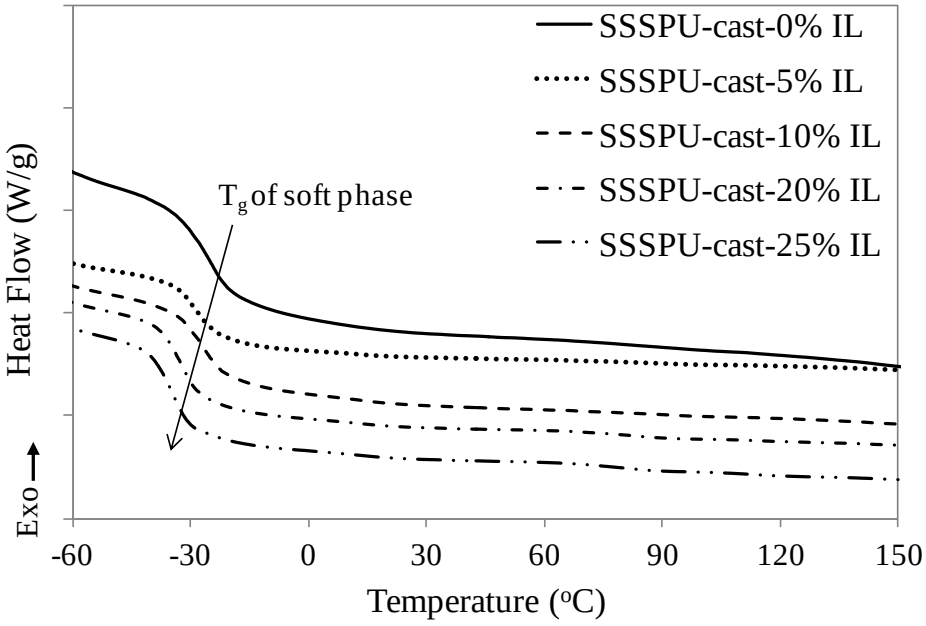

Figure 5.2 DSC curves of SSSPU membranes cast with various contents of ionic liquid (2nd heating cycle, 10 °C/min, N_2 atmosphere)

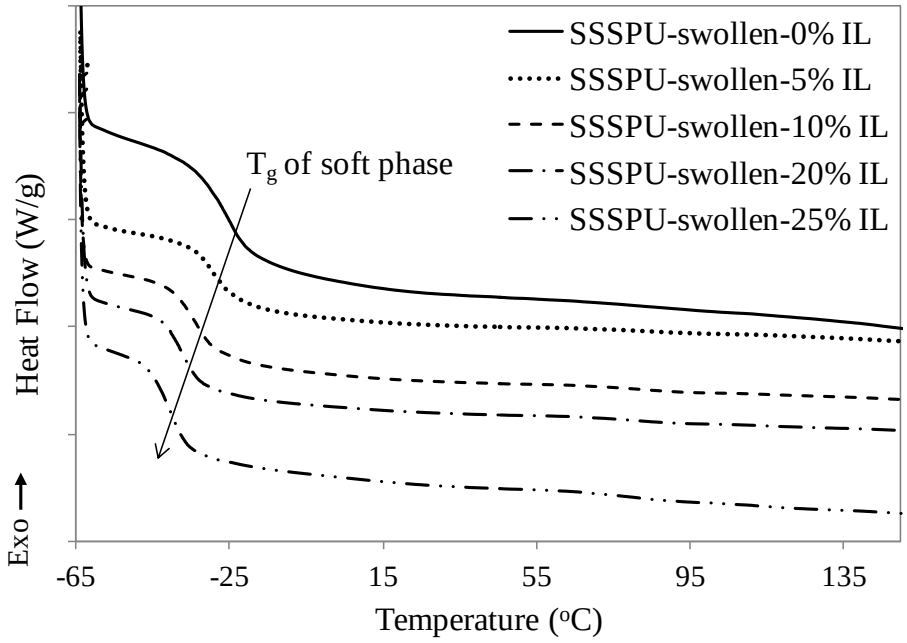

Figure 5.3 DSC curves of SSSPU membranes swollen with various contents of ionic liquid (2nd heating cycle, 10 °C/min, N_2 atmosphere)

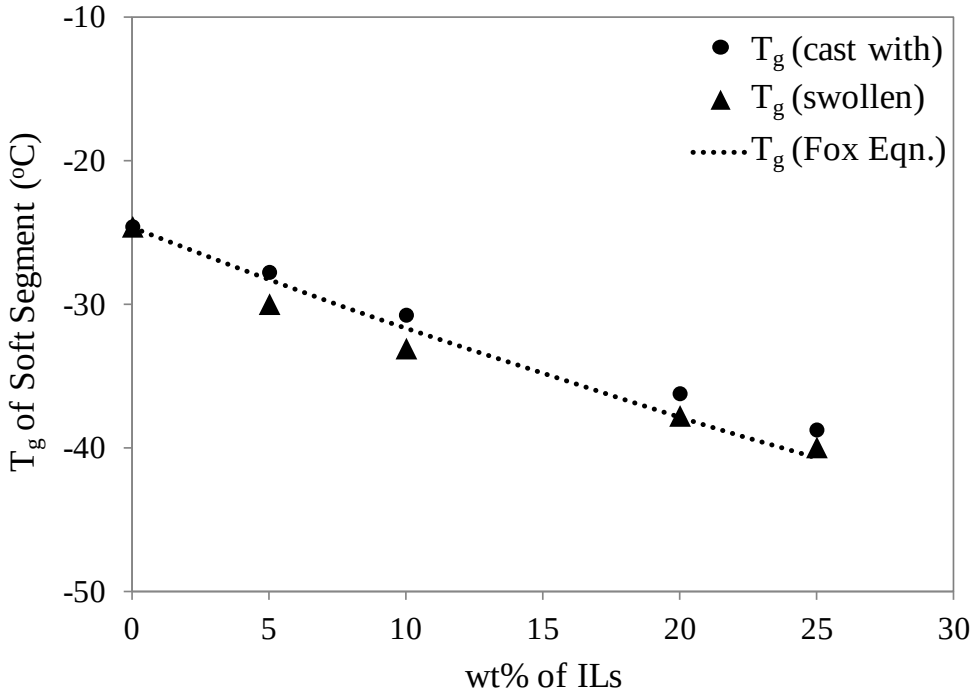

Figure 5.4 Glass transition temperatures (T_g's) of SSSPU soft segment as a function of IL content

5.4.3 Thermomechanical properties

Influence of IL on thermomechanical properties of SSSPU were investigated using DMA. **Figure 5.5** and **Figure 5.6** show the temperature dependence of storage modulus (G') and loss tangent (tan δ) for SSSPU/IL composite membranes prepared with "swollen" and "cast with" methods, respectively. Due to microphase separation of soft and hard segments, SSSPU showed two thermal transitions in DMA curves. The first transition near -20 ^{o}C corresponded to PEG soft segment T_g, while the second transition at a higher temperature corresponded to hard segment T_g and T_m. In both "swollen" and "cast with" samples, soft segment T_g's systematically decreased with increasing IL content as evidenced with shifted tan δ peaks. This observation was consistent with DSC. More interestingly, all samples showed comparable hard segment thermal transitions approximately to 110 ^{o}C, indicating microphase-separated hard domains remained virtually unchanged in the presence of EMIm ES ionic liquid. The different responses of soft and hard segment thermal transitions upon IL incorporation suggested that IL preferentially dissolved in the sulfonated PEG soft phase due to the high compatibility between PEG soft segments and EMIm ES and the presence of sodium sulfonate ionic groups. This observation was consistent with earlier literature.[31] Moreover, due to preferential incorporation of IL into PEG soft phase, hard segments remained undisturbed, which continued to serve as physical cross-links and provide well-defined rubbery plateaus of SSSPU/IL composite membranes. Rubbery plateau moduli of SSSPU membranes decreased with increasing IL content due to the plasticizing effect of IL on sodium sulfonate ion pair association. In comparison of "swollen" and "cast with" samples, IL in "cast with" samples showed a more significant effect on rubbery plateau moduli than "swollen" samples. We presume that IL cast with SSSPU solutions influenced sodium sulfonate ion pair association during membrane formation.

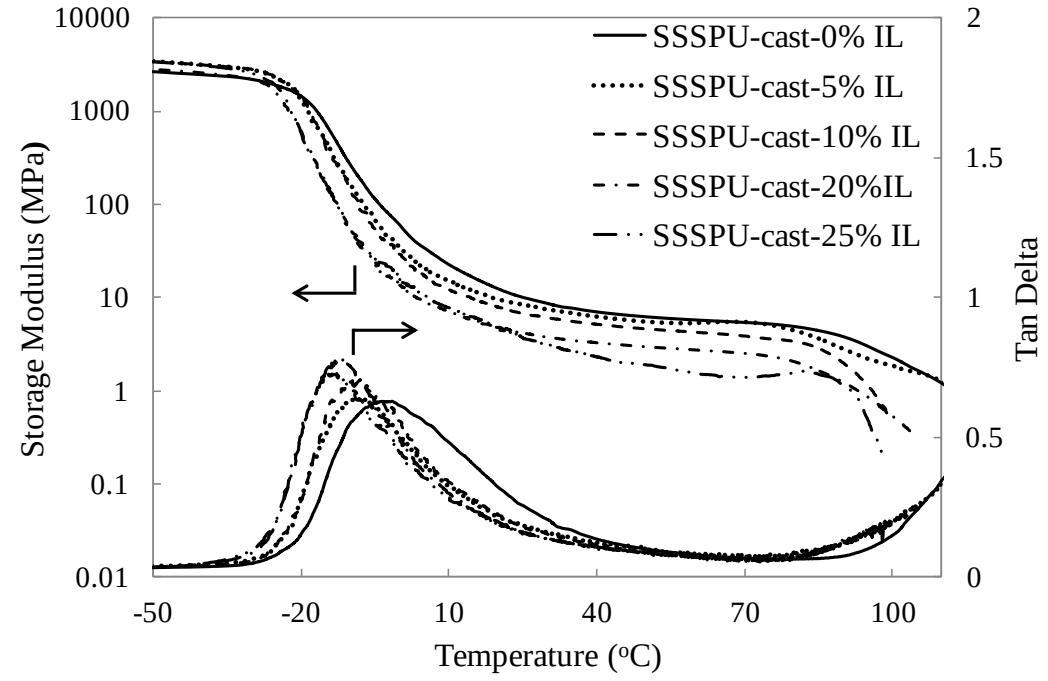

Figure 5.5 Comparison of thermomechanical properties of SSSPU membranes cast with various contents of EMIm ES ionic liquid (film tension mode, 3 °C/min, 1 Hz)

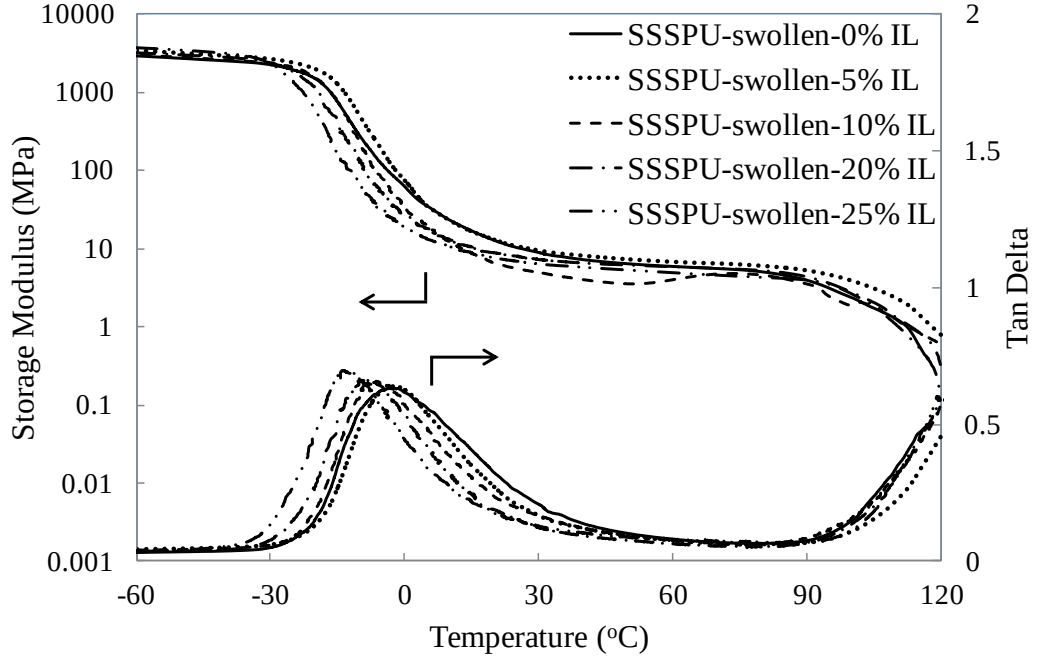

Figure 5.6 Comparison of thermomechanical properties of SSSPU membranes swollen with various contents of EMIm ES ionic liquid (film tension mode, 3 °C/min, 1 Hz)

5.4.4 Morphology

In order to correlate thermal and mechanical properties with the morphologies of SSSPU/IL composite membranes, we investigated the morphological feathers of SSSPU membranes in the presence of various contents of IL using AFM and SAXS. **Figure 5.7** shows AFM phase images of SSSPU cast with various contents of IL. In AFM images, lighter regions represent hard segment domains and darker regions represent soft phases.[39] The data indicated that SSSPU/IL composite membranes possessed well-defined microphase-separated morphologies. Consistent with our previous studies, SSSPU hard segments formed randomly orientated, needle-like hard domains, and SSSPU soft segments formed a continuous soft phase.[34] AFM images also showed that the length of needle-like hard domains increased in the presence of IL, especially at high IL contents. SSSPU with 20 wt% IL and 25 wt% IL showed much longer hard domains (100~200 nm) than neat SSSPU (50~100 nm). We hypothesize that IL preferentially located in the PEG soft phase and enhanced microphase-separation of soft and hard segments. However, reliable AFM images were not obtained for SSSPU/IL composite membranes prepared with the "swollen" method because the membrane surface was significantly disturbed upon removing the surface IL during the swelling experiment.

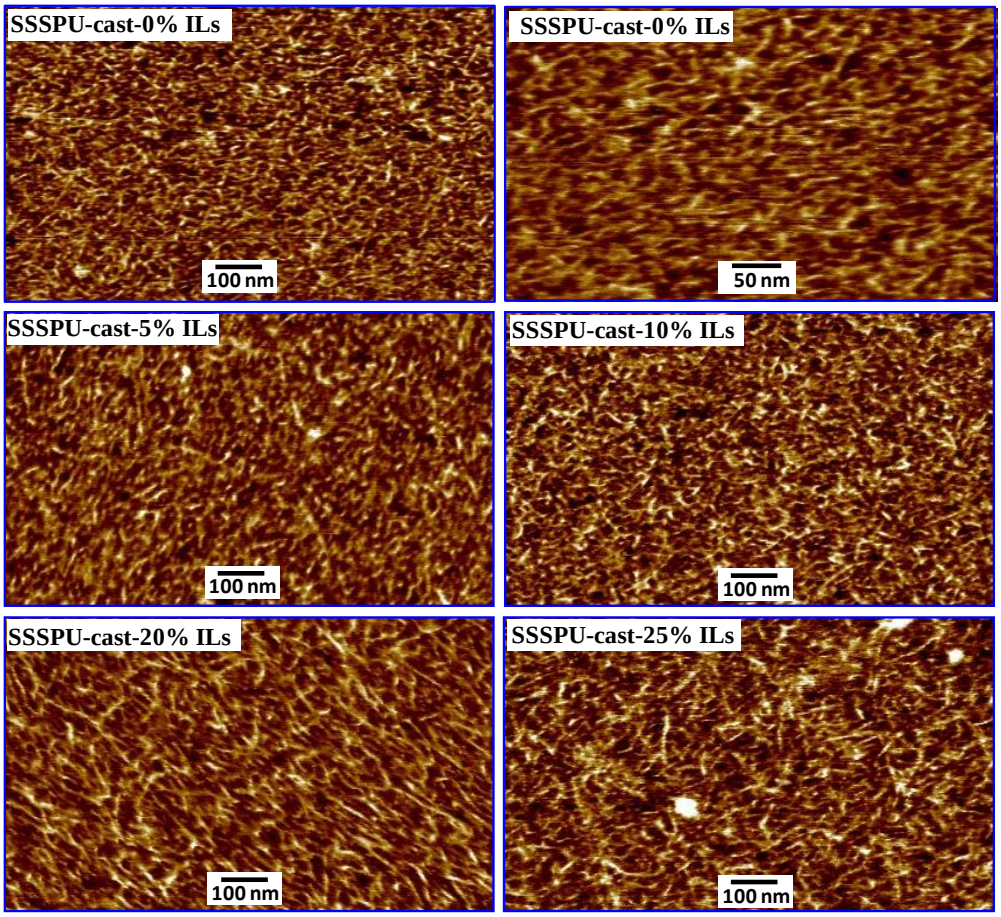

Figure 5.7 Influence of ionic liquid on surface morphologies of SSSPU cast with various contents of ionic liquid (taping mode AFM, spring constant=42 N/m)

In addition to AFM studies, SAXS was performed to investigate the bulk morphological features of these SSSPU/IL composite membranes. **Figure 5.8** shows SAXS profiles plotted as scattering intensity versus scattering vector q (nm^{-1}) for "swollen" samples. The data indicated that neat SSSPU displayed a very weak scattering peak at q=0.5 nm^{-1}, which corresponded to the microphase separation of soft and hard segments.[40,41] Low scattering peak intensity was presumably due to the reduced electron density difference between sulfonated PEG soft segments and hard segments.[34] However, it is interesting to note that the scattering peak intensity systematically increased with increasing IL content. Based on our previous discussion, it is reasonable to speculate that EMIm ES ionic liquid preferentially located into the PEG soft phase

and increased the electron density difference, leading to stronger scattering intensity. Moreover, AFM suggested that IL enhanced microphase separation of soft and hard segments, which also contributed to increased scattering intensity at q=0.5 nm^{-1}. In addition, SAXS profiles for all "swollen" samples showed broad ionomer peaks ranging from q=1~2 nm^{-1}. Our previous studies demonstrated that the ionomer peak in the SAXS profiles of poly(sulfobetaine methacrylate)-*co*-poly(*n*-butyl acrylate) (PSBMA-*co*-PnBA) copolymer membranes also shifted to lower q as EMIm ES ionic liquid content increased.[9] However, SAXS profiles of SSSPU/IL composite membranes showed that the ionomer peak position was independent of IL content. Different dispersion states of IL in these two polymers may contribute to the different responses of ionomer peaks to IL. In a PSBMA-*co*-PnBA copolymer, EMIm ES is not compatible with the PnBA phase, therefore, the IL preferentially joined the zwitterionic domains, causing the shift of ionomer peak in SAXS profiles. In contrast, EMIm ES is completely compatible with SSSPU PEG soft segments. EMIm ES homogenously dispersed in the PEG soft phase with no preference for only the sulfonate ionic domains. Thus, the ionomer peak arising from sodium sulfonate ion pair association showed comparable peak positions for all "swollen" samples. SSSPU/IL composite membranes prepared with "cast with" method showed quite similar SAXS profiles with "swollen" samples.

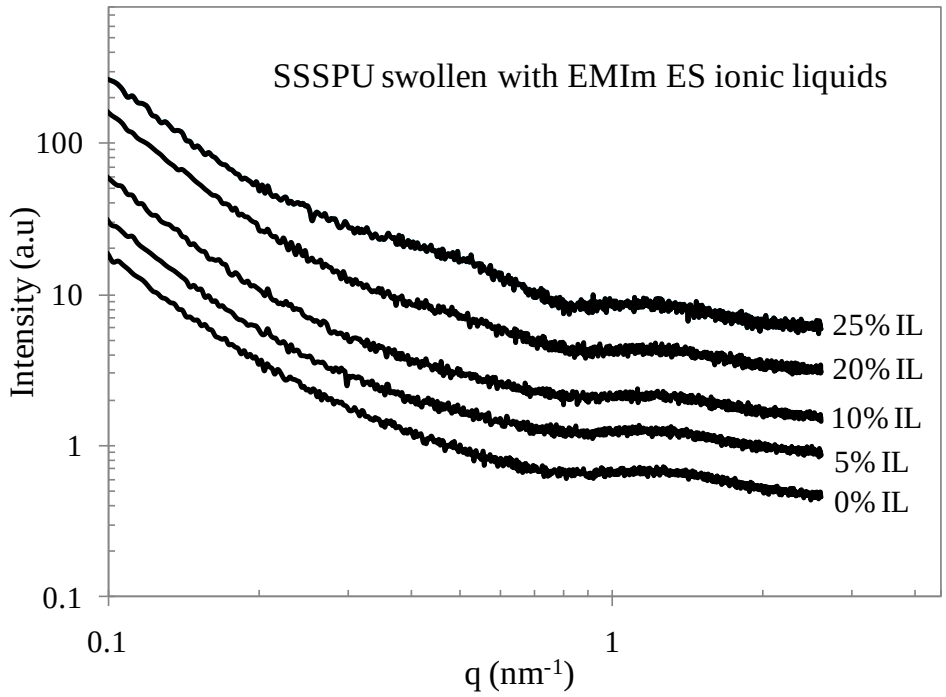

Figure 5.8 SAXS profiles of SSSPU swollen with various contents of EMIm ES ionic liquid

5.4.5 Ionic conductivity

Dielectric relaxation spectroscopy (DRS) is a useful tool to study ionic conductivity behavior of polyurethane ionomers.[2,36] **Figure 5.9** shows the ionic conductivity of SSSPU cast with various contents of EMIm ES ionic liquid. The temperature (T) dependence of ion conductivity (σ) for all SSSPU/IL composite samples showed Vogel-Fulcher-Tammann (VFT) behavior as described with the equation:[37]

$$\sigma = \sigma_0 \exp\left(\frac{-DT_0}{T - T_0}\right) \quad (2)$$

where σ_0 is a prefactor, D is a constant related to fragility, and T_0 is the Vogel temperature, which is related to the equilibrium glass transition temperature of matrix polymers.[42] It is clear that experimental conductivity data fit well to the VFT equation, indicating ion transport in these

samples was strongly related to segmental motions of PEG soft segments.[6] **Figure 5.10** shows ionic conductivity of SSSPU swollen with EMIm ES IL. Not surprisingly, the ionic conductivity data also showed good fit with VFT equation. **Table 5.1** summarizes the best-fit VFT parameters for all samples. It is important to note that all these samples showed comparable Vogel temperature T_0 around 198 K, although it slightly decreased with increasing IL content with no systematic trend. A similar Vogel temperature was presumably due to the slightly changed PEG soft segment T_g with IL content. Moreover, Vogel temperatures determined with VFT model were approximately 50 K lower than sulfonated PEG soft segment T_g's as determined with DSC. This observation agreed well with the literature.[42]

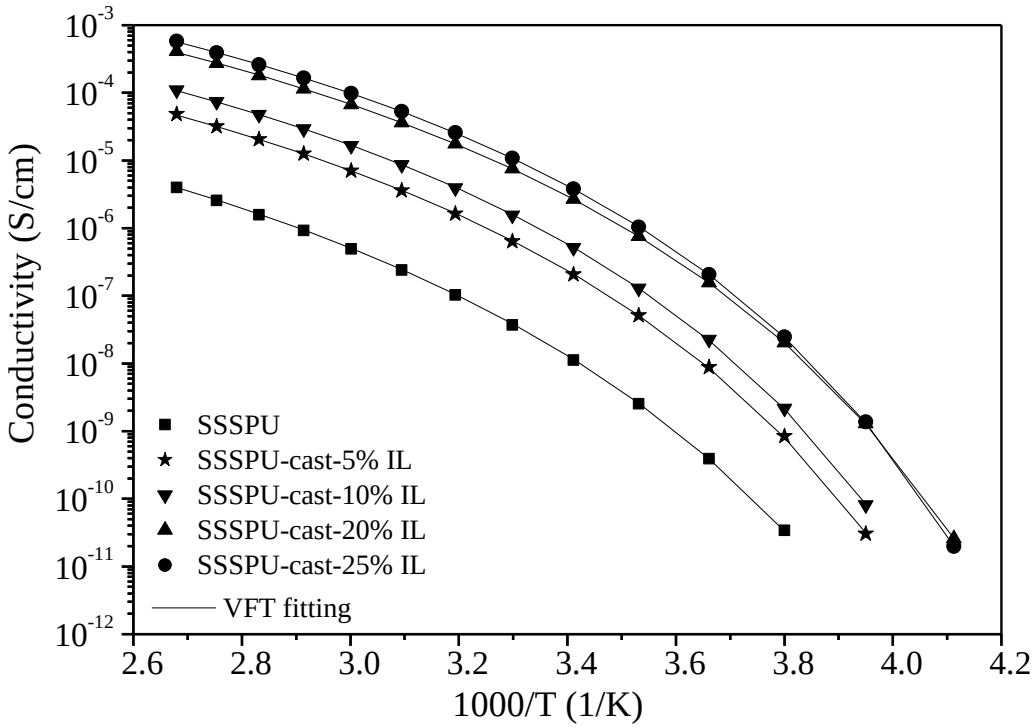

Figure 5.9 Temperature dependence of ion conductivity for SSSPU cast with various contents of EMIm ES ionic liquid

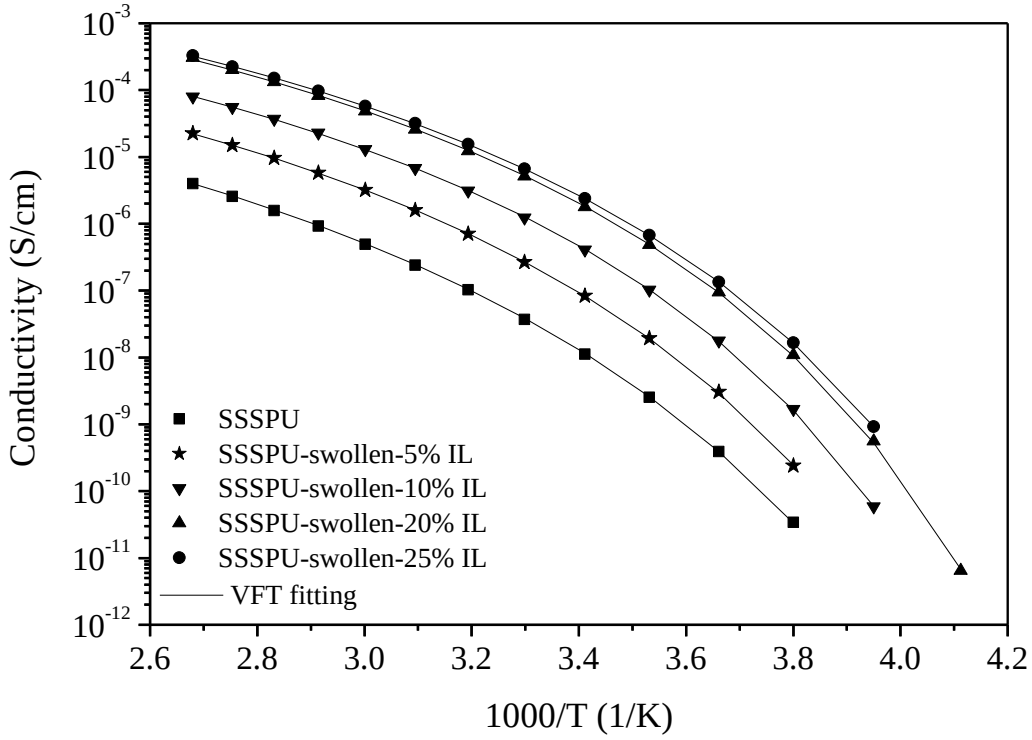

Figure 5.10 Temperature dependence of ion conductivity for SSSPU swollen with various contents of EMIm ES ionic liquid

Table 5.1 VFT fitting parameters for SSSPU cast/swollen with EMIm ES ionic liquid

		σ_0 (S/cm)	T_0 (K)	D	T_g of SS (K)
SSSPU		4.44E-03	197	6.27	248
SSSPU_5wt%IL	swollen	1.36E-02	201	5.47	246
	cast	2.53E-02	200	5.45	244
SSSPU_10wt%IL	swollen	3.14E-02	202	5.04	243
	cast	5.14E-02	201	5.31	240
SSSPU_20wt%IL	swollen	1.08E-01	199	5.18	237
	cast	1.83E-01	195	5.60	236
SSSPU_25wt%IL	swollen	1.05E-01	199	5.08	235
	cast	2.14E-01	198	5.24	234

Figure 5.11 depicts the ionic conductivity as a function of temperature and weight percent of IL for all SSSPU/IL composite membranes prepared with both "swollen" and "cast with"

methods. In both cases, ionic conductivity significantly increased with increasing IL content, especially from 0 to 5 wt% IL. The neat SSSPU membrane showed ionic conductivity on the order of ~10^{-8} S/cm at 20 ^{o}C. In contrast, SSSPU incorporated with 25 wt% IL showed significantly increased ionic conductivity on the order of 10^{-6} S/cm at a same temperature. Two major factors contributed to increased ionic conductivity of SSSPU/IL composite membranes. First, EMIm ES ionic liquid has high bulk ionic conductivity of 3.82×10^{-3} S/cm at 23 ^{o}C. Ionic liquid in SSSPU membranes increases the mobile ion concentration thus provides high ionic conductivity. Second, EMIm ES ionic liquid reduced T_g of PEG soft segments from -26 ^{o}C to -40 ^{o}C. Low PEG soft segment T_g enables easy segmental motion of PEG soft segment and favors fast ion transport. In addition, ionic conductivity of SSSPU/IL composite membranes showed strong dependence on temperature. SSSPU membranes with 25 wt% IL showed ionic conductivity on the order of 10^{-8} S/cm at -10 ^{o}C. In sharp contrast, the ionic conductivity dramatically increased to 10^{-3} S/cm at 100 ^{o}C. In comparison of SSSPU/IL composite membranes prepared with different methods, "cast with' samples showed slightly higher ionic conductivity than "swollen" samples. Difference in ion conductivity between two methods may arise from slight difference in morphology and homogeneity of EMIm ES ionic liquid in SSSPU membranes.

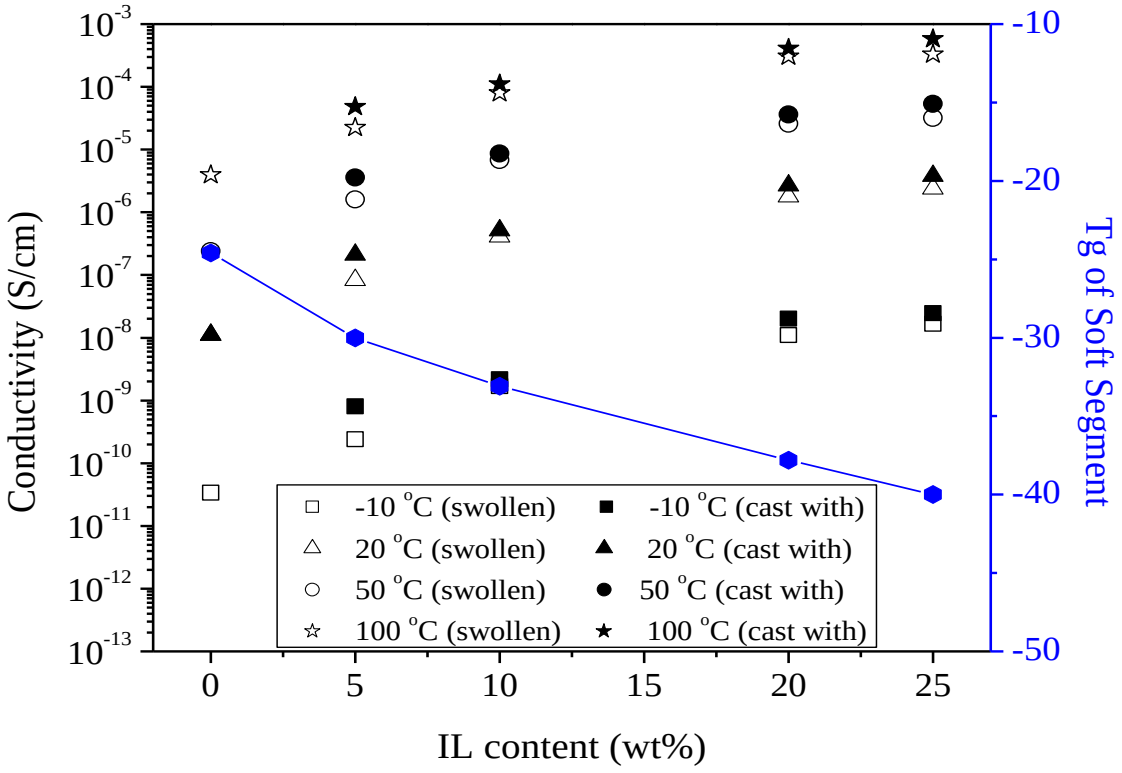

Figure 5.11 Dependence of ion conductivity on IL content of SSSPU/IL composites at various temperatures (ionic conductivity of pure EMIm ES is 3.82×10^{-3} S/cm at 23 °C)

5.5 Conclusions

Influence of room temperature IL, EMIm ES, on thermal and mechanical properties, morphology, and ionic conductivity of PEG-based sulfonated polyurethanes (SSSPU) was investigated with two series of novel SSSPU/IL composite membranes generated with both "swollen" and "cast with" methods. In both cases, EMIm ES ionic liquid preferentially located into the sulfonated PEG soft phase due to their high compatibility, leading to systematically decreased soft segment T_g from -26 ^oC to -40 ^oC. Moreover, all SSSPU/IL composite membranes exhibited well-defined rubbery plateaus in DMA, which was due to the undisturbed, microphase-separated, hard segment domains. Morphologies of SSSPU/IL composite membranes characterized with AFM and SAXS correlated well with their thermal and mechanical properties. AFM images indicated that all "cast with" samples showed well microphase-separated morphologies. Samples with high IL contents at 20 wt% and 25 wt% displayed longer, needle-like, hard domains than neat SSSPU membranes. SAXS profiles for both "swollen" and "cast with" samples showed that scattering peaks near q=0.5 nm^{-1}, arising from microphase-separation of soft and hard segments, increased in peak intensity with increasing IL content. However, ionomer peaks at q=1~2 nm^{-1} remained virtually unchanged due to a homogenous dispersion of EMIm ES in the PEG soft phase. In addition, ionic conductivity of all SSSPU/IL composite membranes followed VFT behavior and showed strong dependence on IL content and temperature. Ionic conductivity of neat SSSPU membranes significantly increased from the order of 10^{-8} to 10^{-6} S/cm upon incorporation of 25 wt% EMIm ES and reached a high value approximately to 5×10^{-4} S/cm at 100 ^oC. "Cast with" samples exhibited slightly higher ionic conductivity than "swollen" samples, which might result from their slightly different morphologies. This study indicates that appropriate design of polymer structures and

use of suitable IL enable to fabricate novel composite materials possessing both high ionic conductivity and good mechanical properties.

5.6 Acknowledgements

This work is supported in part by the U.S. Army Research Office through the Ionic Liquids in Electro-Active Devices Multidisciplinary University Research Initiative (ILEAD MURI) program under Contract/Grant Number W911NF-07-1-0452. The authors also thank Institute for Critical Technology and Applied Science (ICTAS) at Virginia Tech. Aspects of this work were carried out using instruments in the Nanoscale Characterization and Fabrication Laboratory (NCFL) operated by ICTAS. Additionally, this research was partially supported by the National Science Foundation under Grant No. DMR-0923107.

5.7 References

1. Oh, J. M.; Geiculescu, O.; DesMarteau, D.; Creager, S. *J. Electrochem. Soc.* **2011**, *158*, A207.
2. Wang, S. W.; Liu, W. J.; Colby, R. H. *Chem. Mater.* **2011**, *23*, 1862.
3. Ji, J.; Keen, J.; Zhong, W.-H. *J. Power Sources* **2011**, *196*, 10163.
4. Duncan, A. J.; Leo, D. J.; Long, T. E. *Macromolecules* **2008**, *41*, 7765.
5. Angulakshmi, N.; Thomas, S.; Nahm, K. S.; Stephan, A. M.; Elizabeth, R. N. *Ionics* **2011**, *17*, 407.
6. Tudryn, G. J.; Liu, W. J.; Wang, S. W.; Colby, R. H. *Macromolecules* **2011**, *44*, 3572.
7. Xiao, Q. Z.; Wang, X. Z.; Li, W.; Li, Z. H.; Zhang, T. J.; Zhang, H. L. *J. Membr. Sci.* **2009**, *334*, 117.
8. Armand, M.; Endres, F.; MacFarlane, D. R.; Ohno, H.; Scrosati, B. *Nature Materials* **2009**, *8*, 621.
9. Brown, R. H.; Duncan, A. J.; Choi, J. H.; Park, J. K.; Wu, T. Y.; Leo, D. J.; Winey, K. I.; Moore, R. B.; Long, T. E. *Macromolecules* **2010**, *43*, 790.
10. Imaizumi, S.; Kokubo, H.; Watanabe, M. *Macromolecules* **2012**, *45*, 401.
11. Lodge, T. P. *Science* **2008**, *321*, 50.
12. Green, M. D.; Long, T. E. *Polymer Reviews* **2009**, *49*, 291.
13. Hoarfrost, M. L.; Segalman, R. A. *Macromolecules* **2011**, *44*, 5281.
14. Weber, R. L.; Ye, Y. S.; Schmitt, A. L.; Banik, S. M.; Elabd, Y. A.; Mahanthappa, M. K. *Macromolecules* **2011**, *44*, 5727.
15. Virgili, J. M.; Hexemer, A.; Pople, J. A.; Balsara, N. P.; Segalman, R. A. *Macromolecules* **2009**, *42*, 4604.
16. Liu, Y.; Liu, S.; Lin, J. H.; Wang, D.; Jain, V.; Montazami, R.; Heflin, J. R.; Li, J.; Madsen, L.; Zhang, Q. M. *Appl. Phys. Lett.* **2010**, *96*.
17. Green, M. D.; Schreiner, C.; Long, T. E. *J. Phys. Chem. A* **2011**, *115*, 13829.
18. Kim, S. Y.; Yoon, E.; Joo, T.; Park, M. J. *Macromolecules* **2011**, *44*, 5289.
19. Virgili, J. M.; Hoarfrost, M. L.; Segalman, R. A. *Macromolecules* **2010**, *43*, 5417.
20. Matsumoto, K.; Endo, T. *Journal of Polymer Science Part a-Polymer Chemistry* **2011**, *49*, 3582.
21. Zhang, S. P.; Lee, K. H.; Frisbie, C. D.; Lodge, T. P. *Macromolecules* **2011**, *44*, 940.
22. He, Y. Y.; Lodge, T. P. *Chem. Commun.* **2007**, 2732.
23. Gu, Y. Y.; Lodge, T. P. *Macromolecules* **2011**, *44*, 1732.
24. Virgili, J. M.; Nedoma, A. J.; Segalman, R. A.; Balsara, N. P. *Macromolecules* **2010**, *43*, 3750.
25. Meli, L.; Lodge, T. P. *Macromolecules* **2009**, *42*, 580.
26. He, Y. Y.; Li, Z. B.; Simone, P.; Lodge, T. P. *J. Am. Chem. Soc.* **2006**, *128*, 2745.
27. He, Y. Y.; Lodge, T. P. *J. Am. Chem. Soc.* **2006**, *128*, 12666.
28. Cheng, S. J.; Beyer, F. L.; Mather, B. D.; Moore, R. B.; Long, T. E. *Macromolecules* **2011**, *44*, 6509.
29. Gwee, L.; Choi, J. H.; Winey, K. I.; Elabd, Y. A. *Polymer* **2010**, *51*, 5516.
30. Sinha, K.; Maranas, J. K. *Macromolecules* **2011**, *44*, 5381.
31. Simone, P. M.; Lodge, T. P. *Acs Applied Materials & Interfaces* **2009**, *1*, 2812.
32. Trivedi, S.; Pandey, S. *J. Phys. Chem. B* **2011**, *115*, 7405.
33. Triolo, A.; Russina, O.; Keiderling, U.; Kohlbrecher, J. *J. Phys. Chem. B* **2006**, *110*, 1513.
34. Gao, R.; Zhang, M.; Dixit, N.; Moore, R. B.; Long, T. E. *Polymer* **2012**, *(Accepted)*.
35. Choi, J. W.; Cheruvally, G.; Kim, Y. H.; Kim, J. K.; Manuel, J.; Raghavan, P.; Ahn, J. H.; Kim, K. W.; Ahn, H. J.; Choi, D. S.; Song, C. E. *Solid State Ionics* **2007**, *178*, 1235.
36. Fox, T. G. *Bull. Am. Phys. Soc.* **1956**, *1*, 123.

37. Susan, M. A.; Kaneko, T.; Noda, A.; Watanabe, M. *J. Am. Chem. Soc.* **2005**, *127*, 4976.
38. Tiyapiboonchaiya, C.; MacFarlane, D. R.; Sun, J. Z.; Forsyth, M. *Macromol. Chem. Phys.* **2002**, *203*, 1906.
39. Sheth, J. P.; Klinedinst, D. B.; Pechar, T. W.; Wilkes, G. L.; Yilgor, E.; Yilgor, I. *Macromolecules* **2005**, *38*, 10074.
40. Garrett, J. T.; Runt, J.; Lin, J. S. *Macromolecules* **2000**, *33*, 6353.
41. Wei, X.; Yu, X. H. *Journal of Polymer Science Part B-Polymer Physics* **1997**, *35*, 225.
42. Chen, H.; Choi, J.-H.; Cruz, D. S.-d. l.; Winey, K. I.; Elabd, Y. A. *Macromolecules* **2009**, *42*, 4809.

Chapter 6: Cation Functionalized Multi-Walled Carbon Nanotubes for Sulfonated Polyurethane Nanocomposites

Gao, R.; Ramirez, S.M.; Inglefield, D.L.; Bodnar, R.J.; Long, T.E. (*prepared for publication*)

6.1 Abstract

Covalent functionalization of multi-walled carbon nanotubes (MWCNTs) with minimal alteration on the MWCNT structure is important to achieve homogenously dispersed carbon nanotubes while maintaining their unique mechanical and electrical properties. Carboxylic acid derivatized MWCNTs (MWCNT-COOH) were covalently functionalized with 3,3'-iminobis(*N*,*N*-dimethylpropylamine) (DMPA). Upon subsequent quaternization of DMPA, dendritic ammonium cation-functionalized MWCNTs (MWCNT-DMPA$^+$) were formed, where two ammonium cations were incorporated per amide site. Thermogravimetric analysis (TGA) and X-ray photoelectron spectroscopy (XPS) demonstrated successful covalent functionalization and formation of the surface-bound ammonium salt. Raman spectroscopy and atomic force microscopy (AFM) indicated the absence of appreciable destruction of the MWCNT aspect ratio. Compared with pristine MWCNTs and MWCNT-COOH, MWCNT-DMPA$^+$ exhibited enhanced dispersibility in *N*,*N*-dimethylformamide (DMF) as evidenced in UV-Visible spectroscopy and transmission electron microscopy (TEM). In addition, blending MWCNT-DMPA$^+$ with anionic sulfonated polyurethane in DMF generated a series of novel nanocomposite materials with a nanotube content ranging from 0.5 to 5 wt%. Characterization of the composite films using both field emission scanning electron microscopy (FESEM) and TEM revealed that MWCNT-DMPA$^+$ exhibited uniform dispersion in sulfonated polyurethane matrix even at 5 wt%. Tensile analysis showed that the modulus of the sulfonated polyurethane matrix linearly increased with MWCNT-DMPA$^+$ content.

6.2 Introduction

Since their discovery in 1991,[1] carbon nanotubes have received significant attention for their unique thermal, mechanical and electrical properties.[2-5] In particular, carbon nanotubes are reported as excellent additives to enhance the mechanical and electrical properties of polymeric composite materials.[6-8] The efficacy of carbon nanotubes in enhancing these desired properties highly depends on their dispersion homogeneity in the polymeric matrix.[9] However, due to the strong intertube van der Waals interactions, carbon nanotubes tend to aggregate when they are dispersed in a solvent or polymeric matrix even at low levels.[8] Many efforts have identified methods to achieve stable and homogenous dispersions of carbon nanotubes in solvents and polymeric matrices.[10-12]

Covalent or non-covalent chemical modification of carbon nanotubes is a widely employed strategy to enhance their dispersibility.[7,13-15] Polymers or low molar mass functionalized molecules are covalently or non-covalently attached to the carbon nanotube surface to counterbalance the intertube van der Waals interactions and favor uniform dispersion of carbon nanotubes. Among the covalent modification methods, "grafting to" and "grafting from" are the most reported techniques to incorporate polymeric segments onto the carbon nanotube surface.[16-18] Hong and Pan et al. reported the synthesis of water-soluble multi-walled carbon nanotubes (MWCNTs) by grafting poly(*N*-isopropylacrylamide) from the carbon nanotube surface using the reversible addition and fragmentation chain transfer (RAFT) polymerization technique.[17] More recently, Park and Lee et al. investigated the covalent modification of MWCNTs with imidazolium-based ionic liquids. They reported that both the bound imidazolium cation and the mobile counterions significantly influenced the dispersibility of MWCNTs.[19] Although covalent modification is proven as a suitable method to prepare well-dispersed carbon nanotubes,

researchers realize that the covalent modification of carbon nanotubes necessitates alteration of the nanotube surface due to harsh chemical environments during the functionalization process.[13,20,21] Any alteration of the conjugated structure on the nanotube surface will negatively influence the physical properties of carbon nanotubes and their efficacy in enhancing the mechanical and electrical properties of polymeric materials.[22] To mitigate this risk, researchers have proposed different non-covalent modification strategies, which mainly included wrapping polymer chains or adsorbing small molecules onto the carbon nanotube surface through π-π interactions or other non-covalent interactions.[12,13,23] Recently, Chen and Dai et al. modified single-walled carbon nanotubes (SWCNTs) with poly(ethylene glycol)-based amphiphilic dendrimers using a non-covalent strategy, and the functionalized SWCNTs were effectively dispersed in water.[24] Herein, we appreciate the advantage of non-covalent modification strategy over the covalent method in terms of minimizing the chemical alteration of the nanotube surface. However, non-covalent attachment of functional groups onto nanotube surfaces is less effective than covalent bonding due to the reversibility of non-covalent interactions. Thus, effectively modifying carbon nanotubes with stable functional groups and minimizing the chemical alteration on the nanotube surface remains as a challenge for this field.

In the present study, we modified MWCNTs with ammonium cations through a dendritic functionalization strategy. This method enabled the doubling of functionality by incorporating two ammonium cations per initial acidic site. In other words, one can incorporate more functional groups onto less oxidized carbon nanotubes, which minimizes the modification to the conjugated surface. We compared the pristine MWCNTs, acid-oxidized MWCNTs (MWCNT-COOH), and the dendritic ammonium-functionalized MWCNTs (MWCNT-DMPA$^+$) in terms of nanotube composition and their dispersibilities. The characterization data indicated that the

ammonium-functionalized MWCNTs exhibited significantly enhanced dispersibility in both DMF solvent and an anionic sulfonated polyurethane matrix without appreciable destruction of the carbon nanotube aspect ratio.

6.3 Experimental

Materials. Thionyl chloride (97%), 1-bromobutane (99%), dimethyl 5-sulfoisophthalate sodium salt (98%), poly(ethylene glycol) (M_n=950-1000 g/mol), anhydrous *N*,*N*-dimethylformamide (99.8%), and potassium hydroxide (>90%) were purchased from Aldrich and used as received. 3,3'-Iminobis(*N*,*N*-dimethylpropylamine) (97%), triethylamine, and 1,4-butanediol (99%) were purchased from Aldrich and distilled from calcium hydride. Dibutyltin dilaurate (95%) was purchased from Aldrich and diluted to 1 wt% using anhydrous tetrahydrofuran. Pristine multi-walled carbon nanotubes (C150P) and dicyclohexylmethane-4,4'-diisocyanate (HMDI) (99.5 %) were kindly provided by Bayer MaterialScience and used as received.

Preparation of carboxylic acid-functionalized MWCNTs (MWCNT-COOH)

Pristine multi-walled carbon nanotubes (C150P) (3.555 g) and 8 M HNO_3 (120 mL) were charged into a round-bottomed flask equipped with a magnetic stir bar and a condenser. The mixture was sonicated with a sonicator bath for 1 h, and then refluxed at 120 ^oC for 12 h with magnetic stirring. The resulting carbon nanotube suspension was neutralized with 1 M potassium hydroxide water solution. The oxidized MWCNTs were filtered and washed with distilled water 5 times. In a following step, the oxidized MWCNTs were refluxed in 1 M hydrochloric acid for 24 h, subsequently filtered and washed with distilled water 5 times, and washed with methanol for a second time. The resulting MWCNT-COOH product was finally dried under reduced pressure (20 mm Hg) at 40 ^oC for 24 h.

Preparation of 3,3'-iminobis(N,N-dimethyl propylamine)-functionalized MWCNTs (MWCNT-DMPA)

In a two-necked, round-bottomed flask equipped with a magnetic stir bar and a condenser, MWCNT-COOH (0.507 g) was dispersed into thionyl chloride (20.0 mL) using a sonicator bath. The mixture was refluxed for 24 h at 80 ^{o}C in a N_2 atmosphere. The excess thionyl chloride was removed by filtration. The resulting MWCNTs were subsequently washed with anhydrous diethyl ether 5 times, dried under vacuum at room temperature for 30 min, and finally dispersed in anhydrous DMF in another pre-dried, two-necked, round-bottomed flask equipped with a water condenser. Distilled 3,3'-iminobis(*N,N*-dimethyl-propylamine) (5.0 mL) and triethylamine were syringed into the flask. The reaction proceeded at 90 ^{o}C for 48 h. The DMPA-functionalized MWCNTs were purified with filtration, washing with DMF 5 times, and finally dried under reduced pressure (20 mm Hg) at 40 ^{o}C.

Synthesis of dendritic ammonium cation-functionalized MWCNTs (MWCNT-DMPA^{+})

DMPA-functionalized MWCNTs (0.400 g) and 1-bromobutane (8.080 g) were added into a two-necked, round-bottomed flask equipped with a water condenser. The reaction was maintained at 70 ^{o}C in DMF for 72 h. The resulting MWCNTs were purified upon filtration and subsequent washing with DMF and methanol. The MWCNT-DMPA^{+} was dried under reduced pressure (20 mm Hg) at 40 ^{o}C for 24 h.

Synthesis of sulfonated polyurethanes containing sulfonated soft segments

In a two-necked, round-bottomed flask equipped with a magnetic stir bar, dimethyl 5-sulfoisophthalate sodium salt (2.120 g), poly(ethylene glycol)-1K (15.74 g), and dibutyltin oxide (8.9 mg) were introduced and purged with nitrogen. The reaction was allowed to proceed at 170~190 ^{o}C under N_2 flow. Complete reaction was determined using ^{1}H NMR spectroscopy. The

crude product was dissolved in acetone and precipitated in diethyl ether 3 times. The final product, PEG-based sulfonated polyol, was dried *in vacuo* at 50 ^{o}C. The sulfonated polyurethane was synthesized according to a typical prepolymer process. In a three-necked, round-bottomed flask equipped with an addition funnel, nitrogen inlet, and overhead stirrer, PEG-based sulfonated polyol was end-capped with HMDI at 80 ^{o}C for 4 h in the presence of dibutyltin dilaurate (1 wt% in anhydrous THF, 50 ppm). The prepolymer was then chain-extended with 1,4-butanediol and allowed to proceed for an additional 24 h at 80 ^{o}C under a N_2 atmosphere. The reaction solution was directly used to prepare carbon nanotube composites.

Preparation of sulfonated polyurethane (SPU)/MWCNT nanocomposites

Pristine MWCNT or MWCNT-DMPA^{+} (1.5 wt%) in DMF was sonicated with a sonication probe (H7 probe, 60-70% amplitude) for 60 min with magnetic stirring. A calculated amount of MWCNT-DMPA^{+} suspension was charged into the sulfonated polyurethane solution (15 wt% solid in DMF). The mixture was magnetically stirred for 10 min and then cast into a Teflon® mode. The resulting composite films were dried in air for 24 h and under reduced pressure (20 mm Hg) for an additional 48 h at 50 ^{o}C.

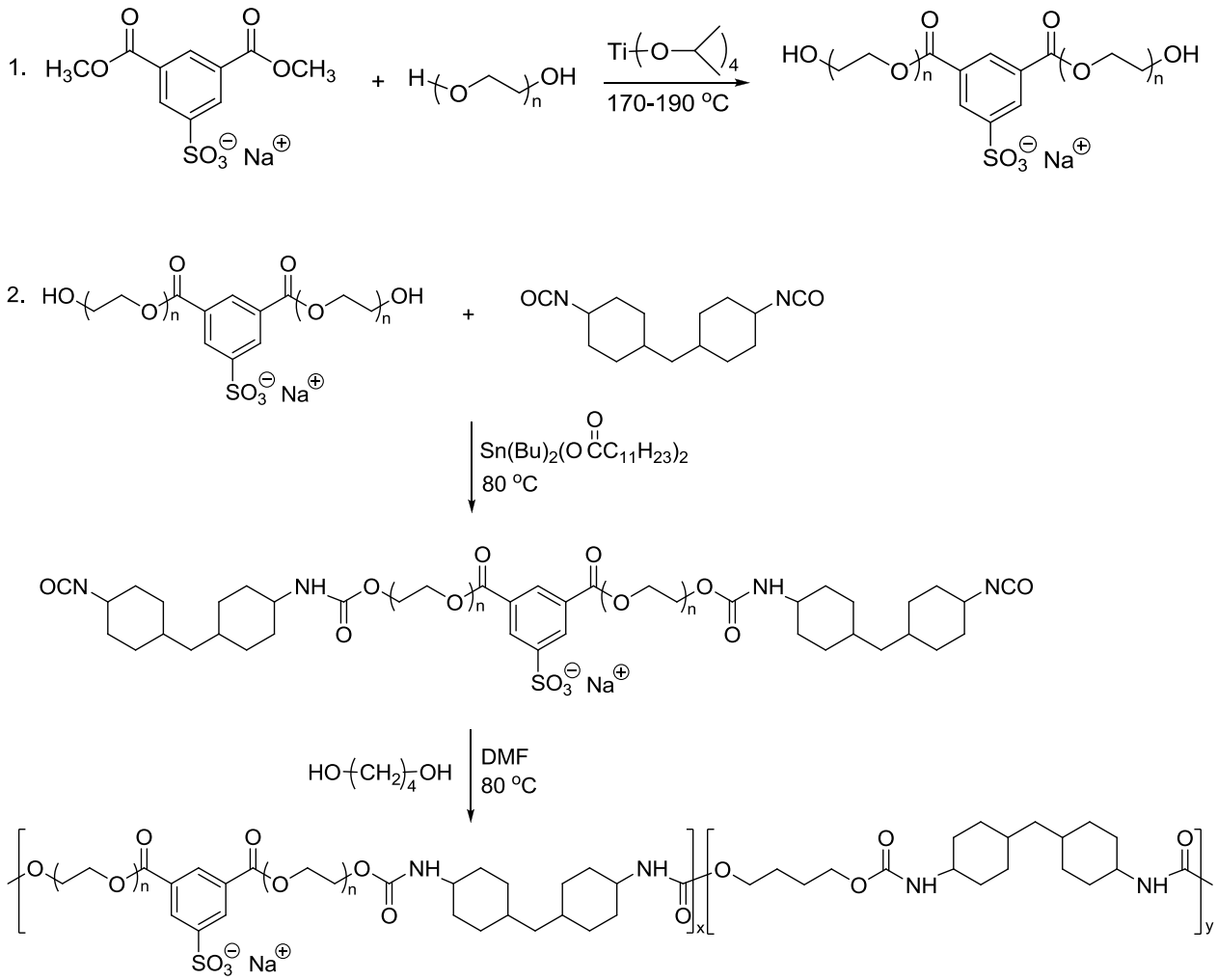

Scheme 6.1 Synthesis of sulfonated polyurethanes containing sulfonated soft segments

Instrumentation

^{1}H NMR spectroscopy performed on a Varian INOVA 400 MHz spectrometer was utilized to confirm the chemical structure of the synthesized PEG-based sulfonated polyol and to determine the number-average molecular weight in $CDCl_3$ at 23 ^{o}C. Thermogravimetric analysis (TGA) was conducted on a TA instrument Q500 with a temperature ramp of 10 ^{o}C/min in a nitrogen atmosphere to confirm the successful functionalization of MWCNTs. The functionalized MWCNTs were further quantitatively characterized using a Perkin-Elmer Model 5400 XPS

spectrometer equipped with a Mg K_α X-ray source. Raman spectra of functionalized MWCNTs were obtained on a Horiba LabRam HR800 Raman microprobe equipped with a 100 mW, air-cooled, 514 nm Argon laser. Atomic force microscopy (AFM) was conducted on a Veeco MultiMode AFM. The dispersibilities of pristine MWCNTs and MWCNT-$DMPA^+$ in DMF were investigated using a Philips EM 420 transmission electron microscope (TEM) operated at an accelerating voltage of 120 kV. The samples for TEM imaging were first sonicated in DMF for 60 min using a UP400S sonication probe. The resulting carbon nanotube suspension was diluted to 0.005 wt% and subsequently cast on carbon-coated TEM grids. The grids were dried in air for 1 h before the TEM imaging. Field emission scanning electron microscopy (FESEM) was performed on a LEO (Zeiss) 1550 with a 5 mm working distance to image the fresh cross-section of the composite films. The fresh cross-section was obtained by fracturing the composite film in liquid nitrogen. The composite specimens for TEM were prepared by embedding a slice of bulk film in epoxy and cryo-ultramicrotoming using a RMC Products PowerTome PC. Mechanical properties of sulfonated polyurethane/MWCNT-$DMPA^+$ composites were investigated using tensile analysis performed on a 5500R Instron universal testing instrument with a cross-head rate of 50 mm/min at ambient conditions.

6.4 Results and Discussion

6.4.1 Synthesis of MWCNT-$DMPA^+$

We utilized a dendritic functionalization strategy to modify MWCNTs with the ammonium salt (**Scheme 6.2**). Pristine MWCNTs were initially oxidized with relatively mild conditions to minimize chemical destruction of the MWCNT structure.[25] In a following step, DMPA was incorporated using quantitative reaction of the surface-bound carbonyl chloride with a secondary amine containing two tertiary amines to double the number of reactive sites on the MWCNT

surface. Subsequent quaternization of DMPA with 1-bromobutane produced the dendritic ammonium salt. In this work, all functionalized MWCNTs were thoroughly washed with various solvents and dried under reduced pressure to remove any physically absorbed, low molar mass contaminant.

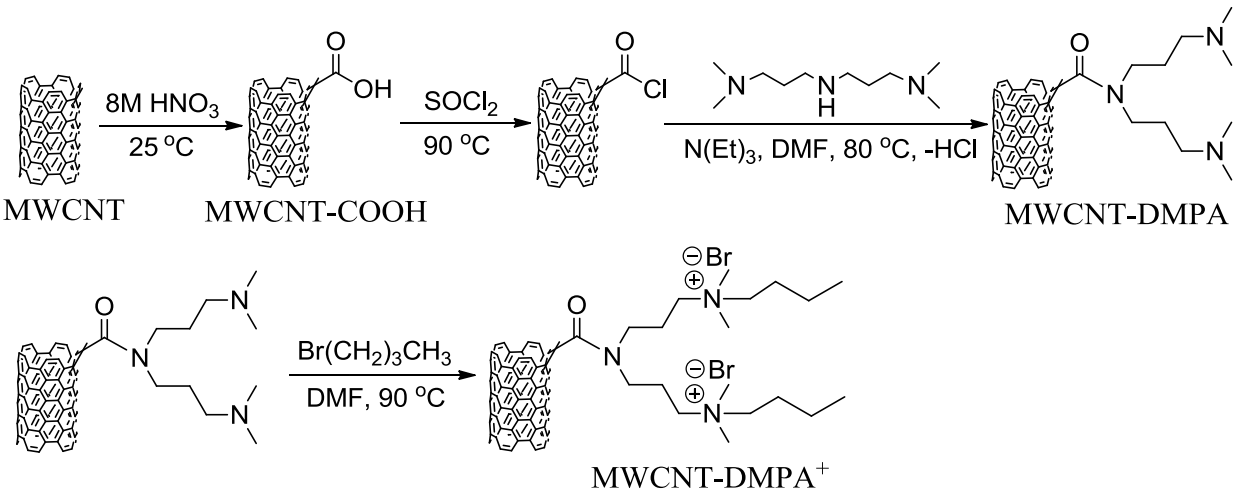

Scheme 6.2 Synthesis of dendritic ammonium-functionalized multi-walled carbon nanotubes

6.4.2 Characterization of MWCNTs using TGA, Raman, XPS, and AFM

Successful covalent functionalization was confirmed in each synthetic step, and we utilized both TGA and XPS to analyze the functionalized MWCNTs. TGA curves in **Figure 6.1** indicated that the pristine MWCNTs had a high thermal stability and showed negligible weight loss during the entire heating cycle. In contrast, functionalized MWCNTs exhibited a significant weight loss in a temperature range from 200 to 400 ^{o}C. The weight loss in this temperature range was attributed to the elimination of the functional groups on the carbon nanotube surface. In addition, as MWCNT-COOH was converted to MWCNT-DMPA and MWCNT-DMPA^{+}, TGA revealed increasing weight loss as a function of weight percent of functional groups on the MWCNT surface. X-ray photoelectron spectroscopy (XPS) confirmed the surface functionality of modified MWCNTs. **Figure 6.2** depicts the XPS spectra of MWCNT-COOH, MWCNT-

DMPA, and MWCNT-DMPA$^+$. A comparison of these XPS spectra revealed that a new nitrogen (N 1s) peak at 400 eV emerged for MWCNT-DMPA and MWCNT-DMPA$^+$. This demonstrated successful covalent attachment of DMPA onto the MWCNT surface. Furthermore, the XPS spectrum of MWCNT-DMPA$^+$ showed two unique Br 3d and Br 3p peaks at the binding energy of 70 eV and 190 eV, respectively, indicating formation of the corresponding ammonium salt.

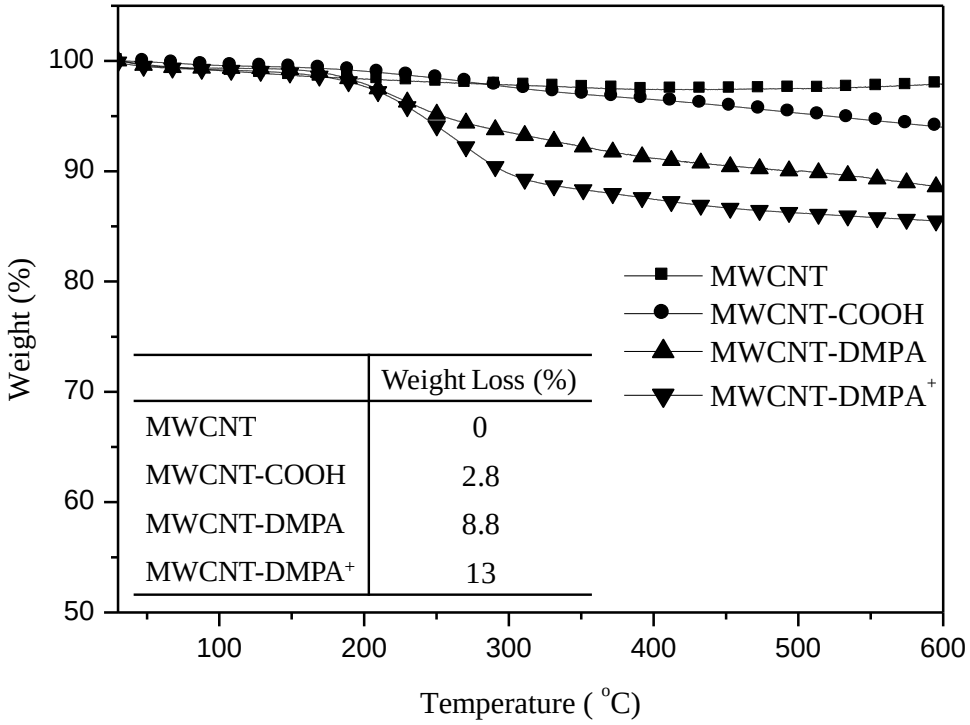

Figure 6.1 TGA (heating rate, 10 ^oC/min; N_2 flow, 10 mL/min, weight loss determined using the 1st derivative of wt% vs. temp.) of MWCNTs with different surface functionalities

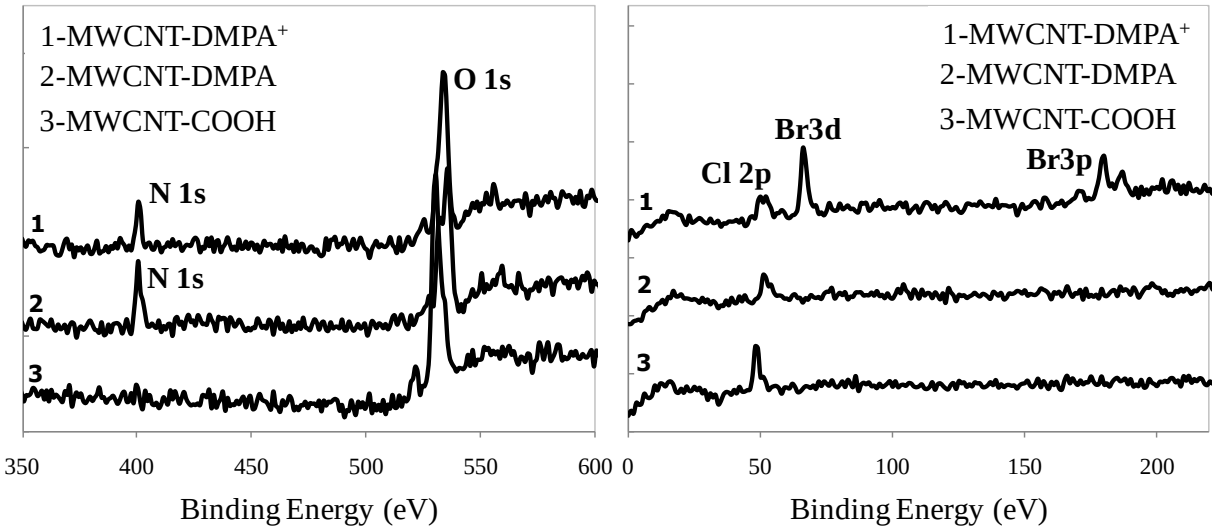

Figure 6.2 XPS of MWCNTs functionalized with different surface functionalities

Raman spectroscopy is a versatile technique to study carbon nanotube composition.[26-30] The most prominent features in a Raman spectrum of MWCNTs are the G band and D band, which correspond to the sp^2 carbons and disordered carbons, respectively. In our study, we utilized the ratio of the D band area (D_a) over the G band area (G_a) to evaluate the chemical alteration of the functionalized MWCNTs. **Figure 6.3** shows a comparison of the Raman spectra of pristine MWCNTs, MWCNT-COOH, and MWCNT-$DMPA^+$. We observed that the area ratio (D_a/G_a) was slightly changed from 1.41 to 1.39 when the pristine MWCNTs were oxidized into MWCNT-COOH. This indicated minimal destruction during the oxidation process. It was noteworthy that the Da/Ga ratio slightly decreased as the MWCNTs were further functionalized. We attributed this to impurities, e.g. amorphous carbon that was removed during the functionalization process. In addition to Raman spectroscopy, atomic force microscopy (AFM) was utilized to compare the nanotube structures of pristine MWCNTs and MWCNT-$DMPA^+$. Both AFM height and phase images are shown in **Figure 6.4**. Compared with pristine MWCNTs, MWCNT-$DMPA^+$ maintained well-defined tube structures after functionalization.

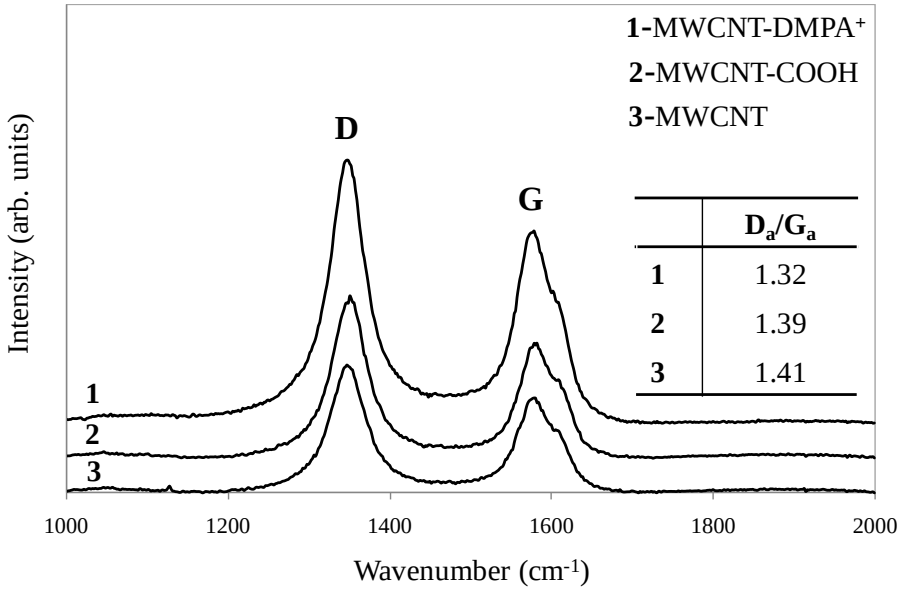

	D_a/G_a
1	1.32
2	1.39
3	1.41

Figure 6.3 Raman spectra (514 nm Argon laser) of MWCNTs functionalized with different surface functionality

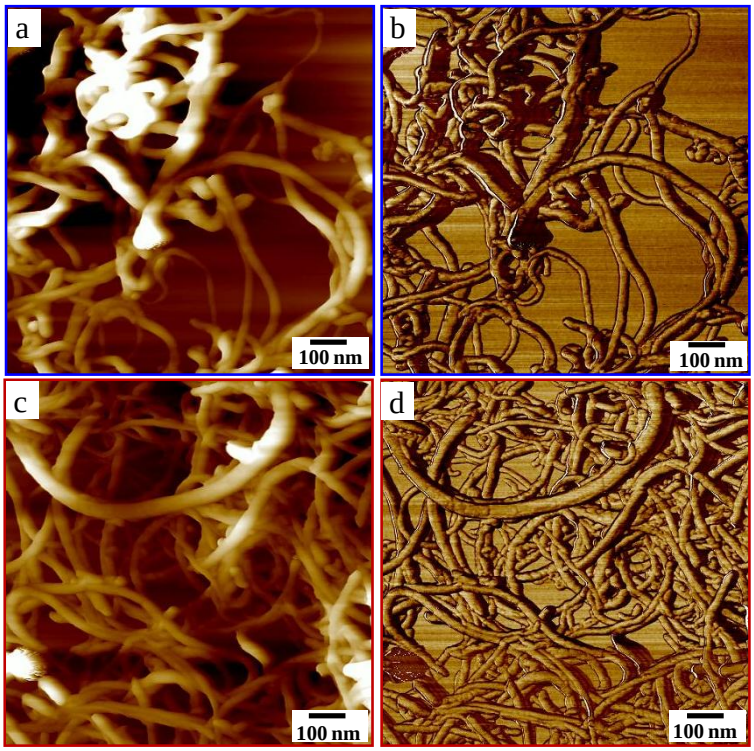

Figure 6.4 Tapping-mode AFM images (tip spring constant, 42 N/m) of pristine MWCNTs (A, B) and MWCNT-DMPA$^+$ (C, D) (cast on silicon wafer, dried in air from 0.05 wt% solution in DMF)

6.4.3 Dispersibility of functionalized MWCNTs in DMF

Dispersibility of pristine MWCNTs, MWCNT-COOH, and MWCNT-$DMPA^+$ was investigated using UV-visible (UV-vis) spectroscopy and TEM. **Figure 6.5** shows the UV-vis spectra for three types of MWCNTs sonicated in DMF for 60 min. Researchers have determined that area below the UV-vis spectra ranging from 200−1000 nm is related to the amount of individual MWCNTs in the solution.[31] For a fixed concentration, more dispersed MWCNTs lead to UV-vis absorbance with higher absorbance intensity and larger area below the spectra. **Figure 6.5** clearly showed that both MWCNT-COOH and MWCNT-$DMPA^+$ exhibited enhanced dispersibility in DMF compared to pristine MWCNTs. MWCNT-$DMPA^+$ showed the most intense UV-vis absorbance, indicating the best dispersion. **Figure 6.6** plots the maximum absorbance values (at ~270 nm) of three types of MWCNTs as a function of sonication time. All samples exhibited systematically increased UV-vis absorbance with increasing sonication time. However, the absorbance value for MWCNT-$DMPA^+$ was significantly higher than that of pristine MWCNT and MWCNT-COOH. This further demonstrated the enhanced dispersibility of MWCNT-$DMPA^+$ in DMF. This observation was consistent with Loos et al. i.e. UV-vis absorbance values of MWCNTs in an aqueous surfactant solution increased with sonication time.[31]

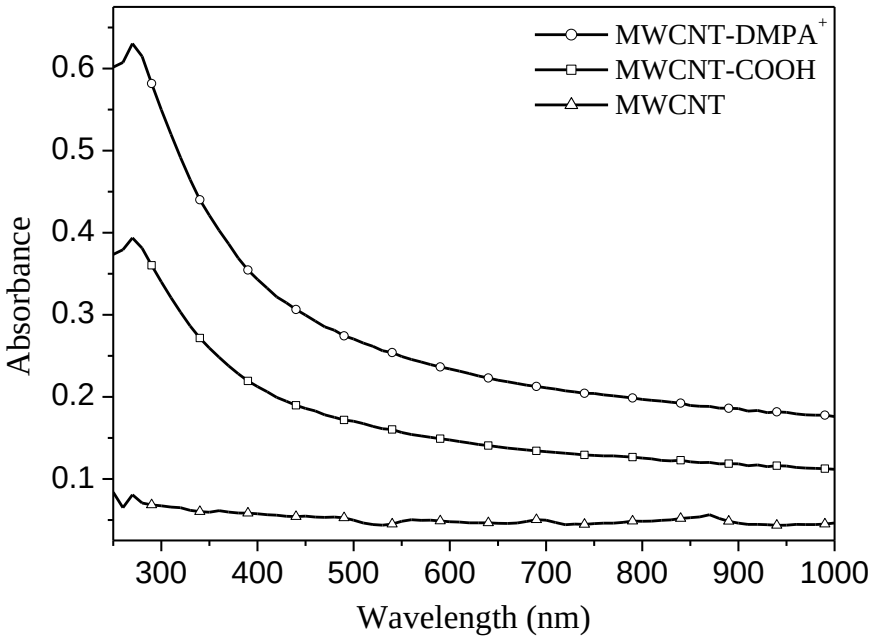

Figure 6.5 UV-vis spectra of pristine MWCNT, MWCNT-COOH, and MWCNT-DMPA$^+$ (1.5 wt% in DMF, sonicated for 60 min, diluted by a factor of 150)

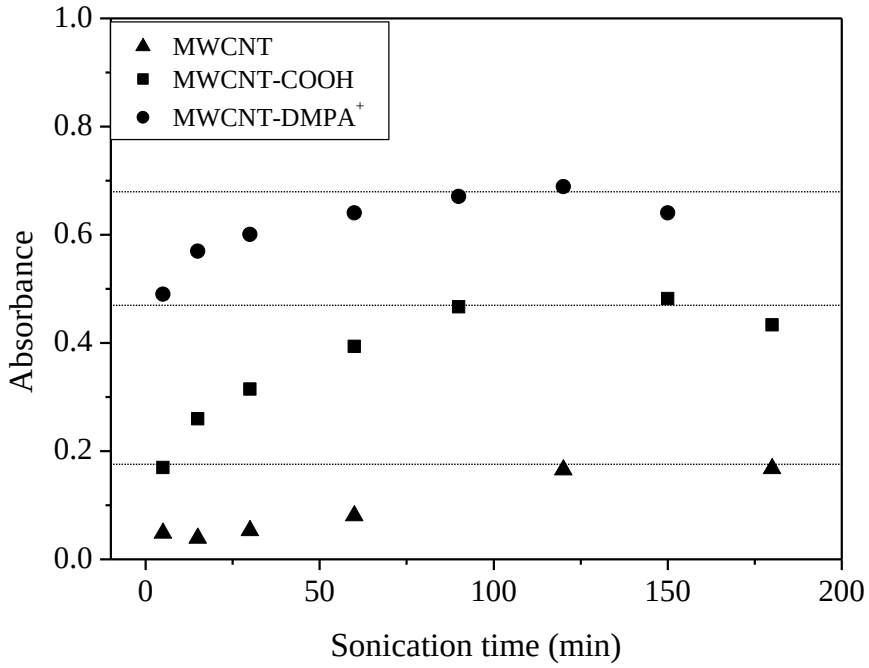

Figure 6.6 Influence of sonication time on dispersion state of MWCNT in DMF (1.5 wt% in DMF, diluted by a factor of 150 after sonication)

To visualize the dispersion states of MWCNTs, we further utilized TEM to compare the dispersibility of pristine MWCNTs, MWCNT-COOH, and MWCNT-$DMPA^+$. The MWCNT samples were dispersed in DMF, subsequently cast on a carbon-coated TEM grid, and dried in air. **Figure 6.7** displays representative TEM images of three types of MWCNTs. **Figure 6.7**(a) indicated that MWCNT-$DMPA^+$ exhibited a homogenous dispersion in DMF. Individual CNTs uniformly dispersed in DMF. Although MWCNT-COOH also displayed dispersed CNTs in **Figure 6.7** (b), TEM zoom-in image clearly showed bundles of CNTs. In sharp contrast, pristine MWCNTs showed large aggregates with a diameter of approximately 1 μm, as shown in **Figure 6.7** (c). The enhanced dispersibility of MWCNT-$DMPA^+$ was attributed to a good solvation of the hydrophilic ammonium cation and bromide anion in DMF. Bo and Yu et al. investigated the influence of anions on the solubility of MWCNTs functionalized with imidazolium-based ionic liquids. They found that the functionalized MWCNTS possessed switchable solubility due to the solvation effect of different anions.[32]

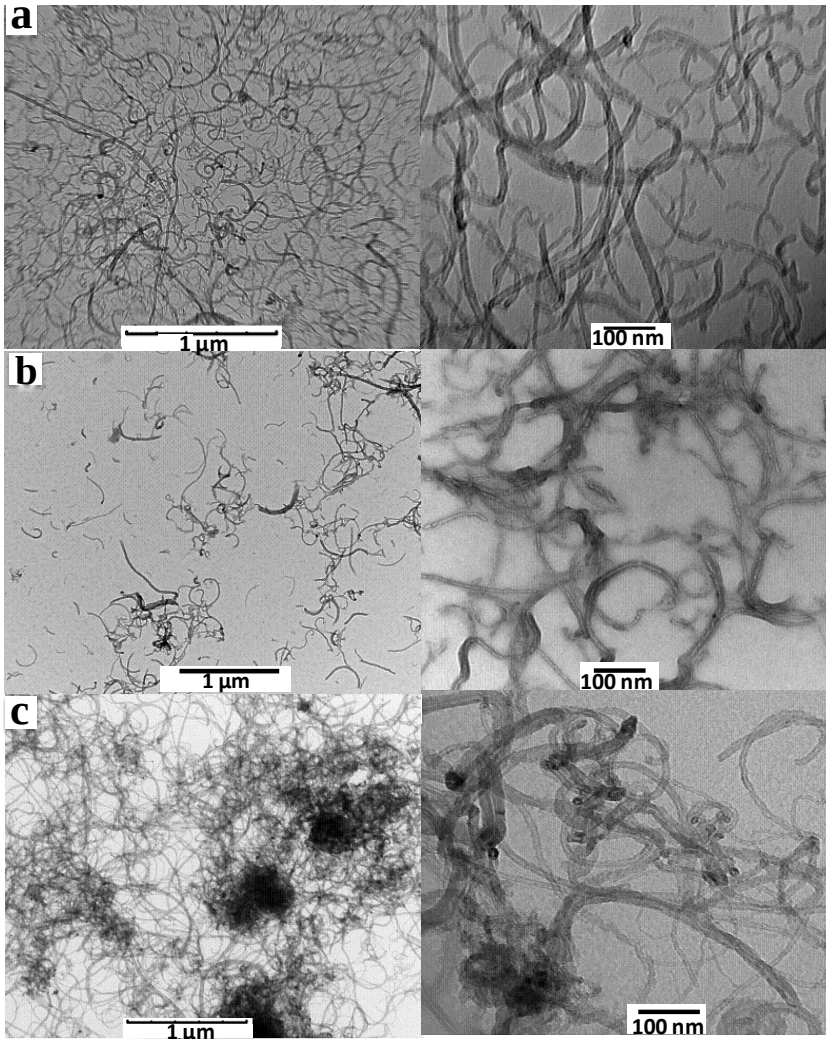

Figure 6.7 TEM images of MWCNT-DMPA$^+$ (a), MWCNT-COOH (b), and pristine MWCNT (c) (cast on copper mesh from 0.005 wt% solution in DMF; dried in air)

6.4.4 Characterization of sulfonated polyurethane/MWCNT-DMPA$^+$ composites

We prepared a series of sulfonated polyurethane composites with a content of MWCNT-DMPA$^+$ ranging from 0.5 to 5 wt%. Pristine MWCNTs were also used to prepare composite films for comparative purposes. The dispersion of pristine MWCNTs and MWCNT-DMPA$^+$ in sulfonated polyurethane matrices was initially investigated using FESEM. **Figure 6.8** (A, B) shows the FESEM images of the cross-section of a sulfonated polyurethane film with 5 wt% MWCNT-DMPA$^+$. We observed that the MWCNT-DMPA$^+$ protruded from the cross-section,

and the nanotubes were uniformly dispersed in the sulfonated polyurethane matrix, without significant carbon nanotube aggregates or bundles. However, FESEM images of a sulfonated polyurethane film with 5 wt% pristine MWCNTs (**Figure 6.8**, C) revealed significant amounts of carbon nanotube aggregates. The image in **Figure 6.8** (D) also indicated a poor dispersion of the pristine MWCNTs in the sulfonated polyurethane matrix.

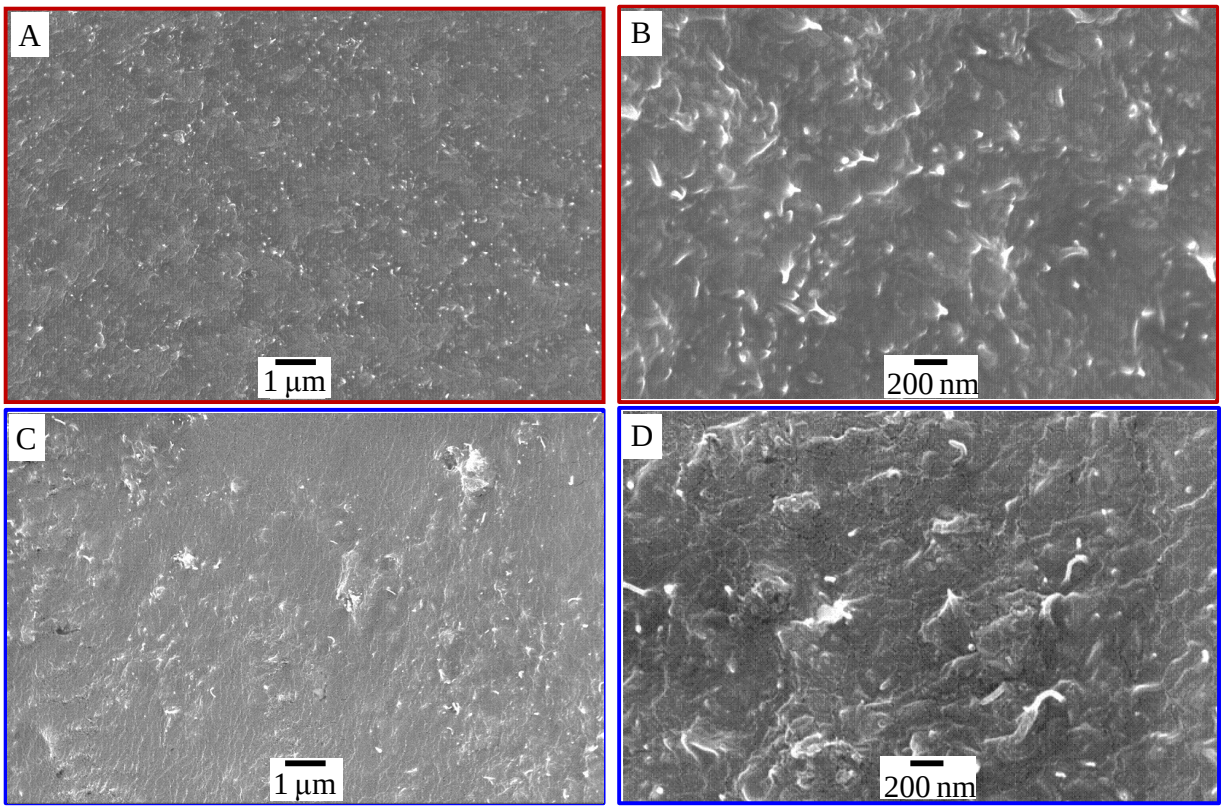

Figure 6.8 FESEM images of 5 wt% of MWCNT-DMPA$^+$ (A, B) and pristine MWCNT (C, D) in SPU matrix

TEM also probed the dispersion of carbon nanotubes in composite samples. All samples for TEM experiments were cryo-ultramicrotomed into a thickness of 100 nm. TEM images in **Figure 6.9** compared the dispersion of pristine MWCNTs and MWCNT-DMPA$^+$ in the sulfonated polyurethane matrix. As shown in **Figure 6.9** (A, B), both 5 wt% and 2 wt% MWCNT-DMPA$^+$ were uniformly dispersed in the sulfonated polyurethane matrix without

aggregates or bundles. We clearly observed many individual nanotubes. As expected, more individual tubes were observed for a 5 wt% MWCNT-DMPA$^+$ sample than 2 wt%. In contrast, **Figure 6.9**(C, D) demonstrated that the pristine MWCNTs, both 5 wt% and 2 wt%, possessed significant nanotube aggregates and bundles, although some individual nanotubes were also observed. It is worth mentioning that TEM observations agreed with FESEM. Both techniques proved that MWCNT-DMPA$^+$ performed enhanced dispersibility in the sulfonated polyurethane matrix compared with the pristine MWCNTs. This was attributed to ionic-dipole and dipole-dipole interactions between the ammonium salt on the MWCNT surface and the sulfonate charge on the polyurethane backbone. In addition, we utilized the nanotube DMF solution to prepare the composite films, thus the enhanced dispersibility of MWCNT-DMPA$^+$ in DMF also contributed to uniform dispersion in the sulfonated polyurethane matrix.

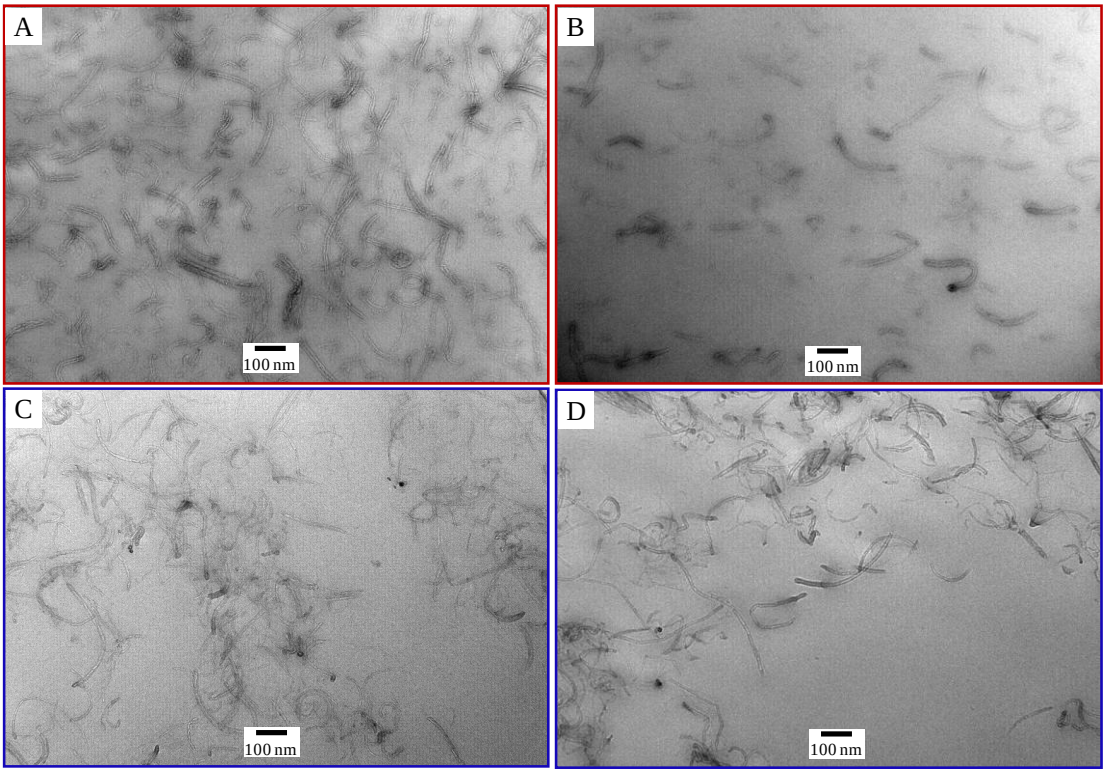

Figure 6.9 TEM images of MWCNT-DMPA$^+$ (A: 5 wt%, B: 2 wt%) and pristine MWCNTs (C: 5 wt%, D: 2 wt%) in SSSPU matrix (sample cryo-microtomed)

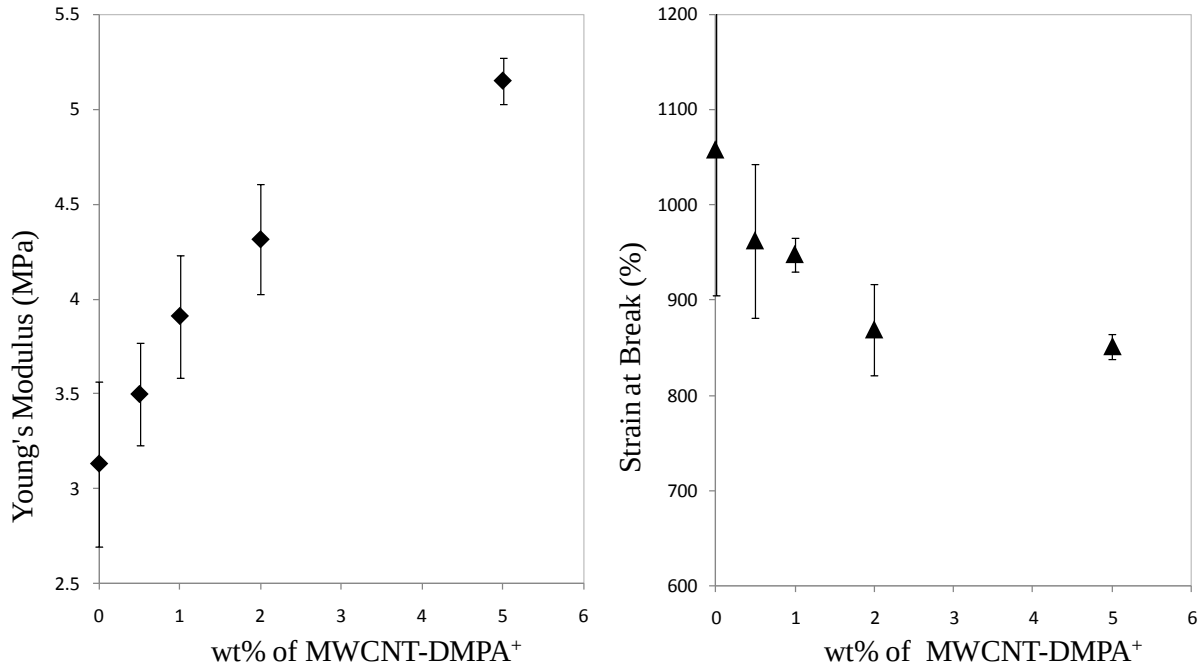

Figure 6.10 Tensile properties of SPU films with 0, 0.5, 1, 2, and 5 wt% of MWCNT-DMPA$^+$

The influence of MWCNT-DMPA$^+$ on the mechanical properties of the sulfonated polyurethane composites was investigated using tensile testing. The Young's modulus was calculated from the slope of the initial stress-strain curve, and three different specimens were averaged. The plots in **Figure 6.10** elucidated the influence of MWCNT-DMPA$^+$ on the Young's modulus and the tensile strain at break of the sulfonated polyurethane matrix. The efficiency of carbon nanotubes in reinforcing mechanical properties of matrix polymers depends strongly on the dispersion homogeneity. Aladyshev et al. investigated the influence of MWCNT content on Young's moduli of a isotactic polypropylene (iPP) matrix.[33] The Young's modulus of iPP increased by 37% at 2.1 wt% MWCNT content and subsequently dropped at a content of 3.5 wt%, which was attributed to nanotube agglomeration. Herein, the Young's modulus linearly increased from 3.1 MPa to 5.2 MPa as 5 wt% MWCNT-DMPA$^+$ was incorporated into the polyurethane matrix. This observation indicated a good dispersion of carbon nanotubes in

sulfonated polyurethanes.[34] In addition, the tensile strain at break decreased from 1058±152% to 850±11% with an increase of MWCNT-DMPA$^+$ content to 5 wt%. In review of the experimental error, the difference in ultimate elongation was attributed to sample heterogeneity arising from the sample preparation process.

6.5 Conclusions

MWCNTs were for the first time covalently modified with ammonium salts using a dendritic functionalization strategy. Successful covalent modification of MWCNTs and formation of ammonium salts were verified using TGA and XPS, which showed systemically increased weight loss and unique Br 3d (70 eV) and Br 3p (190 eV) peaks, respectively. Moreover, Raman spectroscopy and AFM demonstrated that the dendritic functionalization strategy introduced minimal destruction to the nanotube structure, which showed no increase in D_a/G_a ratio in Raman spectra and well-defined nanotube structure in AFM. Significantly enhanced dispersibility of ammonium-functionalized MWCNTs relative to pristine MWCNTs was demonstrated using optical microscopy, TEM, and FESEM. 5 wt% and 2 wt% ammonium-functionalized MWCNTs uniformly dispersed as individual tubes in both DMF and a sulfonated polyurethane matrix with mild sonication conditions. In contrast, pristine MWCNTs at a same content showed significant amounts of aggregates and bundles of carbon nanotubes. The enhanced dispersibility of ammonium-functionalized MWCNTs was attributed to a good solvation of surface-bound ammonium cations and mobile bromide anions in DMF and intermolecular ionic interactions between ammonium cations with the sulfonate anions in polyurethane matrices. Additionally, dendritic ammonium-functionalized MWCNTs linearly increased Young's modulus of the polyurethane matrix from 3.1to 5.2 MPa as 5 wt% MWCNT-$DMPA^+$ was incorporated. This suggested a good dispersion of ammonium-functionalized MWCNTs in the polyurethane matrix.

6.6 Acknowledgements

This material is based upon work supported in part by the Bayer MaterialScience, and we thank Karl Haider and Serkan Unal for insightful discussions. Aspects of this work were carried out using instruments in the Nanoscale Characterization and Fabrication Laboratory (NCFL) operated by Institute for Critical Technology and Applied Science (ICTAS) at Virginia Tech.

6.7 References

1. Iijima, S. *Nature* 1991, *354*, 56.
2. Pop, E.; Mann, D.; Wang, Q.; Goodson, K.; Dai, H. J. *Nano Lett.* 2006, *6*, 96.
3. Takesue, I.; Haruyama, J.; Kobayashi, N.; Chiashi, S.; Maruyama, S.; Sugai, T.; Shinohara, H. *Phys. Rev. Lett.* 2006, *96*, 057701/1.
4. Yu, M. F.; Lourie, O.; Dyer, M. J.; Moloni, K.; Kelly, T. F.; Ruoff, R. S. *Science* 2000, *287*, 637.
5. Moniruzzaman, M.; Winey, K. I. *Macromolecules* 2006, *39*, 5194.
6. Bokobza, L. *Polymer* 2007, *48*, 4907.
7. Fukushima, T.; Kosaka, A.; Yamamoto, Y.; Aimiya, T.; Notazawa, S.; Takigawa, T.; Inabe, T.; Aida, T. *Small* 2006, *2*, 554.
8. Bose, S.; Khare, R. A.; Moldenaers, P. *Polymer* 2010, *51*, 975.
9. Kim, J. Y.; Kim, D. K.; Kim, S. H. *Eur. Polym. J.* 2009, *45*, 316.
10. Rasheed, A.; Dadmun, M. D.; Ivanov, I.; Britt, P. F.; Geohegan, D. B. *Chem. Mater.* 2006, *18*, 3513.
11. Zhu, J.; Kim, J. D.; Peng, H. Q.; Margrave, J. L.; Khabashesku, V. N.; Barrera, E. V. *Nano Lett.* 2003, *3*, 1107.
12. Lin, Y.; Zhou, B.; Fernando, K. A. S.; Liu, P.; Allard, L. F.; Sun, Y. P. *Macromolecules* 2003, *36*, 7199.
13. Star, A.; Stoddart, J. F.; Steuerman, D.; Diehl, M.; Boukai, A.; Wong, E. W.; Yang, X.; Chung, S. W.; Choi, H.; Heath, J. R. *Angewandte Chemie-International Edition* 2001, *40*, 1721.
14. Chen, R. J.; Zhang, Y. G.; Wang, D. W.; Dai, H. J. *J. Am. Chem. Soc.* 2001, *123*, 3838.
15. Leger, B.; Menuel, S.; Landy, D.; Blach, J. F.; Monflier, E.; Ponchel, A. *Chem. Commun.* 2010, *46*, 7382.
16. Mansky, P.; Liu, Y.; Huang, E.; Russell, T. P.; Hawker, C. J. *Science* 1997, *275*, 1458.
17. Hong, C. Y.; You, Y. Z.; Pan, C. Y. *Chem. Mater.* 2005, *17*, 2247.
18. Kong, H.; Gao, C.; Yan, D. Y. *J. Am. Chem. Soc.* 2004, *126*, 412.
19. Park, M. J.; Lee, J. K.; Lee, B. S.; Lee, Y. W.; Choi, I. S.; Lee, S. G. *Chem. Mater.* 2006, *18*, 1546.
20. Luong, J. H. T.; Hrapovic, S.; Liu, Y. L.; Yang, D. Q.; Sacher, E.; Wang, D. S.; Kingston, C. T.; Enright, G. D. *J. Phys. Chem. B* 2005, *109*, 1400.
21. Liu, J.; Rinzler, A. G.; Dai, H. J.; Hafner, J. H.; Bradley, R. K.; Boul, P. J.; Lu, A.; Iverson, T.; Shelimov, K.; Huffman, C. B.; Rodriguez-Macias, F.; Shon, Y. S.; Lee, T. R.; Colbert, D. T.; Smalley, R. E. *Science* 1998, *280*, 1253.

22. Kim, K. T. J., Won Ho *Carbon* 2011, *49*, 819.
23. Shim, M.; Javey, A.; Kam, N. W. S.; Dai, H. J. *J. Am. Chem. Soc.* 2001, *123*, 11512.
24. Chang, D. W.; Jeon, I. Y.; Baek, J. B.; Dai, L. M. *Chem. Commun.* 2010, *46*, 7924.
25. Aviles, F.; Cauich-Rodriguez, J. V.; Moo-Tah, L.; May-Pat, A.; Vargas-Coronado, R. *Carbon* 2009, *47*, 2970.
26. Dresselhaus, M. S.; Dresselhaus, G.; Jorio, A. *Journal of Physical Chemistry C* 2007, *111*, 17887.
27. Salavagione, H. J.; Martinez, G.; Ballesteros, C. *Macromolecules* 2010, *43*, 9754.
28. de Zevallos-Marquez, A. M. O.; Brasil, M. J. S. P.; Iikawa, F.; Abbaspourrad, A.; Verissimo, C.; Moshkalev, S. A.; Alves, O. L. *J. Appl. Phys.* 2010, *108*.
29. Repalle, S.; Chen, J. H.; Drozd, V.; Choi, W. *J. Phys. Chem. Solids* 2010, *71*, 1150.
30. Rao, A. M.; Jorio, A.; Pimenta, M. A.; Dantas, M. S. S.; Saito, R.; Dresselhaus, G.; Dresselhaus, M. S. *Phys. Rev. Lett.* 2000, *84*, 1820.
31. Yu, J.; Grossiord, N.; Koning, C. E.; Loos, J. *Carbon* 2007, *45*, 618.
32. Yu, B.; Zhou, F.; Liu, G.; Liang, Y.; Huck, W. T. S.; Liu, W. M. *Chem. Commun.* 2006, 2356.
33. Koval'chuk, A. A.; Shchegolikhin, A. N.; Shechenko, V. G.; Nedorezova, P. M.; Klyamkina, A. N.; Aladyshev, A. M. *Macromolecules* 2008, *41*, 3149.
34. Halpin, J. C.; Kardos, J. L. *Polym. Eng. Sci.* 1976, *16*, 344.

Chapter 7: Ion-Containing Segmented Polyurethane Chain-Extended with Imidazolium Diol-based Ionic Liquids

Gao, R.; Zhang, M.; Wang, S.; Moore, R.B.; Colby, R.H.; Long, T.E. (*prepared for publication*)

7.1 Abstract

Novel polyurethane ionomers containing imidazolium cations in the hard segments were synthesized using an imidazolium diol-based ionic liquid chain extender. Upon comparison with a nonionic polyurethane analogue, we systematically investigated the influence of imidazolium cation on physical properties, hydrogen bonding, and morphologies of segmented polyurethanes. Differential scanning calorimetry (DSC) revealed that imidazolium-containing polyurethane showed reduced hard segment crystallinity relative to the nonionic polyurethane analogue, which was presumably due to the ionic association and disrupted hard segment regularity. Observation in DSC was consistent with wide angle X-ray diffraction (WAXD). Moreover, dynamic mechanical analysis (DMA) indicated that imidazolium-containing polyurethane exhibited a more well-defined rubber plateau with a higher modulus. Tensile analysis also revealed a higher Young's modus for imidazolium-containing polyurethane than nonionic polyurethane analogue. Although both samples displayed well-defined microphase-separated morphology in atomic force microscopy(AFM), imidazolium-containing segmented polyurethane showed a higher degree of hydrogen bonding and better microphase separation, as evidenced in Fourier transform infrared (FTIR) spectroscopy and small angle X-ray scattering (SAXS), respectively. Moreover, dielectric relaxation spectroscopy demonstrated that imidazolium-containing polyurethane and nonionic polyurethane analogue exhibited comparable ionic conductivity at low temperatures; however, imidazolium-containing polyurethane displayed significantly enhanced ionic

conductivity at higher temperatures (>80 ^{o}C) due to the presence of imidazolium chloride ions in the hard segments.

7.2 Introduction

Segmented polyurethane is one of the most versatile polymers that exhibit a wide range of physical properties due to microphase separation of soft and hard segments.[1-5] Incorporation of ions into polyurethanes generates novel polyurethane ionomers.[6-9] Due to unique combination of hydrogen bonding, ionic, and hydrophobic interactions, polyurethane ionomers possess interesting physical properties that are suitable for many applications.[8,10] Compared to nonionic polyurethanes, polyurethane ionomers display superior mechanical properties due to better microphase separation.[3,11,12] However, many factors influence microphase separation of segmented polyurethanes, including ion type, ion placement, ion density, segment block length, chemical compositions and compatibility between soft and hard segments.[13-21] Another important advantage of polyurethane ionomers over nonionic polyurethane is their enhanced dispersibility in water.[22-28] Water dispersible polyurethanes are attractive materials that can be processed in an environmentally friendly way.[29]

Cation-containing polyurethanes, or polyurethane cationomers are an important class of polyurethane ionomers, which have found wide applications in protective coatings, biocides, antistatic agents, antimicrobial nano-filters, and polymeric colorants.[22,30-32] A typical synthesis of polyurethane cationomers involves the usage of tertiary amine-containing diol as the chain extender and a subsequent alkylation of tertiary amine to generate ammonium cations. For example, Cooper et al. synthesized polyurethane cationomers with pendant ammonium cations using 3-diethylamino-1,2-propanediol as the chain extender.[14] These polyurethane cationomers exhibited enhanced microphase separation, leading to better mechanical properties. However, a

general concern for ammonium-containing polymers is their poor thermal and chemical instability due to the potential Hofmann-type elimination.[33] Thus, replacement of ammonium with more stable cations is necessary to improve performance of polyurethane cationomers.

Imidazolium-based ionic liquids, which are organic salts with melting temperatures below 100 ^{o}C, possess high electrochemical and thermal stability and good ionic conductivity.[34-37] Thus, imidazolium-diol based ionic liquid can potentially serve as superior alternative for ammonium-based chain extender. In addition, researchers have determined that imidazolium-containing polymers are suitable for ion-conductive materials.[38-42] In the present study, imidazolium-diol based ionic liquid was synthesized and utilized as the chain extender to prepare segmented polyurethane cationomers. This imidazolium monomer strategy provided well-defined polyurethane cationomers with imidazolium chloride ions readily incorporated into the hard segments. Upon a systematic comparison with a nonionic polyurethane analogue, we investigated the influence of imidazolium cation on thermal and mechanical properties, hydrogen bonding, and morphologies of polyurethane cationomers.

7.3 Experimental

Material. 2-chloroethanol (99%), imidazole (>99%), anhydrous *N*,*N*-dimethylformamide (DMF) (99.8%), and sodium (99%) were purchased from Aldrich and used as received. Poly(tetramethylene oxide) (PTMO) (M_n=2000 g/mol) was purchased from Aldrich and dried at 60 ^{o}C *in vacuo* overnight immediately prior to use. Calcium hydride (92%) was purchased from Alfa Aesar and used as received. The chain extender *1,4*-butanediol (BD) (99%) was purchased from Aldrich and distilled from calcium hydride. 1,4-Diazabicyclo[2.2.2]octane (DABCO) (>99%) was purchased from Aldrich and diluted to 1 wt% using anhydrous tetrahydrofuran. Ethanol (200 Proof) was distilled from calcium hydride. Chloroform (Optima grade) and

methanol (HPLC grade) were purchased from Fisher Scientific and used as received. Dicyclohexylmethane-*4,4'*-diisocyanate (HMDI) (99.5%) was kindly provided by Bayer MaterialScience and used as received.

Synthesis of 1,3-di(2-hydroxyethyl) imidazolium chloride

In a three-necked, round-bottomed flask equipped with a stir bar and condenser, ethanol (100 mL) was added and cooled to 0 ^{o}C with an ice bath. Sodium (4.70 g, 0.20 mol) was subsequently added to the flask and stirred with ethanol for 7 h at 0 ^{o}C. In a following step, imidazole (13.61 g, 0.20 mol) was slowly added to the flask. The mixture was warmed to 23 ^{o}C for 7 h and then cooled to 0 ^{o}C. 2-Chloroethanol was subsequently added dropwise, and the reaction was allowed to proceed for 7 h at 0 ^{o}C and additional 48 h at 50 ^{o}C. The reaction solution was filtered to remove sodium chloride side product, and the clear solution was precipitated in ethyl ether. The crude product was purified using chromatography with chloroform/methanol (80/20) on silica gel. The final product was obtained as a white solid. ^{1}H NMR: (400 MHz, CD_3OD, 23 ^{o}C) (δ, ppm): 8.75(H_a, s, 1H), 7.44(H_b, s, 2H), 4.22(H_c, t, 4H), 3.83(H_d, t, 4H). FAB MS: M^{+}=157.10 (found), molar mass=175.10 (calcd). Melting point=49 ^{o}C.

Synthesis of Imidazolium-Containing Segmented Polyurethanes

The synthesis was conducted in a three-necked, round-bottomed flask equipped with an addition funnel, nitrogen inlet, and an overhead mechanical stirrer. Following a typical two-step synthetic route as described previously,[43] PTMO (7.00 g, 3.5 mmol) was initially end-capped with HMDI (2.75 mL, 11.1 mmol) at 80 ^{o}C for 4 h using DABCO (50 ppm) as the catalyst. In the second step, 1,3-di(2-hydroxyethyl) imidazolium chloride (15 wt% solids) was dissolved in anhydrous DMF and added dropwise to the prepolymers. The reaction was allowed to proceed

for 24 h at 80 ^{o}C under a N_2 atmosphere. FTIR spectroscopy demonstrated complete consumption of the isocyanate groups. A nonionic PU analogue was synthesized in a similar manner except that *1,4*-butanediol was used as the chain extender. The polyurethane solutions were directly cast in Teflon® molds and air-dried at 23 ^{o}C for 72 h with a relative humidity (RH) of 31% to form solid membranes. The resulting membranes were subsequently annealed *in vacuo* at 110 ^{o}C for 30 min and 60 ^{o}C for additional 72 h.

Instrumentation

^{1}H NMR spectroscopy was performed on a Varian INOVA 400 MHz spectrometer using CD_3OD as the solvent. FAB-MS was obtained on a JEOL HX110 dual-focusing mass spectrometer. Differential scanning calorimetry (DSC) was performed using a TA Instruments Q2000 differential scanning calorimeter under a nitrogen flow of 50 mL/min with a heating rate of 10 ^{o}C/min. Dynamic mechanical analysis (DMA) measurements were performed on a TA Instruments Q800 dynamic mechanical analyzer in the film tension mode at a frequency of 1 Hz and a temperature ramp of 3 ^{o}C/min over the range -80 to 120 ^{o}C. Tensile analysis was performed on a 5500R Instron universal testing instrument with a cross-head rate of 50 mm/min at ambient conditions. FTIR experiments were carried out using a Varian 670-IR spectrometer (DTGS detector). The spectra were collected at a resolution of 4 cm^{-1}, and 32 scans were averaged. Atomic force microscopy (AFM) was conducted on a Veeco MultiMode AFM in a tapping mode at ambient conditions. SAXS and wide angle X-ray diffraction (WAXD) were performed using a Rigaku S-Max 3000 3 pinhole SAXS system equipped with a rotating anode emitting X-rays with a wavelength of 0.154 nm (Cu Kα). Scattering from a silver behenate standard was used to calibrate the sample-to-detector distance. For SAXS, the sample-to-detector distance was 1603 mm, and for WAXD, the sample-to-detector distance was 82.5 mm. Two-

dimensional SAXS patterns were obtained using a fully integrated 2D multi-wire, proportional counting, gas-filled detector during an exposure time of 1 h per sample. SAXS data were corrected for sample thickness, sample transmission, and background scattering. WAXD two-dimensional diffraction patterns were obtained using an image plate with an exposure time of 1 h. All SAXS/WAXD data were analyzed using the SAXSGUI software package to obtain radially integrated SAXS/WAXD intensity versus scattering vector q (SAXS) or 2θ (WAXD) profiles, where $q=4\pi\sin(\theta)/\lambda$, θ is half of the scattering angle, and λ is the X-ray wavelength. WAXD data were corrected for sample thickness, and the profiles were vertically shifted to facilitate a comparison of peak positions. Dielectric relaxation spectroscopy was conducted on a Novo-control GmbH Concept 40 broadband dielectric spectrometer. Samples were dried at 45 ^{o}C under vacuum before measurement. All sample membranes were sandwiched between two 20 mm diameter freshly polished brass electrodes. Dielectric (impedance) spectra were measured in the frequency range of 1×10^{-2} to 1×10^{7} Hz with 0.1 V amplitude. Samples were annealed at 100 ^{o}C in the equipment for 30 min and allowed to reach equilibrium with temperature for at least 5 min before each isothermal measurement.

7.4 Results and Discussion

7.4.1 Monomer and polymer synthesis

An imidazolium diol, 1,3-di(2-hydroxyethyl) imidazolium chloride, was synthesized according to the synthetic route described in **Scheme 7.1**. ^{1}H NMR spectroscopy (**Figure 7.1**) and FAB MS confirmed the chemical structure, and differential scanning calorimetry (DSC) verified the melting point. The synthesizing imidazolium diol was classified as an ionic liquid since its melting point (49 ^{o}C) was well below 100 ^{o}C. Moreover, the synthesizing imidazolium diol-based ionic liquid showed an onset degradation temperature at 322 ^{o}C in TGA, which was

nearly 60 ^{o}C higher than an ammonium diol analogue. Using 1,3-di(2-hydroxyethyl) imidazolium chloride as the chain extender, we synthesized a novel polyurethane cationomer through a two-step process. Post alkylation of tertiary ammine-containing polyurethanes has been a common approach to introduce ammonium cations into polyurethane structures. However, the imidazolium monomer strategy enables to synthesize well-defined polyurethane cationomers with controlled charge density and charge placement. All polyurethane solutions were cast in Teflon® molds, which resulted in optically clear films. It is also import to note that DABCO was utilized as the catalyst in the synthesis of imidazolium-containing polyurethane, rather than DBTDL. FTIR spectroscopy demonstrated that polymerization with DABCO was complete in 24 h at 80 ^{o}C, i.e. isocyanate peaks at 2260 cm^{-1} completely disappeared. However, polymerization with DBTDL was incomplete even for 5 days at 80 ^{o}C. We hypothesize that imidazolium rings bonded to the tin catalyst and poisoned the catalyst in the polymerization with DBTDL. A systematic study is necessary to investigate the polymerization kinetic in the presence of DBTDL. For comparative purposes, a nonionic polyurethane analogue was also synthesized, which contained the sample PTMO soft segments and an equal content (83 mol%) of hard segments (**Table 7.1**). An unprecedented comparison between imidazolium-based polyurethane and nonionic polyurethane analogue elucidated the influence of imidazolium cations on physical properties and morphology of polymer cationomers.

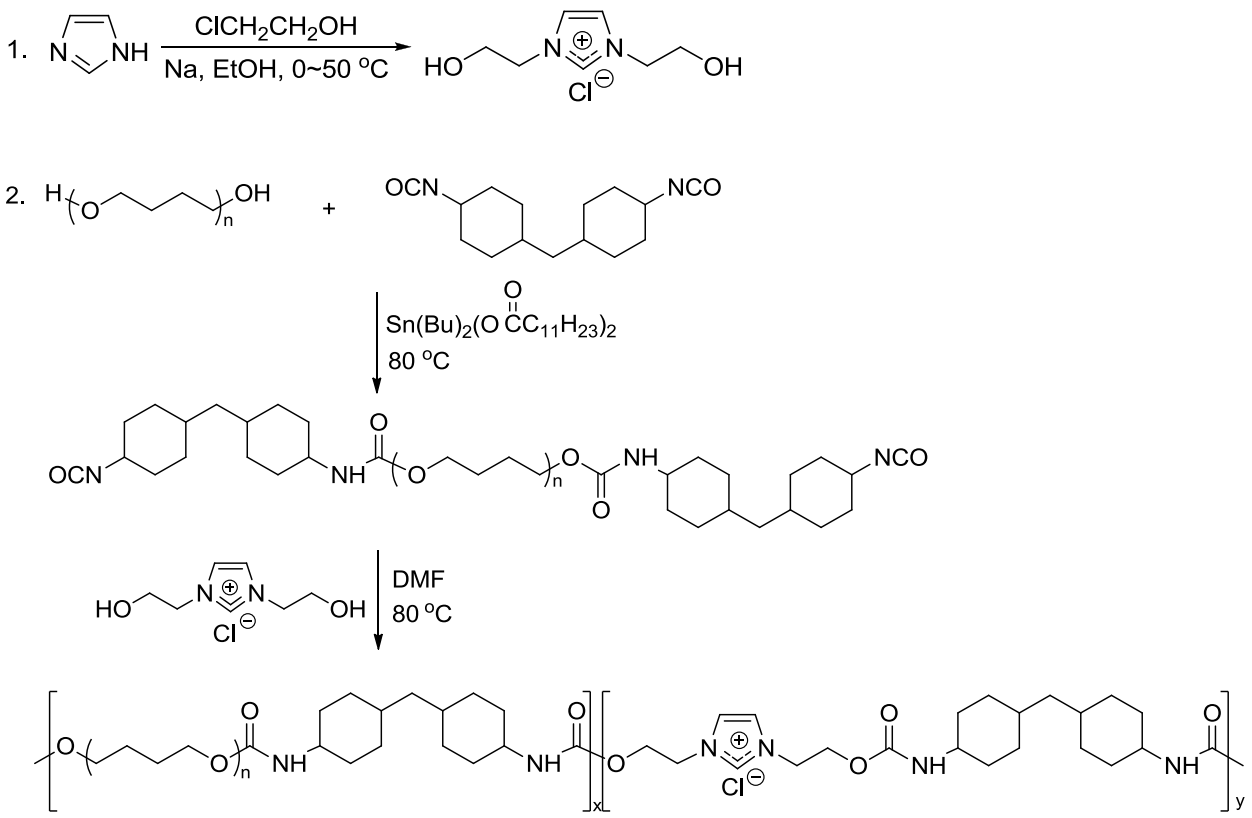

Scheme 7.1 Synthesis of 1,3-di(2-hydroxyethyl) imidazolium chloride (1) and imidazolium-containing segmented polyurethane cationomer, HMDI-IMI-2KPTMO (2)

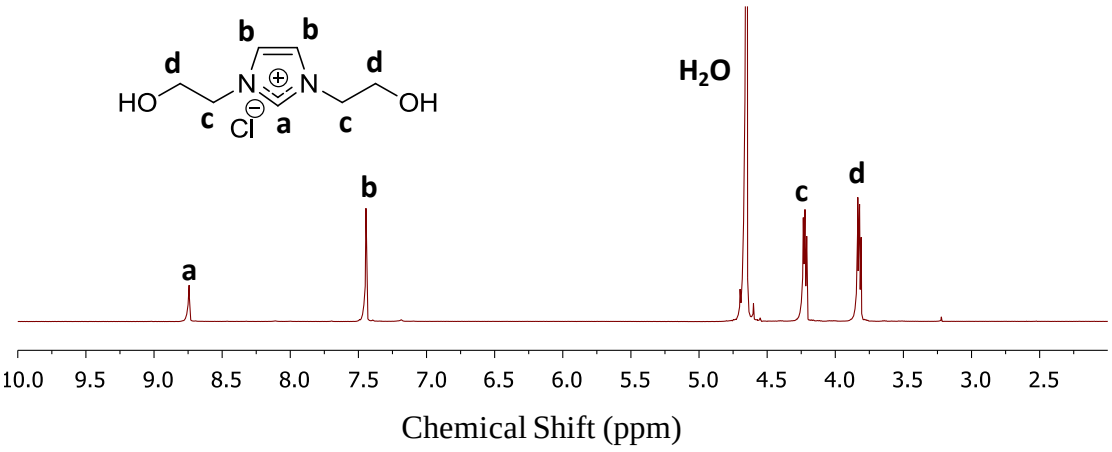

Figure 7.1 ^{1}H NMR spectrum of 1,3-di(2-hydroxyethyl) imidazolium chloride

7.4.2 Thermal properties

Thermal properties of imidazolium-containing polyurethane cationomer (HMDI-IMI-2KPTMO) and the nonionic analogue (HMDI-IMI-2KPTMO) were characterized using DSC. **Figure 7.2** shows first and second heat DSC curves of both samples. In the first heat DSC, HMDI-BD-2KPTMO exhibited an endothermic transition at 107 ^{o}C, corresponding to the melting of crystalline hard segments. In contrast, HMDI-IMI-2KPTMO did not show clear thermal transitions in the first heat DSC curve. This suggested that imidazolium cations in polyurethane hard segments suppressed hard segment crystallization, which might be due to the disrupted hard segment regularity and ionic association of imidazolium chloride ion pairs. However, the endothermic peak disappeared in the second heat DSC curve of HMDI-BD-2KPTMO, which was due to a slow recrystallization rate of rigid hard segments relatively to the DSC cooling rate (10 ^{o}C/min). In addition, second heat DSC curves of both samples displayed thermal transitions around -80 ^{o}C, corresponding to the glass transition temperature (T_g) of PTMO soft segments. PTMO soft segment T_g's were comparable to the T_g of pure PTMO homopolymers, indicating a high degree of microphase separation in both polyurethanes. HMDI-IMI-2KPTMO showed a slightly lower soft segment T_g (-82 ^{o}C) than HMDI-BD-2KPTMO (-77 ^{o}C), suggesting a slightly better microphase separation. This observation was consistent with the literature. Cooper et al. studied poly(propylene oxide) (PPO)-based polyurethane cationomers containing pendant ammonium cations in the hard segments.[11] They reported that PPO (2000 g/mol) soft segment T_g in a polyurethane cationomer was 3 ^{o}C lower than that in a nonionic polyurethane analogue.

Table 7.1 Chemical composition and thermal transition temperatures of HMDI-BD-2KPTMO and HMDI-IMI-2KPTMO

	HMDI/Diol/PTMO	HS (mol%)	HS (wt%)	T_g (^oC)	T_m (^oC)
HMDI-BD-2KPTMO	3/2/1	83	33	-77	107*
HMDI-IMI-2KPTMO	3/2/1	83	37	-82	ND

*data obtained from first heat DSC. ND=not detected

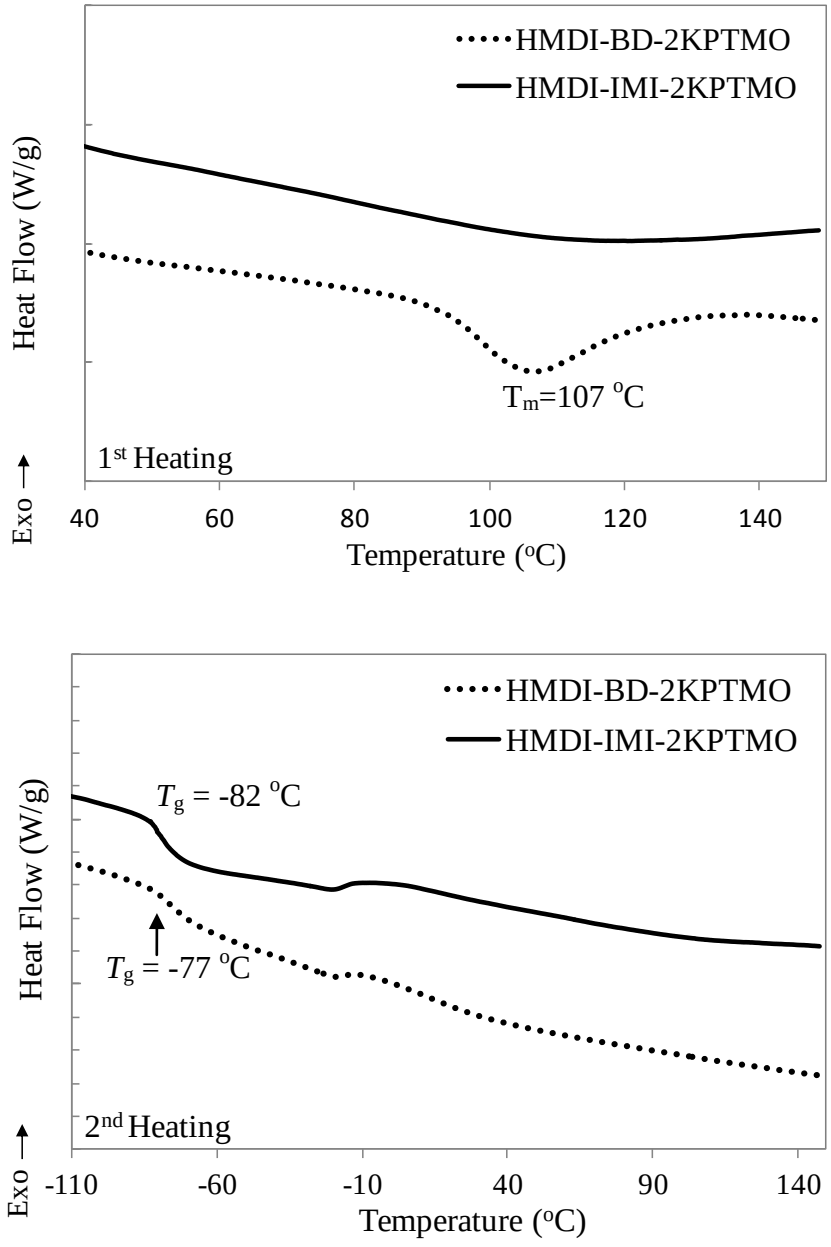

Figure 7.2 DSC traces of HMDI-BD-2KPTMO and HMDI-IMI-2KPTMO (1st heating, 10 ^oC/min, He; 2nd heating, 10 ^oC/min, He)

7.4.3 Thermomechanical properties

Dynamic mechanical (DMA) studies on imidazolium-based polyurethane cationomer and the nonionic polyurethane analogue elucidated the influence of imidazolium cation on thermomechanical properties. **Figure 7.3** depicts the storage modulus (G') and tan delta (tan δ) of two polyurethane samples as a function of temperature. In the tan δ curves, both HMDI-IMI-2KPTMO and HMDI-BD-2KPTMO exhibited maxima at -59 ^{o}C and -48 ^{o}C, respectively. This transition corresponded to the PTMO soft segment T_g. HMDI-IMI-2KPTMO displayed a narrower glass transition at a lower temperature relative to HMDI-BD-2KPTMO, which might be due to a better microphase separation in HMDI-IMI-2KPTMO. In addition, HMDI-BD-2KPTMO displayed a second tanδ peak at 25 ^{o}C, which was attributed to the melting of crystalline PTMO soft segments. Due to the low degree of crystallinity of PTMO soft segments, this transition was very broad in DMA tanδ curve and even invisible in the second heat DSC curve. In the storage modulus curves, both polyurethane samples displayed well-defined rubbery plateau ranging from -50 ^{o}C to 100 ^{o}C. However, HMDI-IMI-2KPTMO showed a much higher rubbery modulus (68 MPa at 25 ^{o}C) than HMDI-BD-2KPTMO (21 MPa at 25 ^{o}C). DMA results agreed well with tensile analysis data shown below. In addition, HMDI-IMI-2KPTMO showed a higher onset flow temperature (~150 ^{o}C) compared to HMDI-BD-2KPTMO, which was presumably due to the presence of imidazolium chloride ion associations.

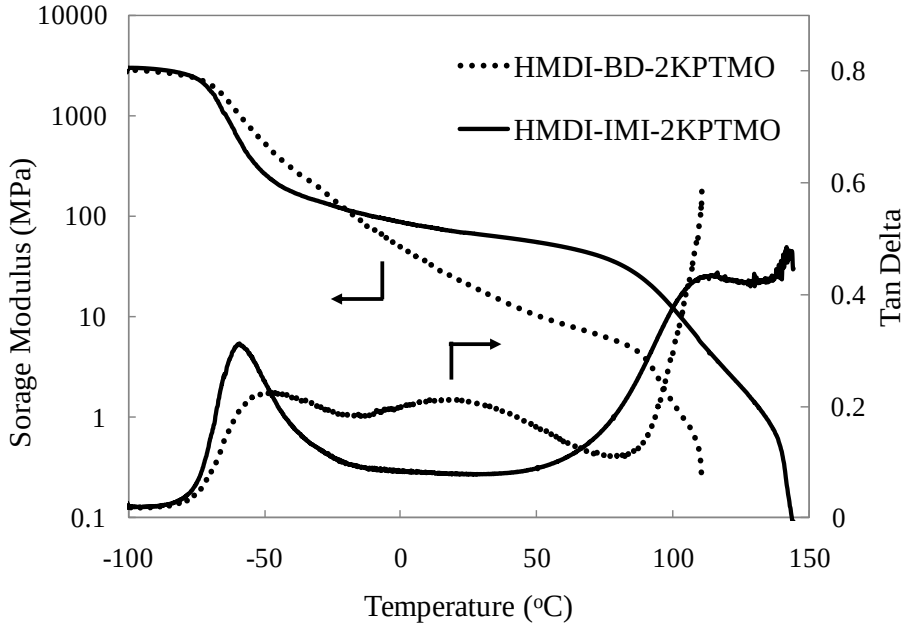

Figure 7.3 DMA curves of HMDI-BD-2KPTMO and HMDI-IMI-2KPTMO (film tension mode, 3 ^{o}C/min, 1 Hz, air)

7.4.4 Mechanical properties

Mechanical properties of imidazolium-based polyurethane cationomer and the nonionic polyurethane analogue were further evaluated with uniaxial tress-strain tensile analysis. **Figure 7.4** shows the stress-strain curves for both HMDI-BD-2KPTMO and HMDI-IMI-2KPTMO. The slope of the initial stress-strain curve (<2.5 % elongation) provided the Young's moduli of two polyurethane samples. It is clear that HMDI-IMI-2KPTMO exhibited a significantly enhanced Young's modulus (55.10±3.46 MPa) compared to HMDI-BD-2KPTMO, which showed a Young's modulus of 11.11±0.71MPa. This observation was consistent with DMA. The difference in Young's moduli of these polyurethanes was related to their. It is also interesting to note that the tensile strength of HMDI-BD-2KPTMO (40.19±8.07 MPa) was higher than HMDI-IMI-2KPTMO (30.32±2.24 MPa). This is presumably due to higher cohesion of crystalline hard segment in HMDI-BD-2KPTMO. In addition, HMDI-IMI-2KPTMO and HMDI-BD-2KPTMO

showed comparable ultimate elongation, which were 929±196% and 956±137%, respectively. This suggests that both samples are high molecular weight polymers.

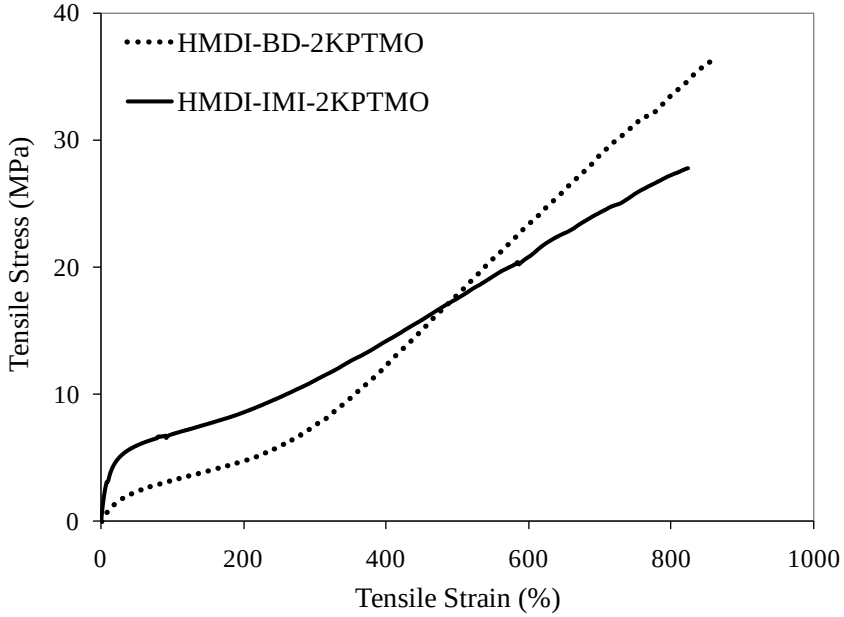

Figure 7.4 Tensile properties of HMDI-BD-2KPTMO and HMDI-IMI-2KPTMO

7.4.5 FTIR spectroscopy

Hydrogen bonding is an important driving force for microphase separation of segmented polyurethanes, which in turn, influences the thermal and mechanical properties.[44] Therefore, understanding hydrogen bonding interactions in segmented polyurethanes is important to correlate polyurethane structure and properties with their morphologies. FTIR spectroscopy is a simple and sensitive method to study hydrogen bonding in polyurethanes.[45] Hydrogen bonding acceptor "C=O" groups in polyurethanes exhibited clear peak position shift in FTIR spectra upon formation of hydrogen bonding. **Figure 7.5** shows the FTIR spectra of both HMDI-IMI-2KPTMO and HMDI-IMI-2KPTMO in the C=O region and N-H region. In the C=O region, HMDI-BD-2KPTMO displayed three distinct carbonyl peaks at 1714 cm^{-1}, 1695 cm^{-1}, and 1662 cm^{-1}, respectively. The peak at 1714 cm^{-1} was attributed to the vibration peak of free carbonyl,

and the peaks at 1695 cm^{-1} and 1662 cm^{-1} corresponded to hydrogen-bonded carbonyl. Although HMDI-IMI-2KPTMO also displayed free carbonyl peak and hydrogen bonded carbonyl peak at 1716 cm^{-1} and 1702 cm^{-1}, respectively, the hydrogen bonded carbonyl was in a much less extent. This suggests that HMDI-BD-2KPTMO possessed stronger hydrogen bonding than HMDI-IMI-2KPTMO. This observation was consistent with the literature. Our previous study demonstrated that polyurethanes with phosphonium cations in the hard segments showed significantly reduced hydrogen bonding.[10] It is also interesting to note that hydrogen bonding in these polyurethanes was related to their hard segment crystallization. HMDI-BD-2KPTMO with stronger hydrogen bonding showed clear melting peak of crystalline hard segments in the first heat DSC. In contrast, HMDI-IMI-2KPTMO with reduced hydrogen bonding showed absence of hard segment crystallization. Moreover, FTIR spectra of HMDI-BD-2KPTMO in N-H region displayed a sharper vibration peak relative to HMDI-IMI-2KPTMO. This is also indicative of stronger hydrogen bonding for HMDI-BD-2KPTMO.

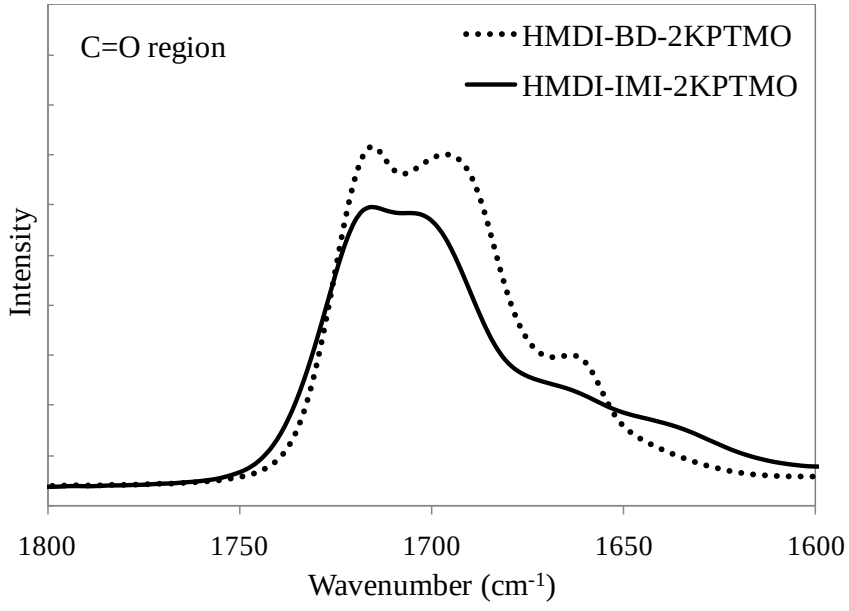

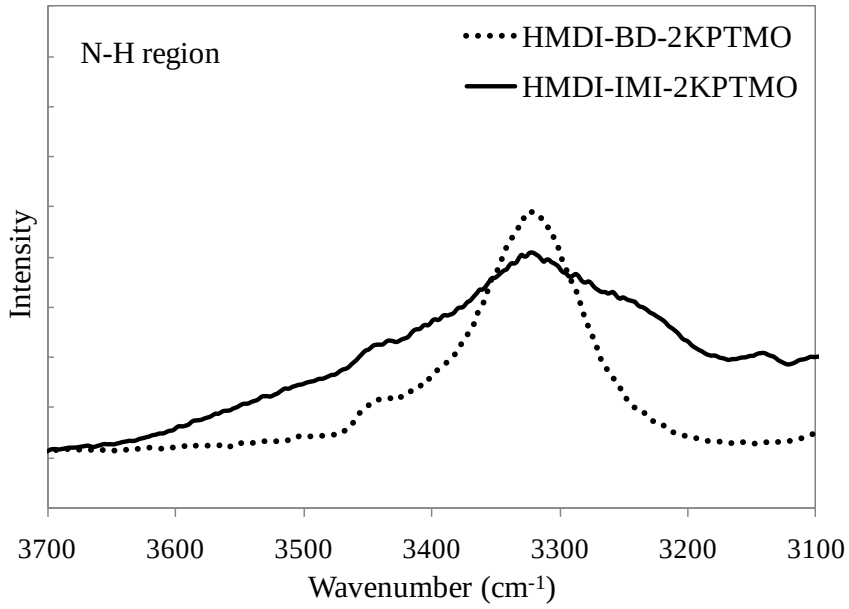

Figure 7.5 FTIR to characterization of hydrogen-bonding interactions

7.4.6 Morphological Characterization

Properties of segmented polyurethanes depend strongly on their microphase-separated morphologies. **Figure 7.6** illustrates AFM phase images of both imidazolium-containing polyurethane cationomer and the nonionic polyurethane analogue that obtained with tapping mode AFM at ambient conditions. In AFM phase images of polyurethanes, high-modulus hard domains appear as bright regions and low-T_g soft domains appear as dark regions.[43] It is clear that both HMDI-BD-2KPTMO and HMDI-IMI-2KPTMO displayed well-defined microphase-separated morphology. Polyurethane hard segments associated into needle-like hard domains at the nanoscale. These needle-like domains randomly distributed within the continuous PTMO phase and served as physical cross-links to afford polyurethane mechanical strength. In comparison of these two samples, HMDI-IMI-2KPTMO displayed hard domains that were more percolated than HMDI-BD-2KPTMO, which was responsible for an enhanced modulus as determined with DMA and tensile analysis.

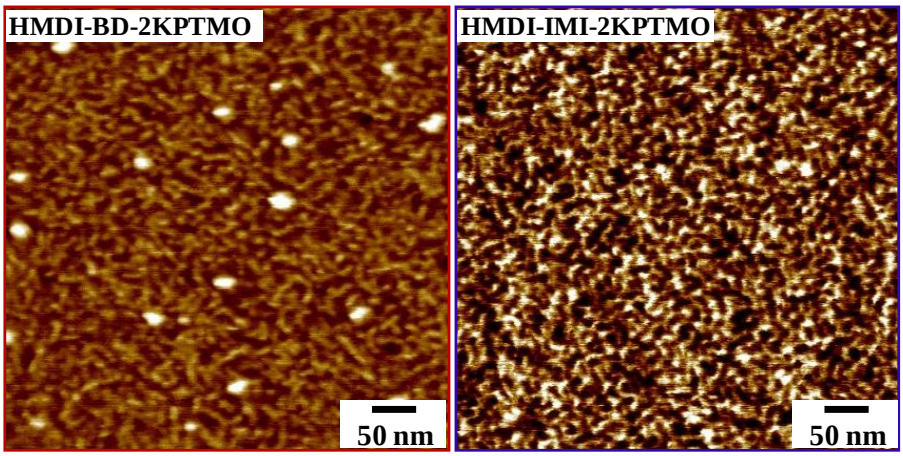

Figure 7.6 AFM phase images of HMDI-BD-2KPTMO and HMDI-IMI-2KPTMO (tapping mode, spring constant=42 N/m)

In addition to AFM, small angle X-ray scattering (SAXS) and wide angle X-ray diffraction (WAXD) provide important information on bulk morphologies of these polyurethanes. **Figure 7.7** shows their SAXS profiles plotted as scattering intensity versus scattering vector q (nm^{-1}). Both samples displayed a scattering peak near q_{max}=0.5 nm^{-1} in the profiles, which resulted from microphase separation of the soft and hard segments. Moreover, q_{max} is related to inter-domain spacing of polyurethane hard segments ($d=2\pi/q_{max}$).[46] Calculated *d* spacing of HMDI-IMI-2KPTMO and HMDI-BD-2KPTMO was 12.3 nm. Two polyurethane samples possessed comparable inter-domain spacing due to a similar hard segment content, which was 37 wt% (83 mol%) for HMDI-IMI-2KPTMO and 33 wt% (83 mol%) for HDMI-BD-2KPTMO. However, the scattering peak at q=0.5 nm^{-1} in the SAXS profile of HMDI-IMI-2KPTMO was sharper and in a higher intensity compared to that of HMDI-BD-2KPTMO, which might be due to a higher degree of microphase separation and increased electron density difference between PTMO soft phase and imidazolium ionic hard domains. HMDI-IMI-2KPTMO also displayed a weak shoulder near q=1 nm^{-1}, suggesting the presence of ionic association of imidazolium chloride ion pairs. **Figure 7.8** shows the WAXD profile for both polyurethanes, a PTMO (2000 g/mol) and a

HMDI-BD hard segment analogue. It is clear that PTMO (2000 g/mol) showed two sharp crystalline peaks at $2\theta=19.6^{o}$ and $2\theta=24.0^{o}$, and the HS analogue showed three weak crystalline peaks at $2\theta=17.6^{o}$, 18.5^{o}, and 23.5^{o}. In contrast, HMDI-IMI-2KPTMO displayed a monomodal amorphous halo peak, indicating the absence of crystalline soft and hard segments. However, HMDI-BD-2KPTMO exhibited a weak shoulder on the amorphous halo peak near $2\theta=17.6^{o}$, suggesting the presence of crystalline hard segments. WAXD results agreed well with DSC, in which only HMDI-BD-2KPTMO showed an endothermic peak at 107 ^{o}C due to the melting of crystalline hard segments.

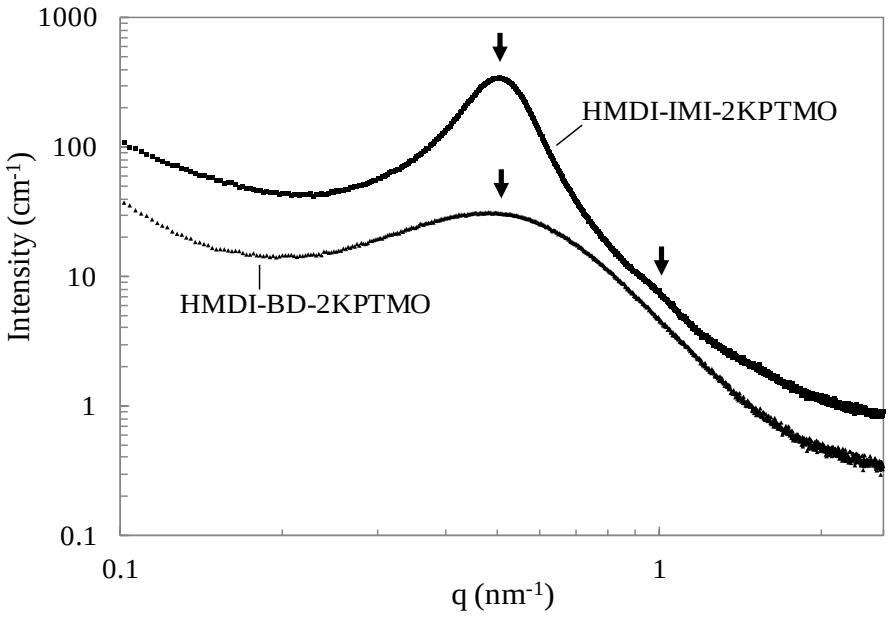

Figure 7.7 Small angle X-ray scattering traces of HMDI-BD-2KPTMO and HMDI-IMI-2KPTMO

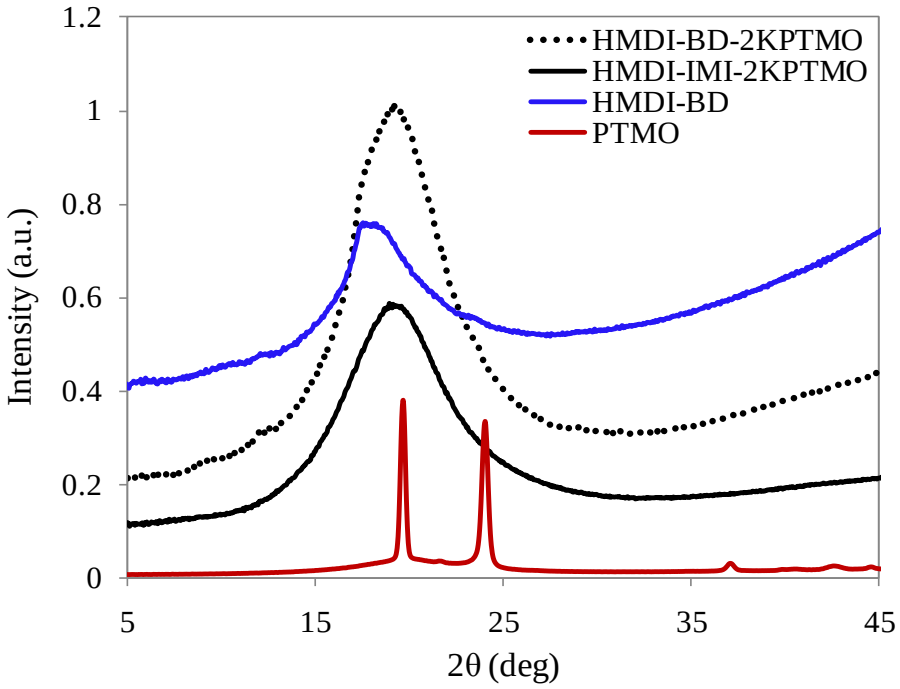

Figure 7.8 Wide angle X-ray diffraction of HMDI-BD-2KPTMO and HMDI-IMI-2KPTMO

Ionic Conductivity

Dielectric relaxation spectroscopy is a useful tool to investigate ion conduction behavior of polyurethane ionomers.[47,48] **Figure 7.9** depicts the ionic conductivity (σ) of HMDI-BD-2KPTMO and HMDI-IMI-2KPTMO as a function of temperature (T). It indicates that two samples showed comparable temperature dependence of ionic conductivity at low temperatures (<80 ^{o}C). Ionic conductivity slightly increased as temperature increased from 20 ^{o}C to 70 ^{o}C. However, ionic conductivity of HMDI-IMI-2KPTMO dramatically increased in a high temperature region (>80 ^{o}C). In contrast, HMDI-BD-2KPTMO only showed a slight increase in ionic conductivity as temperature increased from 80 ^{o}C to 100 ^{o}C. We hypothesize that the transition in ionic conductivity near 80 ^{o}C is related to the hard segment T_g. At temperatures below 80 ^{o}C, only low-T_g PTMO soft segments were mobile. Some impurities in PTMO soft segments provided the low ionic conductivity on the order of 10^{-12} S/cm. Imidazolium-containing polyurethane and nonionic polyurethane analogue contained identical nonionic

PTMO soft segments, thus, exhibited similar temperature dependence of ionic conductivity. At high temperatures above 80 ^{o}C, imidazolium chloride ions in HMDI-IMI-2KPTMO hard segments became mobile and contributed to the ion conduction, which gave a significantly increased ionic conductivity above 5×10^{-10} S/cm at 100 ^{o}C. However, HMDI-BD-2KPTMO did not possess any ions in the hard segments and showed slight increase in ionic conductivity with temperature. It is worth to point out that the transition temperature (~80 ^{o}C) in ionic conductivity agreed well with onset flow temperatures (~80 ^{o}C) of HMDI-IMI-2KPTMO, as determined in the DMA storage modulus curve. This supports our hypothesis that both transitions are related to the hard segment T_g.

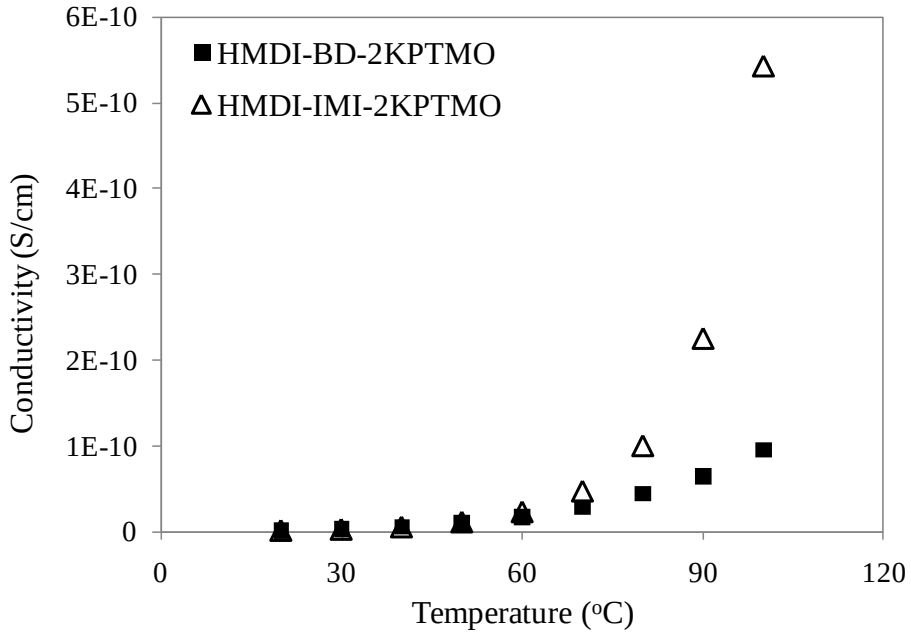

Figure 7.9 Ion-conductivity of HMDI-BD-2KPTMO and HMDI-IMI-2KPTMO

7.5 Conclusions

Novel segmented polyurethanes containing imidazolium cations in the hard segments were synthesized through a conventional prepolymer method using an imidazolium diol-based ionic liquid as the chain extender. An unprecedented comparison of imidazolium-containing polyurethane (HMDI-IMI-2KPTMO) with a nonionic polyurethane analogue (HMDI-BD-2KPTMO) elucidated the influence of imidazolium cation on performance of imidazolium polyurethane cationomer. HMDI-IMI-2KPTMO exhibited reduced hard segment crystallinity and less hydrogen bonding relative to HMDI-BD-2KPTMO, which was presumably due to the disrupted chain regularity and ionic association. However, AFM and SAXS studies demonstrated that HMDI-IMI-2KPTMO possessed a well-defined microphase-separated morphology. HMDI-IMI hard segments formed worm-like hard domains in AFM phase images. SAXS profile of HMDI-IMI-2KPTMO displayed a clear scattering peak at q=0.5 nm^{-1} (inter domain spacing d=12.3 nm) due to the microphase separation of soft and hard segments. This suggests that enhanced immiscibility between hydrophobic PTMO soft segments and imidazolium ionic hard segments, rather than hard segment crystallinity and hydrogen bonding, serve as the major driving force for the microphase separation of imidazolium-containing polyurethane cationomer. Morphologies of these polyurethanes correlated well with their mechanical properties. Both imidazolium and nonionic polyurethane exhibited well-defined rubbery plateau and high maximum elongation (~900%). However, HMDI-IMI-2KPTMO possessed a higher rubbery plateau modulus (68 MPa at 25 ^{o}C) and a higher onset flow temperature (~150 ^{o}C) relative to the nonionic polyurethane due to the presence of ionic association. Moreover, DRS study demonstrated that imidazolium chloride ions in hard segments significantly increased the ionic conductivity of HMDI-IMI-2KPTMO above the hard segment T_g.

7.6 Acknowledgements

This work is partially supported by the Institute for Critical Technology and Applied Science (ICTAS) at Virginia Tech. Aspects of this work were carried out using instruments in the Nanoscale Characterization and Fabrication Laboratory (NCFL) operated by ICTAS. The authors also thank the U.S. Army Research Laboratory and the U.S. Army Research Office for their support through the Ionic Liquids in Electro-Active Devices Multidisciplinary University Research Initiative (ILEAD MURI) program under Contract/Grant Number W911NF-07-1-0452. Additionally, this research was partially supported by the National Science Foundation under Grant No. DMR-0923107.

7.7 References

1. Xia, H. S.; Song, M.; Zhang, Z. Y.; Richardson, M. *J Appl Polym Sci* 2007, *103*, 2992.
2. Choi, T.; Masser, K. A.; Moore, E.; Weksler, J.; Padsalgikar, A.; Runt, J. *J. Polym. Sci., Part B: Polym. Phys.* 2011, *49*, 865.
3. Chen, S. J.; Cao, Q.; Jing, B.; Cai, Y. L.; Liu, P. S.; Hu, J. L. *J. Appl. Polym. Sci.* 2006, *102*, 5224.
4. Vishnevskaya, I. A.; Chalykh, A. E. *Macromolecular Symposia* 2001, *175*, 249.
5. Sudaryanto; Nishino, T.; Asaoka, S.; Nakamae, K. *Int. J. Adhes. Adhes.* 2001, *21*, 71.
6. Dieterich, D.; Keberle, W.; Witt, H. *Angew. Chem. Internat. Edit.* 1970, *9*, 40.
7. Alsalah, H. A.; Xiao, H. X.; Mclean, J. A.; Frisch, K. C. *J. Polym. Sci., Part A: Polym. Chem.* 1988, *26*, 1609.
8. Chen, S. A.; Chan, W. C. *J. Polym. Sci., Part B: Polym. Phys.* 1990, *28*, 1499.
9. Chen, S. A.; Chan, W. C. *J. Polym. Sci., Part B: Polym. Phys.* 1990, *28*, 1515.
10. Williams, S. R.; Wang, W. Q.; Winey, K. I.; Long, T. E. *Macromolecules* 2008, *41*, 9072.
11. Velankar, S.; Cooper, S. L. *Macromolecules* 2000, *33*, 382.
12. Velankar, S.; Cooper, S. L. *Macromolecules* 2000, *33*, 395.
13. Visser, S. A.; Cooper, S. L. *Macromolecules* 1991, *24*, 2576.
14. Velankar, S.; Cooper, S. L. *Macromolecules* 1998, *31*, 9181.
15. Visser, S. A.; Cooper, S. L. *Polymer* 1992, *33*, 920.
16. Wang, W. Q.; Liu, W. J.; Tudryn, G. J.; Colby, R. H.; Winey, K. I. *Macromolecules* 2010, *43*, 4223.
17. Silver, J. H.; Marchant, J. W.; Cooper, S. L. *J. Biomed. Mater. Res. A.* 1993, *27*, 1443.
18. Goddard, R. J.; Cooper, S. L. *Macromolecules* 1995, *28*, 1401.
19. Chen, Y.; Chen, Y. L. *J. Appl. Polym. Sci.* 1992, *46*, 435.
20. Lee, D. K.; Tsai, H. B.; Tsai, R. S. *J. Appl. Polym. Sci.* 2006, *102*, 4419.
21. Nanda, A. K.; Wicks, D. A.; Madbouly, S. A.; Otaigbe, J. U. *J. Appl. Polym. Sci.* 2005, *98*, 2514.
22. Krol, P.; Krol, B.; Pielichowska, K.; Pikus, S. *Colloid. Polym. Sci.* 2011, *289*, 1757.
23. Mequanint, K.; Sanderson, R. *Eur. Polym. J.* 2006, *42*, 1145.
24. Krol, B.; Krol, P. *Colloid. Polym. Sci.* 2009, *287*, 189.
25. Zhang, Q. C.; Hu, J. K.; Gong, S. L. *J. Appl. Polym. Sci.* 2011, *122*, 3064.
26. Barikani, M.; Ebrahimi, M. V.; Mohaghegh, S. M. S. *J. Appl. Polym. Sci.* 2007, *104*, 3931.
27. Kim, B. K.; Kim, T. K.; Jeong, H. M. *J. Appl. Polym. Sci.* 1994, *53*, 371.
28. Lu, M. G.; Lee, J. Y.; Shim, M. J.; Kim, S. W. *J. Appl. Polym. Sci.* 2002, *86*, 3461.
29. Dieterich, D. *Angew. Makromol. Chem.* 1981, *98*, 133.
30. Wynne, J. H.; Fulmer, P. A.; McCluskey, D. M.; Mackey, N. M.; Buchanan, J. P. *Acs Appl Mater Inter* 2011, *3*, 2005.
31. Buruiana, E. C.; Buruiana, T. *J. Biomater. Sci., Polym. Ed.* 2004, *15*, 781.
32. Jeong, E. H.; Yang, H.; Youk, J. H. *Mater. Lett.* 2007, *61*, 3991.
33. Cheng, S. J.; Zhang, M. Q.; Wu, T. Y.; Hemp, S. T.; Mather, B. D.; Moore, R. B.; Long, T. E. *J. Polym. Sci., Part A: Polym. Chem.* 2012, *50*, 166.
34. Green, M. D.; Long, T. E. *Polym. Rev.* 2009, *49*, 291.
35. Green, O.; Grubjesic, S.; Lee, S. W.; Firestone, M. A. *Polym. Rev.* 2009, *49*, 339.
36. Wang, H. F.; Zhu, Y. Z.; Yan, X. P.; Gao, R. Y.; Zheng, J. Y. *Adv. Mater.* 2006, *18*, 3266.
37. Yoshio, M.; Mukai, T.; Kanie, K.; Yoshizawa, M.; Ohno, H.; Kato, T. *Adv. Mater.* 2002, *14*, 351.

38. Texter, J.; Vasantha, V. A.; Crombez, R.; Maniglia, R.; Slater, L.; Mourey, T. *Macromol. Rapid Commun.* 2012, *33*, 69.
39. Wanakule, N. S.; Virgili, J. M.; Teran, A. A.; Wang, Z. G.; Balsara, N. P. *Macromolecules* 2010, *43*, 8282.
40. Green, O.; Grubjesic, S.; Lee, S. W.; Firestone, M. A. *Polymer Reviews* 2009, *49*, 339.
41. Weber, R. L.; Ye, Y. S.; Schmitt, A. L.; Banik, S. M.; Elabd, Y. A.; Mahanthappa, M. K. *Macromolecules* 2011, *44*, 5727.
42. Lee, M.; Choi, U. H.; Salas-de la Cruz, D.; Mittal, A.; Winey, K. I.; Colby, R. H.; Gibson, H. W. *Adv. Funct. Mater.* 2011, *21*, 708.
43. Gao, R.; Zhang, M.; Moore, R. B.; Long, T. E. 2012, *(Accepted)*.
44. Mattia, J.; Painter, P. *Macromolecules* 2007, *40*, 1546.
45. Yilgor, I.; Yilgor, E.; Guler, I. G.; Ward, T. C.; Wilkes, G. L. *Polymer* 2006, *47*, 4105.
46. Hernandez, R.; Weksler, J.; Padsalgikar, A.; Choi, T.; Angelo, E.; Lin, J. S.; Xu, L. C.; Siedlecki, C. A.; Runt, J. *Macromolecules* 2008, *41*, 9767.
47. Wang, S. W.; Liu, W. J.; Colby, R. H. *Chem. Mater.* 2011, *23*, 1862.
48. Fragiadakis, D.; Dou, S. C.; Colby, R. H.; Runt, J. *Macromolecules* 2008, *41*, 5723.

Chapter 8: Influence of Ionic Liquids on Performance of Segmented Polyurethanes Containing Imidazolium Cations in Hard Segments

Gao, R.; Wang, S.W.; Zhang, M.; Colby, R.H.; Moore, R.B.; Long, T.E. (*prepared for publication*)

8.1 Abstract

Polymeric materials with both high ionic conductivity and good mechanical properties are highly desirable for electromechanical transducer applications. Here we report our fundamental investigation on imidazolium-containing polyurethanes (IPU) incorporated with room temperature ionic liquid (IL) to elucidate the influence of IL on thermal and mechanical properties, morphologies, and ionic conductivity of IPU. Novel poly(tetramethylene oxide) (PTMO)-based IPU was synthesized through a conventional prepolymer method using an imidazolium diol as the chain extender. Resulting IPU solutions cast with various contents (5~30 wt%) of IL, 1-ethyl-3-methylimidazolium ethylsulfate (EMIm ES), generated a novel series of IPU/IL composite membranes. Differential scanning calorimetry (DSC) revealed that IPU exhibited a constant PTMO soft segment T_g at -81±1 ^oC, which was independent of IL content. In contrast, dynamic mechanical analysis (DMA) clearly showed that T_g of the imidazolium-containing hard segments systematically shifted to lower temperatures with increasing IL content. This observation suggested that IL preferentially located into the imidazolium ionic hard domains of IPU, which was evident in small angle X-ray scattering (SAXS). SAXS profile of IPU displayed a scattering peak near q=0.5 nm^{-1} due to the microphase separation of soft and hard segments. The scattering peak position sequentially shifted to a lower q upon incorporation of EMIm ES ionic liquid, indicating increased inter-domain spacings. Moreover, dielectric relaxation spectroscopy demonstrated that ionic conductivity of IPU membrane increased by five

orders of magnitude upon incorporation of 30 wt% EMIm ES. IL-free IPU and IPU with low contents of ionic liquid (≤15 wt%) exhibited Arrhenius temperature dependence of ionic conductivity, while IPU with 30 wt% IL showed VFT behavior .

8.2 Introduction

Ionic liquids, which are defined as salts with melting temperatures below 100 ^{o}C,[1] have attracted increasing attention for their unique physiochemical properties, including high ionic conductivity, exceptional thermal and electrochemical stability, low volatility, and low flammability.[2-4] Properties of ionic liquids depend strongly on the chemical structures of cations and anions. Combination of various cations and anions in different ways generates millions of novel ionic liquids that are suitable for many applications in electromechanical transducers,[5-7] lithium batteries,[8-10] fuel cells,[11-13] gas separation membranes,[14-17] and solar cells.[18-20]

Particularly, imidazolium-based ionic liquids have emerged as suitable dilutes to enhance the ionic conductivity of polymeric materials.[21-23] Watanabe et al. reported the synthesis of ion gels through polymerization of methyl methacrylate in a 1-ethyl-3-methyl imidazolium bis(trifluoromethane sulfonyl)imide (EMIm TFSI) ionic liquid. Resulting poly(methyl methacrylate)-based ion gels exhibited dramatically enhanced ionic conductivity at ambient temperatures.[24] Lodge et al. studied self-assembly of poly(styrene-*b*-ethylene oxide-*b*-styrene) block copolymer in the presence of EMIm TFSI, which generated ion gels with high ionic conductivity and appreciable mechanical strength.[25] Winey and Elabd et al. studied the ionic conductivity of poly(styrene-*b*-methyl methacrylate) (PS-*b*-PMMA) in the presence of EMIm TFSI ionic liquid. They reported that ionic conductivity of PS-*b*-PMMA increased by four orders of magnitude upon incorporation of 50 wt% ionic liquid.[26] It is important to note that all these

polymers contained blocks that were compatible with EMIm TFSI ionic liquid and cross-linking sites that were provided with either chemical cross-linkers or high glass transition temperature (T_g) blocks. Ionic liquid-compatible polymer blocks exhibited low T_g and provided high ionic conductivity, while chemical or physical cross-links provided required mechanical strength.

Most recent studies on ionic liquid-incorporated polymers have mainly focused on block copolymers.[23,27-32] Segmented copolymers with well-defined chemical structures are relatively unexplored. Among the many types of segmented copolymers, polyurethanes are one of the most versatile segmented copolymers that possess a wide range of physical properties. Polyurethanes contain alternated soft and hard segments, which readily microphase separate to form unique morphological features at the nanoscale.[33] Segmented polyurethanes offer several beneficial attributes including tailored chemical structure and tunable physical properties in a facile way. Particularly, poly(ethylene oxide) (PEO)-based polyurethane or ion-containing polyurethane have high compatibility with ionic liquids, which makes them suitable for preparation of polyurethane/IL composite membranes. In a recent study, we incorporated room temperature ionic liquid, 1-ethyl-3-methyl imidazolium ethylsulfate (EMIm ES), into a segmented polyurethane containing sulfonated PEO soft segments. Our results indicated that EMIm ES preferentially located into the PEO soft phase, leading to significantly enhanced ionic conductivity and well-maintained mechanical properties.

In the present study, we designed and synthesized a novel segmented polyurethane that contained hydrophobic poly(tetramethylene oxide) (PTMO)-based soft segments and imidazolium ionic hard segments. Hydrophilic ionic liquid, EMIm ES, was utilized in this study due to the high ionic conductivity, good thermal and chemical stability, and low cost. Differential scanning calorimetry (DSC) and dynamic mechanical analysis (DMA) elucidated the

influence of ionic liquid on thermal and mechanical properties of IPU membranes. Small angle X-ray scattering (SAXS) revealed the bulk morphology of IPU cast with various contents of ionic liquid. Dielectric relaxation spectroscopy demonstrated significantly enhanced ionic conductivity of IPU membranes upon incorporation of EMIm ES ionic liquid.

8.3 Experimental

Materials. The matrix polymer used in this study was a segmented polyurethane with PTMO-based soft segments and imidazolium-containing ionic hard segments. Synthetic details of this polyurethane have been described in a previous paper. An imidazolium diol-based ionic liquid, 1,3-di(2-hydroxyethyl) imidazolium chloride, was initially synthesized and utilized as the chain extender in the polyurethane synthesis. Following a typical two-step process, PTMO (2000 g/mol) was initially end-capped with dicyclohexylmethane-*4,4'*-diisocyanate (HMDI) to synthesize the polyurethane prepolymers, which were subsequently chain extended with 1,3-di(2-hydroxyethyl) imidazolium chloride to prepare high molecular weight imidazolium-containing polyurethanes (**Scheme 8.1**). Hydrophilic ionic liquid, 1-ethyl-3-methyimidazolium ethylsulfate (EMIm ES) was purchased from Alfa Aesar and stored over molecular sieves.

Preparation of Composite Membranes

Preparation of imidazolium-containing polyurethane/ionic liquid composite membranes was following a "cast with" method as described previously. Imidazolium-containing polyurethane solution in *N,N*-dimethylformamide (DMF) (20 wt% solids) was blended with room temperature ionic liquid, 1-ethyl-3-methylimidazolium ethylsulfate (EMIm ES) (**Figure 8.1**). The mixture was directly cast in Teflon® molds and air-dried at 23 ^{o}C for 3 days. Resulting membranes were subsequently annealed *in vacuo* at 60 ^{o}C for 72 h to remove residual solvent and moisture. All

membranes were stored in a dessicator (relative humidity<15%) and dried *in vacuo* for 24 h at 60 ^{o}C immediately prior to DSC, DMA, and SAXS characterization.

Instrumentation

Differential scanning calorimetry (DSC) was performed using a TA Instruments Q2000 differential scanning calorimeter under a nitrogen flow of 50 mL/min with a heating rate of 10 ^{o}C/min over the range from -110−180 ^{o}C. Second heat DSC curves were utilized to determine glass transition temperatures of IPU/IL composite membranes. Dynamic mechanical analysis (DMA) measurements were performed on a TA Instruments Q800 dynamic mechanical analyzer in the film tension mode at a frequency of 1 Hz and a temperature ramp of 3 ^{o}C/min over the range -110−180 ^{o}C. Glass transition temperatures were determined according to the peak values in tanδ curves. SAXS was performed using a Rigaku S-Max 3000 3 pinhole SAXS system equipped with a rotating anode emitting X-rays with a wavelength of 0.154 nm (Cu Kα). Scattering from a silver behenate standard was used to calibrate the sample-to-detector distance, which was 1603 mm. Two-dimensional SAXS patterns were obtained using a fully integrated 2D multi-wire, proportional counting, gas-filled detector during an exposure time of 1 h per sample. SAXS data were corrected for sample thickness, sample transmission, and background scattering, and analyzed using the SAXSGUI software package to obtain radially integrated SAXS intensity versus scattering vector q profiles, where $q=4\pi\sin(\theta)/\lambda$, θ is half of the scattering angle, and λ is the wavelength of X-ray. The profiles were vertically shifted to facilitate a comparison of peak positions. Dielectric relaxation spectroscopy (DRS) was conducted on a Novo-control GmbH Concept 40 broadband dielectric spectrometer. Samples were dried at 45 ^{o}C under vacuum before measurement. All sample membranes were sandwiched between two 20 mm diameter freshly polished brass electrodes. Dielectric (impedance) spectra were measured in

the frequency range of 1×10^{-2} to 1×10^{7} Hz with 0.1 V amplitude. Samples were annealed at 100 ^{o}C in the equipment for 30 min and allowed to reach equilibrium with temperature for at least 5 min before each isothermal measurement.

8.4 Results and Discussion

8.4.1 Preparation of IPU/IL composite membranes

PTMO-based polyurethane prepolymers chain extended with an imidazolium diol-based ionic liquid, 1,3-di(2-hydroxyethyl) imidazolium chloride, afforded well-defined polyurethane ionomers with imidazolium cations readily introduced into the hard segments (IPU, **Scheme 8.1**). Incorporation of hydrophilic room temperature ionic liquid (IL), 1-ethyl-3-methylimidazolium ethylsulfate (EMIm ES, **Figure 8.1**), provided a series of novel IPU/IL composite membranes. Here, EMIm ES was selected for the good thermal and electrochemical stability, high ionic conductivity, and relatively low cost. IPU/IL composite membranes were prepared with a "cast with" method, in which, IPU solutions were blended with a calculated amount of IL. This method enabled a precise control of IL content incorporated into the IPU membranes. All IPU membranes with up to 30 wt% EMIm ES were optically clear, indicating a good dispersion of IL in the IPU membranes. However, a nonionic polyurethane membrane, which contained the same PTMO soft segments but nonionic hard segments, changed from optically clear to opaque upon incorporation of only 5 wt% EMIm ES. This comparative study indicates that imidazolium cations in IPU favored the dispersion of IL. In addition, previous studies indicated that polymer/ionic liquid composite membranes suffered poor mechanical properties at high contents of ionic liquids.[22,34,35] In order to obtain high ionic conductivity and maintain good mechanical properties of IPU membranes, we kept the ionic liquid content at

relatively low levels (≤30 wt%). Moreover, low contents of ionic liquid reduced possible leakage.

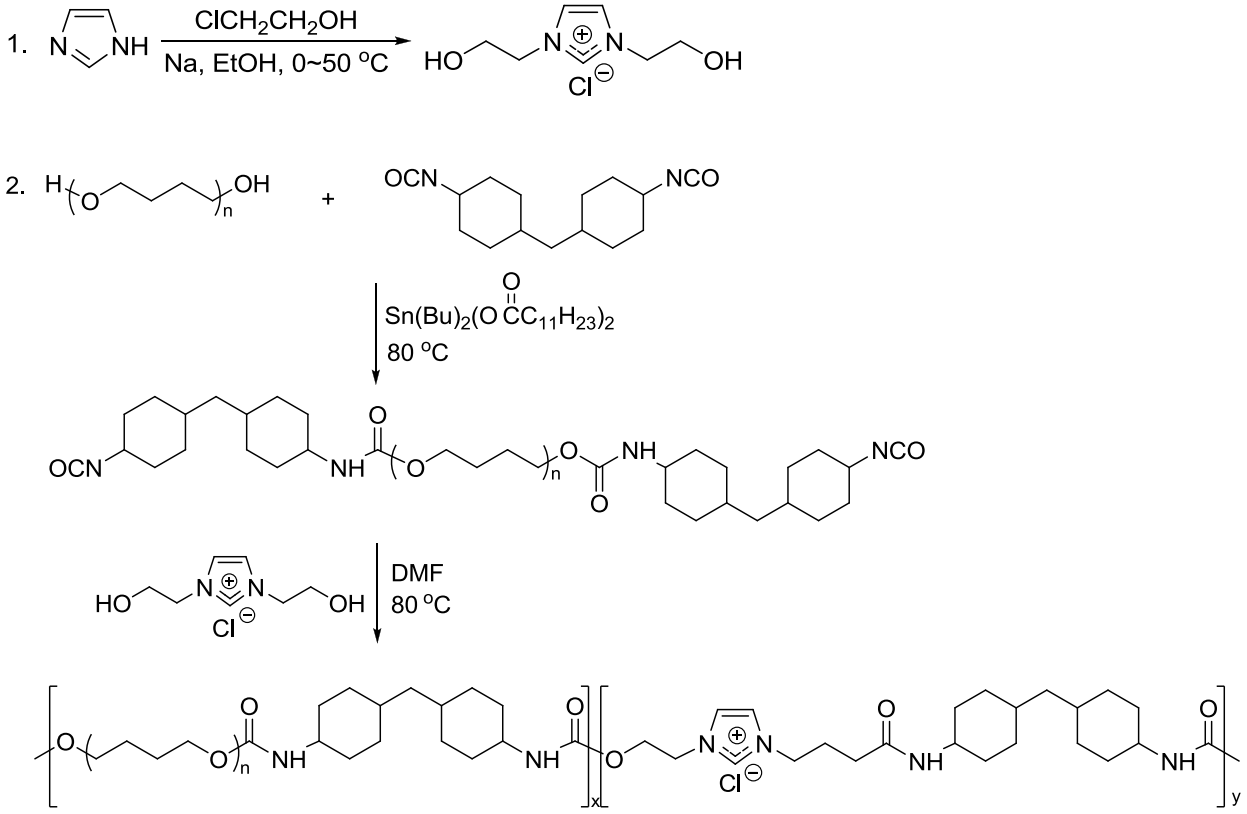

Scheme 8.1 Synthesis of imidazolium diol chain extender (1) and imidazolium-containing segmented polyurethane (2)

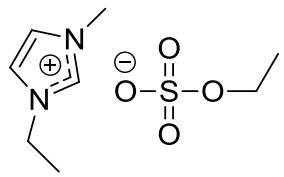

Figure 8.1 Chemical structure of 1-ethyl-3-methylimidazolium ethylsulfate (EMIm ES)

8.4.2 Thermomechanical properties

Dynamic mechanical analysis (DMA) elucidated the influence of EMIm ES on thermal transitions and mechanical properties of IPU membranes. **Figure 8.2** displays the storage modulus (G') curves of IPU membranes incorporated with various contents of EMIm ES ranging from 5 wt% to 30 wt%. All samples exhibited clear thermal transitions near -60 ^{o}C, which corresponded to the glass transition temperature (T_g) of PTMO soft segments. IL-free IPU membrane displayed a well-defined rubbery plateau above the PTMO soft segment T_g and showed another thermal transition above 130 ^{o}C, which was attributed to the glass transition of imidazolium-containing hard segments. It is clear that hard segment T_g systematically decreased with increasing EMIm ES content, leading to narrowed rubbery plateau and reduced rubbery plateau modulus. This indicates that EMIm ES ionic liquid selectively located into the imidazolium ionic hard segments. **Table 8.1** summarizes the rubbery plateau storage moduli of all IPU membranes at 40 ^{o}C, which decreased from 180 MPa to 10 MPa upon incorporation of 30 wt% IL. Modulus of segmented polyurethanes is strongly related to the morphological features of hard domains, which serve as physical cross-links and reinforcing "fillers" to provide mechanical strength. Ionic liquid in imidazolium ionic hard domains plasticized these "cross-links" and "fillers", leading to reduced modulus. Our previous studies demonstrated that PEO-based sulfonated polyurethanes with nonionic hard segments showed a rubbery plateau modulus independent of ionic liquid content due to the absence of ionic liquid in the nonionic hard segment domains. It is also important to note that all composite membranes displayed onset flow temperatures above 150 ^{o}C.

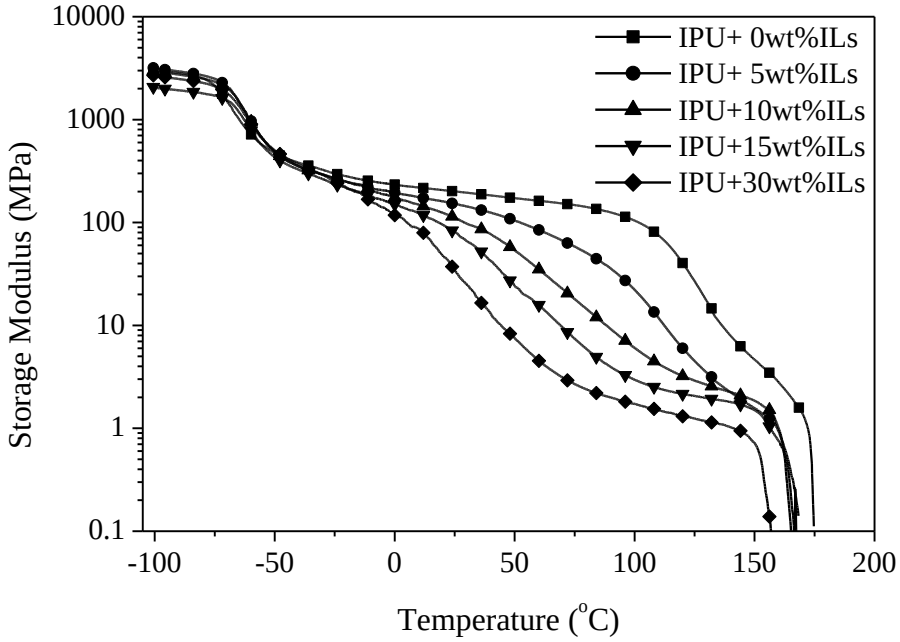

Figure 8.2 Thermomechanical properties of IPU membranes cast with various contents of ionic liquids. DMA conditions: 3 °C/min, 1Hz, film tension mode

Figure 8.3 depicts the tanδ curves of IL-free IPU and IPU/IL composite membranes. T_g's of both PTMO soft segments and imidazolium ionic hard segments were determined with the tanδ peaks. It shows that all samples displayed well-defined peaks at -63 °C, corresponding to the glass transition of PTMO soft segments. Differential scanning calorimetry (DSC) also confirmed a constant PTMO soft segment T_g that was independent of IL content. In sharp contrast, tanδ peaks at high temperatures, arising from the glass transition of imidazolium ionic hard segments, systematically shifted from 132 °C to 37 °C as IL content increased from 0 to 30 wt%. Reduced hard segmented T_g was due to the plasticizing effect of IL. **Figure 8.4** plots the T_g's of soft and hard segments as a function of ionic liquid content. It clearly shows that EMIm ES systematically reduced the hard segment T_g without influencing the T_g of PTMO soft segments. This observation suggests that hydrophilic EMIm ES ionic liquid preferentially located in the imidazolium ionic hard segments. Watanabe et al. studied the thermal transition behavior of a

polystyrene-*b*-poly(methyl methacrylate)-*b*-polystyrene (PS-*b*-PMMA-*b*-PS) block copolymer in the presence of EMIm TFSI ionic liquid.[36] They found that T_g of PS blocks was virtually unchanged, however, T_g of PMMA block systematically decreased with increasing ionic liquid content due to the preferential location of ionic liquid into the PMMA phase.

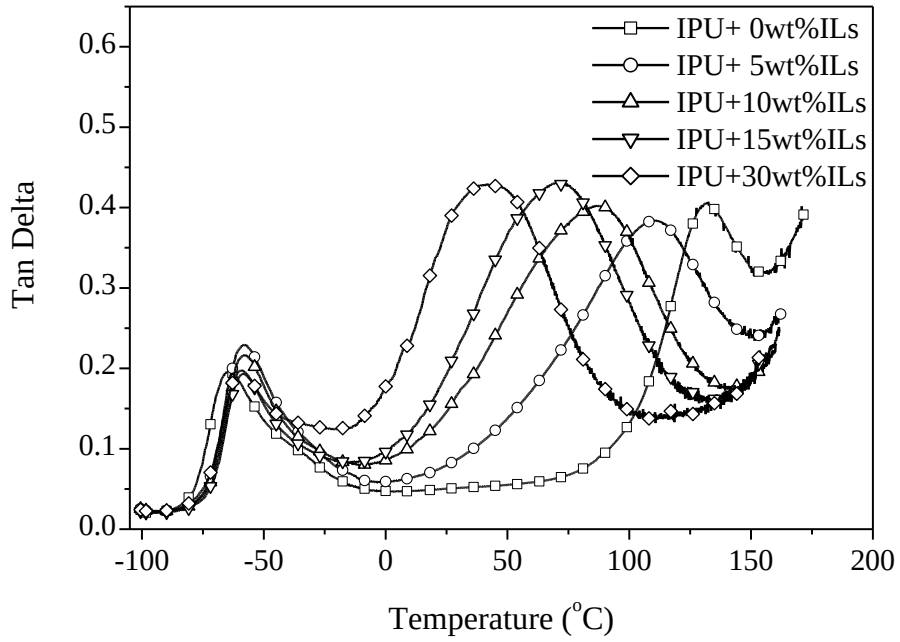

Figure 8.3 Tan delta curves of IPU membranes cast with various contents of ionic liquids. DMA conditions: 3 °C/min, 1Hz, film tension mode

Table 8.1 Thermal transition temperatures and storage modulus (G') of IPU/IL composites

	$T_g^{SS}{}_{(DSC)}$ (°C)	$T_g^{SS}{}_{(DMA)}$ (°C)	$T_g^{HS}{}_{(DMA)}$ (°C)	G' at 40 °C (MPa)
IPU+0 wt% ILs	-81	-63	132	183
IPU+5 wt% ILs	-81	-62	106	116
IPU+10 wt% ILs	-80	-63	82	66
IPU+15 wt% ILs	-81	-63	67	34
IPU+30wt% ILs	-80	-63	37	10

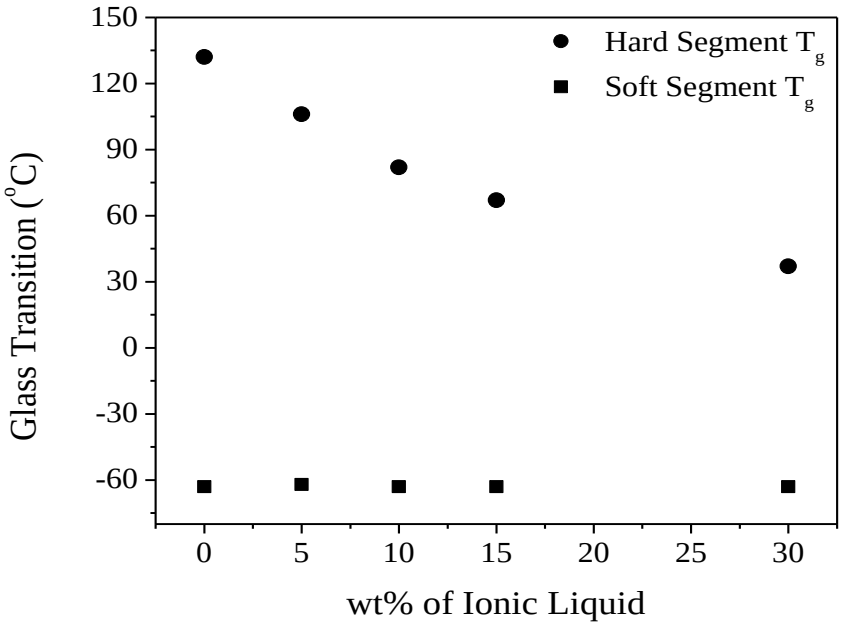

Figure 8.4 Influence of ionic liquid on glass transition temperature of soft and hard segments of imidazolium-containing polyurethanes

8.4.3 Morphological characterization

SAXS data provided morphological information of IL-free IPU membrane and IPU/IL composite membranes with ionic liquid content ranging from 5 wt% to 30 wt%. **Figure 8.5** displays the SAXS profiles of all membranes plotted as scattering intensity versus scatting vector q (nm^{-1}) at a logarithmic scale. The profiles were vertically shifted to facilitate a comparison of peak positions. The SAXS profile of IL-free IPU membrane displayed a scattering peak near q=0.5 nm^{-1}, arising from the microphase separation of soft and hard segments. Earlier studies have determined that q value at the scatting peak is related to mean inter-domain spacings (*d*) between polyurethane hard domains according to the equation: $d=2\pi/q$.[37,38] In the case of IL-free IPU membrane, the calculated inter-domain spacing was 12.3 nm. SAXS profiles of IPU/IL composite membranes clearly showed that the scattering peak at q=0.5 nm^{-1} sequentially shifted to a lower q with increasing the ionic liquid content. **Table 8.2** summarizes the scattering peak position and calculated *d* spacings for all IPU/IL composite membranes. **Figure 8.6** plots the *d*

spacings (nm) as a function of ionic content (wt%). It is clear that *d* spacing between polyurethane hard domains linearly increased with ionic liquid content. Previous studies have showed that preferential incorporation of ionic liquid into block copolymers lead to increased *d* spacing, which was due to the configuration change of polymer chains in the presence of ionic liquid. Segalman et al. studied a polystyrene-*b*-poly(2-vinylpyridine) block copolymer incorporated with EMIm TFSI ionic liquid, which displayed systematic increase in *d* spacing with ionic liquid content.[39] Similar observation of increased *d* spacing upon incorporation of ionic liquid has been reported for several other block copolymers.[40] However, to the best of our knowledge, studies on segmented copolymers, particularly segmented polyurethane ionomers, are much less noted in the literature. Our previous AFM studies demonstrated that IPU possessed well-defined microphase-separated morphology.[33] Imidazolium ionic hard segments microphase separated into worm-like hard domains that randomly distributed in the PTMO-based soft phase. Morphology of IPU resembled a cylindrical morphology typically generated with block copolymers. Thus, it is not surprising that IPU displayed increased *d* spacing due to the preferential incorporation of EMIm ES in the imidazolium ionic hard domains.

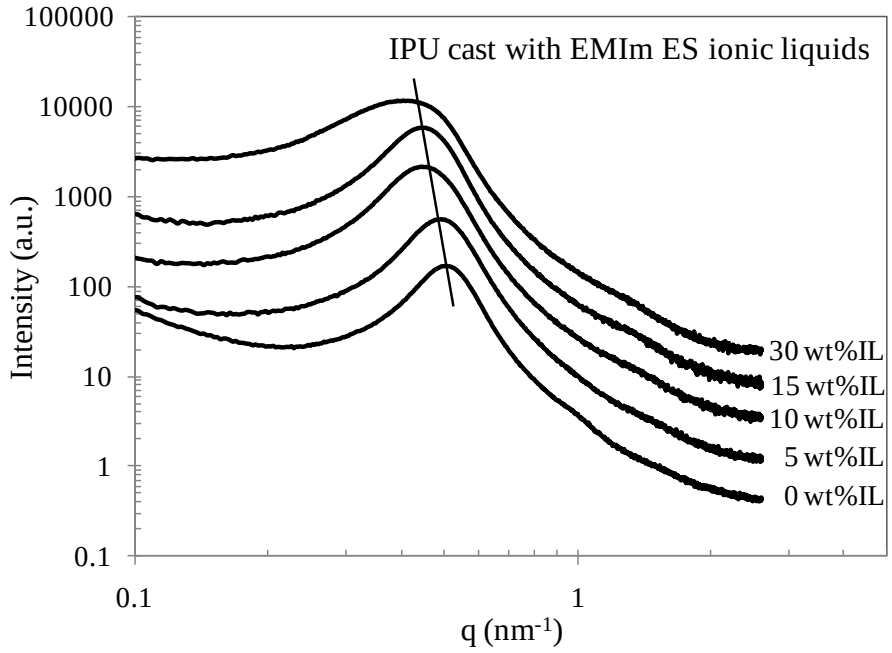

Figure 8.5 SAXS profiles of IPU membranes cast with various contents of EMIm ES ionic liquid

Table 8.2 Summary of scattering peak position and *d* spacing of IPU/IL composite membranes

	wt% of IL	wt% IL: wt% HS	peak position (nm^{-1})	*d* spacing (nm)
IPU+0 wt% IL	0	0:1	0.51	12.3
IPU+5 wt% IL	5	0.14:1	0.49	12.8
IPU+10 wt% IL	10	0.27:1	0.46	13.8
IPU+15 wt% IL	15	0.41:1	0.45	14.0
IPU+30 wt% IL	30	0.81:1	0.41	15.2

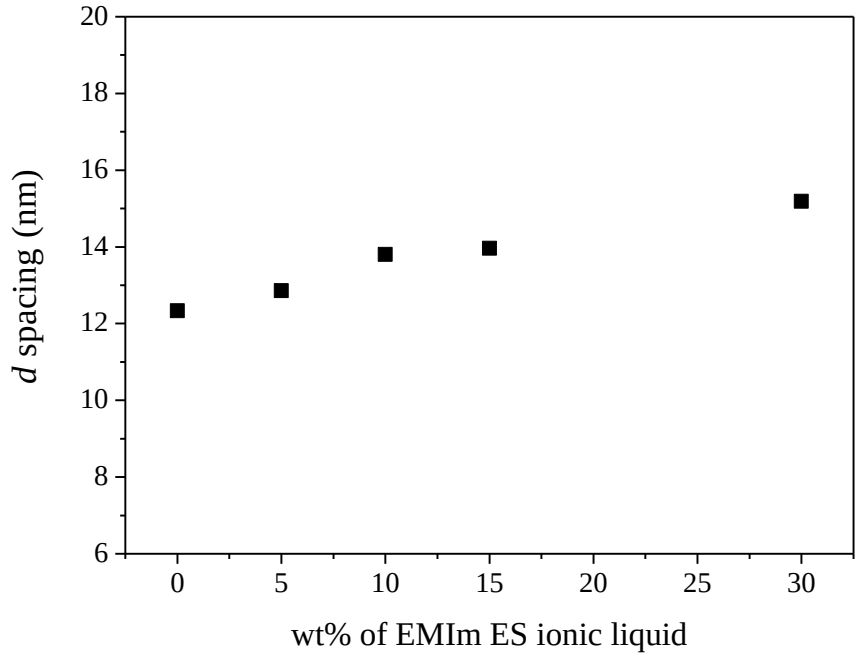

Figure 8.6 Inter-domain spacings (*d*) of IPU/IL composite membranes as a function of IL content

8.4.4 Ionic conductivity

DRS studies on IL-free IPU and IPU/IL composite membranes elucidated the ionic conductivity of all membranes as a function of temperature and ionic liquid content. **Figure 8.7** plots the ionic conductivity of all IPU membranes versus temperature (1000/T) at a logarithmic-linear scale. It clearly showed that ionic conductivity of IPU membranes systematically increased with ionic liquid content at each temperature. Moreover, ionic conductivity of IPU/IL composite membranes also exhibited strong dependence on temperature. Arrhenius equation ($\sigma = \sigma_0 \exp(E_a/RT)$) and Vogel-Fulcher-Tammann (VFT) equation ($\sigma = \sigma_0 \exp[-B/(T-T_0)]$) are frequently applied to describe the correlation between temperature and ionic conductivity of polymeric materials.[41] Arrhenius equation describes the temperature dependence of ionic conductivity that is related to thermal ion hopping; however, VFT equation describes the ionic conductivity versus temperature behavior when segmental motions of polymer chains are

responsible for the ionic conductivity. Our previous studies showed that PEO-based sulfonated polyurethanes with EMIm ES preferentially located in the sulfonated PEO soft phase exhibited VFT behavior. This suggested that ion conduction strongly coupled with PEO segmental motions due to a low PEO soft segment T_g that was 40 K below the minimum measurement temperature. However, in the case of IPU, where EMIm ES ionic liquid located in the imidazolium ionic hard domains, IL-free IPU and IPU with low contents of IL (≤15 wt%) exhibited Arrhenius behavior; however, IPU with 30 wt% IL exhibited VFT behavior. A previous comparative study on ionic conductivity of IPU and a nonionic polyurethane analogue showed that mainly imidazolium-containing hard segments contributed to the ion conduction above the hard segment T_g. Thus, it is reasonable to speculate that ion conduction of IL-free IPU and IPU with low contents of IL (≤15 wt%) was associated with thermal ion hopping. In contrast, IPU+30 wt% IL showed VFT temperature dependence of ionic conductivity, suggesting that ion conduction was related to polymer chain relaxation. Significantly reduced hard segment T_g (37 ^oC) as determined with DMA was presumably responsible for the VFT behavior of IPU+30 wt% IL. However, it is also possible that some IL was trapped in the interfaces between the PTMO soft phase and hard domains during membrane formation, which coupled with the polymer segmental motion and contributed to the ion conduction.

Figure 8.8 depicts the ionic conductivity of IPU membranes as a function of ionic liquid content at different temperatures. The data revealed that ionic conductivity linearly increased with ionic liquid content. For example, IL-free IPU exhibited a low ionic conductivity on the order of 10^{-11} S/cm at 20 ^oC, which was significantly enhanced by 5 orders of magnitude upon incorporation of 30 wt% EMIm ES ionic liquid. Moreover, ionic conductivity of IPU/IL composite membranes strongly depended on temperature. In the case of IPU+30 wt% IL, ionic

conductivity increased from the order of 10^{-10} S/cm to the order of 10^{-5} S/cm as temperature increased from -10 °C to 100 °C.

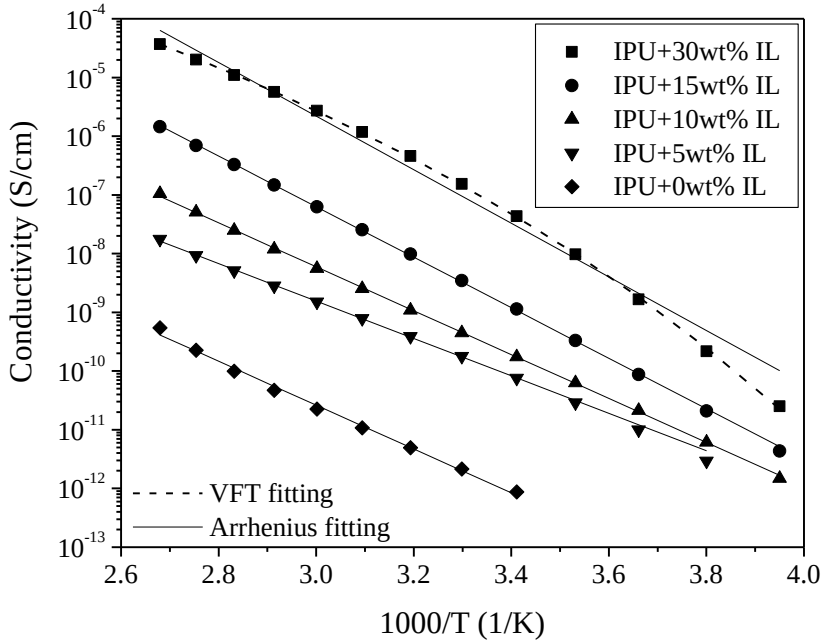

Figure 8.7 Temperature dependence of ionic conductivity of IPU cast with various contents of EMIm ES ionic liquid

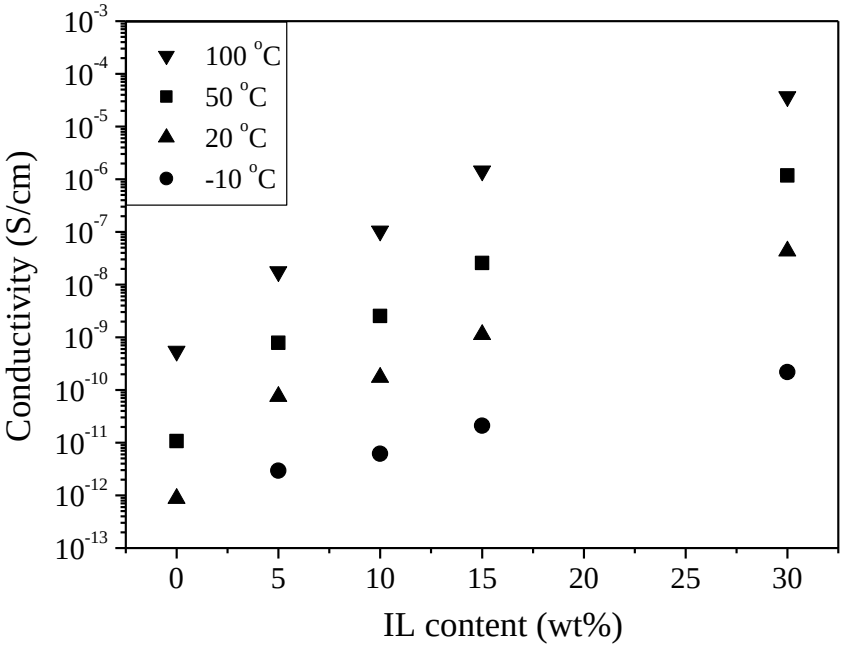

Figure 8.8 Ionic conductivity of IPU/IL composite membranes as a function of temperature and IL content

8.5 Conclusion

We investigated the influence of a hydrophilic ionic liquid, EMIm ES, on performance of a novel segmented polyurethane ionomer containing imidazolium cations in the hard segments (IPU). Complementary characterization using DSC, DMA, SAXS, and DRS elucidated the influence of EMIm ES on thermal and mechanical properties, morphology, and ionic conductivity of IPU membranes. Both DSC and DMA demonstrated that PTMO soft segment T_g was independent of ionic liquid content; however, T_g of ionic hard segments systematically decreased from 132 ^oC to 37 ^oC with increasing ionic liquid content, as determined with DMA tanδ peaks. This observation suggested that EMIm ES ionic liquid preferential located into the ionic hard domains. SAXS profiles of IPU membranes displayed a scattering peak near q=0.5 nm^{-1}, which systematically shifted to a low q upon incorporation of EMIm ES ionic liquid. Scattering peak position (q) was related to mean inter-domain spacings of polyurethane hard segments ($d=2\pi/q$)). Calculation results revealed linearly increased *d* spacing from 12.3 to 15.2 nm with increasing ionic liquid content to 30 wt%, which supported the hypothesis that ionic liquid preferentially located in the ionic hard domains. Moreover, DRS demonstrated that ionic conductivity of IPU membranes increased by 5 orders of magnitude upon incorporation of 30 wt% EMIm ES. IL-free IPU membrane and IPU/IPU composite membranes with low ionic liquid content (≤15 wt%) exhibited Arrhenius temperature dependence of ionic conductivity, suggesting ion conduction through thermal ion hoping. However, ionic conductivity of IPU membrane with 30 wt% IL exhibited VFT behavior, suggesting the ion conduction in this case was coupled with segmental motion of polyurethane chains. Ionic conductivity of IPU/IL composite membranes also depended strongly on temperature. All membranes displayed

significantly enhanced ionic conductivity by approximately 5 orders of magnitude as temperature increased from -10 ^{o}C to 100 ^{o}C.

8.6 Acknowledgments

This work is supported in part by the U.S. Army Research Office through the Ionic Liquids in Electro-Active Devices Multidisciplinary University Research Initiative (ILEAD MURI) program under Contract/Grant Number W911NF-07-1-0452. The authors also thank Institute for Critical Technology and Applied Science (ICTAS) at Virginia Tech. Aspects of this work were carried out using instruments in the Nanoscale Characterization and Fabrication Laboratory (NCFL) operated by ICTAS. Additionally, this research was partially supported by the National Science Foundation under Grant No. DMR-0923107.

8.7 References

1. Green, M. D.; Long, T. E. *Polym Rev* **2009**, *49*, 291.
2. Rogers, R. D. *Nature* 2007, *447*, 917.
3. Smiglak, M.; Metlen, A.; Rogers, R. D. *Accounts Chem Res* **2007**, *40*, 1182.
4. Wilkes, J. S. *Green Chem* **2002**, *4*, 73.
5. Mahadeva, S. K.; Yun, K.; Kim, J.; Kim, J. H. *J Nanosci Nanotechno* **2011**, *11*, 270.
6. Mahadeva, S. K.; Kang, K. S.; Kim, J.; Ha, S. H.; Koo, Y. M. *Soft Mater* **2010**, *8*, 254.
7. Fukushima, T.; Asaka, K.; Kosaka, A.; Aida, T. *Angew Chem Int Edit* **2005**, *44*, 2410.
8. Kim, G. T.; Jeong, S. S.; Xue, M. Z.; Balducci, A.; Winter, M.; Passerini, S.; Alessandrini, F.; Appetecchi, G. B. *J Power Sources* **2012**, *199*, 239.
9. Chou, S. L.; Wang, J. Z.; Sun, J. Z.; Wexler, D.; Forsyth, M.; Liu, H. K.; MacFarlane, D. R.; Dou, S. X. *Chem Mater* **2008**, *20*, 7044.
10. Seki, S.; Kobayashi, Y.; Miyashiro, H.; Ohno, Y.; Usami, A.; Mita, Y.; Watanabe, M.; Terada, N. *Chem Commun* **2006**, 544.
11. Gao, J.; Liu, J. G.; Liu, W. M.; Li, B.; Xin, Y. C.; Yin, Y.; Jungu; Zou, Z. G. *Int J Electrochem Sc* **2011**, *6*, 6115.
12. Lin, B. C.; Qiu, L. H.; Lu, J. M.; Yan, F. *Chem Mater* **2010**, *22*, 6718.
13. Nakamoto, H.; Noda, A.; Hayamizu, K.; Hayashi, S.; Hamaguchi, H. O.; Watanabe, M. *J Phys Chem C* **2007**, *111*, 1541.
14. Jiang, Y. Y.; Zhou, Z.; Jiao, Z.; Li, L.; Wu, Y. T.; Zhang, Z. B. *J Phys Chem B* **2007**, *111*, 5058.
15. Bara, J. E.; Gabriel, C. J.; Hatakeyama, E. S.; Carlisle, T. K.; Lessmann, S.; Noble, R. D.; Gin, D. L. *J Membrane Sci* **2008**, *321*, 3.
16. Scovazzo, P.; Havard, D.; McShea, M.; Mixon, S.; Morgan, D. *J Membrane Sci* **2009**, *327*, 41.
17. Bara, J. E.; Lessmann, S.; Gabriel, C. J.; Hatakeyama, E. S.; Noble, R. D.; Gin, D. L. *Ind Eng Chem Res* **2007**, *46*, 5397.
18. Wei, D.; Unalan, H. E.; Han, D. X.; Zhang, Q. X.; Niu, L.; Amaratunga, G.; Ryhanen, T. *Nanotechnology* **2008**, *19*.
19. Bhattacharya, B.; Tomar, S. K.; Park, J. K. *Nanotechnology* **2007**, *18*.
20. Stathatos, E.; Lianos, P.; Zakeeruddin, S. M.; Liska, P.; Gratzel, M. *Chem Mater* **2003**, *15*, 1825.
21. Matsumoto, K.; Endo, T. *J Polym Sci Pol Chem* **2011**, *49*, 3582.
22. Brown, R. H.; Duncan, A. J.; Choi, J. H.; Park, J. K.; Wu, T. Y.; Leo, D. J.; Winey, K. I.; Moore, R. B.; Long, T. E. *Macromolecules* **2010**, *43*, 790.
23. Hoarfrost, M. L.; Segalman, R. A. *Macromolecules* 2011, *44*, 5281.
24. Susan, M. A.; Kaneko, T.; Noda, A.; Watanabe, M. *J. Am. Chem. Soc.* **2005**, *127*, 4976.
25. Zhang, S. P.; Lee, K. H.; Frisbie, C. D.; Lodge, T. P. *Macromolecules* **2011**, *44*, 940.
26. Gwee, L.; Choi, J. H.; Winey, K. I.; Elabd, Y. A. *Polymer* **2010**, *51*, 5516.
27. Cheng, S. J.; Beyer, F. L.; Mather, B. D.; Moore, R. B.; Long, T. E. *Macromolecules* **2011**, *44*, 6509.
28. Kim, S. Y.; Yoon, E.; Joo, T.; Park, M. J. *Macromolecules* **2011**, *44*, 5289.
29. Weber, R. L.; Ye, Y. S.; Schmitt, A. L.; Banik, S. M.; Elabd, Y. A.; Mahanthappa, M. K. *Macromolecules* **2011**, *44*, 5727.
30. He, Y. Y.; Li, Z. B.; Simone, P.; Lodge, T. P. *J. Am. Chem. Soc.* **2006**, *128*, 2745.
31. Meli, L.; Lodge, T. P. *Macromolecules* **2009**, *42*, 580.
32. Virgili, J. M.; Nedoma, A. J.; Segalman, R. A.; Balsara, N. P. *Macromolecules* **2010**, *43*, 3750.

33. Gao, R.; Zhang, M.; Dixit, N.; Moore, R. B.; Long, T. E. *Polymer* **2012**, (Accepted).
34. Zhang, S. P.; Lee, K. H.; Sun, J. R.; Frisbie, C. D.; Lodge, T. P. *Macromolecules* **2011**, *44*, 8981.
35. Lodge, T. P. *Science* **2008**, *321*, 50.
36. Imaizumi, S.; Kokubo, H.; Watanabe, M. *Macromolecules* **2012**, *45*, 401.
37. Li, Y. J.; Gao, T.; Chu, B. *Macromolecules* **1992**, *25*, 1737.
38. Hernandez, R.; Weksler, J.; Padsalgikar, A.; Choi, T.; Angelo, E.; Lin, J. S.; Xu, L. C.; Siedlecki, C. A.; Runt, J. *Macromolecules* **2008**, *41*, 9767.
39. Virgili, J. M.; Hexemer, A.; Pople, J. A.; Balsara, N. P.; Segalman, R. A. *Macromolecules* **2009**, *42*, 4604.
40. Simone, P. M.; Lodge, T. P. *Macromolecules* **2008**, *41*, 1753.
41. Chen, H.; Choi, J. H.; Salas-de La Cruz, D.; Winey, K. I.; Elabd, Y. A. *Macromolecules* **2009**, *42*, 4809.

Chapter 9: Sulfonated Pentablock Copolymers Containing Structured Imidazolium Cations

Gao, R. and Long, T.E. (prepared for publication)

9.1 Abstract

Combination of living anionic polymerization and post functionalization strategies generated well-defined sulfonated pentablock copolymers containing structured imidazolium cations in sulfonated polystyrene middle block. Varying alkyl substitute lengths on imidazolium cations tailored physical properties and morphologies of sulfonated pentablock copolymers. Solution rheology revealed that sulfonated pentablock copolymers with shorter alkyl substituents (methyl, ethyl, butyl, and octyl) on imidazolium cations exhibited shear thinning behavior, i.e. measured viscosity linearly decreased with shear rate. In contrast, block copolymers with dodecyl imidazolium cations showed a Newtonian plateau at low shear rates and shear thinning at high shear rates. Solution rheological behavior of sulfonated pentablock copolymers was related to their micellar morphologies in cyclohexane. Field emission scanning electron microscopy (FESEM) demonstrated that sulfonated pentablock copolymers with smaller imidazolium cations (alkyl= methyl, ethyl, butyl, and octyl) possessed uniform, spherical, micellar morphology. However, block copolymers with dodecyl imidazolium cations did show clear spherical micellar structures in FESEM. Atomic force microscopy (AFM) revealed surface morphology of sulfonated pentablock polymer membranes, which strongly depended on alkyl substitute length on imidazolium cations. Thermogravimetric analysis (TGA) demonstrated that sulfonated pentablock copolymers with imidazolium cations exhibited enhanced thermal stability. Moreover, dynamical mechanical analysis (DMA), tensile analysis, and water uptake experiment indicated that varying length of alkyl substitutes on imidazolium cations systematically tailored

thermal and mechanical properties and water uptake behavior of imidazolium-containing sulfonated pentablock copolymers.

9.2 Introduction

Ion-containing block copolymers have attracted increasing attention for their unique properties and applications in emerging energy and biomedical applications.[1-5] Particularly, sulfonated block copolymers are an important class of ion-containing polymers that have found wide applications in water purification,[6-9] fuel cell membranes,[10-16] and electromechanical transducers.[17-19] Syntheses of sulfonated block copolymers with well-defined structures are of great importance in terms of fundamentally understanding their structure-morphology-property relationships.

However, polymerization of sulfonated monomers in a living/controlled manner remains as a challenge in this field.[20] Controlled polymerization of sulfonated monomers is often thwarted to the side effect of ions on the polymerization process. Moreover, solubility issues of sulfonated monomers restrict their copolymerization with non-ionic hydrophobic monomers.[20] Thus, post polymerization has been an alternative strategy that is widely used to synthesize well-defined sulfonated block copolymers. A typical post polymerization method includes the living anionic polymerization of styrene and diene monomers, and the subsequent sulfonation of the styrene block with acetyl sulfate. Living anionic polymerization has been known as a very useful synthetic method to prepare well-defined polymers with controlled molecular weight, near-monodispersed molecular weight distribution, controlled microstructure, and stereochemistry. The sulfonation of the styrene blocks can be completed with controlled sulfonate density and placement.[21-24] Our research group recently reported the synthesis of site-specifically sulfonated acrylic graft copolymers using living anionic polymerization and post sulfonation strategies.[11]

These sulfonated graft copolymers possessed well-defined chemical structures containing sulfonated blocks either adjacent to the backbone or at the branch termini. In addition, morphology and physical properties of sulfonated copolymers are tunable through counter cation structures.[25-27] Moore et al. reported a systematic study on perfluorosulfonate ionomers with ammonium cations in different sizes. They determined that thermal transition and dynamic mechanical relaxation of perfluorosulfonate ionomers were strongly related to the size of counter cations.[28] Colby et al. investigated the influence of counter cations on properties of sulfonated polyester ionomers.[29]They demonstrated that ionic conductivity of sulfonated polyesters was dramatically tailored with counter cation structures.

In the present study, we synthesized a novel series of sulfonated pentablock copolymers containing structured imidazolium cations. The base sulfonated pentablock copolymer, Nexar^{TM}, is a commercially available sulfonated pentablock copolymer from Kraton Polymers LLC. Living anionic polymerization and selective hydrogenation and sulfonation afforded these polymers well-defined chemical structures. Quantitative neutralization of sulfonic acid sites with 1-alkylimidazole generated novel imidazolium-containing sulfonated pentablock copolymers, which were classified as polymerized ionic liquids. Imidazolium cations are particularly interesting due to their high thermal and electromechanical stability and tunable chemical structures. In this study, alkyl substitutes on imidazolium cations varied from methyl, ethyl, butyl, octyl, to dodecyl, which provided imidazolium cations with different sizes. A systematic study on these imidazolium-containing sulfonated pentablock copolymers elucidated the influence imidazolium cation structure on solution rheology, morphology, thermal stability, thermomechanical properties, and water uptake property of sulfonated pentablock copolymers.

9.3 Experimental

Materials. Thionyl chloride (>99%), 1-bromoethane (>99%), 1-bromobutane (99%), 1-bromooctane (99%), 1-bromododecane (>95%), 1-methylimidaolze (99%), and potassium hydroxide (95%) were purchased from Aldrich and utilized without further purification. Acetonitrile (HPLC grade) was purchased from Fisher Scientific and used as received. The sulfonated block copolymer utilized in this study, Nexar^{TM}, was synthesized and provided by Kraton Polymers LLC. The synthetic details have been described in the literature. Neutral block copolymer poly(*t*-butyl styrene-*b*-styrene-*b*-hydrogenated isoprene-*b*-*t*-butyl styrene) was synthesized through the sequential living anionic polymerization of *t*-butyl styrene, isoprene, styrene, isoprene and *t*-butyl styrene, and a subsequent hydrogenation of the polyisoprene blocks. The corresponding sulfonated block copolymers were obtained through a selective sulfonation of the styrene middle block.

Synthesis of 1-alkyllimidazole

A typical synthesis of 1-alkylimidazole was as follows: in a two-necked, round-bottomed flask equipped with a magnetic stir bar and condenser, imidazole (8.00 g, 0.117 mol) and potassium hydroxide (7.59 g, 0.129 mol) were added to acetonitrile (120 mL) and stirred for1 h at 85 ^{o}C. 1-bromoocatane (20.45 mL, 0.118 mol) was subsequently added dropwise to the flask. The reaction was allowed to proceed at 85 ^{o}C for additional 4 h. The reaction suspension was filtered and the clear solution was concentrated in a rotary evaporator to remove all the solvents. The crude product was purified using chromatography with chloroform/methanol (98/2) on silica gel. The pure product was obtained as a liquid with a yield of 95%. Different 1-alkylimidazole compounds were synthesized in a similar manner. ^{1}H NMR spectroscopy was utilized to verify chemical structures.

Synthesis of imidazolium-containing sulfonated pentablock copolymers

Nexar™ polymer solution in cyclohexane (10 wt% solids) was weighed into a 250 mL round-bottomed flask equipped with a magnetic stir bar. 1-alkylimidazole was added to the Nexar™ polymer solution at a 1:1 stoichiometry. The mixture was stirred (1000 rpm) at 23 ^{o}C for 24 h. The resulting solutions were directly cast on a Mylar® substrate using an adjustable film applicator. All membranes were air-dried at 23 ^{o}C for 4 h and dried *in vacuo* at 60 ^{o}C for additional 72 h to remove residual solvent and moisture. Membranes were stored in a dessicator (<15% relative humidity) and dried *in vacuo* at 60 ^{o}C for 24 h immediately prior to characterization.

Instrumentation

^{1}H NMR spectra were collected on a Varian INOVA spectrometer (400 MHz, 23 ^{o}C). $CDCl_3$ and $CDCl_3/CD_3OD$ (95/5) was utilized for 1-alkylimidazole and sulfonated pentablock copolymers, respectively. Field emission scanning electron microscopy (FESEM) was performed on a LEO (Zeiss) 1550 with a 4 mm working distance. Solutions of imidazolium-containing sulfonated pentablock copolymers were diluted with cyclohexane (0.001 wt% solids) and cast on a silica wafer. The samples were air-dried for 24 h and subsequently imaged under FESEM. Atomic force microscopy (AFM) was conducted on a Veeco MultiMode AFM using a tapping mode. The spring constant of Vecco's Nanocensor silicon tips is 42 N/m. Dynamic mechanical analysis (DMA) was conducted on a TA instrument Q800 using a film tension mode under a temperature ramp of 3 ^{o}C/min. Stress-strain tensile analysis of these membranes was performed on a 5500R Instron universal testing instrument with a cross-head rate of 50 mm/min at ambient conditions. More than three samples were averaged to determine the Young's modulus. Solution rheology was conducted on a TA instruments AR-G2 strain-controlled rheometer equipped with

a cone-plate geometry. The solutions were allowed to equilibrate for 2 min at 25 ^{o}C prior to the first measurement, and the second measurement started immediately after the first measurement was complete. Data from both the first and second measurement were reported. Thermogravimetric analysis (TGA) was conducted on a TA instruments Q500 from ambient to 600 ^{o}C under a N_2 flow of 50 mL/min.

9.4 Results and Discussion

9.4.1 Synthesis of imidazolium-containing sulfonated pentablock copolymers

Scheme 9.1 depicts the synthesis of imidazolium-containing sulfonated pentablock copolymers. Base Nexar^{TM} polymers were synthesized with living anionic polymerization, followed with quantitative hydrogenation of polyisoprene blocks and selective sulfonation of polystyrene block. Living anionic polymerization afforded these polymers well-defined ABCBA pentablock copolymer structures with controlled molecular weight and narrow molecular weight distribution on each block. Sulfonation of polystyrene middle block was completed in a controlled fashion. Sulfonated pentablock copolymers utilized in this study have an ion exchange capacity (IEC) of 2.0. Here, IEC is defined as the milliequivalents of sulfonic acid per gram of polymer (mequiv/g). Quantitative neutralization of sulfonic acid sites with 1-alkylimidazole at a 1:1 stoichiometry generated a novel series of imidazolium-containing sulfonated pentablock copolymers, in which high-T_g poly(*t*-butyl styrene) (A) blocks served as physical cross-links to provide mechanical strength, low T_g hydrogenated polyisoprene (B) blocks imparted flexibility and elasticity, and hydrophilic imidazolium sulfonated polystyrene (C) block provided water or ion transport pathway. In the following discussion, all imidazolium-containing sulfonated block polymers were referred to as MD9200-SO_3[*Cn*Im]$^{+}$, where *Cn* indicated the length of alkyl substitute on imidazolium cations and varied from methyl (C1), ethyl (C2), butyl (C4), octyl

(C8) to dodecyl (C12). These polymers can be classified as block copolymers of polymerized ionic liquids because 1-alkylimidazolium 4-ethylbenzene sulfonate, which is an analogue of the sulfonated polystyrene repeat unit, are all ionic liquids with melting points below 100 ^{o}C. In addition, ^{1}H NMR spectroscopy verified the chemical structures of all imidazolium-containing sulfonated pentablock copolymers.

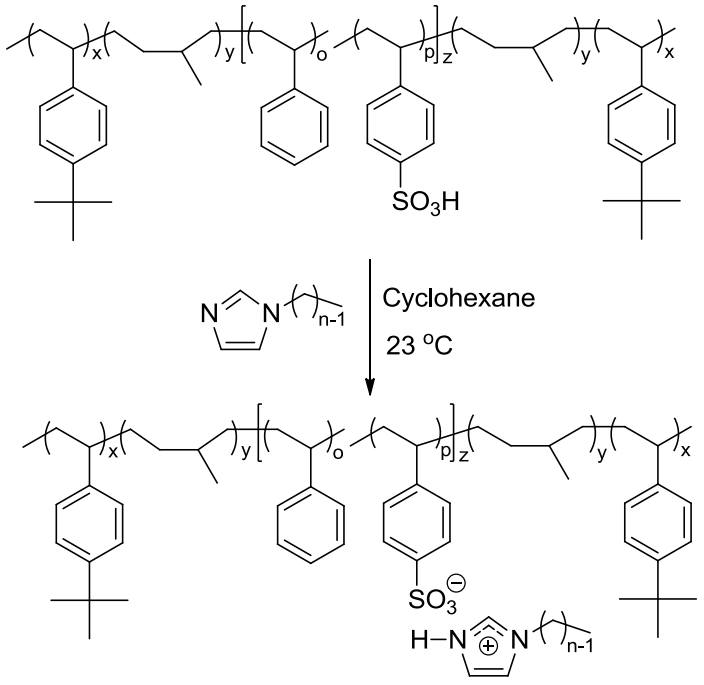

Scheme 9.1 Quantitative functionalization of sulfonated pentablock copolymers with 1-alkyimidazole, where alkyl substitute varied from methyl (n=1), ethyl (n-2), butyl (n=4), octyl (n=8), to dodecyl (n=12)

9.4.2 Solution rheology

Influence of imidazolium counter cation structures on rheological properties of sulfonated pentablock copolymers was investigated using a cone/plate geometry on a strain-controlled rheometer. All polymer solutions were allowed to equilibrate for 2 min and viscosity was measured as shear rate increased stepwise from 0.01 to 1000 S^{-1}. A second run was conducted immediately after the first measurement was complete. **Figure 9.1** shows the shear rate

dependence of viscosity of three representative samples from both first and second measurements. Sulfonated block copolymers with shorter alkyl substitutes on imidazolium cations (MD9200-SO_3[CnIm]$^+$, n=1, 2, 4, 8) showed comparable shear rate dependence of viscosity, as represented with the plot of MD9200-SO_3[C2Im]$^+$. Although the second run showed a slightly higher viscosity than the first run due to cyclohexane evaporation, both measurements indicated shear thinning behavior for MD9200-SO_3[C2Im]$^+$, where viscosity linearly decreased with shear rate. MD9200-SO_3H also exhibited shear thinning behavior but with a much lower viscosity. In contrast, MD9200-SO_3[C12Im]$^+$ displayed a short Newtonian plateau in the first run and a more well-defined Newtonian plateau in the second run. **Figure 9.2** depicts the plots of viscosity versus shear rate for all samples in the second run. MD9200-SO_3[C1Im]$^+$, MD9200-SO_3[C2Im]$^+$, MD9200-SO_3[C4Im]$^+$, and MD9200-SO_3[C8Im]$^+$ showed comparable rheological behavior relative to MD9200-SO_3H, although imidazolium-containing sulfonated pentablock copolymers showed a higher viscosity at each shear rate due to the electrostatic interactions. In sharp contrast, MD9200-SO_3[C12Im]$^+$ with long dodecyl chain on imidazolium cations displayed a well-defined Newtonian region with a viscosity near 2 Pa.S and a shear thinning region ranging from 10 to 1000 S^{-1}. Rheological behaviors of MD9200-SO_3[CnIm]$^+$ (n=1, 2, 4, 8) resembled that of latex and suspension particles.[30,31] However, MD9200-SO_3[C_{12}Im]$^+$ exhibited a typical rheological behavior of linear polymers. In order to understand the rheological behavior of these imidazolium-containing pentablock copolymers, studies on their solution morphologies were necessary.

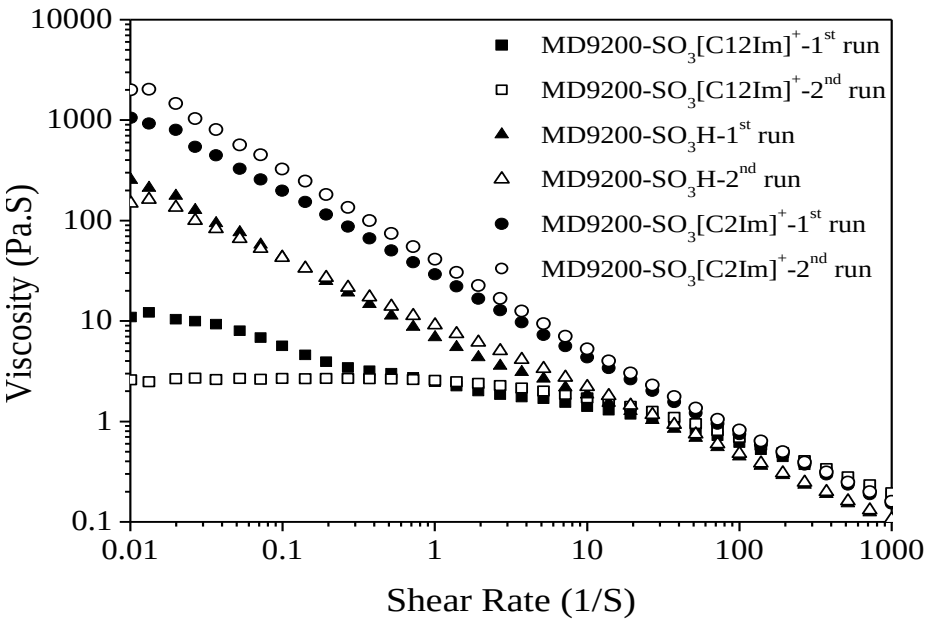

Figure 9.1 Comparison of shear rate dependence of viscosity of representative samples from both first and second run of solution rheology

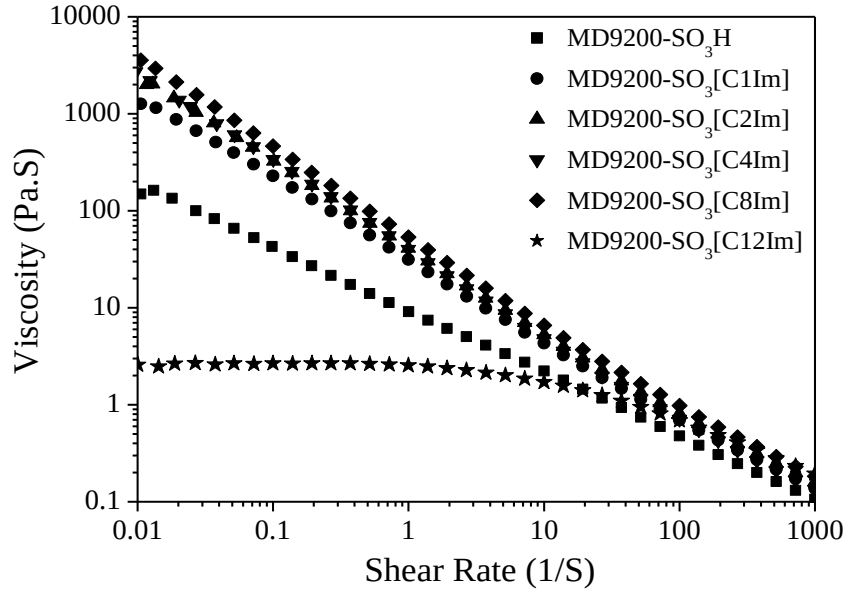

Figure 9.2 Solution rheology of MD9200-SO_3[CnIm]$^+$ with various structured imidazolium cation structures

9.4.3 Morphological characterization

Solution morphology of all imidazolium-containing sulfonated pentablock copolymers were studied using FESEM. Winey et al. previously investigated the solution morphology of

MD9200-SO_3H (IEC=2.0) using small angle X-ray scattering (SAXS) and transmission electron microscopy (TEM).[32] These earlier efforts demonstrated that MD9200-SO_3H formed spherical, core-corona, micellar structures in cyclohexane with polystyrene sulfonate (C) block forming a dense core and hydrogenated polyisoprene (B) and poly(*t*-butyl styrene) (A) blocks forming soft coronas. Here, we utilized FESEM to visually compare the micellar morphologies of sulfonated pentablock copolymers containing various imidazolium cations. **Figure 9.3** displays the FESEM images of all sulfonated pentablock copolymers. It is clear that MD9200-SO_3H and MD9200-$SO_3[CnIm]^+$ (n=1, 2 ,4) displayed uniformly dispersed spherical domains with diameters approximately 30~50 nm. Spherical domains were still visible in MD9200-$SO_3[C8Im]^+$; however, some of the domains were agglomerated. In contrast, MD9200-$SO_3[C12Im]^+$ did not show clear and uniform spherical domains in FESEM image. Micellar morphologies of these sulfonated pentablock copolymers correlated well with their solution rheological properties as we discussed above. MD9200-SO_3H and MD9200-$SO_3[CnIm]^+$ (n=1, 2, 4, 8) formed core-corona micellar structures in cyclohexane, which associated at high concentrations and provided high viscosity of the polymer solutions. Shear thinning occurred due to the shear-induced breakdown of the micelle association. In contrast, MD9200-$SO_3[C12Im]^+$ did not show micellar structures, which was presumably due to the weak electrostatic interactions in the polystyrene sulfonate block and its enhanced compatibility with cyclohexane. Thus, MD9200-$SO_3[C12Im]^+$ exhibited a Newtonian region in the solution rheology measurement.

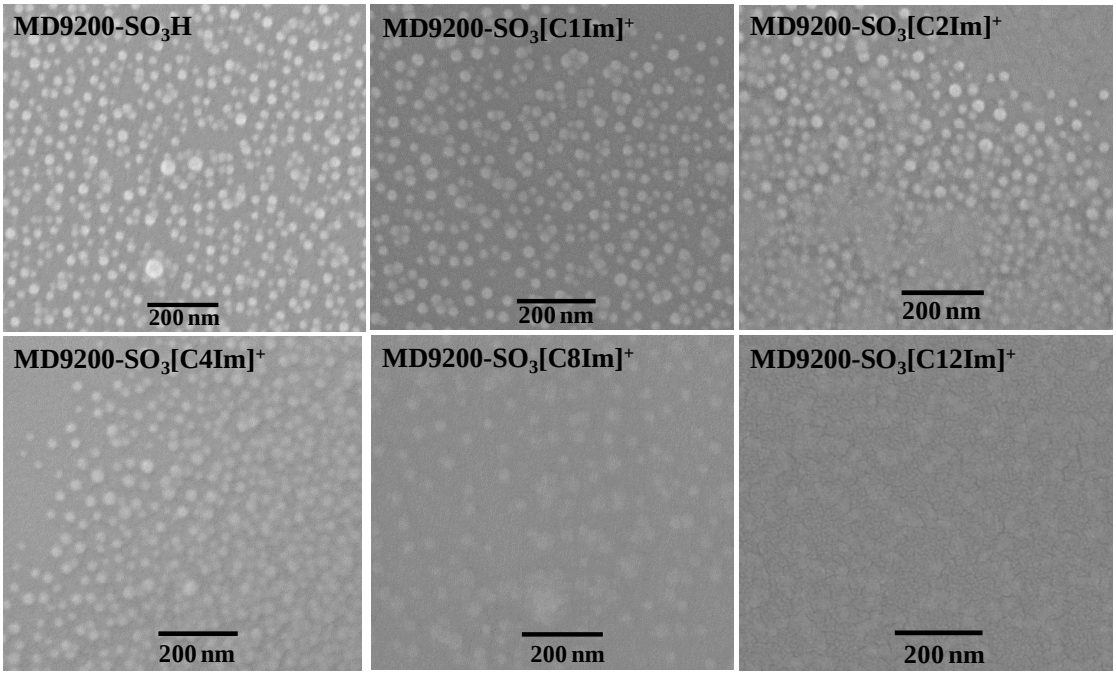

Figure 9.3 FESEM images of micellar structures of MD9200-SO_3H and MD9200-$SO_3[CnIm]^+$ (n=1, 2, 4, 8, 12) formed in cyclohexane

Influence of imidazolium cations on the surface morphologies of sulfonated pentablock copolymers was investigated using atomic force microscopy (AFM). **Figure 9.4** displays the AFM phase images of all sulfonated pentablock copolymers with various alkyl substitute lengths on imidazolium cations. In AFM phase images, rigid high-T_g domains appear as bright regions and flexible low-T_g soft domains appear as dark regions. It is clear that all polymers displayed we-defined microphase-separated morphology. Sulfonated pentablock copolymers with shorter alkyl substitute on imidazolium cations (MD9200-$SO_3[CnIm]^+$, n= 1, 2, 4) exhibited uniformly dispersed, spherical hard domains at the nanoscale (~60-80 nm). In sharp contrast, MD9200-$SO_3[C8Im]^+$ and MD9200-$SO_3[C12Im]^+$ displayed significantly reversed morphological features, where the hard domains were the dominant continuous phases and the soft phase became the isolated soft domains. In light of the micellar morphologies of these polymers in cyclohexane, it is reasonable to speculate that their surface morphologies were strongly related to their solution

morphologies. MD9200-SO_3H and MD9200-$SO_3[CnIm]^+$ (n=1, 2, 4) formed spherical micellar structures in cyclohexane. These polymers maintained the spherical structures in their bulk surface morphologies. However, long alkyl substitutes in MD9200-$SO_3[C8Im]^+$ and MD9200-$SO_3[C12Im]^+$ dramatically influenced their solution morphologies, as evidenced in FESEM and solution rheology experiments. We hypothesize that large imidazolium cations reduced the electrostatic interactions among ions, leading to micelles with flexible cores. These flexible micelles underwent multi-scale microphase separation upon membrane formation.

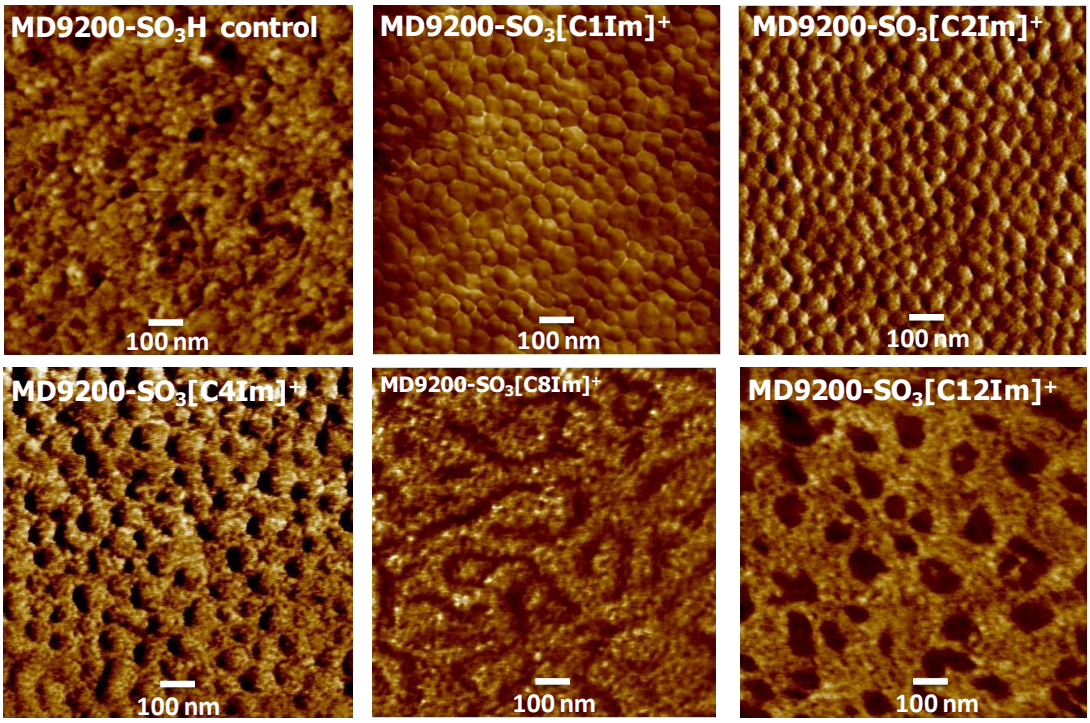

Figure 9.4 AFM phase images indicating surface morphology of MD9200 with various imidazolium cation structures

9.4.4 Thermal stability

In addition to morphological characterization, we also studied the influence of imidazolium cation on thermal stability of sulfonated pentablock copolymer using TGA. **Figure 9.5** shows the TGA curves of all sulfonated pentablock copolymer samples obtained in a N_2 atmosphere.

MD9200-SO_3H showed a weight loss of 15 wt% ranging from 200~350 ^oC. The weight loss in this temperature range was attributed to the degradation of sulfonic acid. Scherer et al. investigated the thermal degradation mechanism of poly(tetrafluoroethylene-*co*-hexafluoropropylene)-*g*-poly(sulfonate styrene) in an inert gas atmosphere. They demonstrated that the weight loss in TGA ranging from 270 to 350 ^oC corresponding to degradation of sulfonic acid sites, as demonstrated with FTIR spectroscopy.[33] In contrast, all imidazolium-containing sulfonated pentablock copolymers showed enhanced thermal stability upon neutralization of sulfonic acid sites. This observation was consistent with earlier literature. Crawford et al. reported that highly sulfonated poly(styrene-*b*-isobutylene-*b*-styrene) displayed enhanced thermal stability in TGA when converting counter cations from H^+ into Mg^{2+}, Ca^{2+}, and Ba^{2+}.[34]

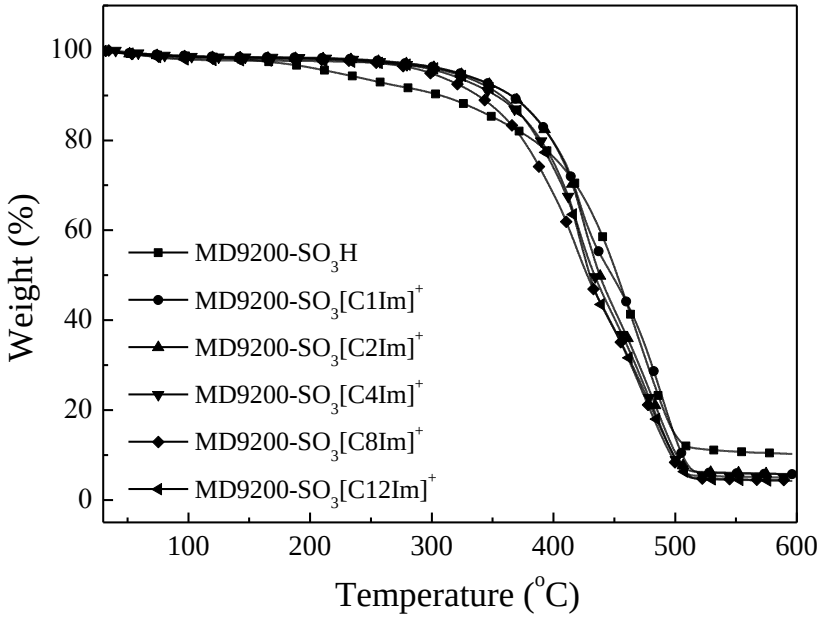

Figure 9.5 Thermal stability of MD9200 with various imidazolium cation structures

9.4.5 Thermomechanical properties

Thermomechanical properties of sulfonated pentablock copolymer bearing different imidazolium cations were investigated using DMA. **Figure 9.6** depicts the storage moduli (G') of tall polymer membranes as a function to temperature. All sulfonated pentablock copolymers showed comparable thermal transitions ranging from -50 ^{o}C to 0 ^{o}C, corresponding to the T_g of hydrogenated polyisoprene blocks. In addition, all polymers displayed well-defined rubbery plateaus above the hydrogenated polyisoprene T_g, indicating a high degree of microphase separation. **Figure 9.7** shows the zoom-in image of the rubbery plateau region (a) and rubbery plateau moduli as a function of alkyl substitute length on imidazolium cations (b). The data indicated that rubbery plateau moduli (40 ^{o}C) systematically decreased with increasing the alkyl substitute length, which was presumably due to the plasticizing effect of alkyl substitutes. In addition, **Figure 9.8** shows the dependence of onset flow temperature of sulfonated pentablock copolymers on the length of alkyl substitutes. It indicates that onset flow temperature systematical decreased with from 95 ^{o}C to 70 ^{o}C as alkyl substitute varied from methyl to dodecyl. Moreover, tanδ curves in **Figure 9.9** provided important information on thermal transition behavior of these polymers. tanδ curves of all samples displayed similar maxima near -30 ^{o}C, corresponding to the T_g of hydrogenated polyisoprene. More interestingly, samples with larger imidazolium cations also displayed β transitions around -80 ^{o}C, which corresponded to dynamic mechanical relaxation of alkyl substitutes on the imidazolium cations.

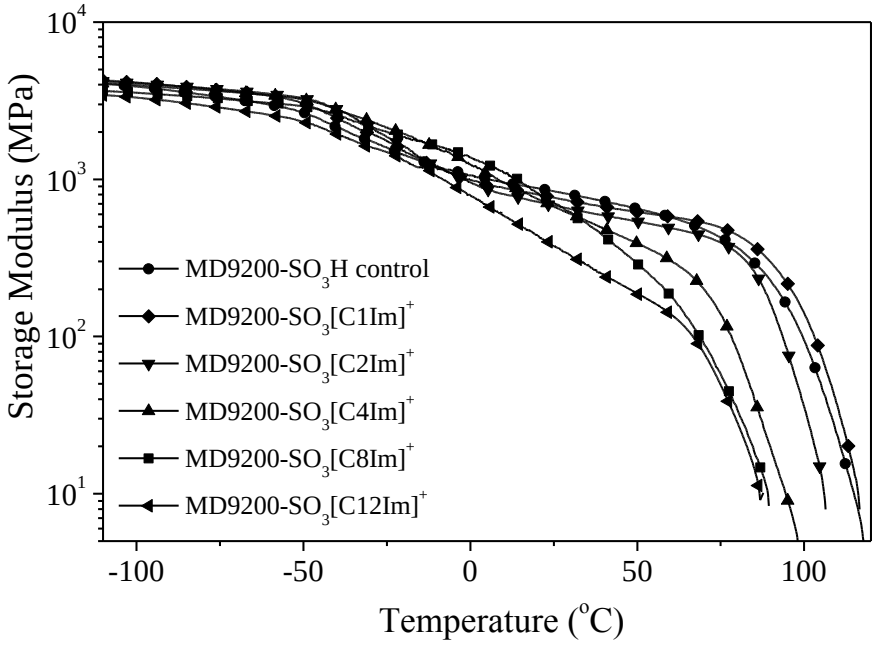

Figure 9.6 DMA curves of MD9200 with various imidazolium cation structures

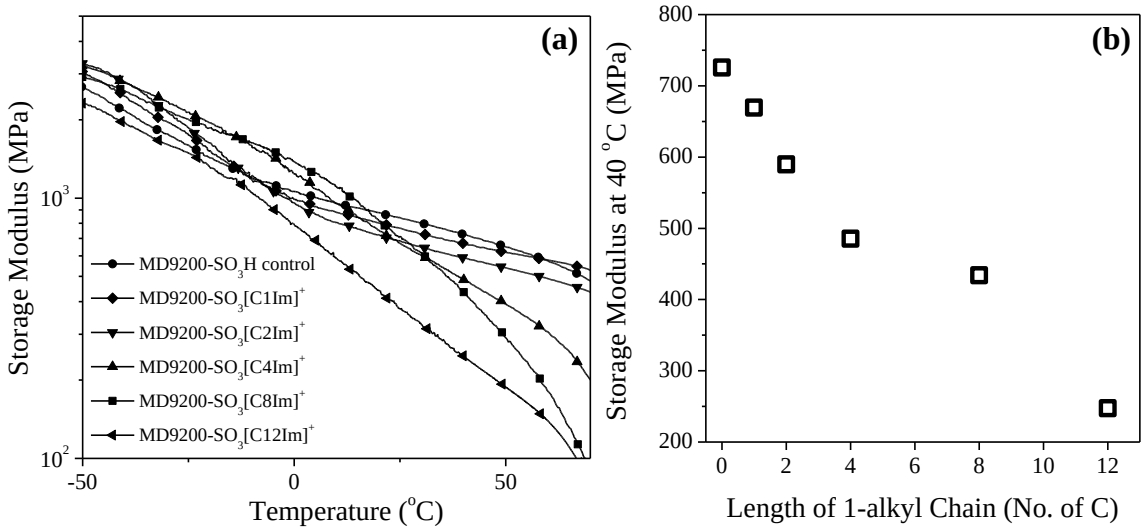

Figure 9.7 Influence of imidazolium cation structure on rubbery plateau moduli of MD9200-$SO_3[CnIm]^+$: storage modulus versus temperature (a) and dependence of alkyl substitute length of storage modulus (b)

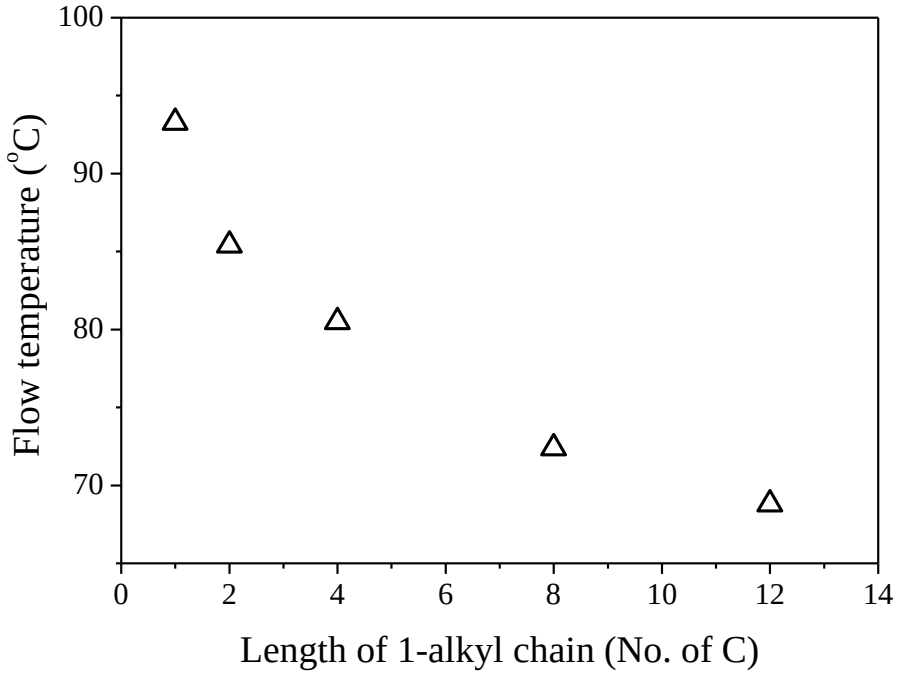

Figure 9.8 Influence of alkyl substitute length on onset flow temperature of MD9200-$SO_3[CnIm]^+$

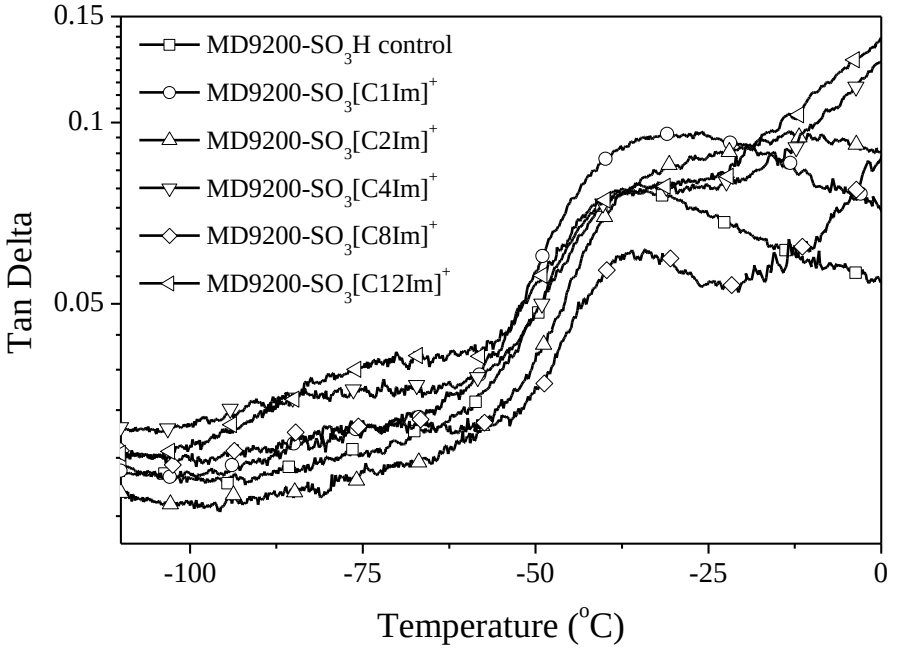

Figure 9.9 Influence of imidazolium cation structure on thermal transitions of MD9200-$SO_3[CnIm]^+$ in a low temperature range

9.4.6 Mechanical properties

Stress-strain tensile analysis was conducted to evaluate the mechanical properties of these polymers. **Figure 9.10** shows the stress-strain curves for all sulfonated pentablock copolymers. The strain was stopped at 50% in order to clearly compare the Young's modulus and strength at yield. Young's moduli of these polymers were determined according to the slopes of the initial stress-strain curves at strains less than 2.5 %. **Figure 9.10** clearly shows that Young's moduli of sulfonated pentablock copolymers systematically decreased with increasing alkyl substitute length on imidazolium cations. This observation agreed well with DMA. Both cases indicated a plasticizing effect of alkyl substitute on mechanical properties of sulfonated pentablock copolymers. Moreover, all polymers yielded at strain=5%; however, the strength at yield systematically decreased with alkyl substitute length on imidazolium cations.

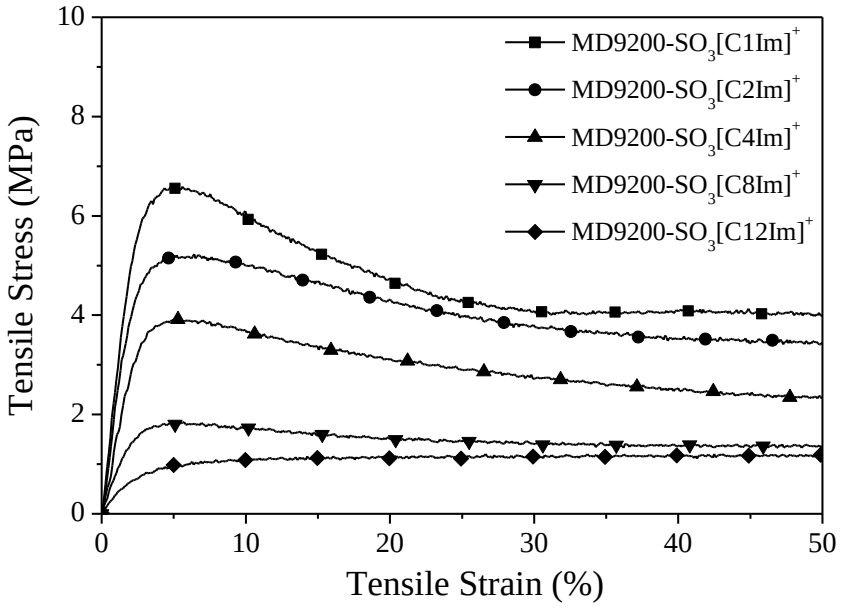

Figure 9.10 Tensile properties of MD9200 with various structured imidazolium cations

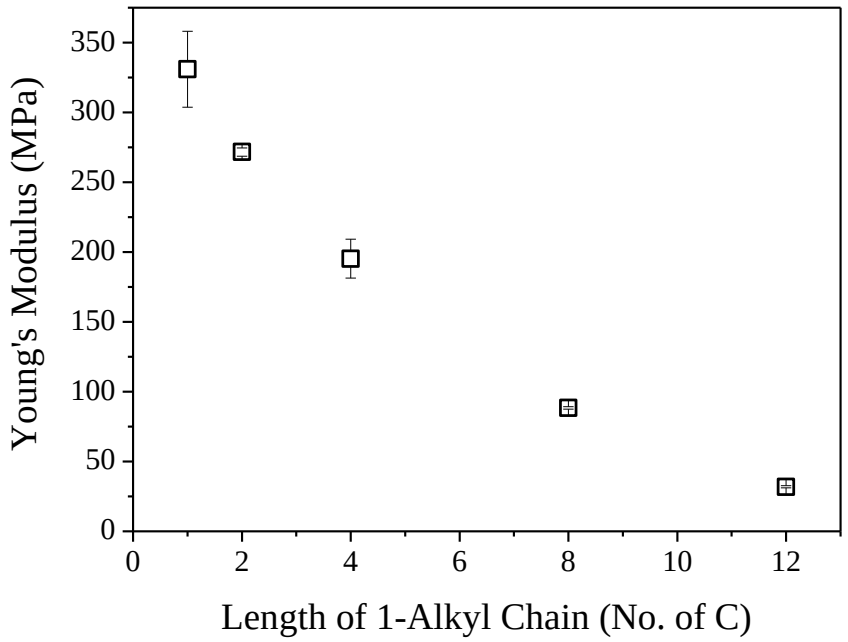

Figure 9.11 Influence of substitute alkyl chain length on Young's modulus of MD9200-$SO_3[CnIm]^+$

9.4.7 Water uptake properties

Figure 9.12 depicts the pure water uptake behavior of sulfonated pentablock copolymers with various imidazolium cations. Water uptake was determined according to the equation: water uptake wt%=$(m-m_o)/m_o$, where m is the swollen membrane mass and m_o is the initial membrane mass. Imidazolium-containing sulfonated pentablock copolymers showed less water uptake than sulfonated block copolymers in the sulfonic acid form. Moreover, water uptake of imidazolium-containing sulfonated block polymers decreased significantly with increasing alkyl substitute length on imidazolium cations. MD9200-$SO_3[C1Im]^+$, MD9200-$SO_3[C2Im]^+$, and MD9200-$SO_3[C4Im]^+$ showed comparable water uptake around 45 wt%. However, sulfonated block polymers with longer alkyl substitute (octyl and dodecyl) displayed significantly reduced water uptake. MD9200-$SO_3[C8Im]^+$ showed a water uptake around 8 wt%. However, MD9200-$SO_3[C_{12}Im]^+$ showed negligible water uptake. Altered polarity of imidazolium cations and

reversed morphology were responsible for the significantly reduced water uptake of MD9200-$SO_3[C_8Im]^+$ and MD9200-$SO_3[C_{12}Im]^+$. This study indicates water uptake behavior of sulfonated pentablock copolymers can be tuned for different levels through simply changing the length of alkyl substitutes on the imidazolium counter cations.

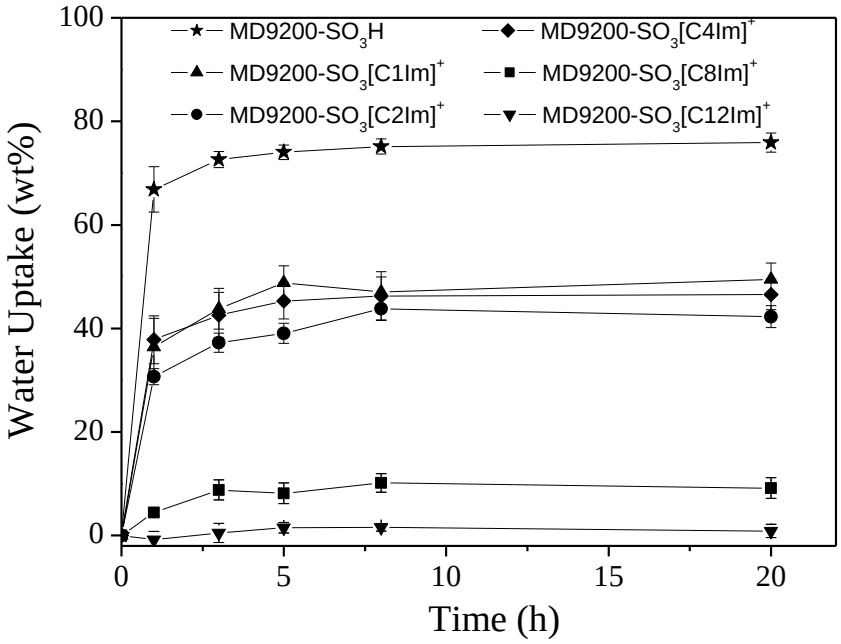

Figure 9.12 Water swelling behavior of MD9200 with various imidazolium cation structures

9.5 Conclusions

Quantitative neutralization of sulfonic acid sites of a commercially available pentablock copolymer, Nexar^{TM}, with 1-alkylimdazole generated a novel series of pentablock copolymers containing structured imidazolium cations. Alkyl substitutes on imidazolium cation varied from methyl, ethyl, butyl, octyl, to dodecyl. Complementary studies with solution rheology, FESEM, AFM, TGA, DMA, and tensile analysis elucidated the influence the alkyl substitute of imidazolium cations on morphology and physical properties of sulfonated pentablock copolymers. Block copolymers with shorter alkyl substitutes on imidazolium cations (MD9200-$SO_3[CnIm]^+$, n=1, 2, 4, 8) exhibited shear thinning behavior in solution rheology due to their micellar morphologies, as evidenced in FESEM. In contrast, MD9200-$SO_3[C12Im]^+$ showed a well-defined Newtonian region with a much lower viscosity of 2 Pa.S, suggesting weaker polymer association. Morphological characterization with FESEM and AFM demonstrated that alkyl substitutes on the imidazolium cations significantly influenced solution and bulk morphologies of sulfonated pentablock copolymers. MD9200-$SO_3[CnIm]^+$ (n=1, 2, 4) showed uniformly dispersed spherical domains at the nanoscale in both FESEM and AFM. However, MD9200-$SO_3[C8Im]^+$ and MD9200-$SO_3[C12Im]^+$ displayed reversed morphology, which was presumably due to weaker electrostatic interactions in polystyrene sulfonate block. Moreover, DMA studies indicated that storage moduli and onset flow temperatures of sulfonated pentablock copolymers systematically decreased with increasing alkyl substitute length on imidazolium cations due to the plasticizing effect. Observation in DMA was consistent with tensile analysis, which displayed a systematically decreased Young's modulus from 330 MPa to 32 MPa as the alky substitute varied from methyl to dodecyl. Moreover, water swelling experiment suggested

that alkyl substitutes on imidazolium cations tailored water uptake of MD9200-SO_3[CnIm]$^+$ for different levels.

9.6 Acknowledgements

This material is based upon work supported by the Kraton Polymers LLC. This work is partially supported by the Institute for Critical Technology and Applied Science (ICTAS) at Virginia Tech. Aspects of this work were carried out using instruments in the Nanoscale Characterization and Fabrication Laboratory (NCFL) operated by ICTAS. The authors also thank the U.S. Army Research Laboratory and the U.S. Army Research Office for their support through the Ionic Liquids in Electro-Active Devices Multidisciplinary University Research Initiative (ILEAD MURI) program under Contract/Grant Number W911NF-07-1-0452. We also thank Carl Willis and George Gumulka for insightful discussions.

9.7 References

1. Suga, T.; Takeuchi, S.; Nishide, H. *Adv. Mater.* 2011, *23*, 5545.
2. Cheng, S. J.; Beyer, F. L.; Mather, B. D.; Moore, R. B.; Long, T. E. *Macromolecules* 2011, *44*, 6509.
3. Oberoi, H. S.; Laquer, F. C.; Marky, L. A.; Kabanov, A. V.; Bronich, T. K. *J. Controlled Release* 2011, *153*, 64.
4. Oh, K. T.; Bronich, T. K.; Bromberg, L.; Hatton, T. A.; Kabanov, A. V. *J. Controlled Release* 2006, *115*, 9.
5. Solomatin, S. V.; Bronich, T. K.; Bargar, T. W.; Eisenberg, A.; Kabanov, V. A.; Kabanov, A. V. *Langmuir* 2003, *19*, 8069.
6. Jamroz, D.; Marechal, Y. *J. Phys. Chem. B* 2005, *109*, 19664.
7. Geise, G. M.; Freeman, B. D.; Paul, D. R. *Polymer* 2010, *51*, 5815.
8. Geise, G. M.; Lee, H. S.; Miller, D. J.; Freeman, B. D.; Mcgrath, J. E.; Paul, D. R. *Journal of Polymer Science Part B-Polymer Physics* 2010, *48*, 1685.
9. Park, C. H.; Lee, C. H.; Sohn, J. Y.; Park, H. B.; Guiver, M. D.; Lee, Y. M. *J. Phys. Chem. B* 2010, *114*, 12036.
10. Li, W. M.; Cui, Z. M.; Zhou, X. C.; Zhang, S. B.; Dai, L.; Xing, W. *J Membrane Sci* 2008, *315*, 172.
11. Saito, T.; Mather, B. D.; Costanzo, P. J.; Beyer, F. L.; Long, T. E. *Macromolecules* 2008, *41*, 3503.
12. Bae, B.; Hoshi, T.; Miyatake, K.; Watanabe, M. *Macromolecules* 2011, *44*, 3884.
13. Takamuku, S.; Jannasch, P. *Macromol. Rapid Commun.* 2011, *32*, 474.
14. Bae, B.; Yoda, T.; Miyatake, K.; Uchida, M.; Uchida, H.; Watanabe, M. *J. Phys. Chem. B* 2010, *114*, 10481.
15. Bi, H. P.; Chen, S. W.; Chen, X. B.; Chen, K. C.; Endo, N.; Higa, M.; Okamoto, K.; Wang, L. J. *Macromol. Rapid Commun.* 2009, *30*, 1852.
16. Bae, B.; Miyatake, K.; Watanabe, M. *ACS Applied Materials & Interfaces* 2009, *1*, 1279.
17. Wang, X. L.; Oh, I. K.; Lu, J.; Ju, J. H.; Lee, S. *Mater. Lett.* 2007, *61*, 5117.
18. Vargantwar, P. H.; Roskov, K. E.; Ghosh, T. K.; Spontak, R. J. *Macromol. Rapid Commun.* 2011, *33*, 61.
19. Jung, J. Y.; Oh, I. K. *Journal of Nanoscience and Nanotechnology* 2007, *7*, 3740.
20. Cavicchi, K. A. *ACS Applied Materials & Interfaces* 2012, *ASAP*.
21. Webster, O. W. *Science* 1991, *251*, 887.
22. Szwarc, M. *Adv Polym Sci* 1983, *49*, 1.
23. Cheng, C.; Yang, N. L. *Macromolecules* 2010, *43*, 3153.
24. Higashihara, T.; Ueda, M. *Macromolecules* 2009, *42*, 8794.
25. Barreto, S. M. A.; Suleiman, D. *J. Membr. Sci.* 2010, *362*, 471.
26. Suleiman, D.; Napadensky, E.; Sloan, J. M.; Crawford, D. M. *Thermochim. Acta* 2007, *460*, 35.
27. Zhou, N. C.; Burghardt, W. R.; Winey, K. I. *Macromolecules* 2007, *40*, 6401.
28. Phillips, A. K.; Moore, R. B. *Journal of Polymer Science Part B-Polymer Physics* 2006, *44*, 2267.
29. Tudryn, G. J.; Liu, W. J.; Wang, S. W.; Colby, R. H. *Macromolecules* 2011, *44*, 3572.
30. Takamura, K.; van de Ven, T. G. M. *J. Rheol.* 2010, *54*, 1.
31. Saito, Y.; Ogura, H.; Otsubo, Y. *Colloid. Polym. Sci.* 2008, *286*, 1537.
32. Choi, J. H.; Kota, A.; Winey, K. I. *Industrial & Engineering Chemistry Research* 2010, *49*, 12093.
33. Gupta, B.; Highfield, J. G.; Scherer, G. G. *J. Appl. Polym. Sci.* 1994, *51*, 1659.
34. Sloan, J. M.; Suleiman, D.; Npadensky, E.; Crawford, D. M. *ARL-TR-4357* 2008.

Chapter 10: Imidazolium Sulfonate-Containing Pentablock Copolymer/Ionic Liquid Composite Membranes for Electroactive Actuators

Gao, R.; Wang, D.; Heflin, J.R.; Long, T.E. (*submitted to Journal of Material Chemistry*)

10.1 Abstract

Block copolymer-ionic liquid composite materials emerge as promising candidates for electromechanical transducer applications. Herein, a novel imidazolium sulfonate-containing pentablock copolymers-ionic liquid composite material was prepared and fabricated into electroactive actuators, which exhibit effective actuation response under a low applied potential of 4V.

10.2 Introduction

Electromechanical polymeric transducers have received significant attention recently for many emerging applications, including electromechanical actuators, sensors, electro-active coatings, and artificial muscles. Desirable physical properties for polymeric membranes in electromechanical transducers include high ionic conductivity, tunable modulus *versus* temperature behavior, efficient response at relatively low voltages (<5 V), and facile fabrication processes.[1] However, only a few families of polymeric materials fully satisfy these requirements, and in most instances, anionic ionomers with random placement of sulfonates and carboxylates are leading candidates. There remains a unique opportunity for the design of multiphase block copolymers wherein the nanoscale morphology presents (1) a polar phase for ion-conductivity in the presence of added electrolyte, and (2) a nonpolar phase that imparts acceptable thermomechanical performance.

Block copolymer-ionic liquid composite membranes have emerged as promising candidates for electromechanical transducer applications. Due to microphase separation of different immiscible sequences, block copolymers self assemble into nanostructured materials and exhibit a combination of multiple properties.[2] Tailoring sequence length, molecular weight distribution, and chemical composition of each block generate various nanostructured materials for applications in water purification, fuel cell membranes, and energy storage.[3-5] Spontak et al. recently described the fabrication of electroactive membranes using non-neutralized sulfonated pentablock copolymers swollen with high levels of ethylene glycol and glycerol (~450 and ~500 wt%, respectively).[6] However, the morphology and dynamic mechanical properties of the composite membranes were not described. In order to achieve effective actuation response (high free displacement and blocked force) at low applied potentials (<4V), block copolymer-diluent composite materials with well-defined nanostructured morphology and good mechanical properties are necessary. Our research group has demonstrated the potential synergy of charged copolymers with imidazolium and phosphonium ionic liquids (ILs), which are defined as salts with melting temperatures below 100 ^{o}C. The introduction of ionic liquids into charged copolymer membranes improves the performance of electromechanical polymeric transducers due to their negligible volatility, high ionic conductivity, and high electrochemical and thermal stabilities.[7, 8] Therefore, a combination of block copolymers and ILs affords a unique platform to develop tunable membranes for electromechanical transducers. More interestingly, charged block copolymers enable preferential incorporation of ILs into the IL-compatible phase to form an organized IL dispersion in the polymeric matrix, leading to high ionic conductivity.[9] However, block copolymer-IL composite membranes, which simultaneously possess high ionic conductivity and excellent mechanical strength, are rarely reported in the literature.

10.3 Results and Discussion

10.3.1 Polymer design

Recent studies revealed that imidazolium-containing polymers showed promise as electromechanical transducers due to their reasonable high ionic conductivity, acceptable affinity to ionic liquids, and tailored structures and morphologies.[10, 11] Long et al. developed a series of *N*-vinylimidazolium- and vinylbenzylimidazole-based homopolymers with tailored ionic conductivity and thermal properties.[12] Gibson et al. investigated imidazolium-containing polyesters for high ionic conductive materials.[13] However, most recent studies focused on imidazole-containing homopolymers, random copolymers, and diblock copolymers. In order to achieve desired mechanical properties, triblock (ABA) and multiblock copolymers are particularly interesting candidates. Herein, we described a facile strategy to prepare imidazolium-containing pentablock copolymers from Nexar^{TM}, which is a commercially available sulfonated pentablock copolymer from Kraton Polymers LLC.[14] Combination of living anionic polymerization with a selective sulfonation strategy affords Nexar^{TM} well-defined pentablock architectures containing a selectively sulfonated polystyrene central block with an ion exchange capacity (IEC) at 2.0 (**Figure 10.1**, acid form). IEC is defined as the milliequivalents of sulfonic acid per gram of polymer (mequiv/g). Nexar^{TM} serves as a precursor for novel imidazolium-containing sulfonated pentablock ABCBA copolymers through facile and quantitative neutralization of sulfonic acid sites with various *N*-alkyl imidazoles (**Figure 10.1**). Modified Nexar^{TM} contains a hydrophilic, imidazolium polystyrene sulfonate central (C) block that enables incorporation of ionic liquids for ion transport, hydrogenated polyisoprene (B) blocks that impart membrane flexibility and elasticity, and hydrophobic poly(*t*-butyl styrene) (A) blocks that serve as physical crosslinks to provide mechanical strength in the presence of ILs.

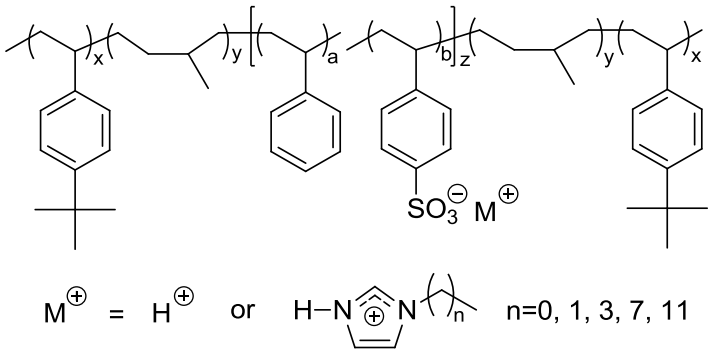

Figure 10.1 Sulfonated poly(*t*-butyl styrene-*b*-styrene-*b*-hydrogenated isoprene-*b*-*t*-butyl styrene) (KP-SO_3M^+) (IEC=2.0) with structured counter cations

10.3.2 Morphology

Field emission scanning electron microscopy (FESEM) and atomic force microscopy (AFM) revealed the microphase-separated morphologies of imidazolium-neutralized Nexar™ with 1-ethylimidazolium cations (KP-SO_3[EtIm]$^+$). **Figure 10.2**-a shows the FESEM image of KP-SO_3[EtIm]$^+$ cast from a dilute cyclohexane solution (1 mg/mL) onto a silicon wafer. FESEM demonstrated that KP-SO_3[EtIm]$^+$ formed uniformly dispersed spherical domains at the nanoscale (~30 nm), which presumably resulted from the micellar structures of KP-SO_3[EtIm]$^+$ in cyclohexane. Winey et al. previously characterized the solution morphology of the sulfonic acid form of Nexar™ in cyclohexane and demonstrated spherical micellar structures using transmission electron microscopy (TEM) and small angle X-ray scattering (SAXS).[15] These earlier efforts demonstrated that the polystyrene sulfonate central block formed a dense core of spherical micelles, and hydrogenated polyisoprene and poly(*t*-butyl styrene) blocks formed soft coronas. AFM confirmed that KP-SO_3[EtIm]$^+$ solid membranes displayed well-defined microphase-separated morphology (**Figure 10.2**-b). Lighter regions in AFM images represent hard phases, and darker regions represent soft phases. In light of the micellar structures observed in FESEM, the spherical structures, which are uniformly distributed in the AFM phase image,

arise from the polystyrene sulfonate central blocks. In a similar fashion to Winey et al., the bulk morphology of KP-SO_3[EtIm]$^+$ films was strongly related to solution morphology. Future complementary morphological characterization will fully understand the microphase separation behavior of these imidazolium-containing pentablock polymers.

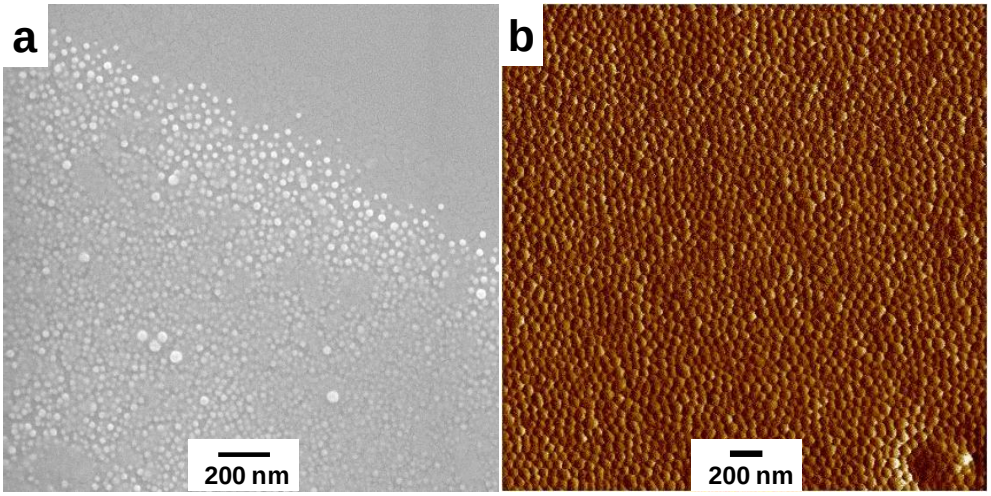

Figure 10.2 FE SEM image of micellar structures formed from KP-SO_3[EtIm]$^+$ in cyclohexane (a), surface morphology of KP-SO_3[EtIm]$^+$ solid membrane imaged with AFM (b)

10.3.3 Ionic liquid composite membranes for electromechanical actuators

Swelling KP-SO_3[EtIm]$^+$ films with 1-ethyl-3-methylimidazolium trifluoromethanesulfonate (EMIm TfO) (**Figure 10.3**-a.) generated pentablock copolymer-ionic liquid composite membranes. IL uptake was determined according to the following equation: wt% uptake = $(m-m_0)/m_0$, where m_0 is the initial film mass and m is the swollen film mass. **Figure 10.3**-b shows the swelling behavior of KP-SO_3[EtIm]$^+$ membranes in EMIm TfO as a function of time. EMIm TfO gradually swelled into the membrane with time and reached a maximum uptake near 35 wt%. Previous studies in our laboratories indicated that IL swelling behavior of polymer membranes strongly depended on polymer structure, ionic liquid type, sample dimensions, and

swelling conditions.[16] Mechanical property characterization using dynamic mechanical analysis (DMA) revealed that KP-SO_3[EtIm]$^+$/EMIm TfO composite membranes displayed well-defined rubbery plateaus with high storage moduli near 700 MPa. All samples showed two distinct thermal transitions due to a microphase-separated morphology (**Figure 10.3**-c). Thermal transitions near -35 ^oC and 110 ^oC corresponded to hydrogenated polyisoprene and poly(*t*-butyl styrene), respectively, which were independent of ionic liquid uptake (**Figure 10.3**-d). This observation supported that EMIm TfO preferentially located in the imidazolium-containing polystyrene sulfonate phase. Moreover, KP-SO_3[EtIm]$^+$/EMIm TfO composite membranes showed reduced rubbery plateau moduli relative to ionic liquid-free KP-SO_3[EtIm]$^+$ membrane due to plasticization.

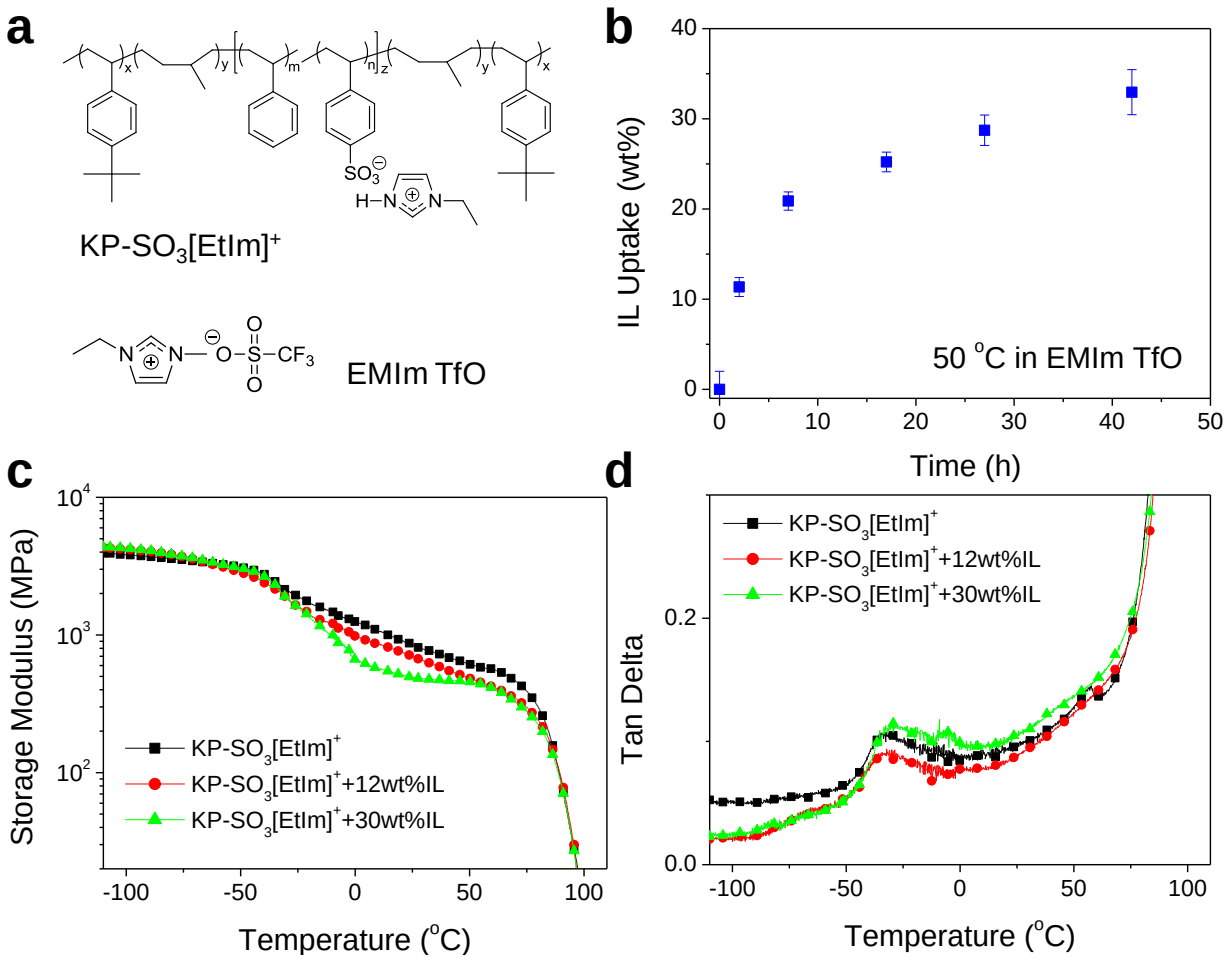

Figure 10.3 Chemical structures of KP-SO_3[EtIm]$^+$ and the ionic liquid EMIm TfO (a), swelling behavior of KP-SO_3[EtIm]$^+$ (40 μm thick) in EMIm TfO as a function of time (b), influence of EMIm TfO on storage modulus (c) and thermal transitions (d) of KP-SO_3[EtIm]$^+$ membrane (DMA, tension mode, 3 ^{o}C/min)

Fabrication of electromechanical actuators with KP-SO_3[EtIm]$^+$/EMIm TfO composite membranes employed a layer-by-layer, direct assembly method.[17] A KP-SO_3[EtIm]$^+$/EMIm TfO composite membrane of 40 μm thickness was placed between a 30-layer conductive network composite (CNC) layer and a 3 nm anionic gold nanoparticle layer. A layer-by-layer method affords uniform CNC coatings on ionomeric membranes with precisely controlled thickness at the nanoscale. **Figure 10.4**-a illustrates the structure of an electromechanical

actuator, which includes a central, ionomeric membrane, CNC layers, and gold electrode layers. The actuator mechanically deforms (actuates) upon an applied potential. **Figure 10.4** (b1~b4) shows the actuation performance under an applied potential of 4 V at ambient conditions (23 ^{o}C, ~43% relative humidity). The data confirms that the device deformed effectively upon an applied potential of 4V. **Figure 10.4**-c shows the actuator curvature of the device as a function of time. The actuator containing KP-SO_3[EtIm]$^+$/EMIm TfO composite membranes bended toward the anode and reached a maximum curvature of 0.26 mm^{-1} up to 20 s. The device under continued applied potential decayed back to the original position at t=46 s and further bended to the cathode side with a final curvature of 0.67 mm^{-1} at t=120 s. This actuation mechanism was described in the earlier literature, which is unique from typical back-relaxation behavior.[1] Zhang et al. proposed a two-carrier model to explain this phenomenon, where both cations and anions were mobile and accumulated on electrodes during bending. However, mobile cations and anions accumulated on electrodes at different rates due to different ion sizes and mobility, resulting in different bending directions at different times.[18] However, this model does not fully explain the actuation behavior of KP-SO_3[EtIm]$^+$/EMIm TfO actuators, where EMIm cations and TfO anions have comparable size, while the backward bending curvatures is approximately two times higher than the forward bending curvature. Thus, a fundamental understanding of the ion transport mechanism in KP-SO_3[EtIm]$^+$/EMIm TfO actuator represents an important future effort for this novel class of actuators.

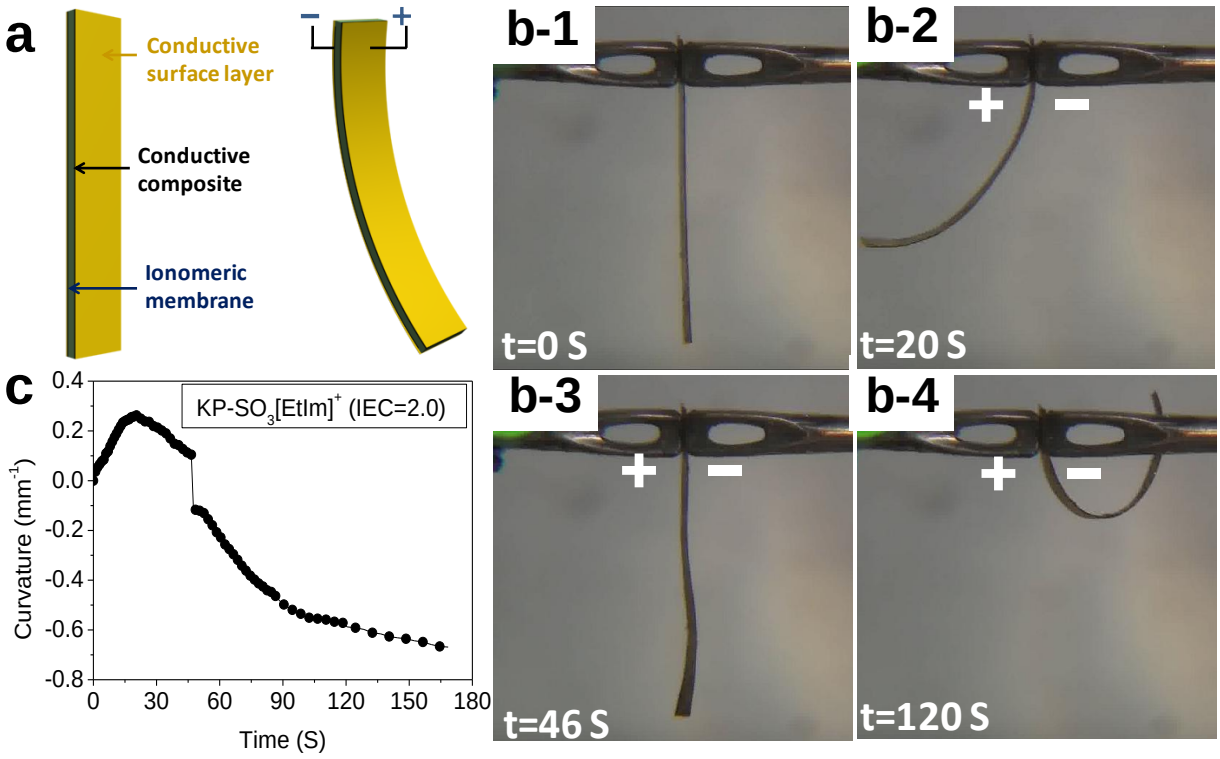

Figure 10.4 Schematic representation of an electromechanical transducer, deforming under an applied potential (a), images of an electromechanical transducer prepared with KP-SO_3[EtIm]$^+$ /EMIm TfO composite membrane, a poly(allylamine hydrochloride)/anionic gold nanoparticle CNC, and gold electrodes under an applied potential of 4V (b-1~4), curvature of electromechanical transducer as a function of time (c)

10.4 Summary

In summary, we described a facile materials strategy to fabricate electromechanical transducers from a pentablock copolymer-ionic liquid composite membrane. Imidazolium-containing pentablock copolymers were prepared from a commercially available sulfonated pentablock copolymer, and the ionic membranes possessed well-defined chemical compositions and microphase-separated morphologies. Combination of imidazolium-containing pentablock copolymers with EMIm TfO ionic liquid generated novel nanocomposite materials, which possessed good mechanical properties and exhibited actuation response with the application of a

low applied potential (4V). This study expands the class of multiphase copolymers that are suitable for electromechanical transducer applications. Fundamental understanding of the actuation behavior of pentablock copolymer-ionic liquid composite membranes will lead to optimal electroactive materials for electromechanical transducers in the future.

10.5 Acknowledgements

This work is partially supported by the U.S. Army Research Laboratory and the U.S. Army Research Office through the Ionic Liquids in Electro-Active Devices Multidisciplinary University Research Initiative (ILEAD MURI) program under Contract/Grant Number W911NF-07-1-0452. The authors also thank Kraton Polymers LLC. for their support. Additionally, many experiments were performed using instruments in the Nanoscale Characterization and Fabrication Laboratory (NCFL) operated at Virginia Tech.

10.6 Notes and references

Material: 1-Ethyl-3-methylimidazolium trifluoromethanesulfonate (EMIm TfO) (>98%) and *N*-ethylimidazole (99%) were purchased from Aldrich and used as received. Sulfonated pentablock copolymer was synthesized and provided by Kraton Polymers LLC. The neutral block copolymer poly(*t*-butyl styrene-*b*-styrene-*b*-hydrogenated isoprene-*b*-*t*-butyl styrene) was synthesized through the sequential living anionic polymerization of *t*-butyl styrene, isoprene, styrene, isoprene, and *t*-butyl styrene, and a subsequent hydrogenation of the isoprene blocks. The corresponding sulfonated pentablock copolymers were obtained through a selective sulfonation of the styrene middle block.

Preparation of KP-SO_3[EtIm]$^+$membrane: Sulfonated pentablock copolymer solution in cyclohexane (10 wt%) was added to a two-necked, round-bottomed flask equipped with a magnetic stir bar. A calculated amount of *N*-ethylimidazole (1:1 stoichiometry) was added dropwise to the flask under magnetic stirring (800 rpm). The solution was stirred at 23 ^oC for 24h and directly cast on a Mylar® substrate using an adjustable film applicator. This method generated uniform membranes with controlled thickness at 40 μm.

Fabrication of electromechanical actuators: The actuator device was prepared in a two-step process. CNC coating was initially applied to the KP-SO_3[EtIm]$^+$membrane using a layer-by-layer method. Framed membrane was alternatively soaked in a cationic poly(allylamine hydrochloride) aqueous solution (PAH, 10 mM, pH=4, Aldrich) and an anionic gold nanoparticles suspension (20 ppm, pH=9, diameter=3 nm, zeta potential=-40 mV, Purest Colloids Inc.). Alternated cationic and anionic thin layers were bounded tightly through electrostatic self-assembly, generating uniform coatings with well-controlled thickness at the nanoscale through adjusting the number of layers. In the second step, CNC-coated membrane

was soaked in EMIm TfO ionic liquid at 50 ^{o}C for 10 h and finally compression molded at 700 psi for 20 s between 50 nm thick gold foils to prepare the actuator.

Characterization: Atomic force microscopy (AFM) was conducted on a Veeco MultiMode AFM using a tapping mode at ambient conditions. Field emission scanning electron microscopy (FESEM) was performed on a LEO (Zeiss) 1550 with a 4 mm working distance. Dynamic mechanical analysis (DMA) measurements were performed on a TA Instruments Q800 dynamic mechanical analyzer in the film tension mode at a frequency of 1 Hz and a temperature ramp of 3 ^{o}C/min over the range -110 to 120 ^{o}C.

1. Duncan,A.J.; Leo, D. J.; T. E. Long, *Macromolecules* **2008**, 41, 7765.
2. Bucknall, D. G.; Anderson, H. L. *Science* **2003**, 302, 1904.
3. Peckham, T,J.; Holdcroft, S. *Adv. Mater*. **2010**, 22, 4667.
4. Geise, G. M.; Lee, H. S. Miller, D. J. Freeman, B. D. Mcgrath, J. E.; Paul, D. R. *J. Polym. Sci. Pol. Phys.* **2010**, 48, 1685.
5. Orilall, M. C.; Wiesner, U. *Chem. Soc. Rev*. **2011**, 40, 520.
6. Vargantwar, P.H.; Roskov, K.E.; Ghosh, T.K.; Spontak, R.J. *Macromol. Rapid Commun*. **2011**, 32,-
7. Green, M. D. Long, T. E. *Polym. Rev.* **2009**, 49, 291.
8. Lodge, T.P. *Science* **2008**, 321, 50.
9. Kim,S.Y.; Yoon, E.; Joo, T. ; Park, M.J. *Macromolecules* **2011**, 44, 5289.
10. Gu, Y.Y.; Lodge, T.P. *Macromolecules* **2011**, 44, 1732.
11. Weber, R.L.; Ye, Y.S.; Schmitt, A.L.; Banik, .M.; Elabd, Y.A.; Mahanthappa, M.K. *Macromolecules* **2011**, 44, 5727.
12. Green, M.D. Cruz, D. S.-d. l.; Ye. Y.; Layman, J.M.; Elabd, Y.A.; Winey, K.I.; Long, T.E. *Macromol. Chem. Phys.* **2011**, Accepted.
13. Lee, M.; Choi, U. H.; Cruz, D. Salas-de la.; Mittal, A.; Winey, K.I.; Colby, R.H.; Gibson, H.W. *Adv. Funct. Mater*. **2011**, 21, 708.
14. Willis, C. L.; Handlin, D. L.; Trenor, S. R.; Mather, B. D. (Kraton Polymers US LLC, Houston, TX). U.S. Patent Application 11/458856, January 25 **2007**.
15. Choi, J. H.; Kota, A.; Winey, K. I. *Ind. Eng. Chem. Res.* **2010**, 49, 12093.
16. Brown, R. H.; Duncan, A. J.; Choi, J. H.; Park, J. K.; Wu, T. Y.; Leo, D. J.; Winey, K. I.; Moore, R. B.; Long, T. E. *Macromolecules* **2010**, 43, 790.
17. Liu, S.; Montazami, R.; Liu, Y.; Jain, V.; Lin, M. R.; Heflin, J. R.; Zhang, Q. M. *Appl. Phys. Lett.* **2009**, 95.
18. Liu, Y.; Liu, S.; Lin, J. H.; Wang, D.; Jain, V.; Montazami,R.; Heflin, J. R.; Li, J.; Madsen, L.; Zhang, Q. M. *Appl. Phys. Lett*. 2010, 96.

Chapter 11: Overall Conclusion

Sulfonated polyurethanes with well-defined segmented structures were synthesized through direct polymerization of sulfonated monomers. Complimentary characterization on these sulfonated polyurethanes elucidated the influence of sulfonate charge placement, charge density and soft segment structures on physical properties and morphologies. PEO-based sulfonated polyurethanes with controlled sulfonate charge placement either in the soft segments (SSSPU) or hard segments (SHSPU) revealed the influence of sulfonate charge placement on thermal and mechanical properties, hydrogen bonding, and morphologies. SSSPU exhibited increased soft segment T_g (from -52 ^oC to -26 ^oC), suppressed PEG crystallization, high Young's modulus (9.11±0.88 MPa), and more well-defined rubbery plateau. In contrast, SHSPU displayed significantly increased soft segment T_g (from -52 ^oC to -5 ^oC), suppressed crystallization of both soft and hard segments, dramatically decreased Young's modulus (1.34±0.27 MPa), and narrowed rubbery plateau. Properties of SSSPU and SHSPU correlated well with their morphologies: SSSPU exhibited well-defined microphase-separated morphology, where hard segments microphase separated into needle-like hard domains. In contrast, SHSPU displayed phase-mixing of hard and soft segments due to their increased compatibility. Replacing hydrophilic PEO soft segments with hydrophobic PTMO soft segments generated sulfonated polyurethanes with good mechanical properties and high degree of microphase separation, which was due to the increased dynamic immiscibility between PTMO soft segments and sulfonated ionic hard segments. Moreover, incorporation of ammonium-functionalized MWCNTs (MWCNT-DMPA$^+$) or hydrophilic ionic liquids (IL) into sulfonated polyurethanes (SSSPU) provided novel nanocomposite membranes with tailored thermal and mechanical properties, and ionic conductivity. MWCNT-DMPA$^+$ exhibited uniform dispersion in DMF and SSSPU due to

good solvation of ammonium cations in DMF and inter-molecular ionic interactions between anionic SSSPU and cationic MWCNT-DMPA^{+}, respectively. In the case of SSSPU/IL nanocomposites, hydrophilic ionic liquid, 1-ethyl-3-methylimidazolium ethyl sulfate (EMIm ES), preferential located into the sulfonated PEO soft phase due to their high compatibility. SSSPU/IL exhibited significantly enhanced ionic conductivity (5×10^{-4} S/cm at 100 ^{o}C) and good mechanical properties that were independent of IL content. All SSSPU/IL composite membranes exhibited Vogel-Fulcher-Tammann (VFT) temperature dependence of ionic conductivity, indicating ion conduction in these composite membranes was strongly related to segmental motions of polymer chains.

Additionally, novel segmented polyurethanes containing imidazolium cations in the hard segments were synthesized through a conventional prepolymer method using an imidazolium diol-based ionic liquid as the chain extender. An unprecedented comparison of imidazolium-containing polyurethane (HMDI-IMI-2KPTMO) with a nonionic polyurethane (HMDI-BD-2KPTMO) analogue elucidated the influence of imidazolium cation on performance of polyurethane ionomers. Characterization results revealed that HMDI-IMI-2KPTMO exhibited reduced hard segment crystallinity and less hydrogen bonding relative to HMDI-BD-2KPTMO. However, AFM and SAXS data demonstrated that HMDI-IMI-2KPTMO possessed a well-defined microphase-separated morphology. This study suggests that enhanced immiscibility between hydrophobic PTMO soft segments and ionic imidazolium hard segments serves as the major driving force for microphase separation of imidazolium-containing segmented polyurethanes. Morphologies of these polyurethanes correlated well with their thermal and mechanical properties. Both imidazolium and nonionic polyurethane exhibited well-defined rubbery plateau and high maximum elongation (~900%). However, HMDI-IMI-2KPTMO

showed a higher rubbery plateau modulus (68 MPa at 25 ^{o}C) and a higher onset flow temperature (~150 ^{o}C) relative to the nonionic polyurethane due to the presence of imidazolium cations. Moreover, DRS demonstrated that imidazolium chloride ions in hard segments significantly increased the ionic conductivity of segmented polyurethane above the hard segment T_g. Studies on the HMDI-IMI-2KPTMO/IL composites revealed that EMIm ES preferentially located in the imidazolium ionic hard segments, as evidenced with systematically reduced hard segment T_g and increased inter-domain spacings. DRS demonstrated that ionic conductivity of HMDI-IMI-2KPTMO increased by five orders of magnitude upon incorporation of 30 wt% EMIm ES.

In addition, sulfonated pentablock copolymers with structured imidazolium cations were explored to elucidate the influence of imidazolium counter cation structure on physical properties and morphologies. Alkyl substitutes on imidazolium cation varied from methyl, ethyl, butyl, octyl, to dodecyl. Complementary studies revealed that block copolymers with shorter alkyl substitutes on imidazolium cations (MD9200-SO_3[CnIm]$^+$, n=1, 2, 4, 8) exhibited shear thinning behavior in solution rheology due to their micellar morphology. In contrast, MD9200-SO_3[C12Im]$^+$ showed a well-defined Newtonian region with a much lower viscosity of 2 Pa.S, suggesting weak polymer association. Morphological characterization with FESEM and AFM demonstrated that alkyl substitutes on imidazolium cations significantly influenced solution and bulk morphologies of sulfonated pentablock copolymers. MD9200-SO_3[CnIm]$^+$ (n=1, 2, 4) showed uniformly dispersed spherical domains at the nanoscale in both FESEM and AFM. However, MD9200-SO_3[C8Im]$^+$ and MD9200-SO_3[C12Im]$^+$ displayed reversed morphology, which was presumably due to the reduced electrostatic interactions in polystyrene sulfonate block. Moreover, DMA, tensile analysis, and water swelling experiments demonstrated that the mechanical properties and water uptake properties of sulfonated pentablock copolymers were

easily tailored with varying alkyl substitutes on imidazolium cations. Moreover, incorporation of ionic liquid, 1-ethyl-3-methylimidazolium trifluoromethanesulfonate (EMIm TfO), into sulfonated pentablock copolymers generated novel composite membranes, which enabled to fabricate electromechanical actuators. These actuators exhibited effective response with the application of a low applied potential (4V).

Chapter 12: Suggested Future Work

12.1 Sulfonated polyurethanes for adhesive applications

PEO-based sulfonated polyurethanes containing sulfonated ionic hard segments exhibited low mechanical strength due to the phase mixing between PEO soft segments and sulfonated hard segments. However, these polyurethanes displayed good adhesion properties, which were tunable with varying the sulfonation levels in the hard segments. Thus, a fundamental investigation of the influence of sulfonation level on adhesion and cohesion properties of PEO-based sulfonated polyurethanes will be interesting in the future study.

12.2 Sulfonated polyurethane/Li^+ composites for lithium battery applications

PEO-based copolymers have been extensively investigated for lithium battery applications due to their relatively high ionic conductivity and good solvation of lithium ions. However, most PEO-based lithium batteries suffer from crystallization of PEO segments due to the dramatically reduced ionic conductivity below PEO crystallization temperature. This dissertation described the synthesis and characterization of sulfonated polyurethanes containing sulfonated PEO-based soft segments, which exhibited suppressed PEO crystallization and extended rubbery plateaus. Thus, this material will be suitable for lithium battery applications. Future work will focus on preparation and characterization of sulfonated polyurethane/Li^+ composites and sulfonated polyurethane/ionic liquid/Li^+ composites for lithium battery applications.

12.3 Self-crosslinkable PEO-based polyurethanes for electromechanical actuators

This dissertation reported that PEO-based sulfonated polyurethanes enabled to fabricate sulfonated polyurethane/ionic liquid composite membranes for electroactive applications. However, stronger cross-linking sites are necessary to prepare ion gels with further enhanced

ionic conductivity and good mechanical properties. **Scheme 12.1** exemplifies the synthesis of self-crosslinkable PEO-based polyurethanes, in which, PEO soft segments enable incorporation of ionic liquids due to their high compatibility and self-crosslinkable hard segments provide desired mechanical strength. Incorporation of ionic liquids into these PEO-based polyurethane networks will generate novel ion gels that are suitable for applications in electromechanical transducers.

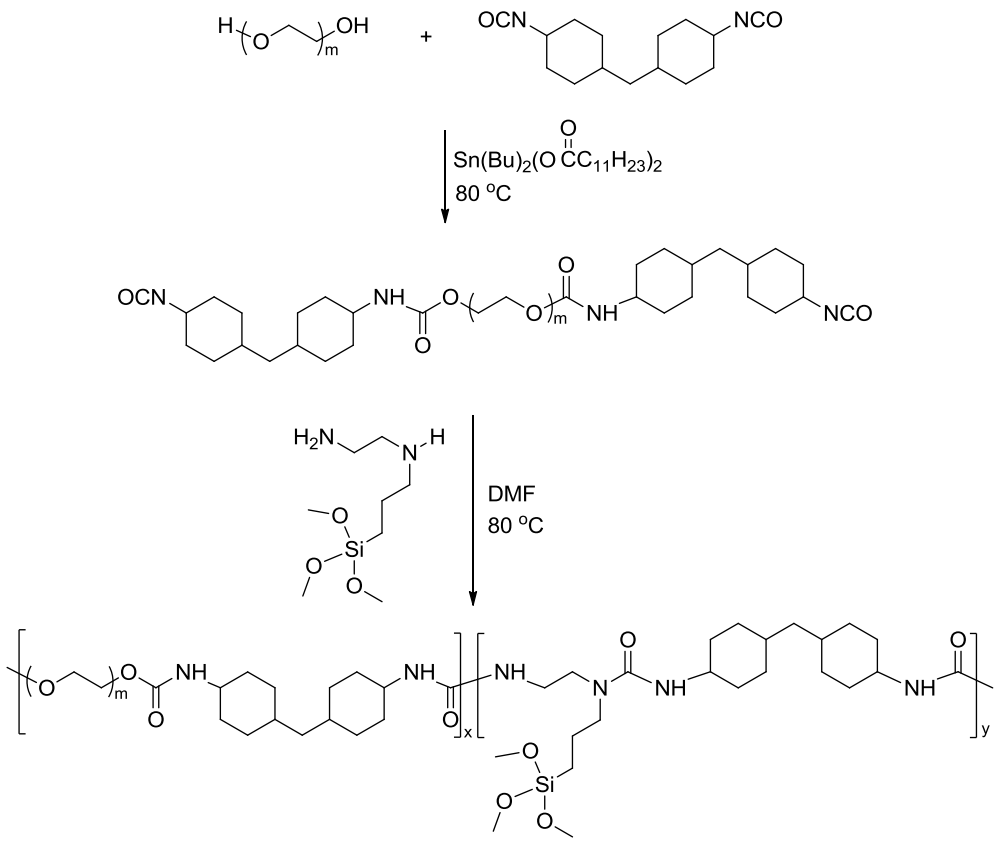

Scheme 12.1 Synthesis of self-crosslinkable PEO-based polyurethane networks

12.4 Sulfonated pentablock copolymers "cast with" ionic liquids

Previous studies reported in this dissertation indicated that Nexar^{TM} sulfonated pentablock copolymers formed micellar morphologies in cyclohexane, which dramatically influenced the bulk morphologies and physical properties of sulfonated pentablock copolymer membranes.

Preliminary data from AFM suggested that sulfonated pentablock copolymers cast with ionic liquid, 1-ethyl-3-methylimidazolium ethylsulfate, exhibited long-range ordered morphological features, which will favor high ionic conductivity and high water transport rate. Thus, future work will focus on a systematic investigation of morphology and physical properties of sulfonated pentablock copolymers cast with various contents of ionic liquids.

12.5 Structure-morphology-property relationships of sulfonated pentablock copolymer/ionic liquid composite membranes

Sulfonated pentablock copolymer/ionic liquid composite membranes presented in Chapter ten enabled to fabricate electromechanical actuators that exhibited effective actuation response under a low applied voltage (4 V). However, a fundamental investigation of the structure-morphology-property relationships of these composite membranes is necessary to understand their actuation performance and develop novel polymers for enhanced properties. Thus, future work will focus on several aspects including:

(1) ion diffusion rate measurements with ^{1}H NMR to understand the actuation behavior
(2) influence of sulfonation level on mechanical properties, ionic conductivity, and morphologies of sulfonated pentablock copolymers and the correlation with actuation performance
(3) influence of ionic liquid type and content on actuation performance
(4) influence of counter cation structures on actuation performance